Laser cooling of rubidium atoms in a magneto-optical trap

Thesis

Laser Cooling of Rubidium Atoms in a Magneto-optical Trap

Stephen Antony Hopkins B.A.(Open)

A thesis submitted in partial fulfilment of the requirements for the degree of Doctor of Philosophy in Physics at The Open University
30th September 1995

But leave the Wise to wrangle, and with me
The Quarrel of the Universe let be:
And, in some corner of the Hubbub coucht,
Make Game of that which makes as much of Thee.

Abstract

This thesis describes theoretical and experimental work concerning radiation forces on atoms, with particular reference to rubidium atoms confined in a magneto-optical trap.

After a short history of the field of laser cooling, a review of the semiclassical theory of mechanical interactions between two-level atoms and electromagnetic radiation is given. Different formulations of the semiclassical theory are discussed, including a new formulation in terms of momentum transfer amongst the plane wave modes of the electromagnetic field. Two important applications of light forces on atoms, namely 'optical molasses' and the 'magneto-optical trap', are then described with emphasis on experimental parameters.

Three sub-Doppler cooling mechanisms, 'sisyphus cooling', 'motion-induced orientation cooling' and the 'magnetically-assisted sisyphus effect', are described and their role in optical molasses and the magneto-optical trap is discussed. A new study of the polarisation gradients which occur in 3-D monochromatic light fields is presented and quantifies their relative presence in different light field configurations. Polarisation gradient parameters are developed and shown to be directly related to the relativistic spin tensor of the light field. Implications of this polarisation gradient study for laser cooling work are discussed.

The design, construction from scratch, operation and testing of a magneto-optical trap for rubidium are described, including novel designs for two vacuum cells. Preliminary experiments to characterise the trap are described and results are presented; they primarily concern the number and distribution of atoms in the trap.

Finally, the theory of time domain spectroscopy is reviewed. The construction and testing of a pulsed dye laser for study of coherent transients in samples of laser-cooled atoms and a proposed experiment to measure the temperature of cold atoms using coherent transients are described. Factors expected to influence the shape of coherent transients in cold atoms are discussed.

Acknowledgements

I would like to thank first of all Dr Alan Durrant and Dr Joy Manners who conceived and supervised this work. I particularly thank Alan for his faith in my abilities and Joy for her unwavering faith in the correspondence principle! I would also like to thank Dr Eric Usadi, who was my colleague and mentor in the laboratory for the first years of this work, for the skills he imparted to me and for the working experiment which he left behind. I thank Dr Robert Hasson for his assistance with computer programmes and footballs, Hongxin Chen for his enthusiastic assistance in the laboratory. Robert Blake for his introduction to 'tyan' and Dr Andrew Steane of Oxford for the very useful copy of his D.Phil thesis. Thanks also to the many other members of the O.U. physics department who have made this work a pleasure, and in particular to Roger Bence, Nobby Lowndes, Martin Sydee, Yvonne McKay, Fraser Robertson, Graham Jeffs and John Bellis for their friendly and invaluable help.

Finally, I would like to thank my friends, especially Emma Creighton, and all my family for their help and encouragement over the years.

Contents

List of Figures

List of Tables

Chapter 1
Introduction

This thesis describes both theoretical and experimental work related to the cooling and trapping of rubidium atoms by resonant laser light. Laser cooling and laser trapping are two distinct but related manifestations of the mechanical interaction between atoms and light, i.e. the exertion of 'light forces' upon atoms. Laser cooling refers to the deceleration of neutral atoms (or ions) in a gas by a velocity-dependent light force and laser trapping refers to the confinement of gaseous atoms within a small region by a spatially-dependent light force. Studies of the mechanical interaction of light and matter are traditionally classified within the field of atomic spectroscopy, a field which was given dramatic new impetus by the invention of the laser in 1960. Lasers opened the door to a large range of new experiments exploiting the high spectral brightness and monochromaticity of their radiation. This was certainly true as regards studies of light forces on atoms, an area of spectroscopy which developed steadily from 1970 onwards. Significant developments came during the period 1985 to 1986, which saw the construction of the first 'optical molasses'[1], a fully three-dimensional arrangement for cooling sodium atoms to sub-millikelvin temperatures, and the first observation of optically trapped atoms[2] in a dipole trap, which confined ~500 sodium atoms in a volume ~10^3 μm^3. These two breakthroughs might reasonably be said to mark the start of the modern age of 'laser cooling and trapping'. Since then, the field of laser cooling and trapping has continued to grow, as demonstrated by the steady increase in the number of research groups entering this area, and great progress has been made in the understanding and control of the motion of the cold atoms. The field is important for the following two reasons. Firstly, the new, high level of control of atomic motion is opening up many new areas of potential applications and secondly, the field of atomic physics

continues to provide some of the most precise tests of basic theories of physics, e.g. quantum electrodynamics and quantum mechanics.

The remainder of this introduction is in three sections. The first section is a brief history of studies of the mechanical interaction of atoms and light. The second section aims to give a non-specialist overview of the field as it has developed since 1985 with particular emphasis on existing or potential applications of cold atoms. The third section outlines the structure of this thesis and identifies those components which constitute 'original' research.

1.1 A short history of the physics of mechanical interactions between atoms and light

1.1.1 Mechanical interactions of atoms and light before 1985

Detailed reviews of studies of the mechanical interaction of atoms and light up to around 1985 may be found in [3-5]. This subsection is confined to describing the key developments. The idea that light might exert pressure on bodies existed as far back as Kepler's time. He postulated[6] that a comet's tail pointed away from the sun as a result of bombardment by a light flux emanating from the sun. This idea was only partially correct, nevertheless stellar radiation pressure is known today to be an important mechanism in the particle dynamics of the interstellar medium[7]. The quantitative study of mechanical interactions between atoms and light probably began when Maxwell postulated a radiation pressure[8] on any body in the path of a light wave. We now know that what Maxwell had derived was not the radiation pressure, but the momentum flux density due to the light wave. The actual light pressure then depends on the proportions of the radiations' momentum absorbed and reflected by the body[9]. The numerical value of the light pressure due to sunlight on the Earth's surface is about 10^{-5} Nm^{-2}. The very small values of light pressure due to either the sun or laboratory thermal sources made it difficult to study. The first experimental proof of the existence of radiation pressure was obtained by Lebedev[10] in 1901 and Nichols and Hull[11] in 1903; both observed the deflection by a light beam of metal vanes suspended in a vacuum. In 1910 Lebedev[12] also proved experimentally that gases were subject to radiation pressure.

The next important contribution[13] to the field was made by Einstein in 1917 in a paper devoted to the theory of quantum radiation. Firstly, he showed that radiation was absorbed and emitted by atoms not as spherical waves, but in discrete bundles (later called photons) which carried (directional) momentum of magnitude equal to $h\nu/c$. Secondly he established that the Maxwellian velocity distribution of atoms in thermodynamic equilibrium with black-body radiation was due to atomic momentum fluctuations caused by discrete radiation emission and absorption processes. The quantised nature of the momentum of light was confirmed in the celebrated experiments of A.H.Compton[31] between 1919 and 1923.

In the period 1900 to 1970, further laboratory studies of radiation pressure were few owing to the absence of suitable light sources. In 1933, O.Frisch[14] observed a 0.01 mm deflection of a sodium atomic beam by resonant light from a sodium lamp. In 1936 R.A Beth[15], using a sensitive torsion pendulum, was able to observe the angular momentum of light. Nevertheless, during this 1900 to 1970 period, radiation pressure had been recognised by astrophysicists to play a vital part in the evolution and structure of stars.

Following its invention in 1960, the laser began to make an impact in research laboratories. The first studies of radiation pressure due to laser light were performed by Ashkin et al[16] in experiments on laser light control of the motion of small macroscopic particles. The force on such a particle depends on the particle's properties of absorption, reflection and refractive index, and on the laser field configuration. In their first experiments, small spheres (~1 μm) made of transparent plastic and suspended in water were pushed and manipulated by 10 mW of argon-ion laser light. In [16], Ashkin also describes how his group were able to levitate small glass spheres (20 μm) in air by using an upwards propagating laser beam (250 mW). As discussed later in chapter 2, the total light force can be conveniently divided into a 'scattering force', which for a single beam acts along the propagation direction of the laser beam, and a 'dipole force', which acts along the gradient of the intensity of the light field. In this 'levitating' experiment, the laser beam was in its TEM_{00} mode with a gaussian intensity profile, so the dipole force acted radially towards the central beam axis, whilst the scattering force acted upwards along the beam and counterbalanced gravity.

Around the time of such experiments, interest naturally turned to investigations of laser light forces on individual atoms as opposed to macroscopic particles. If laser light resonant with an atomic transition could be made sufficiently intense, it would saturate the transition, i.e. produce an absorption rate close to the spontaneous emission rate. Strong light forces were predicted to occur for such high-intensity, resonant laser light, and theory appropriate to this new regime developed from the 1960's onwards. For a while, experiment lagged behind theory owing to the lack of laser sources of sufficient power and tunability. However, rapid strides were being made in the development of tunable dye lasers and during the 1970's experimental results began to flow. For instance, in 1972, Frisch's 1933 atomic beam deflection experiment was repeated twice using both spectral line lamps[17] and a dye laser[18,19]. As expected, the laser experiments showed beam deflections at least ten times greater than those obtained by the spectral line lamps.

In 1974 and 1975 respectively, Hänsch and Schawlow[21] and Wineland and Dehmelt[20] proposed a new idea, now known as 'Doppler cooling', to use resonant laser light to cool ions[20] and atoms[21] to very low temperatures in the range 10^{-4} to 10^{-3}K. The mechanism of Doppler cooling is described in detail in chapters two and three. The

possibility of such low temperatures encouraged research into the use of cold atoms in high-resolution spectroscopy and frequency standards work where precision was usually limited by the unavoidable Doppler line broadening and transit times. The first successful demonstrations[22] of laser cooling were in 1978 on Ba^+ and Mg^+ ions in (respectively) Paul and Penning ion traps. In the early 1980's, other significant experiments using Doppler cooling involved the longitudinal slowing of atomic beams[23] to a 1-D temperature of 70 mK and the transverse cooling of an atomic beam[24] to a 2-D temperature of 3.5 mK. Also around this time, another theoretically predicted effect of light forces, the diffraction of an atomic beam by a standing wave of light, was observed[25-27].

1.1.2 Laser cooling and trapping from 1985 onwards

In 1985, the construction of the first 'optical molasses'[1], in which sodium atoms were cooled to sub-millikelvin temperatures, began the 'modern age' of laser cooling. 1986 saw the first observation of optically trapped atoms in a dipole trap formed at the focal point of an intense red-detuned laser beam[2]. This was the analogue for neutral atoms of the earlier experiments of Ashkin on small plastic and glass spheres. In 1988 came the important invention of the magneto-optical trap[28], in which the addition of a quadrupole magnetic field to the apparatus of optical molasses brings about a spatially dependent light force on the atoms. Optical molasses and the magneto-optical trap (MOT) are currently the most commonly used arrangements for laser cooling; they are discussed in detail in subsequent chapters. When first constructed, both molasses and the MOT were loaded with atoms from an atomic beam. In 1990 however, it was found that an MOT could be loaded directly from a room temperature vapour in a small vacuum cell[29], thus avoiding the elaborate vacuum chambers required for atomic beams.

Magneto-optical traps are to be distinguished from the entirely different 'magnetic traps', e.g.[29,30,32,33], which are also used to trap neutral atoms. Magnetic traps rely on the attraction of the magnetic dipole moment towards potential energy minima in a suitably configured magnetic field. They do not involve light forces and typically require much larger magnetic fields than the magneto-optical trap. A magnetic trap[30] was first achieved in 1985, and they have recently become important with regard to 'evaporative cooling'[32,33] and the observation of Bose-Einstein condensation[34].

As progress was made with techniques for trapping and cooling neutral atoms, parallel developments were taking place in the cooling of atomic ions; see review[5]. The Paul and Penning traps are both designs of ion trap where the trapping is achieved by exploiting the force on the ionic charge in an AC electromagnetic field. The thermal velocities of trapped ions may be damped by laser cooling techniques similar to those employed for neutral atoms, and again the low temperatures attainable allow an increase in spectroscopic precision. Other interesting ion experiments are those in which a single ion is trapped and

cooled[35], allowing the detailed study of fundamental aspects of the interaction of light and atoms such as quantum jumps and photon anti-bunching.

Up until 1988, laser cooling and trapping had been understood in terms of so-called 'Doppler cooling' theory (chapter 3) which is based on an idealised atom with only two non-generate energy levels. However, experiments around that time measured temperatures an order of magnitude lower than the predicted 'Doppler cooling limit'[36,37,38]. This discrepancy led to the development in 1989 of 'sub-Doppler cooling' theories (chapter 4), which also take into account the Zeeman degeneracy of the energy levels[39,40]. Initially just three different sub-Doppler mechanisms were proposed. From 1989 up to the present day, the field has been evolving rapidly with discoveries and developments occurring on both theoretical and experimental fronts. For instance, on the theory side, several more cooling mechanisms, such as velocity selective coherent population trapping[41,42], Raman cooling[43,44,59], and magnetically assisted sisyphus cooling[40] have been discovered. On the experimental side, many new techniques such as 'moving molasses'[45,46], 'evaporative cooling'[33,47,48] and 'dark-state' trapping[49-51] have been developed. Reviews of recent developments may be found in [52-56].

After the Doppler cooling limit had been breached in 1989, a lower theoretical temperature limit known as the 'photon recoil' limit became the next target for experiments. The photon recoil limit exists because most cooling mechanisms rely on the continual exchange of quanta of energy between the atoms and the light field, which implies that even the slowest atoms will have a residual momentum of around $\hbar k$, the momentum of one photon. As a numerical example, the photon recoil temperature of rubidium, cooled on the 780 nm transition, is ~180 nK. One-dimensional temperatures below the recoil limit were achieved[42] in 1988 and two dimensional temperatures[58] corresponding to a sixteenth of the recoil limit in 1994, using the technique of velocity-selective coherent population trapping. To the best of my knowledge at the time of writing, 3-D cooling below the recoil limit has not yet been achieved in an optical trap using light forces, although Raman cooling has reached a 3-D temperature of just twice the recoil limit[43]. However 3-D cooling below the photon recoil limit was recently achieved in a magnetic trap[34], when temperatures as low as 20 nK were reported for a Bose-Einstein condensate of a gas of rubidium atoms (see section 4.7.11).

1.2 Practical applications of laser cooling and trapping

In what follows, I have somewhat arbitrarily divided the existing and potential applications of laser cooling and trapping into two subdivisions: firstly, technological applications and applications pertaining to other related areas of physics, and secondly, laser cooling and trapping as an application in its own right.

1.2.1 Laser cooling: technological applications and applications in related areas of physics

Considerable research is taking place into the development of higher precision caesium clocks for time standards using cold atoms[60,61]. A caesium clock measures the frequency of a hyperfine ground state transition when a caesium atomic beam passes through a microwave interaction region. The precision of the best conventional caesium clock is limited by the short interaction time of the atoms and the microwaves. The use of cold, slow atoms to observe Ramsey fringes[62] in a fountain arrangement[61] firstly allows an increase in the interaction time, and can also lead to a reduction in some other systematic errors such as the second order Doppler shift. A 10^2 increase in precision has been predicted[61], which would bring the clock resolution to around 10^{-16} seconds. Potential uses for such clocks include higher resolution timing for particle physics experiments, refined tests of general relativity using clocks in satellites and/or planes, and the development of highly accurate geopositioning methods using time data broadcast from satellites. Should the radio signals from pulsars eventually become the most precise time standard, high precision caesium clocks will be needed as a link in the frequency standards chain.

The reduced Doppler broadening and long interaction times associated with laser-cooled atoms or ions allow improved accuracy in the measurements of transition frequencies and hence in the determination of some universal constants. An eventual precision of 1 part in 10^{18} has been predicted[5]. As an example, cold atoms are being used[63] as part of a frequency chain linking measurements of hydrogen spectral frequencies to standard clock frequencies in order to enable more accurate determination of the Rydberg constant.

Laser cooling techniques were proposed as a method of isotope separation[64] as early as 1970, and demonstrated for barium in 1974[65]. More recently, laser trapping has been proposed as a method of storing and handling radioactive materials such as ^{21}Na[66], ^{79}Rb and Fr[67] and even antihydrogen, and also as a means of providing a sensitive target for electron scattering experiments[68]. Laser cooling is also used to damp the transverse motion of particles in accelerator storage rings[69].

Light forces have also found a use in biology as 'optical tweezers'[70], whereby live bacteria and objects within individual living cells can be manipulated under a microscope by a laser beam focused to a point. Related techniques were used[53] to manipulate and measure properties of a single molecule of DNA.

Another example of the precise manipulation of atoms allowed by laser cooling is in the proposed use (see review[71]) of laser cooling in nano-fabrication. The transverse velocities in atomic beams used to deposit atoms on a semiconductor surface may be controlled to allow the creation of structures of widths around 10 nm. Such techniques may ultimately lead to further miniaturisation of integrated chip circuitry.

Cold atoms may be used in investigations of aspects of quantum mechanics such as measurement theory, non-locality, Bell's inequalities, quantum non demolition and 'Schrödinger cats'. For instance, new tests of quantum non-locality have been proposed and are being constructed[72]; these experiments require highly collimated, mono-velocity atomic beams which are created using laser cooling techniques.

A project at Sussex University, continuing work described in [73], proposes to use cold atoms in fundamental research in particle physics; one possibility is to measure the electric dipole moment of the electron (if it is other than zero), or at least to reduce the uncertainty in the best current measurements. The use of cold atoms should reduce the systematic errors associated with the relevant spectroscopic measurements. Other applications in this 'low energy particle physics' field include the measurement[74] of parity non-conservation in atomic caesium, and an improved test[75] of the charge neutrality of atoms.

1.2.2 Laser cooling and the developing field of atomic optics

The study of laser cooled atoms is a worthy subject in its own right, as the low temperature and low density (the atoms remain in the gas phase) represent a new physical regime. One study area of considerable interest is the localisation of atoms in 'optical lattices'[76-86,49,50] which are formed by the intersecting laser beams used in optical molasses. Optical lattices are discussed in section 4.6. Another area of active research is that of 'cold collisions'[87-102], discussed in section 3.5.2. This is the study of interatomic collisions in the new low temperature regime of laser cooling, where the de Broglie wavelengths of the atoms become large (~ 1 μm) and where the interaction time is long enough to allow the atoms to change internal state during the collision. The large de Broglie wavelength of cold atoms also allows the realisation of atomic interferometry. Beams of atoms have been divided coherently by diffraction gratings made either from light [103,104] or from a nanofabricated thin wire grating[105,106] and recombined after the atoms have traversed different paths. The resulting interference pattern allows the measurement of the phase difference between the two atomic paths; as examples, this has been used to measure the Sagnac phase shift[103] of a rotating interferometer, and the index of refraction of various gases for sodium matter waves[106].

Considerable research has been directed towards the improvement of cooling and trapping arrangements, where 'better' might mean, (as examples only) a colder trap[107], a fuller trap[108], a simpler trap[109] or a cheaper trap[110]. Experimentally, a large variety of cooling and trapping arrangements have been studied, exploiting the known cooling mechanisms in one, two and three dimensions. Most of the observed phenomena are understood in principle, but the three dimensional experimental arrangements represent a complex theoretical problem as far as exact quantitative calculations are concerned. Quantitative predictions of trap parameters such as temperature and number density for 3-D

arrangements are often made via numerical simulations and the development of numerical techniques such as the 'Monte Carlo wave function method'[111-117], discussed in section 2.5.2, is an area of ongoing research.

Cooling and trapping techniques allow a new level of manipulation of neutral atoms. As well as the storage of cold atoms in traps, and the production of collimated atomic beams with slow velocities and narrow velocity distributions, one might include the published *reports of atomic funnels*[45], *atomic fountains*[46], *atomic trampolines* [118] and atomic mirrors[119-121]. Atomic beams may be coherently split, reflected and diffracted by atomic analogues of the corresponding optical devices for light. These beamsplitters, gratings and mirrors for atoms are often made purely from resonant light. Thus there is an ironic inversion of conventional optics, and this new field of study has become known as 'atomic optics'. One of its exciting goals is the construction of a 'boser' or 'atom-laser', the atomic analogue of a laser, in which a beam of coherent atoms is produced in a resonant cavity made of atom-mirrors. Such research has been greatly encouraged by the recent (July and September 1995) observations of Bose-Einstein condensation (B.E.C.) of rubidium atoms[34] and lithium atoms[122], in which the atoms condense into the ground state of the atomic centre-of-mass wavefunction in the trapping potential. B.E.C. had previously been dubbed the 'holy grail' of laser-cooling, as it had always been a major goal of the field, e.g. see[123]. These recent observations have opened a door to new studies in laser spectroscopy, superfluidity and quantum mechanics.

1.3 The specific work of the O.U. research group

The Open University laser spectroscopy group entered the field of laser cooling in October 1991 with the intention of building a magneto-optical trap for rubidium atoms. Successful trapping was achieved around two years later in August 1993. Meanwhile the group had received an EPSRC grant to study coherent transients induced in cold atoms by short (~ns) laser pulses. Particular areas to be studied include the possibility of Bragg diffraction of pulses from atoms localised in an optical lattice, and the possibility of superradiance in cold atoms. The shape of the coherent transient signals should also yield information on line-broadening mechanisms within the cold sample. We set about the construction of the necessary ancillary apparatus, including two new vacuum cells suitable for these purposes and the construction of a dye laser to generate the light pulses. The vacuum cell for our first experiments came into operation in August 1994, and at the time of writing is used daily for magneto-optical trapping. Parameters such as beam intensity, detuning, number of atoms trapped, cloud size etc can all be measured quickly to reasonable accuracy (chapter 6). We are presently installing equipment to perform time of flight temperature measurements and equipment to allow computer control of aspects of the experiment. Operation of the dye laser at the appropriate frequency, resonant with the $5S_{1/2}$ to $6P_{3/2}$ transition in rubidium was

achieved in February 1995, and its performance is presently being optimised. The next phase of our work will be to undertake a series of proposed experiments on coherent transients in cold atoms, which have not been undertaken elsewhere so far. These experiments are discussed in chapter 7.

1.3.1 The layout of the thesis

In organising the material of chapters 2, 3 and 4, I chose to follow approximately the actual chronological development of the field of laser cooling itself. Hence sub-Doppler mechanisms are not described until chapter 4.

Chapter 2 gives an account of the semiclassical theory of the mechanical interaction of two-level atoms and electromagnetic radiation, commonly known as 'light forces'. Various differing formulations of the semiclassical theory, including a recent formulation by our group, are compared. The theory is developed in the first place for stationary atoms, then secondly for moving atoms and then finally the effects of momentum diffusion due to the quantum nature of the atom-light interaction are discussed. The implications of all these results for laser cooling and trapping are discussed. Finally, the semiclassical approach to light forces is compared with fully quantised approaches.

Chapter 3 is concerned with the two most important practical applications of light forces, namely optical molasses and the magneto-optical trap. The experimental arrangements and theory of operation for these two applications are described and examples of typical experimental parameters (e.g. number and temperature etc of trapped atoms) are given. The relationships between and constraints upon the important experimental parameters are discussed from both theoretical and experimental points of view.

Chapter 4 is concerned with the extension of laser cooling and trapping theory to multilevel atoms. It begins by describing three important components of sub-Doppler theories: optical pumping, polarisation gradients and light shifts. It then explains three specific sub-Doppler cooling mechanisms in detail; these are sisyphus cooling, the magnetically-assisted sisyphus effect and motion-induced orientation cooling. The discussion then turns to the role of sub-Doppler mechanisms in molasses and the magneto-optical trap, and in particular the phenomenon of atomic localisation in optical lattices. The chapter ends with brief descriptions of several recently developed new cooling/trapping arrangements.

Chapter 5 consists of theoretical studies which I have made of polarisation gradients in 3-D electromagnetic standing waves. The first part is concerned with ways of describing and comparing the various electric fields which may occur in the common laser cooling arrangement at the intersection of three orthogonal 1-D standing waves. The second part is concerned with ways of quantifying the extent to which an arbitrary 3-D electromagnetic standing wave contains the polarisation gradients associated with the sisyphus and

corkscrew cooling mechanisms. The third part is a mathematical demonstration that the sisyphus and corkscrew polarisation gradients are each related to the density and flux respectively of intrinsic spin in the electromagnetic field.

Chapter 6 describes the experimental apparatus used in the construction of our magneto-optical trap for rubidium atoms, which includes lasers and their controls, optical equipment, magnetic field equipment, vacuum equipment and diagnostic instruments. The chapter ends with the results of preliminary experiments performed with the trap, primarily concerning the distribution and number of atoms in the trap.

Chapter 7 is concerned with our group's current and future work, which is the study of coherent transients induced in cold atoms by sequences of short laser pulses. The chapter begins with a basic review of the relevant theoretical concepts. The construction and testing of a pulsed dye laser to be used in this work is described, followed by a detailed discussion of a proposed experiment to measure the temperature of cold atoms by coherent transients. Finally, factors which may influence the shape of the coherent transients are discussed.

1.3.2 Original work in this thesis

Theory

i) In chapter 2, I compare various published approaches to the semiclassical theory of light forces on two-level atoms; this includes discussion of a treatment recently published by our group and to which I contributed.

ii) In chapter 5, I make an extensive study of the nature of polarisation gradients in 3-D standing waves. This chapter is entirely original work and contains new results.

iii) In chapter 7, new experiments involving the interaction of coherent transients and cold atoms as proposed by our research group are described. I have contributed to the theory behind these experiments.

Experimental

iv) In chapter 6, I describe the apparatus used for our magneto-optical trap. Though the MOT is now a 'standard', many of the design aspects of our particular set-up are original, and the product of considerable thought. I mention in particular the design of the two vacuum cells for our specific experimental purposes. I also designed and built many other parts of our apparatus, and am responsible for the current working arrangement for the apparatus, which was arrived at after much trial and error experimentation. Chapter 6 also include results of some preliminary quantitative experiments made with the MOT, which allow comparison of the performance of our trap with those of other groups.

v) In chapter 7, I describe work which I have carried out regarding the construction, testing and optimisation of the pulsed dye laser to be used in our work.

Chapter 2
Semiclassical theory of light forces for two-level atoms

The main objective of this chapter is to introduce the semiclassical theory of light forces, i.e. the mechanical interaction of atoms and electromagnetic radiation. The scope of the chapter is deliberately restricted entirely to two-level atoms; the theory of light forces in multilevel atoms is discussed in chapter 4. Section 2.1 describes the principles and assumptions behind the semiclassical approach. The next three sections derive various expressions for the light forces with new complexities being added section by section. Thus section 2.2 gives the semiclassical derivation of the mean force experienced by a stationary atom in a general monochromatic light field. Section 2.3 then discusses the extension of that derivation to moving atoms and section 2.4 deals with the 'diffusion' of atomic momentum due to quantum fluctuations of the light force. Finally, for completeness, section 2.5 gives an overview of fully quantised approaches to light forces and compares them with the semiclassical approach.

2.1 Theoretical approaches to light forces

Since the advent of the laser around 1960 the subject of atomic motion in laser light has been studied intensively, both theoretically and experimentally. Real atoms can have many degenerate energy levels, are usually moving and mutually colliding, and are subject to spontaneous emission. Electromagnetic fields can be polychromatic and contain many different plane wave modes. To take all these factors into account for even the simplest atom/field interaction results in great theoretical complexity. It is necessary to make various simplifying assumptions and to separate several distinct physical regimes.

Theoretical treatments may be categorised, for instance, into those dealing with short interaction times, where spontaneous emission may be neglected because the interaction time is shorter than the spontaneous lifetime, and those dealing with long interaction times where spontaneous emission must be included and transients may be neglected. Short interactions (pulses) are discussed further in chapter 7. A second categorisation is into either *'semiclassical' or 'fully quantised' theoretical treatments. In principle, a rigorous treatment* will take into account the coupling of the atom with all the quantised modes of the electromagnetic field and will also quantise both the internal and external (centre of mass) degrees of freedom of the atom. Such fully quantised treatments have the disadvantage of resulting in complicated calculations. In the simpler semiclassical approaches the internal state of the atom is quantised, but the centre of mass of the atom is assumed to be a small wavepacket which can be treated classically. A second use of the term 'semi-classical' distinguishes approaches where the light field is treated classically (as an oscillating field) as opposed to quantum mechanically (as photons occupying field modes). In such approaches, spontaneous emission is introduced phenomenologically into the equations of motion of the internal state of the atom via dissipative constants.

Except at the very lowest temperatures, the 'doubly' semiclassical theory (i.e. classical light field and classical centre-of-mass motion) is adequate for most purposes, giving results which have been confirmed by the more rigorous fully quantised approach. The semiclassical theory also gives physical insight into the nature of 'light forces' which remains useful even where the semiclassical model is no longer valid.

2.1.1 Underlying assumptions of semiclassical theory

The semiclassical approach used in this chapter depends on two underlying fundamental assumptions[41,124,125]. The first assumption is that the centre of mass of the atom is described by a small wavepacket, in quantitative terms: $\Delta x << \lambda$ where Δx is the uncertainty in position of the atom and λ is the light wavelength. This ensures that the electric field is well defined over the atomic wavepacket. This is normally easily satisfied, a typical atomic wavepacket being ~ 1Å, and a typical optical wavelength being ~ 1 μm. The second assumption is that the speed of the atom should be well defined so that the uncertainty in the atomic Doppler shift should be less than the atomic transition linewidth. Quantitatively, this is $k\Delta v << \Gamma$, where k is the light wavenumber, Δv is the uncertainty in atomic velocity and Γ is the natural linewidth of the atomic transition. These two restrictions may be combined with a further condition, namely Heisenberg's uncertainty principle $m\Delta x\Delta v \geq \hbar / 2$, to give the requirement

$$E_R << h\Gamma$$

where E_R is the recoil energy given by $E_R = \frac{\hbar^2 k^2}{2m}$. E_R is the change in kinetic energy of an atom caused by absorption of one photon, and m is the mass of the atom. This condition is well satisfied for most usable transitions e.g. $\hbar\Gamma/E_R \approx 10.000$ for rubidium atoms on the D_2 transition, which is the subject of the work described herein.

2.2 The semiclassical mean light force on a stationary two-level atom

2.2.1 Overview of the derivation of the mean light force

This section contains the semiclassical derivation of the mean force experienced by a stationary two-level atom in a general monochromatic light field. The two-level model is often appropriate because the phenomena of interest occur only when the light field is near resonance with an atomic transition. thus the two levels involved in the transition are singled out by the laser frequency and polarisation. The derivation parallels that used in references[124-127], and hopefully clarifies the relationships between the diverse, though equivalent, formulae therein. A number of basic tools of laser spectroscopy are employed in the derivation, namely: the density matrix representation of the atomic state[128,129], the Rabi frequency[130.131], the rotating wave approximation and the optical Bloch equations[128-131]. A brief introduction to these topics is included in appendix A-1.

The derivation method has two parts. The first part is a standard calculation[128-131] of the steady state of the laser-driven atom. The equation of motion of the atomic density matrix is written down with a Hamiltonian containing only the internal energy of the atom and the interaction energy due to the atomic dipole in the laser light field. At this stage spontaneous decay is not included. The equation of motion is simplified by the rotating wave approximation and then rearranged in terms of the Bloch vector. The effect of spontaneous decay on the atomic state is incorporated by the addition of appropriate relaxation terms, giving the well known 'optical Bloch equations' for the atomic inversion and dipole moment. The steady state solution of these Bloch equations is then found. The second part of the calculation consists of an application of Ehrenfest's theorem (appendix A-2) to find an expression for the mean light force on the atom in terms of the driving field and the atomic dipole moment. In order to facilitate quantitative calculations, and also to gain greater physical insight, the force expression obtained is then recast in three different ways, following different authors: firstly in terms of the Bloch vector components (as per [126,127]), secondly in terms of a complex atomic polarisability (as per [125,132]) and thirdly in terms of momentum loss and exchange amongst the plane wave modes of the field (as per [133]).

2.2.2 Calculation of the atomic density matrix and Bloch vector without relaxation terms

The calculation is given here in outline only, so as to retain the flow of the arguments, and to set up definitions of terms and symbols for later use. Some further details are given in Appendix A-1.

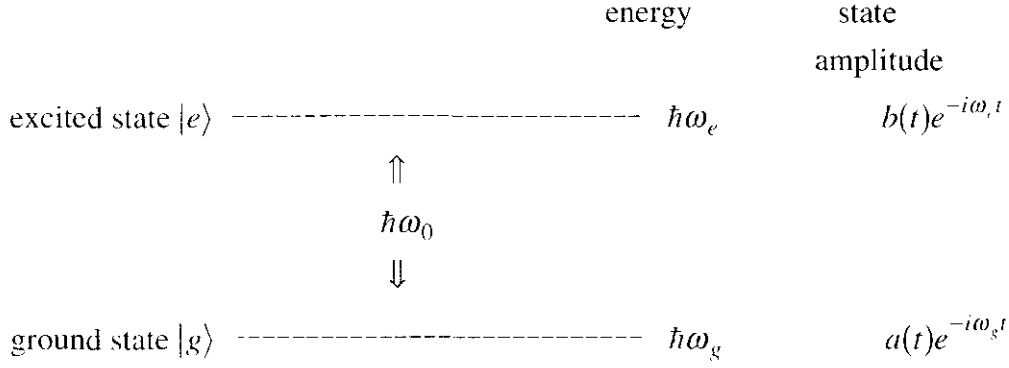

Figure 2-1 Symbols used to describe a two-level atom

Consider the stationary atom as a closed system with non-degenerate ground and excited levels $|g\rangle$ and $|e\rangle$ coupled by an electric dipole transition as depicted in figure 2-1. The two states have amplitudes $a(t)e^{-i\omega_g t}$ and $b(t)e^{-i\omega_e t}$ and energies $\hbar\omega_g$ and $\hbar\omega_e$ as shown. The transition frequency is $\omega_0 = \omega_e - \omega_g$. The system can be described at time t by the state vector

$$|t\rangle = a(t)e^{-i\omega_g t}|g\rangle + b(t)e^{-i\omega_e t}|e\rangle \tag{2-1}$$

interacting with a general monochromatic light field described by

$$\mathbf{E} = \frac{1}{2}\boldsymbol{\varepsilon}(\mathbf{r})E_0(\mathbf{r})e^{-i\omega_L t} + \text{c.c.} \tag{2-2}$$

where $\boldsymbol{\varepsilon}(\mathbf{r})$ is the polarisation unit vector at the position $\mathbf{r}$ of the atomic centre of mass, $E_0(\mathbf{r})$ the field amplitude and ω_L the light field angular frequency. From hereon the $\mathbf{r}$-dependence of quantities like $E_0(\mathbf{r})$ etc will be omitted except where a need for clarity dictates otherwise. The atomic density matrix ρ is

$$\rho = |t\rangle\langle t| = \begin{bmatrix} a^*a & b^*ae^{i\omega_0 t} \\ a^*be^{-i\omega_0 t} & b^*b \end{bmatrix} \tag{2-3}$$

where ρ_{gg}, ρ_{ge}, etc are the individual matrix elements.

The density matrix equation of motion[1] without relaxation terms is

$$\frac{d\rho}{dt} = -\frac{i}{\hbar}[H,\rho] \tag{2-4}$$

---

[1] *Note that, by the chain rule, the total time derivative in equation 2-4 is* $\frac{d}{dt} = \frac{\partial}{\partial t} + \mathbf{v}\cdot\nabla$ *where* $\mathbf{v}$ *is the atomic velocity. In this section dealing with stationary atoms* $\mathbf{v}$ *is zero, but in the next section (2.3), this distinction between the total and partial derivatives is important.*

where H, the Hamiltonian matrix is comprised of two parts $H_{\text{Atom}} + H_{\text{Dipole}}$ representing the internal energy of the atom and the atom-field interaction energy respectively. H_{Dipole} is equivalent to the operator $-\mathbf{d}\cdot\mathbf{E}$ where $\mathbf{d}$ is the electric dipole operator. In the rotating wave approximation, H is then given by

$$H = \hbar\begin{bmatrix} \omega_g & \dfrac{-\Omega_0^{c^*} e^{i\omega_L t}}{2} \\ \dfrac{-\Omega_0^{c} e^{-i\omega_L t}}{2} & \omega_e \end{bmatrix} \tag{2-5}$$

where the on-resonance Rabi frequency $\Omega_0^c = \dfrac{E_0\langle e|\mathbf{d}\cdot\boldsymbol{\varepsilon}|g\rangle}{\hbar}$ is necessarily complex for a general monochromatic light field. From hereon, Ω_0^c will be written as $\Omega_0 e^{i\theta}$ where Ω_0 and θ are both real and both functions of $\mathbf{r}$. Using the above expression for H in equation 2-4 leads to a set of four coupled equations giving the elements of the matrix $\dfrac{d\rho}{dt}$ as linear combinations of the elements of ρ. It is standard practice to rewrite these equations in terms of the 'Bloch vector', giving a new set of coupled equations, which are associated with a physically intuitive picture[134-136]. The Bloch vector is defined by (see Appendix A-1)

$$\begin{bmatrix} u \\ v \\ w \end{bmatrix} = \begin{bmatrix} \rho_{eg} e^{i(\omega_L t-\theta)} + c.c. \\ i\rho_{eg} e^{i(\omega_L t-\theta)} + c.c \\ \rho_{ee} - \rho_{gg} \end{bmatrix} \qquad \text{and} \qquad \rho_{ee} + \rho_{gg} = 1 \tag{2-6}$$

where the second equation is just the normalisation condition of a closed two level system. After simplification, the resulting set of coupled equations is:

$$\begin{aligned} \dot{u} &= \Delta v \\ \dot{v} &= -\Delta u + \Omega_0 w \\ \dot{w} &= -\Omega_0 v \end{aligned} \tag{2-7}$$

where Δ is the laser 'detuning' from the atomic resonance given by $\Delta = \omega_L - \omega_0$ and $\Omega_0(\mathbf{r})$ is the magnitude of the Rabi frequency at the location of the atom.

The above equations 2-7 describe the evolution of the atomic density matrix without relaxation terms. The population inversion is given by the component w and the in-phase and phase quadrature components of the atomic dipole moment are proportional to the components u and v respectively. (It is noteworthy that the expectation value of any atomic observable can be expressed as a linear combination of u, v and w [136].)

2.2.3 Calculation of the steady state atomic density matrix with relaxation terms

It is possible to add decay terms phenomenologically to the above equations, as the density matrix represents the state of an ensemble of atoms. The components of the Bloch vector may decay in different ways dependent on the experimental situation. These and other relaxation processes are discussed in [128-135]. In the case of the light force derivation for a closed two level atom, we assume there are no collisions with other atoms and that the only

physical process causing decay is spontaneous emission from the excited to the ground state. The effect of spontaneous emission is easily incorporated into the equation for the population inversion w, by using the equations $\left(\frac{d\rho_{ee}}{dt}\right)_{\text{spont}} = -\Gamma\rho_{ee}$ and $\left(\frac{d\rho_{gg}}{dt}\right)_{\text{spont}} = +\Gamma\rho_{ee}$, which describe spontaneous decay for an ensemble of atoms. Γ is the spontaneous decay rate. The effect of spontaneous decay on the other Bloch vector components u and v can be found for a two-level atom by a calculation which fully quantises the radiation field[128-130]. The result is

$$\left.\frac{du}{dt}\right|_{\text{spont}} = -\frac{\Gamma}{2}u, \qquad \left(\frac{dv}{dt}\right)_{\text{spont}} = -\frac{\Gamma}{2}v.$$

These relaxation rates are inserted into equations 2-7 to yield a 'master' equation[137] for the system, known as the 'optical Bloch equations' (in this case for a closed two-level system with spontaneous decay):

$$\begin{aligned}\dot{u} &= \Delta v - \frac{\Gamma}{2}u \\ \dot{v} &= -\Delta u + \Omega_0 w - \frac{\Gamma}{2}v \\ \dot{w} &= -\Omega_0 v - (1+w)\Gamma\end{aligned} \tag{2-8}$$

The steady state solution of equations 2-8 is found by setting $\dot{u} = \dot{v} = \dot{w} = 0$ and solving the resultant simultaneous equations with the result[135] that

$$\begin{aligned}u &= \frac{-4\Delta\Omega_0}{\Gamma^2 + 2\Omega_0{}^2 + 4\Delta^2} \\ v &= \frac{-2\Gamma\Omega_0}{\Gamma^2 + 2\Omega_0{}^2 + 4\Delta^2} \\ w &= \frac{-\Gamma^2 - 4\Delta^2}{\Gamma^2 + 2\Omega_0{}^2 + 4\Delta^2}\end{aligned} \tag{2-9}$$

The above equations may be written more concisely as

$$\begin{bmatrix} u \\ v \\ w \end{bmatrix} = \frac{-1}{\Omega_0(1+s)} \begin{bmatrix} 2\Delta s \\ \Gamma s \\ \Omega_0 \end{bmatrix} \tag{2-10}$$

where the 'saturation parameter' s is defined by

$$s = \frac{2\Omega_0{}^2}{\Gamma^2 + 4\Delta^2}. \tag{2-11}$$

The saturation parameter s is a useful measure of the strength of the atom-field interaction because the atomic inversion w depends only on s. A particular steady state population of the excited state corresponding to a particular value of s may be obtained by either a resonant field or by a more intense field at a large detuning. The steady state population of the excited state is given by $\frac{s}{2(s+1)}$, which saturates at 1/2 when $s = \infty$ and

has a value 1/4 when $s = 1$. Also, when $s = 1$, the ground state absorption rate is equal to half the spontaneous decay rate.

2.2.4 Ehrenfest's theorem for the mean light force.

Having found the steady state atomic density matrix, the expectation values of atomic observables such as the atomic dipole moment may be calculated. This in turn allows the calculation of light forces as follows. As described in appendix A-2, Ehrenfest's theorem gives a quantum mechanical expression for the force experienced by a particle in a spatially dependent potential energy. The potential energy of the atom in a classical light field $\mathbf{E}$ is given by $-\mathbf{d}\cdot\mathbf{E}$ and in such a case Ehrenfest's theorem gives the mean light force $\mathbf{F}$:

$$\mathbf{F} = \langle \nabla(\mathbf{d}\cdot\mathbf{E}) \rangle \tag{2-12}$$

where the outer triangular brackets indicate the expectation value. $\mathbf{F}$ is the 'mean' force in the sense that it does not contain the fluctuations caused by the quantum nature of the light field. Equation 2-12 simplifies (see Appendix A-2) to the 'light force equation'

$$F_i = \langle \mathbf{d} \rangle \cdot \frac{\partial \mathbf{E}}{\partial x_i} \tag{2-13}$$

where the subscripts i indicate the three cartesian components. This important equation gives the mean light force on an atom in a light field in terms of the expectation value of the atomic dipole operator and the spatial gradients of the electric field at the centre of mass of the atom. Various authors have developed this equation in different ways for the purposes of performing practical calculations or in order to gain new physical insight. One of the objectives of this chapter is to gather together the various expressions given for the light force and to show their interrelationship. Three such developments are now considered in turn: the first in terms of the Bloch vector components, the second in terms of a complex atomic polarisability and the third in terms of momentum loss and exchange amongst the plane wave modes of the field.

2.2.5 Development of the light force equation in terms of Bloch vector components

Following the approaches of R.Cook[126] and A.Ashkin and J.Gordon[127], an explicit expression for the expectation value $\langle \mathbf{d} \rangle$ of the atomic dipole moment can be substituted into the light force equation 2-13 to give, after some algebra, the following equivalent results [124,126,127]. (Calculation details are given in appendix A-3).

$$\left.\begin{aligned} \mathbf{F} &= \frac{\hbar}{2}(u\nabla\Omega_0 - v\Omega_0\nabla\theta) \\ \mathbf{F} &= \frac{\hbar}{2}\Omega_0(u\nabla\log_e\Omega_0 - v\nabla\theta) \end{aligned}\right\} \text{ time dependent solutions} \tag{2-14a}$$

If the steady state solutions of the Bloch equations (equation 2-9) are used in equation 2-14a, one obtains the steady state force

$$\left.\begin{aligned}\mathbf{F} = \frac{\hbar s}{2(s+1)}(-2\Delta\nabla\log_e\Omega_0 + \Gamma\nabla\theta)\end{aligned}\right\}\ \text{steady state solution} \qquad (2\text{-}14b)$$

Here Ω_0 and θ are the magnitude and phase of the complex Rabi frequency. Note that the force $\mathbf{F}$ consists of two terms: the first, depending on u is called the 'dipole' force, and the second, depending on v is called the 'scattering' force. This categorisation into two types of light force is discussed later in section 2.2.8.

The dipole force term of equation 2-14b is also sometimes expressed [138] as

$$\mathbf{F}_{\text{Dipole}} = -\frac{\hbar\Delta}{2}\nabla\log_e(1+s) \qquad (2\text{-}15)$$

Equations 2-14 give a concise expression for the force in terms of the Bloch vector components representing the in phase (u) and phase quadrature (v) parts of the atomic dipole. This formulation has the advantage, therefore, of allowing a view of light forces using the Bloch vector picture. A disadvantage is that in practice they require a preliminary calculation of the complex Rabi frequency in the form $\Omega_0 e^{i\theta}$.

2.2.6 Development of the light force equation in terms of atomic polarisability

Following the approaches of A.Hemmerich and T.Hänsch[132] and S.Stenholm[125], it is sometimes convenient to express the light force equation 2-13 in terms of the atomic polarisability. Such an approach[132] introduces a complex, scalar[2] atomic polarisability α defined by $\langle\mathbf{d}\rangle = \alpha\mathbf{E} + \text{c.c.}$ where α has real and imaginary parts $\alpha = \alpha_{\text{Re}} + i\alpha_{\text{Im}}$. To use this approach, the field $\mathbf{E}$ is first expressed in an equivalent form $\mathbf{E} = \sum_q \mathbf{e}_q I_q^{\frac{1}{2}} e^{i\psi_q} e^{i\omega_1 t} + \text{c.c.}$ where the $\mathbf{e}_q$ are the three cartesian unit vectors of the chosen coordinate system. Writing the field in this form constitutes a definition of the I_q and ψ_q. Substituting these expressions for α, $\mathbf{E}$ and $\langle\mathbf{d}\rangle$ into the force equation 2-13 yields, in the rotating wave approximation, the mean force $\mathbf{F}$ (details in appendix A-4):

$$\mathbf{F} = \alpha_{\text{Re}}\nabla I + 2\alpha_{\text{Im}}\sum_q I_q\nabla\psi_q \qquad (2\text{-}16)$$

$I = \sum_q I_q$ is the 'intensity' of the field and corresponds to $\frac{1}{2}\overline{|\mathbf{E}|^2}$, where the bar denotes a cycle average. The polarisability is given by (see appendix A-5)

$$\alpha = \frac{\hbar\Omega_0{}^2(-2\Delta + i\Gamma)}{2I(\Gamma^2 + 2\Omega_0{}^2 + 4\Delta^2)} \qquad (2\text{-}17)$$

A final simplification[124,126,139] occurs in cases where the light field polarisation is independent of spatial position. In such cases the field may be expressed as $\mathbf{E} = \boldsymbol{\varepsilon} I^{\frac{1}{2}} e^{i(\omega_1 t + \psi)} + \text{c.c.}$ and the mean light force equation 2-16 simplifies to

---

[2] *Note that the atom is not necessarily isotropic, in which case this theory may be extended by the adoption of a tensor, as opposed to scalar, atomic polarisability[132].*

$$\mathbf{F} = \alpha_{\mathrm{Re}} \nabla I + 2\alpha_{\mathrm{Im}} I \nabla \psi \tag{2-18}$$

The formulation of the light force as equation 2-16 has the advantage that the light force is expressed in terms of the easily calculated atomic polarisability and in terms of the I_q and ψ_q, which are directly calculable parameters of the light field. Note again the presence of two distinct terms: the dipole force term associated with the real, reactive part of the polarisability and the scattering force associated with the imaginary, dissipative part.

2.2.7 Development of the light force equation in terms of momentum loss and exchange amongst the plane wave modes of the field

Following the approach of Durrant et al[133], the light force equation 2-13 can be described in terms of momentum loss and exchange amongst the plane wave modes of the light field. This viewpoint is developed in [133], of which a brief outline now follows. Conservation of momentum requires that the sum of momentum of the atom and the momentum of the radiation field remains constant. Hence the force **F** on the atom is

$$\mathbf{F} = \frac{\partial \mathbf{P}_{\mathrm{atom}}}{\partial t} = -\frac{\partial \mathbf{P}_{\mathrm{field}}}{\partial t} = -\int_{\mathrm{space}} \frac{1}{c^2} \frac{\partial \mathbf{S}}{\partial t}$$

where $\mathbf{P}_{\mathrm{atom}}$ is the momentum of the atom, $\mathbf{P}_{\mathrm{field}}$ is the momentum of the total radiation field and **S** is the Poynting vector of the total radiation field i.e. the driving laser field and the dipole field of the atom. $\int_{\mathrm{space}} \frac{\partial \mathbf{S}}{\partial t}$ is calculated by summing over a complete set of plane wave modes and is then cycle-averaged to give the mean force **F.** This approach leads to a third expression for the mean light force, which for a stationary two-level isotropic atom is:

$$\begin{aligned} \mathbf{F} = & -2\alpha_{\mathrm{Re}} \sum_{\substack{s \\ s'<s}} (\mathbf{k}_s - \mathbf{k}_{s'}) I_{ss'} (\mathbf{e}_s \cdot \mathbf{e}_{s'}) \sin\left[\phi_{s'} - \phi_s + (\mathbf{k}_s - \mathbf{k}_{s'}) \cdot \mathbf{r}\right] \\ & - 2\alpha_{\mathrm{Im}} \left\{ \sum_s \mathbf{k}_s I_{ss'} + \sum_{\substack{s \\ s'<s}} (\mathbf{k}_s + \mathbf{k}_{s'}) I_{ss'} (\mathbf{e}_s \cdot \mathbf{e}_{s'}) \cos\left[\phi_{s'} - \phi_s + (\mathbf{k}_s - \mathbf{k}_{s'}) \cdot \mathbf{r}\right] \right\} \end{aligned} \tag{2-19}$$

where the driving field has been expressed as a sum over a complete set s of plane wave modes such that $\mathbf{E} = \sum_s \mathbf{e}_s E_s e^{i(\omega_s t - \mathbf{k}_s \cdot \mathbf{r} + \phi_s)} + \mathrm{c.c.}$ and $I_{ss'} = E_s E_{s'}$. $\alpha = \alpha_{\mathrm{Re}} + \alpha_{\mathrm{Im}}$ is the complex scalar polarisability of the atom.

Equation 2-14b, equation 2-16 and equation 2-19 are all exactly equivalent expressions for the mean light force. Although the latter (2-19) appears superficially to be the most complicated of the alternatives, in practice it can be easy to use, particularly when there are several non-parallel laser beams intersecting as is typical in laser cooling work. It can once again be seen that the expression divides into two parts, the dipole and scattering forces associated with α_{Re} and α_{Im} respectively.

2.2.8 Categorisation of light forces into the dipole and scattering force

Each of the three preceding 'developments' gives the light force as the sum of two distinct terms, thus motivating the important categorisation of light forces into the 'dipole' or 'gradient' force, corresponding to the first term of equations 2-14, 2-16, 2-19 and the 'scattering', 'resonance' or 'spontaneous' force corresponding to the second term. As can be seen from an examination of the real and imaginary parts of the atomic polarisability (equation 2-17), both forces share the same resonant denominator. The dipole force has a dispersive frequency dependence because its sign depends on the detuning which occurs in the numerator of the real part of the polarisability. The scattering force shows a (power-broadened Lorentzian) resonant frequency dependence with a F.W.H.M. $\approx \Gamma$.

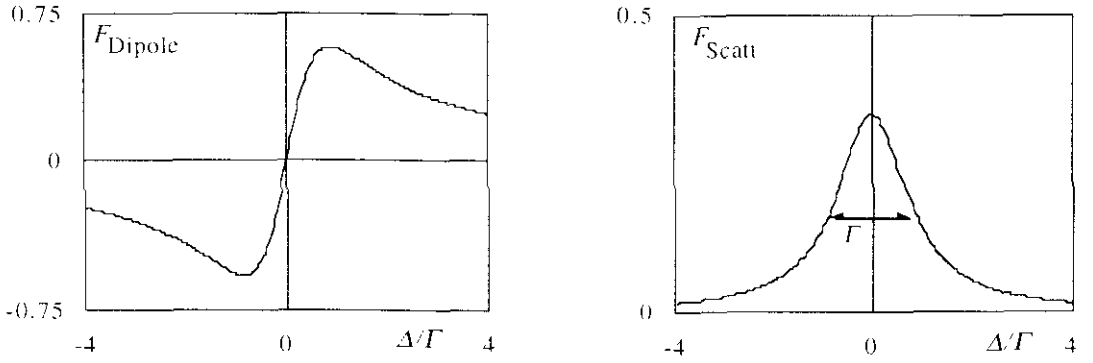

Figure 2-2 The frequency dependence of the dipole and scattering forces. The force is plotted in units of $\hbar k\Gamma$.

The dipole force

The dipole force is proportional to the gradient of the magnitude of the Rabi frequency squared (as seen in equation 2-14a) and is thus a conservative force[3]. Note that the gradient is non-zero only if the field consists of a superposition of more than one occupied plane wave mode. The dipole force is sometimes pictured as the a.c. corollary of the resultant force on an induced dipole in an inhomogeneous electrostatic field[139]. In a phasor picture, figure 2-3, the oscillating electric dipole has a component proportional to u, i.e. in phase with the driving electric field. The alignment (parallel or anti-parallel) of this component with the electric field depends on the detuning. For instance, if the detuning is negative, the dipole moment has a component parallel to and in the same direction as the electric field. The potential energy due to this interaction is negative ($= -\mathbf{E}\cdot\mathbf{d}$) and becomes more negative if the magnitude of $\mathbf{E}$ increases. Thus the force acts towards regions of greater $\mathbf{E}$. It follows that the dipole force is strong-field seeking for negative (red) detunings and weak-field seeking for positive (blue) detunings.

---

[3] *For isotropic atoms, the magnitude of the Rabi frequency squared is proportional to the electric field intensity* $\langle \mathbf{E} \cdot \mathbf{E} \rangle$, *where the brackets denote a cycle average.*

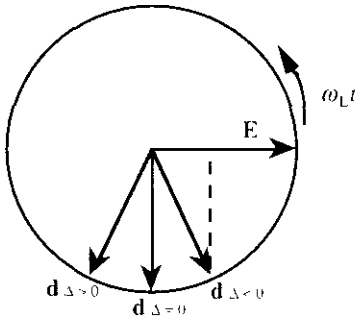

Figure 2-3 Phasor diagram: the phase relationship of the atomic dipole relative to the driving electric field for different detunings. The dashed line shows that for negative detuning, the dipole has a component aligned parallel to the field.

The third development of the light force (equation 2-19) shows that the dipole force is associated with redistribution of photon momenta between different plane wave modes of the field, i.e. by absorption from one mode followed by stimulated emission into another. The presence of the factor $\mathbf{k}_s - \mathbf{k}_{s'}$ in the dipole force term corresponds to the exchange of momentum between modes via absorption/stimulated emission cycles.

One practical example of the dipole force occurs for a stationary atom in a one-dimensional standing wave composed of two counterpropagating linearly polarised plane waves, with resultant electric field $\mathbf{E} = 2\boldsymbol{\varepsilon} E_0 \cos kz \cos \omega t$. In this situation, the scattering force for a stationary atom is zero, but the dipole force is, by equation 2-15,

$$\mathbf{F}_{\text{Dipole}} = \frac{4\hbar k \Omega_s^{\,2} \Delta \sin 2kz}{\Gamma^2 + 2\Omega_0^{\,2} + 4\Delta^2} \hat{\mathbf{z}} \tag{2-20}$$

where Ω_s is the magnitude of the Rabi frequency due to just one of the plane waves, thus $\Omega_0^{\,2}(\mathbf{r}) = 4\Omega_s^{\,2} \cos^2 kz$. This shows that the magnitude and direction of $\mathbf{F}_{\text{Dipole}}$ varies sinusoidally with z, pushing atoms from the nodes towards the antinodes of the standing wave for negative detuning and towards the nodes for positive detuning.

The dipole trap

Another practical example of the dipole force is provided by the optical 'dipole trap', first proposed by Ashkin[138] in 1978 and first demonstrated by Chu et al[2] in 1986.

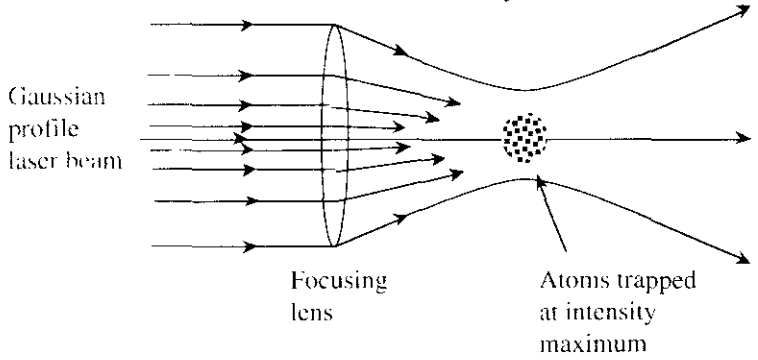

Figure 2-4 A focused Gaussian beam dipole trap

Neutral atoms in a near resonant laser beam with a gaussian intensity profile experience a radial dipole force transverse to the beam. This is because the beam intensity increases to a maximum at the centre. For negative detunings the force is towards the centre of the beam whilst for positive detunings atoms are expelled from the beam. Trapping in the third dimension is achieved by tightly focusing the beam so that the intensity also diminishes

longitudinally away from the focal plane. See figure 2-4. Dipole traps are important within the broad field of laser cooling[e.g. 2,47,138,141,142] but are not studied further in this thesis.

The scattering force

The second of the two light force terms, the scattering force, is associated with the phase quadrature component v of the Bloch vector and with the gradient of the phase ψ of the driving field. In the case of a single plane wave, the gradient of the phase is just the propagation wavevector **k**. In more complicated fields, however, the physical meaning of the phase-gradient is not so simple to interpret (except, tautologically, it must give the direction of the scattering force!). Nevertheless, the scattering force can be easily understood in terms of absorption and emission of photons.

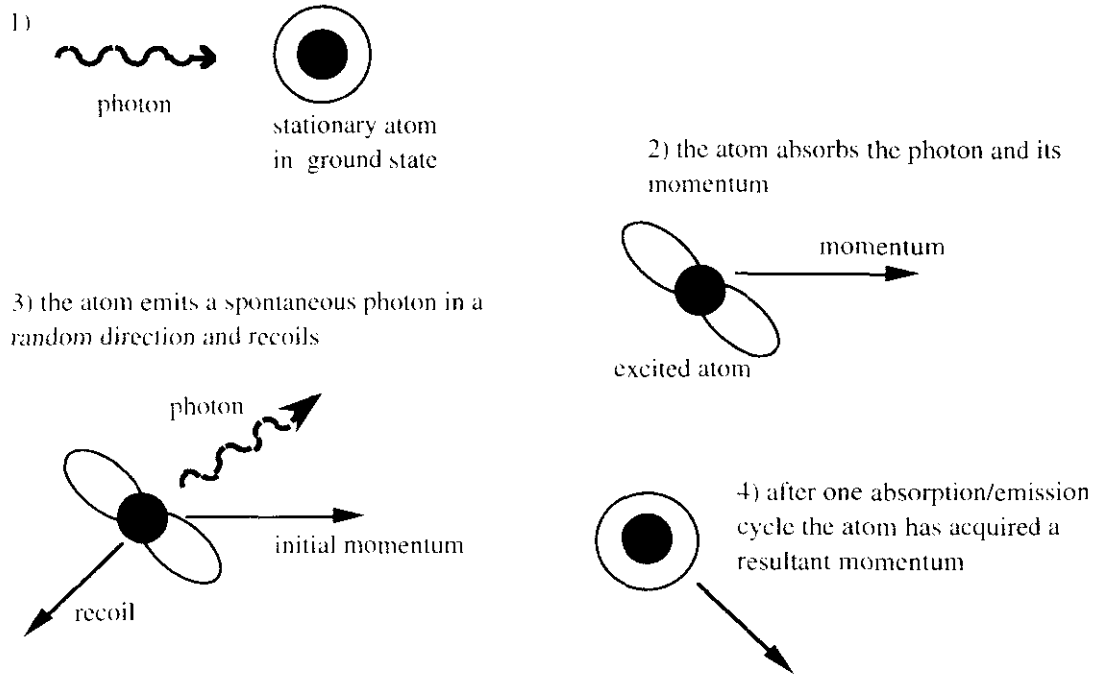

Figure 2-5 The scattering force

Figure 2-5 shows an atom in the path of a plane wave. If the frequency of the light is near an atomic resonance, the atom will absorb a photon, receiving a momentum kick $\hbar\mathbf{k}$. The momentum kick from the subsequent spontaneous emission of a photon has a random direction. Over many cycles the emission kicks cancel out on average, but the absorption kicks are always in the same direction and consequently add. As a result, the atom is subject to a net time-averaged force:

$$\mathbf{F}_{\text{Scatt}} = \begin{pmatrix}\text{photon}\\ \text{momentum}\end{pmatrix} \times \begin{pmatrix}\text{spontaneous}\\ \text{emission rate}\end{pmatrix} \times \begin{pmatrix}\text{excited state}\\ \text{population}\end{pmatrix}$$

$$= \quad (\hbar\mathbf{k}) \quad \times \quad (\Gamma) \quad \times \left(\frac{\Omega_0^{\,2}}{\Gamma^2 + 2\Omega_0^{\,2} + 4\Delta^2}\right)$$

$$\mathbf{F}_{\text{Scatt}} = \frac{\hbar\mathbf{k}\Gamma\Omega_0^{\,2}}{\Gamma^2 + 2\Omega_0^{\,2} + 4\Delta^2} \qquad (2\text{-}21)$$

where the expression for the excited state population follows from equation 2-9c. This equation shows that for low intensity fields ($\Omega_0 < \Gamma$) the scattering force is proportional to the field intensity, but has an upper limit for high intensity fields of

$$\mathbf{F}_{\text{Scatt(Max)}} = \frac{\hbar \mathbf{k} \Gamma}{2} \qquad \text{when } \Omega_0 >> \Gamma, \Delta \tag{2-22}$$

The above discussion, for a simple plane wave, conveys the idea that the scattering force is associated with a process involving absorption followed by incoherent spontaneous emission. This same association carries over to more complex light fields. The third development of the light force (equation 2-19) allows some insight into this idea. The scattering force part of this equation , involving α_{Im}, consists of two terms acting in the directions opposite to $\mathbf{k}_s$ and $\mathbf{k}_s + \mathbf{k}_{s'}$ respectively. For both of these terms, the plus signs immediately in front of the $\mathbf{k}_s$ indicate that the terms correspond to absorptions (of momentum $\hbar\,\mathbf{k}_s$) followed by spontaneous emissions. (A negative sign before a $\mathbf{k}_s$ is the indicator of a stimulated emission). The first of these terms, containing $\mathbf{k}_s$, corresponds to the simple plane wave scattering force of figure 2-4 and is seen to be additive over the modes. The second term, containing $\mathbf{k}_s + \mathbf{k}_{s'}$ is an interference term which can either add to or subtract from the first term, depending on the atom's position in the light field. This interference gives rise to patterns of light forces such as lines of acceleration and vortex forces[132] which are of particular interest in some laser cooling and trapping schemes.

2.3 Light forces on moving atoms

This section will show how the semiclassical theory of light forces, developed so far for stationary atoms, is extended to include moving atoms. The first subsection 2.3.1 considers the simplest possible case: an atom moving in a plane wave. Then, in subsection 2.3.2 a simple model leads to an approximate expression for the light force on an atom moving in a one dimensional standing wave. Subsection 2.3.3 addresses the same one-dimensional standing wave problem more rigorously and, finally, 2.3.4 and 2.3.5 discuss specific solutions of the same problem in the two regimes of weak and strong fields respectively.

Though the action of the light forces will eventually alter the velocity of the atom, it is assumed that the velocity $\mathbf{v}$ is constant in the derivation below. This is justified because, in most situations, the photon momentum $\hbar\mathbf{k}$ is much smaller than the atomic momentum $m\mathbf{v}$, thus many absorption/emission cycles are required to change $\mathbf{v}$ significantly.

2.3.1 The light force on a moving atom in a single plane wave

Consider an atom moving with velocity $\mathbf{v}$ in a plane wave propagating in the z direction. This simple case is easily understood by considering the situation in the reference frame of the moving atom, where the atom is stationary and the plane wave has a Doppler-shifted frequency ω_L'. To first order in v_z/c,

$$\omega_L' \cong \omega_L\left(1 - \frac{v_z}{c}\right) = \omega_L - \mathbf{k}\cdot\mathbf{v}$$

The light field is monochromatic in the atomic reference frame, so the result (equation 2-21) for stationary atoms may be used with the new detuning $\Delta' = \Delta - \mathbf{k}.\mathbf{v}$, giving a force

$$\mathbf{F}_{\text{Scatt}} \cong \hbar\mathbf{k}\left(1 - \frac{v_z}{c}\right)\left(\frac{\Gamma\Omega_0{}^2}{\Gamma^2 + 2\Omega_0{}^2 + 4(\Delta - \mathbf{k}\cdot\mathbf{v})^2}\right)$$

The Lorentz transform of this force[143] back to the original frame in which the atom was moving does not change the above expression for $\mathbf{F}_{\text{Scatt}}$. For speeds $v << c$, however, the predominant velocity dependence is caused by the **k.v** term in the denominator, hence we can write

$$\mathbf{F}_{\text{Scatt}} \cong \hbar\mathbf{k}\left(\frac{\Gamma\Omega_0{}^2}{\Gamma^2 + 2\Omega_0{}^2 + 4(\Delta - \mathbf{k}\cdot\mathbf{v})^2}\right) \qquad (2\text{-}23)$$

Examination of equation 2-23 shows that $\mathbf{F}_{\text{Scatt}}$ will only be significant for the narrow range of velocities with **k.v** close to Δ. In fact, for a fixed detuning and $\Omega_0{}^2 << \Gamma^2$, the force dependence on **k.v** is Lorentzian with a FWHM equal to Γ. For the D_2 line of Rb, this FWHM corresponds to a velocity width of 4.4 ms^{-1}.

2.3.2 A simple model of a moving atom in a 1-D standing wave

Progressing one step to consideration of the light forces on a moving atom in a one dimensional standing wave causes a suprising degree of complexity[4]. A one dimensional standing wave consists of two plane waves of equal frequency and intensity, counterpropagating along the z-axis. In the atomic reference frame, the light field now appears bichromatic with frequencies at $\omega_L \pm \mathbf{k}\cdot\mathbf{v}$. As a result, slow beats of frequency **k·v** appear in the driving field amplitude, which in turn cause corresponding slow oscillations in the atomic dipole moment. These slow oscillations in the driving field and the dipole moment are combined multiplicatively in the master expression for the mean light force (equation 2-13). Calculations to various orders which incorporate such effects are described in the next section 2.3.3. For the moment, however, a useful approximate result can be obtained by simply adding the scattering forces due to each of the two counterpropagating plane waves. This approximation gives F_z', the z-component of the mean light force averaged over a wavelength and in the limit of weak fields ($\Omega_0 << \Gamma$), i.e. it neglects interference and saturation effects. The prime on F_z' is to indicate that this an approximate result.

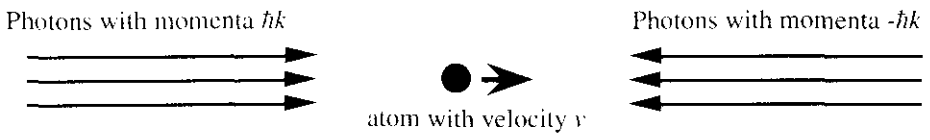

Figure 2-6 A moving atom in a 1-D standing wave

[4]*The theory of light forces on moving atoms is still a subject of ongoing interest for contemporary theorists e.g. reference [144].*

Using equation 2-23 for the scattering force due to each plane wave,

$$F_z' = (\hbar k)\left[\frac{\Gamma\Omega_s^{\,2}}{\Gamma^2 + 2\Omega_s^{\,2} + 4(\Delta - kv_z)^2}\right] + (-\hbar k)\left[\frac{\Gamma\Omega_s^{\,2}}{\Gamma^2 + 2\Omega_s^{\,2} + 4(\Delta + kv_z)^2}\right] \qquad (2\text{-}24a)$$

where Ω_s is the magnitude of the Rabi frequency of each plane wave. This simplifies to

$$F_z' = \frac{16\hbar k^2 \Gamma\Omega_s^{\,2}\Delta v_z}{\left[\Gamma^2 + 2\Omega_s^{\,2} + 4(\Delta - kv_z)^2\right]\left[\Gamma^2 + 2\Omega_s^{\,2} + 4(\Delta + kv_z)^2\right]} \qquad (2\text{-}24b)$$

which may be written as

$$F_z' = \frac{c_1(kv_z/\Gamma)}{1 + c_2(kv_z/\Gamma)^2 + c_3(kv_z/\Gamma)^4} \qquad (2\text{-}24c)$$

where the constants c_1, c_2, c_3 are algebraic combinations of Γ, Ω_s and Δ. In the case when $kv_z << \Delta$ and $kv_z << \Gamma$, equation 2-24b becomes

$$F_z' = \beta v_z \quad \text{where} \qquad \beta = \frac{16\hbar k^2 \Gamma\Omega_s^{\,2}\Delta}{\left(\Gamma^2 + 2\Omega_s^{\,2} + 4\Delta^2\right)^2} \qquad (2\text{-}25)$$

which is generally the most useful of the above expressions.

The sign of the 'friction coefficient' β is the same as the sign of the detuning, therefore the total force is a damping or 'cooling' force for red (negative) detuning and an accelerating or 'heating' force for blue (positive) detuning. When Δ is negative, F_z' is often referred to as a friction force.

It is of interest to know the values of the two variable parameters Δ and Ω_s which maximise the magnitude of the damping force. The answer, by differentiation of 2-25, is

$$|\beta_{max}| = \frac{\hbar k^2}{2} \qquad \text{when} \qquad \Delta = -\frac{\Gamma}{2} \text{ and } \Omega_s = \Gamma^{(5)} \qquad (2\text{-}26)$$

Note however that the answer $\Omega_s = \Gamma$ is at this stage inconsistent with the original assumption $\Omega_s << \Gamma$ used in deriving equation 2-25. It will be useful later on in this chapter to know the maximum value of β in the situation of a very weak field i.e. when $\Omega_s << \Gamma$ or equivalently $s << 1$. In such a case $|\beta|$ is still maximised by setting $\Delta = \frac{-\Gamma}{2}$, but $|\beta|$ then takes the value

$$|\beta_{max}| = 2\hbar k^2 s \qquad \text{(weak fields)} \qquad (2\text{-}27)$$

When the friction coefficient is maximised, this cooling force typically produces an atomic deceleration around $10^5\,g$. Though this may seem large, it is only 10^{-8} of the force felt by a singly-ionised atom in an everyday electrostatic field of 1 Vcm^{-1}.

---

[5] *These values correspond to a saturation parameter s = 1, and the value of light intensity corresponding to $\Omega_s = \Gamma$ is often referred to as the 'saturation intensity'. Strictly, the saturation intensity depends on the detuning, for instance $\Omega_s = \Gamma/\sqrt{2}$ gives the saturation intensity at exact resonance. Note that Ω_s is the intensity for each component plane wave, not the total intensity of the standing wave.*

Velocity damping in three dimensions can be obtained by an arrangement of three intersecting, mutually orthogonal pairs of counterpropagating laser beams. All three velocity components of an atom in the intersection region are then damped. Such an arrangement is known as 'optical molasses', which is an important form of laser cooling, to be described in detail in chapter 3. The reduction of atomic temperatures via the cooling force described above is called 'Doppler cooling'.

2.3.3 Derivations of forces on an atom moving in a 1-D standing wave.

The previous section 2.3.2 gave an approximation for the light force on an atom moving in a 1-D standing wave. This section gives an overview of various semiclassical approaches[124-127,145,146] to more precise, higher order calculations of this force. The main sequence of the calculation proceeds in a similar fashion to that for a stationary atom. It is necessary first to solve the optical Bloch equations for the steady state density matrix, and then to calculate the light force using Ehrenfest's theorem. For a moving atom, as mentioned earlier in subsection 2.2.2, the chain rule gives $\frac{d}{dt} = \frac{\partial}{\partial t} + \mathbf{v}.\nabla$ or, for the simplified picture of an atom moving parallel to a standing wave aligned along the z-axis, $\frac{d}{dt} = \frac{\partial}{\partial t} + v_z \frac{\partial}{\partial z}$

Hence the optical Bloch equations (2-8) take the form:

$$\begin{aligned}
\left[\frac{\partial}{\partial t} + v_z \frac{\partial}{\partial z}\right] u &= \Delta v - \frac{\Gamma}{2} \\
\left[\frac{\partial}{\partial t} + v_z \frac{\partial}{\partial z}\right] v &= -\Delta u + \Omega_0 w - \frac{\Gamma}{2} \\
\left[\frac{\partial}{\partial t} + v_z \frac{\partial}{\partial z}\right] w &= -\Omega_0 v - (1+\omega)\Gamma
\end{aligned} \tag{2-28}$$

To find the steady state solution, we put the terms $\frac{\partial}{\partial t} = 0$. This solution is known from the theory of gas lasers[147], and is obtained by expanding the elements of the density matrix in a spatial Fourier series: i.e.

$$\rho_{ij} = \sum_n \rho_{ij}^n e^{inkz} \tag{2-29}$$

The coefficients ρ_{ij}^n may be determined to a chosen order of n by a continued fraction method[146]. Once the density matrix is known, the atomic dipole moment is easily found and again, as in the previous section on stationary atoms, Ehrenfest's theorem gives the mean light force. The final result for moving atoms is an expression for the mean light force of the form

$$F_z(v_z, z) = F_0(v_z) + \sum_{n=1}^{\infty} \left[F_c^n(v_z) \cos 2nkz + F_s^n(v_z) \sin 2nkz \right] \tag{2-30}$$

where $F_0(v_z)$ represents the spatial average force and the coefficients $F_c^n(v_z), F_s^n(v_z)$ determine the spatial oscillations. Note that this expression is correct for all light field intensities. Various authors[124,126,127,145] have used this or closely related approaches

to analytically calculate the coefficients F_0, F_c^n, F_s^n to a small order of n ($n = 1$ or 2) in specific regimes of light field intensity and atomic velocity. Reference [146], on the other hand, uses a numerical method to calculate F_0, F_c^n, F_s^n to all significant orders.

2.3.4 Light forces on atoms moving in a weak intensity 1-D standing wave

General analytical solutions to the problem of determining the coefficients F_0, F_c^n, F_s^n are hard to obtain. As a consequence, the existing solutions are confined to the specific regime of weak light fields ($\Omega_0 < \Gamma$) and small velocities ($kv_z << \Delta, \Gamma$). For this regime, various authors[124,126,127,133] have obtained equivalent expressions for the first three coefficients F_0, F_c^1, F_s^1. It turns out that $F_c^1 = -F_0$, so that to first order in n,

$$F_z = 2F_0 \sin^2 kz + F_s^1 \sin 2kz \tag{2-31}$$

where

$$F_0 = \frac{16\hbar k^2 \Gamma \Delta \Omega_s^2}{\left(\Gamma^2 + 2\Omega_s^2 + 4\Delta^2\right)^2} v_z \tag{2-32a}$$

$$F_s^1 = \frac{4\hbar k \Omega_s^2 \Delta}{\Gamma^2 + 2\Omega_s^2 + 4\Delta^2} \tag{2-32b}$$

Comparison of equation 2-32a with equation 2-25 shows that the expression obtained for F_0 is equal to βv_z and confirms that the approximate calculation leading to 2-25 gave the correct spatial average force, but failed to predict the $\sin^2 kz$ variation. This spatial variation, which also emerges from our approach to light forces in [133], is interesting in that it shows that the friction coefficient ($\propto \sin^2 kz$) is greatest at points in the wave where the light intensity ($\propto \cos^2 kz$) is least. The second term of equation 2-31, $F_s^1 \sin 2kz$ is independent of velocity and, by comparison with equation 2-20, is seen to be exactly equal to the dipole force previously calculated for stationary atoms. Once again, the force expression 2-31 is seen to consist of the sum of two terms, a dipole force $F_s^1 \sin 2kz$ and a scattering force $2F_0 \sin^2 kz$.

A calculation[124] to the second order $n = 2$ produces corrections to the first order force (equation 2-31); these corrections are equivalent to introducing a more accurate power-broadening factor into the denominators of the coefficients F_0, F_c^1, F_s^1. The power-broadening in equations 2-32 ($2\Omega_s^2$ in the denominator) corresponds to just one plane wave, the second order corrections change this to $4\Omega_s^2$ which is the spatially averaged power-broadening for two counterpropagating waves. For weak fields, it is unnecessary to consider higher terms in the expansion of equation 2-30 as they rapidly tend to zero with n. It remains to consider the effect on the atom of the net force resulting from the sum of the two terms in equation 2-31. For positive detunings, the scattering component of the light force is an accelerative force which leads to unbounded motion with increasing velocity, though this velocity has a small oscillation superposed on it due to the dipole term. For negative detunings, the atom is decelerated by the scattering force until its speed is less than

a certain $v_{capture}$, whereupon it becomes bound, oscillating in a region of size $\lambda/2$ around one of the wave antinodes. Hence the theory, as developed so far in this section, suggests that atoms may be decelerated and then become trapped in wavelength-sized regions by a standing wave. However, the effects of 'momentum diffusion' processes act so as to prevent damping of the atomic speed to much below $v_{capture}$ and so, such traps are 'leaky'. Momentum diffusion is formally introduced and discussed in section 2.4.

2.3.5 Light forces on atoms moving in a strong intensity 1-D standing wave

In the strong field regime $\Omega_0 \geq \Gamma$, there are two semiclassical approaches found in the literature to the calculation of light forces on moving atoms. The first is a continuation of the spatial Fourier series approach already described above and forms the main topic of this subsection. The second approach is the 'dressed atom' approach, which is discussed briefly at the end of this subsection.

Though not all orders of coefficients F_0, F_c^1, F_s^1 in the expansion of equation 2-30 can be obtained analytically other than as a convergent continued fraction, the numerical solutions have been obtained[146] for a large range of saturation parameters ($0 < s < 64$) and atomic speeds ($kv < \Gamma$). The resulting mean force differs from the weak field force in the following respects.

New resonant structures, which have been named 'Dopplerons' were predicted[146,147] and observed[148,149] to appear in the velocity dependence of the force F_z of equation 2-30. These are due to multiphoton processes which are more probable in high intensity fields. As an example, consider the three-photon event pictured in figure 2-7. In this example, conservation of energy requires that

$$\underset{\text{absorption}}{\hbar(\omega_L - kv)} - \underset{\text{stim. emission}}{\hbar(\omega_L + kv)} + \underset{\text{absorption}}{\hbar(\omega_L - kv)} = \underset{\text{spont. emission}}{\hbar\omega_0} \qquad \text{i.e.} \quad kv = \frac{\omega_L - \omega_0}{3} = \frac{\Delta}{3}$$

Hence this three-photon process is most probable when $kv = \Delta/3$, and the resonance at that detuning gives rise to a corresponding resonance in the force versus velocity curve. Similar

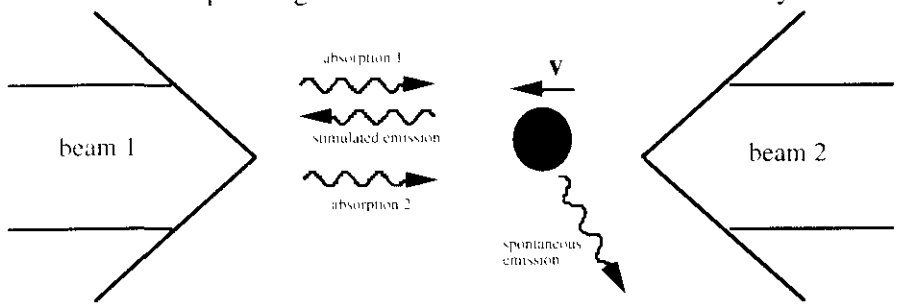

Figure 2-7 A doppleron event

resonances occur at velocities determined by $kv_n = \frac{\Delta}{2n+1}$ for $n = 0,1,2,3.....$, and the resulting shape of the force/velocity graph is complicated. Figure 2-8 shows, for comparison, the velocity dependences of the spatial average force F_0 in the weak and strong field regimes. For both plots, $\Delta = -3\Gamma$. In a) $\Omega_s = \Gamma$, in b) $\Omega_s = 25\Gamma$. F_z is in units of $\hbar k\Gamma$.

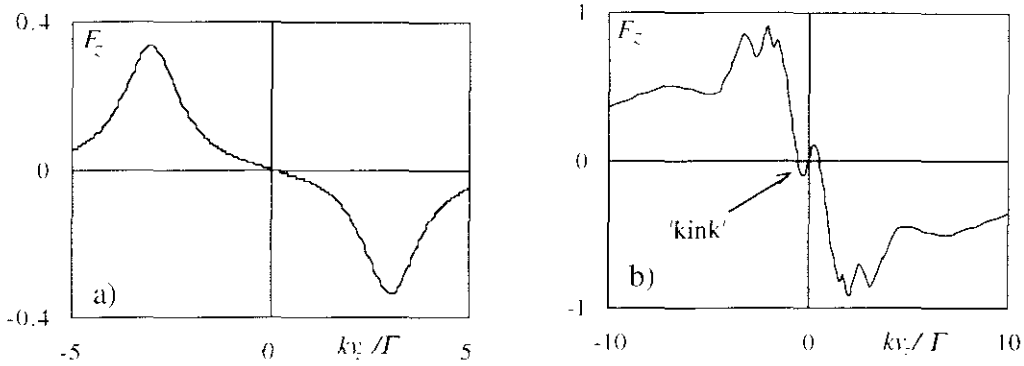

Figure 2-8 The velocity dependence of the spatially averaged force F_0 for a) low laser intensities and b) higher laser intensities. b) is a sketch of figure 2a of [146].

Of particular interest is the 'kink' near $v = 0$ (see figure 2-8b), which results in a reversal of the direction of the force for the slowest atoms. Thus the usual cooling force associated with red detuning can become a heating force in a strong field and vice versa i.e. there is a cooling force for very slow atoms in a high intensity blue-detuned standing wave[6]. This cooling force is discussed further in section 4.7.1.

2.3.6 The dressed atom approach

The dressed atom approach[130,131,150] is a semiclassical model in the sense that the centre of mass motion of the atom is treated classically, but the internal atom and light field are quantised. It is particularly useful in the case of high intensity fields $\Omega_0 >> \Gamma$ or highly detuned fields $\Delta >> \Gamma$. It starts with a Hamiltonian of the form

$$H_{D-A} = H_{Atom} + H_{Laser} + H_{Interaction}$$

The Hamiltonian H_{D-A} is diagonalised so as to have eigenstates corresponding to the possible energies of the combined atom-laser system. Because it starts from this alternative viewpoint, this approach offers new physical insights, for instance in explaining the blue-detuned cooling force mentioned above (see section 4.7.1). Results obtained with the dressed atom approach are in quantitative agreement with the continued fraction approach of previous sections and consequently I do not discuss it further in this thesis, save to point out the excellent discussions in [41,130,150].

2.3.7 Summary of section 2.3

The discussion so far has shown that a rigorous calculation of light forces in all regimes for a two-level atom moving in a one dimensional standing wave is complicated. For a fully three dimensional standing wave comprising several plane waves, such as is used in many cooling and trapping experiments, the situation becomes yet more complicated. Most authors

---

[6] *The standing wave must contain intensity gradients for this force to occur for 2-level atoms, i.e. the counterpropagating beams should have parallel polarisations.*

have analysed the 1-D case and argued that similar qualitative features are to be expected in the 3-D case. Rigorous elucidation of the 3-D case is still a subject of ongoing work. The matter is not pursued further here, because the extension of the theory of light forces from two-level to multilevel atoms brings another set of more important complications to consider. Multilevel atoms are discussed in chapter 4. In summary, there are two key features which arise from the theory and which will be significant in the work of this thesis: firstly, for red detuning, the light force on a moving atom in a standing wave is a damping force for low and moderate intensities, and secondly, in standing waves there can be a localising force acting in regions of size ~ $\lambda/2$.

2.4 Momentum diffusion

Quantum mechanics shows that the light force has its origins in many discrete momentum transfers of magnitude $\hbar k$ between the atoms and radiation field. Such transfers usually occur at random, causing the light force to fluctuate about its mean value. These fluctuations were neglected in the previous sections 2.2 and 2.3 which derived the mean light force acting on stationary and moving atoms in a light field. This section deals with the effects of the fluctuations, which cause a spreading of the momentum distribution known as 'momentum diffusion'. Momentum diffusion is important because it sets a limit on the lowest temperatures achievable by the use of light forces as 'cooling' forces. Much of the necessary theory was developed in connection with Brownian motion around 1900 by Einstein, Planck, Fokker and Langevin.

This section is organised as follows. Firstly, subsections 2.4.1 and 2.4.2 review the basic theory of Brownian motion and the associated topic of Langevin equations. Subsection 2.4.3 then applies this basic theory to the specific case of Doppler cooling and derives the 'Doppler cooling limit'. Subsection 2.4.4 then gives an outline of the Fokker-Planck equation which is a more general mathematical tool often used in the literature to describe the more complicated diffusion effects found in experimental situations.

2.4.1 Review of the theory of Brownian motion

A small particle of mass m immersed in a fluid and initially moving with an average velocity $\mathbf{v}$ experiences an average viscous damping force

$$\mathbf{F}_d = -\beta' \mathbf{v} \tag{2-33}$$

as a result of its many collisions with the smaller fluid molecules. β'[7] is a friction coefficient. The mean velocity is damped until the particle kinetic energy is of the order of the thermal energy, which by the equipartition law is $(3/2)k_B T$ for a 3-D motion, where k_B is Boltzmann's constant. On the other hand, if a particle starts with exactly zero velocity, it will

---

[7] *Note that here β' is primed, as it refers to the generalised damping force of any Brownian motion and should be distinguished from the specific friction coefficient β of laser cooling (equation 2-25).*

swiftly be perturbed by surrounding fluid molecules until its kinetic energy is again of the order of the thermal energy. The particle then undergoes Brownian motion - a random walk in momentum space, where the mean particle momentum $\langle \mathbf{p} \rangle$[8] is zero. The variance of the momentum $\langle p^2 \rangle$ tends to increase, or 'diffuse' with time and the rate at which it increases (in the absence of any damping) is measured by the momentum diffusion coefficient D_p, defined by

$$2D_p = \frac{d\left[\langle p^2 \rangle - \langle \mathbf{p} \rangle . \langle \mathbf{p} \rangle\right]}{dt}, \qquad \text{or, if } \langle \mathbf{p} \rangle = 0 \qquad 2D_p = \frac{d\langle p^2 \rangle}{dt} \tag{2-34}$$

However, the tendency of $\langle p^2 \rangle$ to increase indefinitely is counterbalanced by the damping force $\mathbf{F}_d$. This balance can be put on an approximate quantitative basis as follows. If E_{kin} is the average kinetic energy of a single particle, then in thermal equilibrium

$$\left[\frac{dE_{kin}}{dt}\right]_{damping} + \left[\frac{dE_{kin}}{dt}\right]_{diffusion} = 0 \tag{2-35}$$

But $\left[\frac{dE_{kin}}{dt}\right]_{damping}$ is the average rate of work done by $\mathbf{F}_d$, which $= \langle \mathbf{F}_d . \mathbf{v} \rangle$.

Hence, using $\mathbf{F}_d = -\beta' \mathbf{v}$ gives

$$\left[\frac{dE_{kin}}{dt}\right]_{damping} = -\beta' \langle v^2 \rangle$$

Also $$\left[\frac{dE_{kin}}{dt}\right]_{diffusion} = \frac{1}{2m}\frac{d\langle p^2 \rangle}{dt} = \frac{D_p}{m} \quad \text{by definition of } D_p$$

Thus equation 2-35 becomes $\frac{D_p}{m} - \beta' \langle v^2 \rangle = 0$, which rearranges to $\frac{1}{2} m \langle v^2 \rangle = \frac{D_p}{2\beta'}$. Then, using the equipartition theorem $\frac{1}{2} m \langle v^2 \rangle = \frac{3}{2} k_B T$ we obtain the desired result:

$$k_B T = \frac{D_p}{3\beta'} \tag{2-36a}$$

or in 1-D[9] $$k_B T = \frac{D_{p(1\text{-D})}}{\beta'} \tag{2-36b}$$

Equations 2-36, originally derived by Einstein[151], are important as they determine the lowest temperature achievable by any stochastic damping process. Laser cooling is such a process, and in laser cooling experiments designed to attain the lowest possible temperatures, it is necessary to adopt a design which minimises the ratio D_p/β, whilst bearing in mind that designs which attempt to maximise the friction coefficient β may also have large diffusion coefficients as an unwelcome side-effect.

---

[8] $\langle\ \rangle$ *here means the average value over a thermodynamic ensemble of particles.*

[9] $D_{p(1\text{-D})}$ *is the 1-D momentum diffusion coefficient. For a Maxwell-Boltzmann distribution,* $D_{p(3\text{-D})} = 3D_{p(1\text{-D})}$.

2.4.2 Langevin forces and equations

The above argument leading to equation 2-36 provides a simple picture of how the two opposing processes of diffusion and damping lead to a cooling limit. An alternative approach to the problem of Brownian motion is obtained by the use of Langevin equations, which are now described.

Equation 2-33 gives the average viscous damping force $\mathbf{F}_d$ as

$$\mathbf{F}_d = -\beta'\mathbf{v}, \text{ or } \frac{d\mathbf{v}}{dt} = \frac{-\beta'}{m}\mathbf{v}, \tag{2-37}$$

which implies that $\mathbf{v}(\infty) = 0$. However, $\mathbf{v}(\infty)$ is known to be of order $\sqrt{\frac{k_B T}{m}}$ and so equation 2-37 must be modified. This is done by adding a fluctuating force per unit mass $\mathbf{F}_L(t)$, called a Langevin force, to give

$$\frac{d\mathbf{v}}{dt} = \frac{-\beta'}{m}\mathbf{v} + \mathbf{F}_L(t) \tag{2-38}$$

The properties of a Langevin force are only known statistically. They are:

$$\begin{aligned} \langle \mathbf{F}_L(t) \rangle &= 0 \\ \langle \mathbf{F}_L(t)\mathbf{F}_L(t') \rangle &= q\delta(t-t') \end{aligned} \tag{2-39}$$

where the brackets $\langle\ \rangle$ indicate the average over many particle/fluid systems which are *identical in the thermodynamic sense. The use of the delta function is an idealisation.* It represents the fact that the correlation time τ_L of the Langevin force is very small compared to the time between the collisions. The quantity q gives a measure of the noise strength of the Langevin force and can be determined by formally solving equations 2-38 and 2-39 and then applying thermodynamic considerations such as the equipartition theorem. The result[152] is that $q = \frac{2n\beta' k_B T}{m^2}$, where m is the mass of the particle undergoing the Brownian motion and n is the number of degrees of freedom of the motion. A second equation $q = \frac{2D_{p_{tot}}}{m^2}$ follows from the definitions of q and $\mathbf{F}_L$, and combining these two results gives $k_B T = \frac{D_{p_{tot}}}{n\beta'}$, which confirms equations 2-36.

A useful result which can be obtained[152] by the use of the Langevin equations is the calculation of the diffusion coefficient D_r of the position variable $\mathbf{r}$ of a particle subject to Brownian motion in a fluid. D_r is defined by $2D_r = \frac{d\langle r^2 \rangle}{dt}$ if the mean of $\mathbf{r}$ is zero. Although the particle is undergoing a damped random walk in momentum space, the motion of its position is not technically a random walk, as it is moving continuously. The result of the calculation (for 3-D motion) is

$$D_r = \frac{3k_B T}{\beta'} \tag{2-40}$$

This position diffusion coefficient D_r has relevance to optical molasses arrangements, as the atoms, though cooled, are not confined and will eventually drift out of the active cooling region at a rate determined by D_r.

2.4.3 The Doppler cooling limit

This subsection uses the general result 2-36a, $k_B T = \frac{D_p}{3\beta'}$, of the previous section in a specific calculation of the lowest temperature attainable by Doppler laser cooling. Consider the case of the molasses configuration mentioned earlier consisting of three orthogonal pairs of counterpropagating laser beams. Equation 2-36 reveals that, in order to obtain a low atomic temperature, a high friction coefficient and a low diffusion coefficient are desirable. However these two quantities are not independent and therefore it is the ratio $D_p/3\beta'$ which must be minimised. Initially, each beam is assumed to be a low intensity ($s<<1$) plane wave which means that, in the steady state, the total absorption rate is equal to the total spontaneous emission rate and given by $\frac{\Gamma s}{2(s+1)} \approx \frac{\Gamma s}{2}$ for small s. For low intensity beams there are two contributions to momentum diffusion: one contribution is due to random Poissonian fluctuations in the absorption rates from each of the six beams and the second contribution is due to the random direction of the spontaneous emissions. Both contributions are incorporated in the following calculation.

For low intensity beams the individual absorption events are widely spaced in time and can therefore be treated as independent events with equal likelihood of an absorption of a photon from any of the six molasses beams. The rate of absorptions is therefore 6 x $\Gamma s/2$. Each absorption is followed by a spontaneous emission in a random direction. The rate of spontaneous emissions is therefore also 6 x $\Gamma s/2$. Each absorption or emission gives the atom a random 3-D momentum kick of magnitude $\hbar k$ and the total rate of momentum kicks is $6\Gamma s$. Using a standard result[153] for Brownian motion in either 1-D or 3-D, we find that the variance of the atomic momentum after a time t is given by $\langle p^2 \rangle = 6\Gamma s t(\hbar k)^2$. This is just the momentum step length squared multiplied by the number of steps taken in time t. It then follows from the definition of the momentum diffusion coefficient, $D_p = \frac{1}{2}\frac{d\langle p^2 \rangle}{dt}$, that

$$D_p = 3\hbar^2 k^2 \Gamma s \qquad (2\text{-}41)$$

It was shown earlier that the friction coefficient β is maximised with respect to the detuning Δ when $\Delta = -\Gamma/2$, which gives $\beta_{max} = 2\hbar k^2 s$, (see equation 2-27). Consequently, using this expression for β_{max} and the total diffusion coefficient from equation 2-41 in equation 2-36, the lowest temperature achievable by this cooling process is found to be T_D, where

$$k_B T_D = \frac{D_p}{3\beta_{max}} = \frac{3\hbar^2 k^2 \Gamma s}{6\hbar k^2 s} = \frac{\hbar\Gamma}{2} \qquad (2\text{-}42)$$

The temperature T_D is known as the Doppler cooling limit[216]; for rubidium cooled on the D_2 line it is 136 μK. It may be viewed in the light of Heisenberg's uncertainty principle: as there is an uncertainty of the order Γ^{-1} in the spontaneous emission time, the energy of the atom must be at least as large as the corresponding uncertainty in the energy.

In experimental situations the diffusion and friction coefficients D_p and β depend on the particular laser beam configuration, on the beam intensities and detunings and may also be spatially dependent; thus the precise calculation of cooling limits even for a two-level atom can be quite complex, e.g. see [127,150,154-156]. In the case of intense light fields, $s>1$, diffusion due to spontaneous emission saturates because the excited state population approaches 1/2 for $s>1$. Diffusion due to induced transitions, however, now contains contributions due to both absorption and stimulated emission and does not saturate. It increases monotonically with laser intensity, becoming significantly greater than the diffusion due to spontaneous emission. This validates the assumption made at the start of this subsection, namely that beams with a low saturation parameter would give the lowest temperature.

2.4.4 The Fokker-Planck equation

The most general mathematical description of motion due to stochastic forces is achieved with a 'Fokker-Planck' equation, so called because they were first separately derived by Fokker and Planck as descriptions of Brownian motion. Consider a large statistical ensemble of systems (e.g. particles in a fluid), each described by various macroscopic variables $\{x_i\}$ which are subject to microscopic thermal fluctuations. As an example the $\{x_i\}$ might be three position co-ordinates and three velocity components for a particle undergoing Brownian motion. The ensemble can be described by a 'distribution function' $f(x_i, x_j, \ldots\ldots x_n, t)$ which gives the probability of a system (or particle) being in the state $(x_i, x_j, \ldots\ldots)$ at time t. The Fokker-Planck equation is just the equation of motion of the distribution function, and is derived[152] essentially by performing a Taylor expansion of $f(\{x_i\}, t+\Delta t)$, and taking the limit of $\frac{f(\{x_i\},t+\Delta t)-f(\{x_i\},t)}{\Delta t}$ as $\Delta t \to 0$ to obtain an infinite series for $\frac{\partial f}{\partial t}$, consisting of all orders of the derivatives of f with respect to the $\{x_i\}$. It is then shown that, if the microscopic fluctuations give rise to Langevin forces with a Gaussian distribution, only the first two terms in the expansion are non-zero. This gives the general Fokker-Planck equation:

$$\frac{\partial f}{\partial t} = \left[-\frac{\partial}{\partial x_i} D_i^{(1)} + \frac{\partial^2}{\partial x_i \partial x_j} D_{ij}^{(2)} \right] f \qquad (2\text{-}43)$$

where the drift coefficients $D_i^{(1)}$ and diffusion coefficients $D_{ij}^{(2)}$ may be functions of the $\{x_i\}$ and t.

The particular form of equation 2-43 in specific applications depends on the number of macroscopic variables $\{x_i\}$ and the nature of the functions $D_i^{(1)}$ and $D_{ij}^{(2)}$. These functions may be determined either from consideration of the microscopic processes, or by finding the equivalent Langevin equations and using a thermodynamic argument. Once the drift and diffusion coefficients are known, the Fokker-Planck equation is solved either analytically or numerically to give the distribution function f. Usually the desired objective is the steady state distribution function found by solving equation 2-43 with $\frac{\partial f}{\partial t} = 0$. A point worthy of note is that the Fokker-Planck equation can be written as a continuity equation; as an example in one dimension for simplicity:

$\frac{\partial f}{\partial t} = -\frac{\partial S}{\partial x}$, where S is a probability current given by $S = \left[D^{(1)} - \frac{\partial}{\partial x} D^{(2)} \right] f$. It can be shown that for a stationary (steady-state) process, the probability current must be zero.

The preceding introduction is now clarified with two examples related to laser cooling.

i) One dimensional Brownian motion without a space dependent force.

Consider a one dimensional Brownian motion without a space dependent force. The set $\{x_i\}$ consists of just one variable, the speed v of the atom, obeying equation 2-38:

$$\frac{dv}{dt} = \frac{-\beta'}{m} v + F_L(t)$$

where the Langevin force is defined by

$$\langle F_L(t) \rangle = 0$$

$$\langle F_L(t) F_L(t') \rangle = \frac{2\beta' k_B T}{m^2} \delta(t - t')$$

The drift and diffusion coefficients in this case are $D_v^{(1)} = -\beta' v/m$ and $D_{vv}^{(2)} = \beta' k_B T / m^2$, and hence the equivalent Fokker-Planck equation for this system is

$$\frac{\partial f}{\partial t} = \frac{\beta'}{m} \left[\frac{\partial (vf)}{\partial v} + \frac{k_B T}{m} \frac{\partial^2 f}{\partial v^2} \right]$$

and the probability current is

$$S = \frac{-\beta'}{m} \left[vf + \frac{k_B T}{m} \frac{\partial f}{\partial v} \right].$$

For a stationary process the probability current must be zero, and putting $S = 0$ gives a simple differential equation for f. The solution is $f = Ce^{-\frac{mv^2}{2k_B T}}$, and normalisation gives $f(v) = \sqrt{\frac{m}{2\pi k_B T}} e^{\frac{-mv^2}{2k_B T}}$, which is the Maxwell-Boltzmann velocity distribution in one dimension. The above example shows that the Maxwell-Boltzmann velocity distribution will be obtained in any situation where a damping force proportional to velocity is counterbalanced by a momentum diffusion process. Doppler cooling is such a process.

ii) One dimensional Brownian motion in an external potential.

Consider a particle undergoing one dimensional Brownian motion in an external position-dependent potential which produces an external force F_{ext}. The set $\{x_i\}$ consists of two variables x and v. It is reasonable to assume that the thermal jitter of the molecules causing the Langevin force is not affected by the potential, and so F_L is independent of x. Then the Langevin equations are:

$$\begin{aligned} \frac{\partial v}{\partial t} &= -\frac{\beta'}{m}v - \frac{F_{ext}}{m} + F_L(t) \\ \frac{\partial x}{\partial t} &= v \end{aligned} \tag{2-44}$$

It can be shown[152] that the drift coefficients of the equivalent Fokker-Planck equation are

$$D_v^{(1)} = -\frac{\beta'}{m}v - \frac{F_{ext}}{m} \qquad D_{vv}^{(2)} = \frac{\beta' k_B T}{m^2}$$

$$D_x^{(1)} = v \qquad D_{xx}^{(2)} = D_{xv}^{(2)} = 0$$

The Fokker-Planck equation then takes the following form, also known as Kramer's equation:

$$\frac{\partial f(x,v,t)}{\partial t} = \left[-\frac{\partial}{\partial x}v + \frac{\partial}{\partial v}\left(\frac{\beta' v}{m} + \frac{F_{ext}}{m} \right) + \frac{\beta' k_B T}{m^2}\frac{\partial^2}{\partial v^2} \right] f(x,v,t) \tag{2-45}$$

or in three dimensions:

$$\frac{\partial f(\mathbf{r},\mathbf{v},t)}{\partial t} = \left[-\nabla_{\mathbf{r}}\mathbf{v} + \nabla_{\mathbf{v}}\left(\frac{\beta'\mathbf{v}}{m} + \frac{\mathbf{F}_{ext}}{m} \right) + \frac{\beta' k_B T}{m^2}\nabla_{\mathbf{v}}^2 \right] f(\mathbf{r},\mathbf{v},t) \tag{2-46}$$

Equation 2-46 is the form generally applicable in laser cooling and trapping experiments where $\mathbf{F}_{ext}$ may represent for example a large scale potential well, as in the Zeeman optical trap (see chapter 3), or, as another example, may represent a periodic potential with a period ~ $\lambda/2$. (See chapter 4). When found, a steady state solution of equation 2-46 gives the velocity distribution (temperature) and spatial distribution of cooled or trapped atoms. Calculations to find such solutions are generally complicated and this thesis will not delve deeper, other than to point to relevant literature e.g. [41]. General methods of solution for the Fokker-Planck equation are given in [152].

Summary of section 2.4

The problem of diffusion can be tackled with varying degrees of rigour by simple energy arguments, Langevin equations or the Fokker-Planck equation. The key implication for experimental work is that for the two-level atom, the stochastic nature of the cooling process sets a limit of order $\hbar\Gamma/2$ on the lowest achievable temperatures, which is known as the Doppler cooling limit.

2.5 Fully quantised approaches to light forces.

In the interests of completeness, this section gives an overview of two approaches to the calculation of light forces for two level atoms in which the centre of mass motion of the atom

is quantised. The first section discusses methods which use the Wigner transform of the density matrix, the second section discusses numerical approaches using the 'Monte Carlo wave function method'. The approaches described in this section quantise the internal state of the atom, the centre of mass motion of the atom and the light field including the empty vacuum modes. Such treatments may be found in references[157,158]. Because such methods are fully quantum mechanical, they can be regarded as having more rigour than the semiclassical treatments. Nevertheless, they have the disadvantage of leading to complicated calculations and simplifying assumptions are still required to obtain a solution, e.g. restriction to specific light intensity and atomic velocity regimes. These approaches serve two purposes. Firstly they confirm the results of the simpler semiclassical theory in the regime of its validity. Secondly they extend our understanding into regimes where semiclassical theory may no longer be used, i.e. when the quantum nature of the atomic wave packet may no longer be neglected. For instance, this occurs for atoms with small kinetic energies of the order of a single photon energy, or when an atom is confined in a potential well of very small dimensions.

2.5.1 The density matrix master equation and the Wigner function

The most convenient mathematical methods for dealing with the fully quantised problem were devised by Wigner[159]. The subject of interest is the distribution of the atoms over the possible position and momentum states and this is given by the 'Wigner function' $f_W(\mathbf{r},\mathbf{p})$ which is a 'quasi-distribution function' for the atoms over position and momentum space. If $\Psi(\mathbf{r})$ is the position-representation wavefunction, then

$$f_W(\mathbf{r},\mathbf{p}) = \frac{1}{(2\pi\hbar)^3}\iiint_{\text{space}} \Psi(\mathbf{r}+\frac{1}{2}\mathbf{s})\Psi(\mathbf{r}-\frac{1}{2}\mathbf{s})e^{\frac{-i(\mathbf{p}.\mathbf{s})}{\hbar}}\partial^3 s \qquad (2\text{-}47)$$

The Wigner function has the physically intuitive properties:

$$\int_{-\infty}^{+\infty} f_W(\mathbf{r},\mathbf{p})\partial^3 r = P(\mathbf{p}) \quad \text{the probability density of momentum} \qquad (2\text{-}48a)$$

$$\int_{-\infty}^{+\infty} f_W(\mathbf{r},\mathbf{p})\partial^3 p = P(\mathbf{r}) \quad \text{the probability density of position} \qquad (2\text{-}48b)$$

$$\int_{-\infty}^{+\infty}\int f_W(\mathbf{r},\mathbf{p})\partial^3 r\partial^3 p = 1 \quad \text{normalisation} \qquad (2\text{-}48c)$$

Though the integral of the Wigner function over the whole of its phase space is unity, it is a quasi-probability density because it can take negative values at points in its space. Having defined the Wigner function, calculations proceed in a manner that in some aspects parallels that of semiclassical theory, for instance [157] proceeds by defining a generalised Bloch vector, whose components $(U(\mathbf{r},\mathbf{p}),V(\mathbf{r},\mathbf{p}),W(\mathbf{r},\mathbf{p}))$ are distribution functions for the usual Bloch vector (u, v, w) :

$$u = \iint \partial^3\mathbf{r}\partial^3\mathbf{p}U(\mathbf{r},\mathbf{p}), \qquad v = \iint \partial^3\mathbf{r}\partial^3\mathbf{p}V(\mathbf{r},\mathbf{p}), \qquad w = \iint \partial^3\mathbf{r}\partial^3\mathbf{p}W(\mathbf{r},\mathbf{p}),$$

Note that just as the 'fourth' Bloch vector component is given simply by $\rho_{ee} + \rho_{gg} = 1$ as a consequence of normalisation (see equation 2-6), the Wigner function is normalised in equation 2-48c above. The equations for the generalised Bloch vector, after considerable manipulation, result in a Kramers-Fokker-Planck equation for $f_W(\mathbf{r},\mathbf{p})$, the distribution of the atoms over position and momentum space. This can then be solved in the steady state. The emergence of such an equation demonstrates the close analogy between atomic motion in near-resonant laser light and Brownian motion of a particle in a potential well. As with semiclassical treatments, most fully quantised treatments are confined, for simplicity, to one dimensional light fields; reference [160] is an exception.

One important conclusion[41] is that, for any stochastic cooling process, the lowest temperature achievable is inversely proportional to the correlation time τ_L of the Langevin force. For the two level atom this is simply $\tau_L = 1/\Gamma$ and we have $k_B T \approx \hbar\Gamma$ as before. Chapter 4 will discuss the case of multilevel atoms, where longer internal decay times τ_p are possible, and lower temperatures given by $k_B T \approx \hbar/\tau_p$ are achievable.

2.5.2 The Monte Carlo wave function method

The 'Monte Carlo wave function' method is an approach to calculating atomic observables such as light forces which has been developed since 1990 [111-117]. It is an iterative numerical method which is formally equivalent[112] to solving the master equation for the density matrix. In one variant of the method, applied to spontaneous emission of a single atom, one iteration proceeds as follows. The initial (excited) state of the atom is fully described by a normalised wave function, which is then allowed to evolve for a small time Δt under a Hamiltonian which is non-unitary. After Δt a 'pseudo measurement' is made with either of two possible outcomes whose probabilities are determined by a random number generator programmed to simulate the spontaneous decay rate. Either a spontaneous emission event is simulated, in which the wave function collapses into one of its possible ground states, or a null event (no spontaneous emission) is simulated, in which case the wavefunction continues to evolve under the Hamiltonian. The new wave function after this 'measurement' will no longer be normalised, as there has been a 'loss of probability' owing to the non-unitary Hamiltonian. Thus it is renormalised after each measurement to give a new wave function, and the second iteration begins. Thus, considering one atom only, the internal state and its associated observables follow a stochastic trajectory whose random element is due to the randomised times of the spontaneous emission events. The same simulation is run many times, enabling the time evolution of the distribution function of any observable to be obtained.

The advantage of this approach over the conventional master equation approach is that it requires only a wave function defined by n probability amplitudes, if n is the number of basis eigenstates, whereas the density matrix requires n^2 matrix elements. If the problem is

defined for a multilevel atom using a quantum mechanical treatment of the atomic centre of mass, then n can be large ($>> 100$). The stochastic wavevector method allows a trade-off in which a computer with a smaller memory may run a numerical simulation involving many more iterations which therefore require a longer run-time. This method is becoming an established technique for tackling the dynamics of laser cooling. It produces results which agree with experiments[114], it allows numerical simulation of the difficult three dimensional problem[115] and it provides new insight into laser cooling processes[116].

The master equation and stochastic wavevector approaches illustrate two equivalent views of the density matrix. In the master equation approach, the full density matrix of a large combined system is converted to a 'reduced density matrix' describing a small system interacting with a thermodynamic reservoir through decay terms. The reduced density matrix is not a pure quantum state, but rather a description of an 'average' atom which evolves smoothly under the master equation. In the stochastic wavevector method, each individual atom in the ensemble is always in one of its pure quantum states, and evolves independently according to given quantum mechanical probability laws by making discrete 'jumps' between these states, and the average of all the outcomes is taken.

2.6 Summary of chapter 2

The semiclassical theory of light forces is simpler to implement than the fully quantised description and provides an adequate framework for description of many aspects of cooling and trapping. It shows that light forces can be separated into dipole and scattering forces. The dipole force is position dependent, occurring where there is a light intensity gradient, and offers the possibility of trapping atoms. It is associated with exchange of photon momenta between plane waves, i.e. with coherent absorption/stimulated emission cycles. The scattering force is highly velocity dependent, offering the possibility of cooling atoms. It is associated with incoherent absorption/spontaneous emission cycles. The stochastic nature of light forces leads to momentum diffusion which sets a limit on the lowest temperatures obtainable. The residual kinetic energy also enables atoms to escape from any sufficiently shallow potential well.

Chapter 3
Optical molasses and the magneto-optical trap

Introduction

The history of experiments on the mechanical interaction between atoms and light was summarised in chapter 1. This chapter develops the story post 1985 and is devoted to two important practical applications of light forces, namely 'optical molasses' (described in section 3.2) and the 'magneto-optical trap' or 'MOT' (section 3.3). These two experimental arrangements, first built in 1985 and 1987 respectively, mark the beginning of a surge of growth in studies of the mechanical interaction between atoms and light. They are described in this chapter in terms of the Doppler forces discussed in chapter 2. Before proceeding, it should be stressed that a complete understanding of the processes in molasses and the MOT requires the introduction of further theoretical ideas, namely 'sub-Doppler' cooling mechanisms, which are discussed in chapter 4. The need for a sub-Doppler theory was not apparent until 1989 and thus the development of ideas in this and the following chapter follows the chronology of experimental and theoretical discovery. This chapter contains many simplifying assumptions made in order to estimate experimental parameters. For instance, it is often assumed that light forces in 3-D cooling and trapping arrangements can be modelled by the linear addition of the forces due to the three orthogonal 1-D standing waves. Section 3.4 discusses methods of loading atoms into molasses and traps and sections 3.5, 3.6 and 3.7 deal in turn with the most important parameters of the MOT, namely loading and loss rates, atomic number density and trap temperatures. Before discussing molasses and the MOT, section 3.1 shows how the idealised two-level atom of theory is achieved approximately with the real atoms of experiments.

3.1 Real 'two-level' atoms

How is the theoretical ideal of a two-level atom realised in practice? The alkali metals are useful in that they possess strong transitions at wavelengths accessible by lasers and in that they fairly easily form monatomic vapours and atomic beams suitable for spectroscopy. The D-lines of sodium, rubidium and caesium are commonly used, but they have hyperfine structure. As an example, the D_2 line ($5S_{1/2} \rightarrow 5P_{3/2}$) at 780 nm of the isotope of rubidium ^{85}Rb consists of six separate hyperfine transitions, between energy levels grouped as shown in figure 3-1.

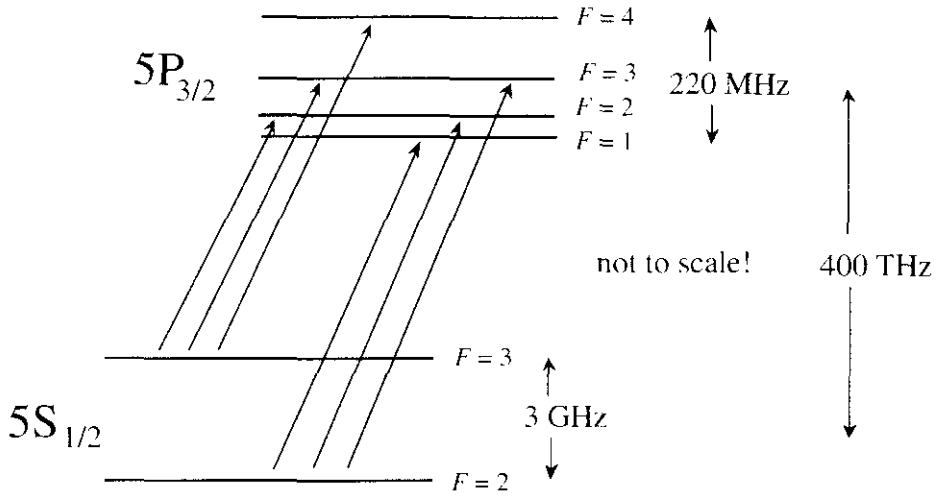

Figure 3-1 The hyperfine structure of the ^{85}Rb D_2 line.

The selection rules for electric dipole transitions allow only $\Delta F = 0, \pm 1$, and so if an atom is excited by a laser tuned to the $F_g = 3 \rightarrow F_e = 4$ hyperfine transition, it can only decay back to $F_g = 3$. Thus this is a two-level transition, with Zeeman degeneracy. Achieving such fine tuning is possible with a laboratory laser, whose linewidth can be orders of magnitude less than the hyperfine natural linewidth. There is however a snag with this scheme, in that the hyperfine lines are homogeneously broadened with a Lorentzian profile and so there is some small overlap between neighbouring hyperfine energy levels. In the specific example of ^{85}Rb, a laser tuned to the $F_g = 3 \rightarrow F_e = 4$ transition has a probability around 0.2% of exciting the $F_g = 3 \rightarrow F_e = 3$ transition, and from $F_e = 3$, the atoms can spontaneously decay into $F_g = 2$. Eventually all the atoms will be transferred (optically-pumped) into the $F_g = 2$ level, and the original two-level system almost completely depleted. To counteract this depletion, a second laser called the 'repumping' laser is used, tuned to the $F_g = 2 \rightarrow F_e = 3$ transition. By a similar process, this repumps a proportion of the atoms back to the $F_g = 3$ level. The final result is a steady state population distribution with a proportion of atoms in $F_g = 3$; the proportion is to some extent controllable by varying the repumping laser intensity. The atoms in $F_g = 3$ are coupled by the main laser to the level $F_e = 4$, creating to a good approximation a 'real' two-level system.

3.2 Optical Molasses

'Optical molasses' is the name given to an experimental arrangment in which intersecting laser beams produce a spatial region where gaseous atoms experience a large velocity-damping force, resulting in very low temperatures. The first builders of such an arrangement, Steve Chu et al[1] at Bell Laboratories, New Jersey, coined the term 'optical molasses' because of the resemblance of the resulting viscous fluid of photons to real molasses. The theoretical concept of 'optical molasses' was first suggested for neutral atoms by Hänsch and Schawlow [21]in 1974, and independently in 1975 for ions by Wineland and Dehmelt[20].

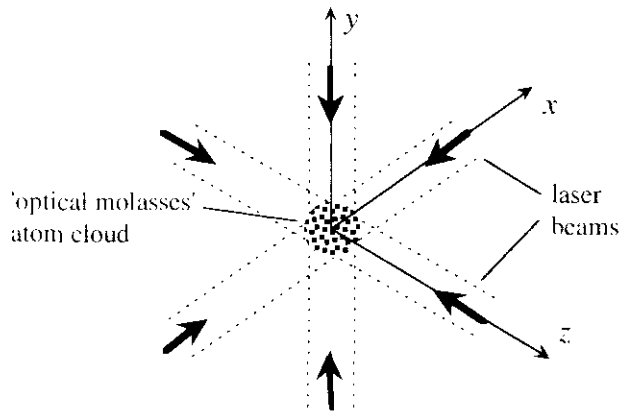

Figure 3-2 Optical molasses

The molasses are formed at the intersection of six weak ($s \leq 1$) laser beams, arranged as three counter-propagating pairs, and with each counter-propagating pair being orthogonal to the other two pairs as shown in figure 3-2. The laser beams all have the same wavelength which is detuned by about one natural linewidth to the red of a chosen atomic transition. The intersection of the beams occurs in a vacuum chamber containing a source of the chosen atomic species. In the first molasses apparatus[1], the sodium atoms to be cooled were injected into the molasses region in the form of a pulsed atomic beam. This and other loading methods are discussed in section 3-4.

The basic theory of operation has already been provided in chapter 2; each counterpropagating pair of beams gives rise to a mean damping force $F_i = \beta_i v_i$ (equation 2-25), where β_i is the (negative) friction coefficient and v_i the atomic speed on the ith axis. Bearing in mind that this result is the spatially averaged force and that it is strictly true only for low intensities ($\Omega_0 < \Gamma$) and low velocities ($kv < \Delta$), we can add the forces due to each of three beam pairs to find that

$$\mathbf{F} = \beta \mathbf{v}, \text{ where } \beta = \frac{16\hbar k^2 \Gamma \Omega_s^2 \Delta}{(\Gamma^2 + 2\Omega_s^2 + 4\Delta^2)^2} \tag{3-1a}$$

A more accurate expression for β, which takes account of power-broadening, is

$$\beta = \frac{16\hbar k^2 \Gamma \Omega_s^2 \Delta}{(\Gamma^2 + 12\Omega_s^2 + 4\Delta^2)^2} \tag{3-1b}$$

where the change to $12\Omega_s^2$ in the denominator is due to the average power-broadening due to 6 laser beams[145,161]. The magnitude of the friction coefficient β as given by equation 3-1b is maximised when $\Delta = -\Gamma/2$ and $\Omega_s^2 = \Gamma^2/6$.

To give some sense of scale before further developing the theory, table 3-1 lists some typical parameters for optical molasses.

Table 3-1 Typical optical molasses parameters for Rb (780 nm)

Cloud and beam diameter	$2r_m$	5 to 10 mm
Temperature	T	20 to 200 μK
Number of atoms in cloud	N	10^4 to 10^7
Atom number density	n	10^6 to 10^{10} cm^{-3} (1)
Capture velocity	v_c	~ 8 ms^{-1}
R.M.S. velocity in cloud	v	6 to 20 cm s^{-1}
Absorption cycles to stop atom		$\leq 10^5$
Stopping time		$\leq$ 1 ms

In the original experiment[1], the beam radius r_m was 3.5mm, creating a spherical molasses region with the same radius. Any atoms which enter this region from the atomic beam are subject to the damping force, and if the initial velocity is less than a certain capture velocity v_c, they are 'stopped'. They then undergo a diffusive motion (as discussed in chapter 2) which will result in their eventually reaching, after a confinement time τ_c, the boundaries of the molasses region and escaping. Other parameters of interest are N, the total number of atoms in the molasses; n, the number density in the molasses and T, the temperature of the captured atoms.

The temperature of the atoms is predicted by the theory of chapter 2 to be $k_B T = D_p/3\beta$ (equation 2-36) where D_p is the momentum diffusion coefficient and β the friction coefficient. It was shown in chapter 2 that because D_p and β are interdependent, there is a theoretical limit, the Doppler cooling limit T_D, given by $k_B T_D = \hbar\Gamma/2$ (equation 2-42). For sodium cooled on the D_2 line, T_D = 240 μK, which agreed with the result of 240^{+200}_{-60} μK measured by the Bell labs group.

The confinement time (or lifetime) can be estimated by using the position diffusion coefficient $D_r = \langle r^2 \rangle / 2t$, which is equal to $3k_B T/\beta$ (equation 2-40). Here r is the distance moved by an atom undergoing diffusive motion. Thus the atom will, on average, reach the boundary of the molasses region (a distance r_m) and escape in a time τ_c given by

[1] *High densities may be obtained transiently by loading the molasses from an MOT*

$\tau_c = r_m^2\beta/6k_BT$, which is of the order of 5 seconds[2] for sodium molasses with r_m = 3.5 mm and T = 240 μK. This calculation assumes a minimum diffusion rate and no superimposed drift velocity. If there is a small imbalance in the intensity of two counterpropagating beams, a drift velocity appears which dramatically reduces the confinement time, e.g. $\tau_c \approx 0.1$ s for an intensity imbalance of 2%[1].

In the case of the Bell labs experiment where the loading atomic beam was pulsed, each pulse loaded the molasses with ~ 10^5 atoms at a density of 10^6 atoms cm^{-3} and then the number of captured atoms decayed exponentially as they diffused away. The measured decay rates agreed well with the rates predicted by diffusion theory.

The capture velocity v_c may be estimated as follows. Assume that the friction coefficient has been optimised by setting $\Delta = -\Gamma/2$, $\Omega_s = \Gamma$. Then for a 1-D counterpropagating pair and an atom whose velocity component along that axis is v, we find that equation 2-24c simplifies to

$$\frac{dv}{dt} = \frac{-\hbar k\Gamma}{2m}\left(\frac{kv/\Gamma}{1+(kv/\Gamma)^2+(kv/\Gamma)^4}\right) \tag{3-2}$$

Solving this with initial condition $v = v_0$ when $t = 0$ we obtain

$$\log_e\left(\frac{v}{v_0}\right)+\frac{k^2}{2\Gamma^2}\left(v^2-v_0^2\right)+\frac{k^4}{4\Gamma^4}\left(v^4-v_0^4\right)=\frac{-\hbar k^2 t}{2m} \tag{3-3}$$

Initial insight into the damping process can be obtained analytically by integrating equation 3-3 in the two velocity regimes $kv << \Gamma$ and $kv >> \Gamma$. For instance it is easy to show that rubidium atoms with $kv_0 = \Gamma/4$, corresponding to v_0 = 1.1 ms^{-1}, are stopped in 0.05 mm, or that for atoms with $kv_0 = 4\Gamma$, corresponding to v_0 = 17.6 ms^{-1}, the stopping distance is 44 mm, i.e. much larger than most practical laser beam diameters. Further insight into the intermediate regime ($kv_0 \approx \Gamma$) may be obtained numerically by plotting the equation for various values of the initial velocity v_0 as in figure 3-3. The distances required to stop atoms with various initial velocities v_0 at $t = 0$ are given by the areas under the graphs. The graphs are plotted for the case of rubidium atoms cooled on the $5S_{1/2} \rightarrow 5P_{3/2}$ transition at 780 nm, and with $\Delta = -\Gamma/2$, $\Omega_s = \Gamma$. For this transition $\Gamma/k \approx 4.4$ ms^{-1} and $2m/\hbar k^2 \approx 40$ μs. In practice, molasses laser beam diameters are usually in the range 5 to 10 mm. Figure 3-3 shows that such stopping distances correspond to atoms with initial speeds of 11 to 13 ms^{-1}.

---

[2] *Note that this estimate is based on Doppler theory only. Longer confinement times are predicted in molasses when sub-Doppler cooling is taken into account, owing to larger β and smaller T.*

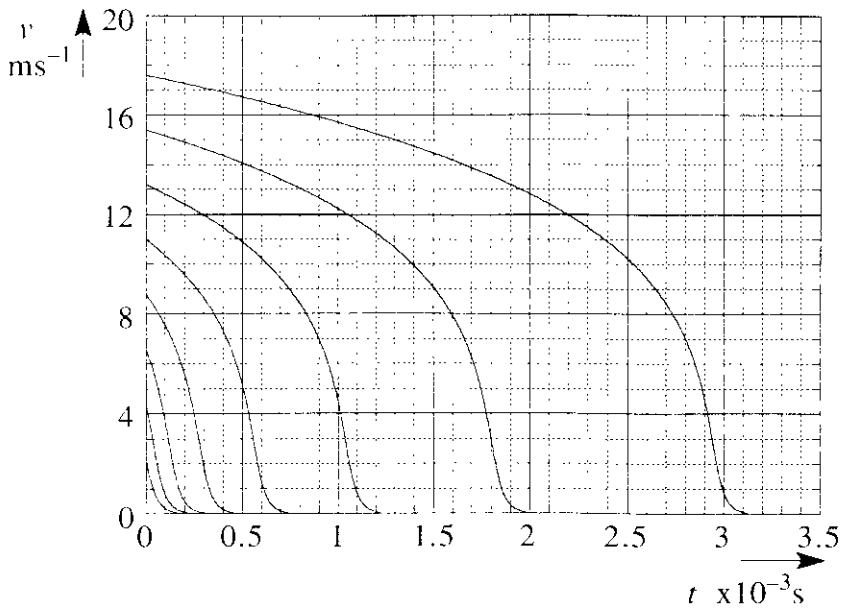

Figure 3-3 Theoretical plots of atomic velocity versus time for the molasses capture process of Rb

In a simple model of molasses, the capture region is spherical, and the maximum speed which can be stopped corresponds to atoms which are incident normally at the spherical boundary and just stopped as they reach the opposite boundary. For real molasses, the beam intensity profiles are Gaussian resulting in a smaller friction coefficient in the outer layers of the cloud. Furthermore, many atoms will enter the spherical molasses region at angles other than 90°. Different definitions of the term 'capture velocity' occur in the literature. Some groups, e.g. [29], have defined it as $v_c = 2\Gamma/k$, because this is the velocity range in which the molasses cooling force is greater than ≈ 1/10th of its maximum value. Others, e.g. [162], have defined it as $v_c = (2ar_{in})^{1/2}$, which is the maximum speed which can be stopped within a molasses beam radius r by a molasses deceleration of magnitude a. This latter definition is more useful as it takes into account the actual stopping distance available.

The invention of molasses opened the door to new areas of studies using these cold atoms, but was still not always an ideal tool in that molasses (or even 'supermolasses'[163]) is not a trap for atoms. Because there is only a velocity damping force and no spatial restoring force, the slowed atoms eventually diffuse out of the trap region, necessitating reloading from an atomic beam. Theorists at that time had invoked what was known as the Optical Earnshaw theorem[164] to prove that the scattering force could never be used to produce a stable trap as the divergence of the Poynting vector is zero in charge-free space[3].

[3] *The dipole force, as distinct from the scattering force, may be used to form a stable trap [2]*

This theory is correct for strictly two-state atoms, but as was first pointed out in 1986[165] and demonstrated experimentally in 1987[28], stable trapping by the scattering force is indeed possible for two-level atoms when the excited level is Zeeman degenerate. Such trapping forms the basis of the magneto-optical trap, discussed next.

3.3 The Magneto-optical Trap

The first magneto-optical trap (MOT) was built by Raab et al in 1987[28], though the seminal idea is credited in that paper to Jean Dalibard. The trap uses the same laser beam configuration as optical molasses, i.e. six detuned lasers in three counterpropagating pairs. Just as a velocity-dependent detuning (the Doppler shift) can lead to a damping force, so can a spatially-dependent detuning lead to a restoring force. This is achieved in an MOT by the addition of two additional features to a molasses arrangement: firstly the six beams are each circularly polarised according to the scheme shown in figure 3-4, and secondly, a quadrupole magnetic field is provided in the beam intersection region by a pair of 'anti-Helmholtz' coils, again as shown in figure 3-4. The magnetic field gradient is usually of order 5 to 15 gauss cm^{-1} at the trap centre, although MOT's with higher gradients have been investigated[166,167].

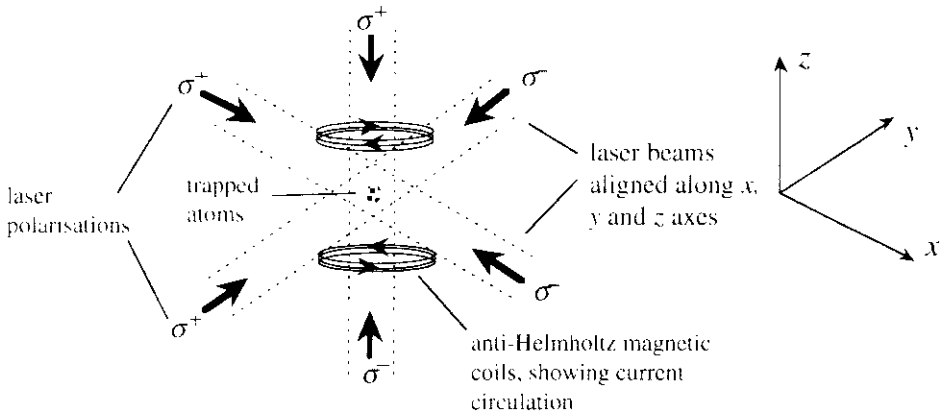

Figure 3-4 The magneto-optical trap (MOT)

The MOT has become a standard starting point for much of the current experimental work on cold atoms (roughly 50 groups worldwide). Once it is built, it is a convenient source of dense, cold atoms which can be used for their Doppler-free spectroscopic properties, studied for interesting physics in their own right, and used as an 'on-tap' supply of cold atoms for other experiments or types of trap. A comprehensive review of the physics of the MOT may be found in [162]. A typical MOT has the parameters given in Table 3-2. Further details of the specific MOT apparatus used in this work are to be found in chapter 6.

Table 3-2 Typical parameters for a magneto-optical trap for Rb

Cloud diameter	0.1 to 1 mm
Temperature	10 to 200 μK
Atom number	10^4 to 10^{10}
Atom number density	10^8 to 10^{11} cm^{-3}
Potential well depth	~ 0.5 K (x k_B)
Capture velocity	5 to 25 ms^{-1}
Beam diameter	3 to 20 mm

3.3.1 The operating principle of the MOT

The operating principle of the MOT is most easily explained in 1-D, and for an atom excited on a $J_g = 0 \rightarrow J_e = 1$ transition. Firstly, note that the experimental set-up is still a molasses arrangement, and so the molasses damping force is present. The magnetic field produced by an anti-Helmholtz pair (the same geometry as a Helmholtz pair but with opposed current circulations in the two coils) is zero at the centre of the molasses/trap region. The field has a magnitude B_z which increases linearly for small displacements from the centre, but the field directions are opposite on either side of the trap. Thus the normally degenerate Zeeman sublevels ($m_e = 0, \pm 1$) of the excited state are split, and the splitting increases with the distance of the atom from the trap centre. Figure 3-5 shows the 1-D spatial variation of the Zeeman sublevels for a $J_g = 0 \rightarrow J_e = 1$ transition.

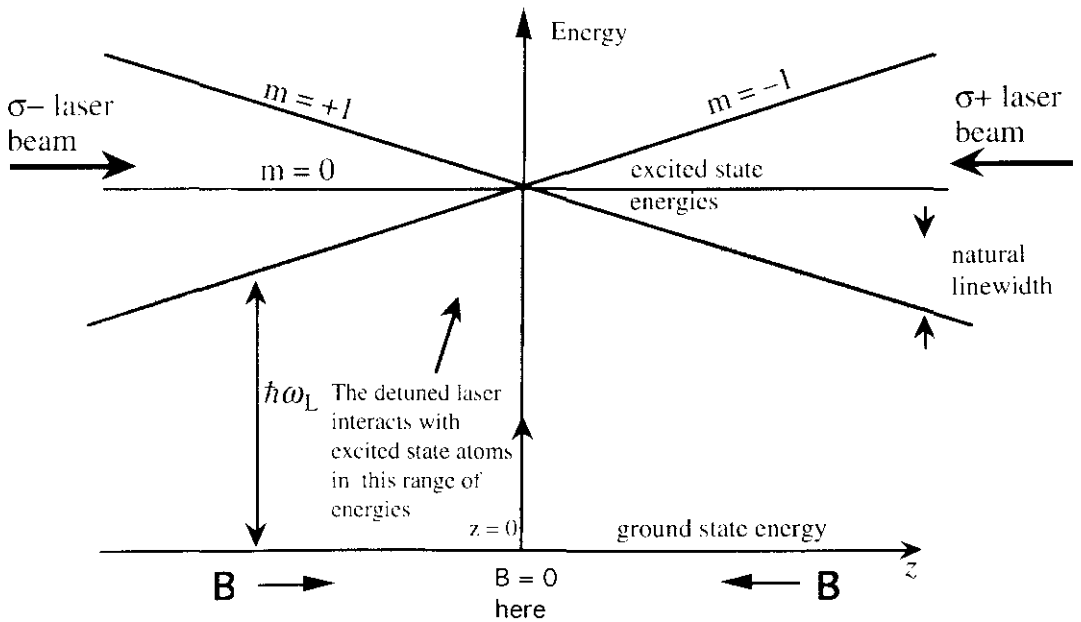

Figure 3-5 Atomic energy levels in a magneto-optical trap

At the centre of the trap the three excited state sublevels have equal energy. Away from the trap centre, however, the energies of the $m_e = -1$ and $m_e = +1$ states shift in opposite

directions. Consider an atom to the left $(-z)$ of the trap centre. Because the laser is detuned, the probability of transition for such an atom from $|g, m_g = 0\rangle$ to $|e, m_e = -1\rangle$ is increased and that of $|g, m_g = 0\rangle$ to $|e, m_e = +1\rangle$ is diminished. The transition $|g, m_g = 0\rangle$ to $|e, m_e = -1\rangle$, however, is excited only by σ^- light, where σ^- indicates that the light carries $-\hbar\hat{\mathbf{z}}$ of angular momentum per photon. Thus the atom preferentially absorbs the σ^- photons gaining $\hbar k\hat{\mathbf{z}}$ of (linear) momentum per event, and as in pure molasses, the momentum kicks due to the subsequent spontaneous emission events cancel out on average. A similar situation exists on the right $(+z)$ side of the trap centre, but involves an increased probability for the $|g, m_g = 0\rangle$ to $|e, m_e = +1\rangle$ transition and σ^+ photons. This particular set-up of two counter-propagating beams with equal intensities, but opposite angular momenta is referred to as a $\sigma^+\sigma^-$ standing wave. It requires the counter-propagating beams to be circularly polarised with either both beams left-handed (or both right -handed). This is usually achieved in experiments by retroreflecting an incoming circularly polarised beam at a quarter-wave plate and mirror combination, i.e. so that it passes through the waveplate twice.

The result is that atoms in the trapping region experience a force towards $z = 0$ and this effect is easily extended in experiments to three dimensions. The quadrupole field for the anti-Helmholtz coils produces a field gradient on each of the three Cartesian axes and it is simply a matter of arranging for the correct arrangement of σ^+ and σ^- beams on each axis to produce a fully three-dimensional trap. Theoretical analysis of the MOT in 3-D is complicated by the interference between the three standing waves and most theoretical papers give estimates for the 3-D case, based on 1-D calculations. Reference [168] gives a 3-D quantum-mechanical analysis of the MOT, using Doppler cooling mechanisms only.

3.3.2 The MOT as a damped harmonic oscillator

The restoring force of the MOT is now discussed quantitatively. The Zeeman detuning due to the magnetic field is additional to the Doppler detuning and laser detuning, and may be incorporated in the denominator of the low-intensity equation of motion (2-24a) for a $J = 0$ to $J = 1$ atom in 1-D optical molasses:

$$F_z = \hbar k\left(\frac{\Gamma\Omega_s{}^2}{\Gamma^2 + 2\Omega_s{}^2 + 4(\Delta - kv_z - \zeta z)^2} - \frac{\Gamma\Omega_s{}^2}{\Gamma^2 + 2\Omega_s{}^2 + 4(\Delta + kv_z + \zeta z)^2}\right) \qquad (3\text{-}4)$$

where $\zeta = \frac{g\mu_B}{\hbar}\frac{dB_z}{dz}$, g is the Lande factor for the excited state and μ_B the Bohr magneton. This may be simplified to a form (compare with equation 2-24c)

$$F_z = \frac{c_1\rho}{1 + c_2\rho^2 + c_3\rho^4} \qquad \text{where} \quad \rho = \frac{kv_z + \zeta z}{\Gamma} \qquad (3\text{-}5)$$

where c_1, c_2 and c_3 depend only on Ω_s, Δ and Γ and the dimensionless variable ρ is the sum of the Doppler and Zeeman detunings. Just as for pure molasses, the coefficient c_1 has

its greatest magnitude when $\Delta = -\Gamma/2$ and $\Omega_s = \Gamma$, and in that case $c_1 = -\hbar k\Gamma/2$, $c_2 = c_3 = 1$, giving

$$F_z = \frac{-\hbar k\Gamma}{2}\frac{\rho}{1+\rho^2+\rho^4} \tag{3-6}$$

As the variable ρ depends on both the atomic velocity and position, equation 3-6 is a non-linear differential equation and difficult to solve, but its behaviour can be analysed as follows. Firstly, the main regime of interest is defined by $\rho << 1$, because this corresponds to atoms which have been slowed and captured. In the limit $\rho << 1$, the denominator of equation 3-6 is approximately equal to one, and we have the equation of a damped harmonic oscillator

$$F_z = -\beta v_z - \kappa z \tag{3-7}$$

Here β is the usual molasses friction coefficient, originally defined in equation 2-25 and κ is the spring constant of the MOT, which is related to β by $\kappa = \frac{\zeta\beta}{k} = \frac{g\mu_B}{k\hbar}\frac{dB_z}{dz}\beta$. It turns out that, in experimental practice, the ratio of β to κ is such that the motion is overdamped, though this is not necessarily predicted by the Doppler theory presented in this chapter. The latter point is further discussed in chapter 4 which deals with sub-Doppler cooling.

As the variable ρ increases from small values towards 1, the effect of the denominator in equation 3-5 becomes increasingly significant. When $\rho = 1$, the magnitude of the force damping coefficient in equation 3-6 is reduced to about 1/3 of its maximum value, and as ρ increases above 1, the force rapidly tends towards zero. The MOT force is effective roughly in the range $-2 < \rho < +2$. Hence the other regime of interest is when $|\rho| \approx 1$, as this corresponds to the initial capture process. The MOT parameter of interest here is the capture velocity v_c. An important point is that because $\rho = (kv_z + \zeta z)/\Gamma$, there are situations in which kv and ζz have opposite signs and this allows higher velocities to be damped to zero than in pure optical molasses. In fact atoms entering the trap region 'too slowly' may first be accelerated inwards and then swiftly stopped close to the trap centre. The result is that atoms with speeds up to $\sim v_c \approx 4\Gamma/k$ may be captured[4]. This is about twice the capture velocity for pure molasses. As a numerical example, consider an MOT for rubidium with $\Delta = -\Gamma/2$ and $\Omega_s = \Gamma$ and a typical magnetic field gradient of 10 Gcm^{-1}. An atom at $z = 4$ mm from the trap centre, has $\zeta z/\Gamma = +2$, and hence experiences no force when $kv_z/\Gamma = -2$ or $v_z = -8.8$ ms^{-1}, because then $\rho = 0$.

A first approximation to the force field in a fully three-dimensional trap is obtained, as was done previously for molasses, by simply adding the forces due to three orthogonal one-

[4] *The effect of this Zeeman-slowing on the capture velocity in the case of a fully three-dimensional model of the MOT is much more complex[57]; the increase in the capture velocity is less than that in the 1-D model described here.*

dimensional models. This approximation ignores effects due to interference between the various laser beams. The quadrupole field has the property, following from Maxwell, div**B** = **0**, that $dB_x/dx = dB_y/dy = -\frac{1}{2}dB_z/dz$ where the z axis runs along the common axis of the anti-Helmholtz coils. As the spring constant in each direction is proportional to the field gradient in that direction, the cloud of trapped atoms is confined by a stronger force in the z direction leading to an ellipsoidal shape (see figure 6-22a on page 160, which is an image of an MOT atom cloud). A complete mathematical treatment would therefore employ a tensor spring constant e.g.[162], but for the simple discussion intended here, either the contraction to the 1-D picture or a spherically symmetric model is sufficient.

The above model of the MOT may be extended (without considering sub-Doppler cooling mechanisms) to atoms undergoing J to $J+1$ transitions where $J > 0$. The MOT operating principle is the same, though there are more ground and excited substates to take into account. An accurate calculation of the MOT spring constant then involves averaging over all the possible transitions and it is necessary to take into account the different Landé g-factors of the ground and excited states and the steady state population brought about by optical pumping[169]. Optical pumping will occur into the ground states with the most negative magnetic quantum number on the side of the trap resonant with σ^- light, and vice-versa. However, further discussion of cooling of atoms with $J_g > 0$ is deferred until chapter 4, where the sub-Doppler cooling mechanisms essential to a correct detailed understanding of the MOT are introduced.

3.4 Loading the magneto-optical trap

There are two basic methods of loading atoms into an MOT: loading from an atomic beam and loading from a background vapour.

3.4.1 Loading from an atomic beam

The first groups to build and experiment with the MOT[28,87] loaded their traps from an atomic beam. Because there is a maximum capture velocity and because the thermal velocities in an atomic beam are usually greater than room temperature thermal velocities, it is necessary to decelerate the atoms in the atomic beam. This is done with a single cooling laser beam counterpropagating with respect to the atomic beam. As the atoms in the beam are decelerated from several hundred ms^{-1} to a capture velocity around 10 ms^{-1}, the optimum laser detuning for efficient slowing also decreases, and it is necessary to sweep this detuning to stay in resonance with the decelerating atoms. There are two techniques for doing this. The first technique shifts the laser frequency in step with the Doppler shift of the slowing atoms and is known as 'chirp-cooling'. For instance in slowing a beam of caesium atoms from a caesium oven, the laser frequency would be scanned over ~ 500 MHz in 5 ms[169,170]. The second technique shifts the atomic transition frequency via a magnetic field which varies along the atomic beam path in such a way as to maintain the optimum

detuning. This is known as 'Zeeman-slowing'[23,171]. In [23], Na atoms were slowed from 900 ms^{-1} in 90 cm, over which distance the magnetic field dropped from 0.16 T to 0.05 T.

Loading from an atomic beam offers some advantages over the method of loading from a vapour. Firstly, the vacuum surrounding the trap can be as good as technology can achieve, which minimises collisions from background atoms and results in a long lifetime (around a few seconds) for atoms in the trap. (Trap loss processes are discussed further in section 3.5.2). A second advantage of atomic beam loading is that the source of atoms can be switched on and off.

3.4.2 Loading an MOT from a background vapour

The alternative loading method, first used in 1990[29], is to load directly from a surrounding vapour of the atomic species to be trapped. Here, atoms from the low speed end of the Maxwell speed distribution, with speeds less than the capture velocity v_c may be captured. From the kinetic theory of gases, such slow atoms constitute only $\left(v_c/v_p\right)^3 \approx 10^{-4}$ of all atoms, where v_p is the most probable velocity in the Maxwell-Boltzmann distribution. One advantage of this method is the simplicity of construction of the apparatus compared to a method requiring an atomic beam. A second advantage is that the trapped cloud will exist in a steady state, facilitating certain types of experiments e.g. measurements of cloud diameter and number density.

3.4.3 Loading molasses from an MOT

Molasses was first loaded directly from an atomic beam, and cannot be usefully loaded directly from a vapour as the continuous outward diffusion prevents a high number density[5]. However, the invention of the MOT allowed loading of molasses from a MOT in a vapour. Once the MOT is loaded from the background vapour, the magnetic field may be switched off, leaving pure molasses with a high number density. The initially small molasses cloud then expands diffusively and also decays as a result of background collisions e.g.[205]. It is also worth mentioning that some groups (e.g. E.N.S. [119]) are now using one MOT to load a second MOT! The first MOT is in a region of high background pressure and is therefore quickly loaded; its contents are then literally dropped into a region of low background pressure where a second MOT awaits to retrap the atoms. Thus the second MOT can also be efficiently loaded but without the disadvantage of a high local vapour pressure.

3.5 MOT loading and loss rates

This chapter now confines itself to discussion of the arrangement used in this work, namely an MOT for rubidium loaded from a vapour. This section reviews simple models and

---

[5] *But see section 4.7.10 (the NOT trap), which appears to be a recently discovered exception.*

calculations for the parameters: number of atoms, number density, cloud size and temperature.

3.5.1 Loading rate

The MOT trapping region can be modelled as a spherical region which swallows any atoms entering with speeds less than v_c. Consider a small region dA on the surface of this sphere. It can be shown from the kinetic theory of gases that the rate of flow of atoms with $v \leq v_c$ into the sphere through this aperture is given to good approximation by $\frac{n_b v_p dA}{4\pi^{1/2}}\left(\frac{v_c}{v_p}\right)^4$ per second; here n_b is the number density of the background vapour. Integrating over the whole spherical surface gives the rate R of atoms captured per second by the MOT as

$$R = \pi^{1/2} n_b v_p r_m^2 \left(\frac{v_c}{v_p}\right)^4 \tag{3-8}$$

where r_m is the radius of the laser beams forming the trap. $R \approx 2 \times 10^8$ s^{-1} for rubidium loaded from a room temperature vapour into a trap with 5 mm diameter laser beams. Equation 3-8 is in good agreement with the result quoted in [29], bearing in mind the simple assumptions made. The result derived here for instance, assumes that all atoms entering the sphere through dA are trapped, whereas in reality the capture velocity v_c will depend on the angle between the normal to the sphere and the atom trajectory. This is because obliquely incident atoms take shorter paths through the trapping region and because the intensity profile of the laser beams is usually gaussian, resulting in reduced damping in the outer trapping layers. If one instead assumes that only those atoms are captured which cross the equatorial plane of the trapping sphere (i.e. enter with angle of incidence $< 45°$), then the estimate of the capture rate R given by equation 3-8 is reduced by a factor of exactly 1/2.

3.5.2 Trap losses and collisions

The loading from the background vapour is limited by loss mechanisms which divide into two categories. Firstly there are collisions with the atoms of the background gases in the vapour cell, including the same species as the trapped atoms and other foreign gases. The rate of collisions of this type is directly proportional to N, the number of trapped atoms. Secondly, there are collisions between trapped atoms themselves; in a simple model the rate of these collisions is proportional to N^2. Thus the number of atoms in the trap is governed by a rate equation

$$\frac{dN}{dt} = R - \frac{N}{\tau} - \beta_c N^2 \tag{3-9}$$

where τ is the lifetime for atoms to remain in the trap against background atom collisions and β_c is a parameter determining the rate of intra-trap (i.e.cold-cold) collisions. Though this equation is exactly soluble, sufficient physical insight is gained by studying the approximate solutions for particular parameter regimes.

Trap losses due to collisions with background vapour atoms

Firstly consider the case when intra-trap collisions may be ignored ($\beta_c N^2 << N/\tau$) and all the collisions are due to the background gas. Then the solution is

$$N(t) = (N(0) - R\tau)e^{-t/\tau} + R\tau$$
$$N_F = N(t = \infty) = R\tau \qquad (3\text{-}10)$$

representing an exponential loading/decay rate with a steady state number of atoms N_F equal to $R\tau$.

The room temperature background atoms are travelling with thermal energies of ~ 295 k_B and the trap is a potential well with a depth of < 1 k_B, so it is easy for such collisions to result in ejection of the cold atom from the trap. The rate at which this occurs may be estimated from kinetic theory to be $N/\tau = N\sigma n_b \bar{v}$, where σ is the cross-section for such 'trap-loss' collisions, n_b the number density of background atoms and $\bar{v}$ the mean velocity of background atoms. Thus $\tau = 1/\sigma n_b \bar{v}$, and using $n_b = P/k_B T$ and $\bar{v} = \sqrt{8k_B T/\pi m}$, we find

$$\tau = \frac{\sqrt{\pi m k_B T}}{2\sqrt{2}\sigma P} \qquad (3\text{-}11)$$

This may be combined with the previous results for R (equation 3-8) and N_F (equation 3-10) to give

$$N_F = \frac{\pi r_m^2}{2\sigma}\left(\frac{v_c}{v_p}\right)^4 \qquad (3\text{-}12)$$

Equation 3-12 shows that the number of trapped atoms depends critically upon both the capture velocity and the laser beam radii, but as was illustrated in figure 3-3, the capture velocity also depends on the laser beam radii. Substituting the expression for the capture velocity $v_c = (2ar_m)^{1/2}$ into equation 3-12 yields the approximate relationship $N_F \propto r_m^4$ (in the regime where intra-trap collisions are negligible). An important conclusion therefore is that the way to capture large numbers of atoms is to use the largest diameter trapping beams possible, the largest number recorded[108] being 3.6 x 10^{10} Cs atoms when using beams 4 cm in diameter. Various other methods of increasing the number of trapped atoms have been published[174]. It is also worth noting that N_F does not depend on the pressure of the background vapour.

The trap-loss cross-section due to collisions with background atoms is made up of two elements: 'hard-sphere' collisions involving the van der Waals $1/r^6$ interaction when the colliding atoms are both in the ground state and 'long range' collisions involving the dipole-dipole $1/r^3$ interaction when one of the colliding atoms is in the excited state. Trapped atoms spend a significant proportion of the time in the excited state and fast background atoms passing through the trap region can become excited once they enter the molasses beams. The cross-section for long-range collisions can be one or two orders of magnitude greater than

that for hard-sphere collisions[169]. As the trapping beam intensity increases, the occupation of the excited state by trapped atoms increases, increasing the rate of long-range collisions, and thus acting to increase the trap-loss cross-section. One might therefore expect a decreased trap lifetime: however, a higher intensity also implies a higher escape velocity, which acts to decrease the trap-loss cross-section and could lead to an increased trap lifetime. Hence an exact value of the trap-loss cross-section is difficult to calculate theoretically. Experimental measurements, however, of the lifetime of the MOT have been used to estimate the trap-loss cross-section σ for Na and Cs [29,88,162] and the variation of the trap-loss cross-section with intensity[91].

Trap losses due to intra-trap (cold-cold) collisions

The second category of collision which can eject cold atoms from the trap is that of 'intra-trap' or 'cold-cold' collisions (i.e. which occur between pairs of trapped atoms). They are represented in equation 3-9 (for the number of trapped atoms N) by the parameter β_c. As the number of atoms in the trap increases, the effect of intra-trap collisions becomes significant (when $\beta_c N^2 \approx N/\tau$). In this case, rather than write the complicated general solution to equation 3-9, I give the solutions for two specific situations. Firstly, when the trap is loaded from a background vapour with the initial condition $N(t=0) \approx 0$, the steady state solution is

$$N(t=\infty) = \frac{1}{2\beta_c \tau}\left((1+4\beta_c R\tau^2)^{1/2} - 1\right) \qquad (3\text{-}13)$$

In the second situation, when the trap is initially loaded with N_0 atoms from an atomic beam and the loading beam then switched off, the number of atoms decays as

$$N(t) = \frac{N_0 e^{-t/\tau}}{1+\beta_c \tau N_0 (1-e^{-t/\tau})} \qquad (3\text{-}14)$$

The non-exponential decay implied by equation 3-14 formed the basis of an experimental method to determine β_c [88].

The intra-trap collisions fall into three types: 'fine structure changing' collisions, 'radiative redistribution' collisions and 'hyperfine changing' collisions. These collisions are an important new area for study[87-102] which is currently highly active. Only a very brief review is possible here. For cold atoms, the collision interaction time can be longer than the spontaneous lifetime, allowing the excitation and de-excitation of the atom to occur during a collision: this is a new regime for collisional studies. Intra-trap collisions are also important because they are a major obstacle to attempts to reach high densities of ultracold atoms in optical and other types of trap.

In fine structure changing collisions, a rubidium atom excited to a $5P_{3/2}$ state is transferred to a $5P_{1/2}$ state by collision with another atom of the same species. The energy difference is shared as kinetic energy of the two atoms and corresponds to a post-collision speed of ~ 180 ms^{-1} per rubidium atom.

Radiative redistribution occurs when one of two nearby atoms becomes excited. This changes the atom interaction from a negligible $1/r^6$ Van der Waals interaction to a strong $1/r^3$ dipole-dipole interaction which pulls the atoms towards each other, resulting in a lower mutual potential energy before the spontaneous emission occurs. The emitted photon has less energy than that absorbed and the balance appears as atomic kinetic energy.

In hyperfine changing collisions one of the colliding atoms transfers between ground state hyperfine levels and so this type of intra-trap collision is present even for low laser intensities. Again the energy difference appears as kinetic energy corresponding to a post-collision speed of ~ 4 ms^{-1} per (Rb) atom which, for a typical MOT, is slightly less than the escape speed.

Both fine structure changing and radiative redistribution collisions involve excited atoms and so are expected to occur at a rate which increases with intensity, whereas hyperfine changing collisions involve only ground state atoms and so are expected to be the predominant loss mechanism at low intensities. These predictions have been confirmed experimentally [87,91].

3.6 Number density distribution and collective effects

The total number of atoms trapped in an MOT loaded from a vapour can vary in the range ~10^3 to ~10^{10}, depending on the parameters: beam radius, intensity and detuning. For a typical experimental set-up with a beam diameter around 8 mm and normal intensity and detuning, the number range is observed[57] to be ~10^6 to ~5 x 10^7. This section 3.6 discusses the spatial distribution of the atoms in the cloud. The type of spatial distribution obtained depends upon whether the atoms are interacting weakly or strongly with each other through long range forces, and this in turn depends on the total number of atoms in the cloud. When the interaction is weak, the atom cloud may be modelled as an ideal gas. The 'ideal gas regime', corresponding to numbers of atoms less than ~10^5, is discussed below.

3.6.1 Cloud size and spatial distribution of atoms in the ideal gas regime

The Fokker-Planck equation for Brownian motion in an external potential (equations 2-45 and 2-46) may be solved[152] for either a 1-D harmonic well or a spherically symmetric 3-D harmonic well with spring constants κ_z and κ respectively. The solutions give the phase space distributions of the atoms

1-D
$$f(z,v_z)=\frac{(m\kappa_z)^{1/2}}{2\pi k_B T}\exp\left(\frac{-\left(\tfrac{1}{2}mv_z^2+\tfrac{1}{2}\kappa_z z^2\right)}{k_B T}\right)$$

3-D
$$f(r,v)=\left(\frac{(m\kappa)^{1/2}}{2\pi k_B T}\right)^3\exp\left(\frac{-\left(\tfrac{1}{2}mv^2+\tfrac{1}{2}\kappa r^2\right)}{k_B T}\right)$$

The marginal distributions of z and r are obtained by integrating over the speeds v_z and v respectively, and the results are the Gaussian number density[6] distributions

1-D $$n(z) = n_{z0} \exp\left(-\kappa_z z^2 / 2k_B T\right) \tag{3-15a}$$

3-D $$n(r) = n_0 \exp\left(-\kappa r^2 / 2k_B T\right) \tag{3-15b}$$

where $n_{z0} = N_0 \left(\frac{\kappa_z}{2\pi k_B T} \right)^{1/2}$ and $n_0 = N_0 \left(\frac{\kappa}{2\pi k_B T} \right)^{3/2}$ are the (1-D and 3-D) number densities at the trap centre and N_0 is the total number of atoms in the trap. The r.m.s. values of z, v_z, r and v may be obtained directly by integration of the marginal distributions (equations 3-15a, b) or alternatively by use of the Equipartition theorem. The results are

$$\text{1-D: } \frac{1}{2} m \langle v_z^2 \rangle = \frac{1}{2} \kappa_z \langle z^2 \rangle = \frac{1}{2} k_B T \qquad \text{3-D: } \frac{1}{2} m \langle v^2 \rangle = \frac{1}{2} \kappa \langle r^2 \rangle = \frac{3}{2} k_B T \tag{3-16}$$

A typical value for $z_{r.m.s.}$ in an MOT is ~0.4 mm, though it can vary from ~0.05 mm to ~6 mm, depending on the experimental set-up.

The above solutions of the Fokker-Planck equation are based on a classical model of the harmonic well, i.e. a harmonic well with a continuum of allowed energies. In a quantum mechanical treatment of the harmonic well, the expression for the average energy $\langle \xi \rangle$ of an ideal gas of bosons in a 1-D harmonic well with oscillation frequency ϖ is

$$\langle \xi \rangle = \frac{\hbar \varpi}{\exp(\hbar \varpi / k_B T) - 1} + \frac{\hbar \varpi}{2} \tag{3-17}$$

One must consider equation 3-17 in the two regimes: $k_B T >> \hbar \varpi$ and $k_B T \leq \hbar \varpi$. In the limit when $k_B T >> \hbar \varpi$, equation 3-17 becomes $\langle \xi \rangle = k_B T$, and one simply obtains again the classical result, equation 3-16, in accordance with the Equipartition theorem and the correspondence principle. In the case when $k_B T \leq \hbar \varpi$, equation 3-17 becomes $\langle \xi \rangle = \hbar \varpi / 2$, corresponding to the energy of the ground state of the oscillator. Thus it follows that in 1-D

$$\frac{1}{2} \hbar \varpi = \frac{1}{2} \kappa_z \langle z^2 \rangle + \frac{1}{2} m \langle v_z^2 \rangle \qquad k_B T \leq \hbar \varpi \tag{3-18}$$

In most experimental cases, $k_B T >> \hbar \varpi$ and equation 3-16 will apply. However, equation 3-18 applies to the recently observed Bose-Einstein condensate[34], where all the atoms are in the ground state of the trapping potential well (if it is assumed to be harmonic).

Consider a typical MOT. As atoms are steadily loaded into the trap, the spatial distribution given by equation 3-15 is maintained, whilst the number density throughout the cloud increases in time, i.e. the atoms are independently occupying the same space. At some number (around 10^5 atoms for Cs[175]), the density at the centre will reach a point where repulsive forces between the atoms due to 'radiation pressure' become significant, preventing any further increase in density and the number density distribution enters a new 'static' regime, discussed next.

---

[6] *Note this is a number density distribution, not a number distribution.*

3.6.2 Radiation pressure and collective behaviour

As the number density of atoms increases, the probability of reabsorption of a spontaneous emission photon by another trapped atom increases. Such a process involves momentum recoils on both atoms which move the atoms apart[176]. Quantitatively there is a repulsive 'radiation pressure' force F_R between the atoms given by $F_R = \frac{\hbar k \Gamma s}{(s+1)} \frac{\sigma_R}{4\pi r^2}$, where r is the separation of the two atoms and σ_R the cross-section for reabsorption of a photon. Also, as the cloud density increases, the trapping laser beams are themselves attenuated as they pass through the cloud, resulting in an intensity imbalance which is larger in the outer regions of the cloud, and which acts so as to push the atoms towards the centre[177]. Quantitatively this 'attenuating' force F_A is given by $F_A = \frac{I\sigma_L^{\,2}}{4\pi r^2 c}$ where I is the intensity of one beam and σ_L the cross-section for absorption of laser light. The cross-sections σ_R and σ_L are different ($\sigma_R > \sigma_L$) because the spectrum of the re-radiated light contains Mollow triplet components[180] associated with the AC-Stark shifts induced by the trapping beams. As the trapping lasers are detuned, the blue-shifted Mollow component is closer to the atomic resonance than the laser light and hence more likely to be absorbed. The interplay of the two forces F_R and F_A results in a variety of collective effects, first studied systematically in [175-179].

Using an MOT loaded from an atomic beam, the authors of [178] identified three regimes of dramatically different behaviour, demarcated by the total number of atoms in the trap: an 'ideal gas' regime, a 'static' regime and an 'orbital' regime. In the ideal gas regime, corresponding to numbers up to ~ 10^5 Cs atoms, the atom cloud formed an ellipsoidal shape with a fixed diameter ~ 0.2 mm and with a Gaussian number density distribution on each axis. Increasing the number of atoms above ~5 x 10^4 one enters the static regime, where the cloud diameter increases smoothly with the number of atoms up to a total number around 3×10^8 in a cloud about 3 mm in diameter. In the static regime the cloud shows a fairly uniform number density distribution around 10^{10} cm^{-3} provided the laser beams are well aligned. The increasing size of the cloud and the constant density show that the repulsive force between atoms is significant in this regime. In the orbital regime, the cloud behaviour is similar to the static regime provided the laser beams are perfectly aligned. But for small misalignments of the beams, i.e. a small angle between the two beams in a counter-propagating pair, the cloud takes up one of a variety of possible distributions: rings with specific radii, rings with a central clump and orbiting clumps of atoms. These phenomena have been studied further in [181,182]. Another phenomenon caused by the misalignment of the laser beams is that of 'interference fringes'[179], which are bright bands of fluorescing atoms alternating with dark empty bands within the cloud. These are discussed in section 4.5.

For the purpose of this work, the key points are that the collective behaviour is a result of long range forces between the atoms due to absorption and reabsorption effects. These rings and interference fringes have been observed with our apparatus (see figure 6-21), but we have not undertaken any quantitative studies. An interesting point to note is that Raab et al, the first builders of the MOT, found they obtained the maximum number of trapped atoms when they limited the density by misaligning their laser beams and using low laser intensities.

3.7 Temperature and its measurement

A number of ways of measuring the temperature of atoms in molasses and/or the MOT have been used. The most common method employed is the 'time of flight' method, which is discussed below. Other methods include the 'spring constant' method (also discussed below), methods using low-frequency oscillations of the trapping force[29,183] and a method using velocity dependent Raman transitions[184,185]. A new technique using coherent transients, proposed by our own group[186] is discussed in chapter 7.

3.7.1 Measurement of MOT temperature by the 'spring constant' method

In the 'spring constant' method of temperature measurement, the temperature of trapped atoms in an MOT is calculated from equation 3-16, $\frac{1}{2}\kappa_z\langle z^2\rangle = \frac{1}{2}k_B T$, using measured values of the cloud r.m.s radius and the trap spring constant κ_z. The cloud radius can be measured directly from a CCD camera image of the cloud fluorescence. The spring constant may be obtained[28,162,169,187] by measuring the displacement of the cloud from the trap centre when an intensity imbalance is introduced between the two beams in a counterpropagating pair[7]. The force produced by this imbalance is variable and can be calculated theoretically. Use of the measured displacement with the calculated value of the imbalance force then allows the spring constant to be determined.

The 'inverse' of the above experiment was performed in [188], where the cloud radius and temperature (by time of flight) were measured in order to calculate the spring constant for Rb in an MOT. This enabled the variation of spring constant with intensity to be studied.

3.7.2 Time of flight temperature measurement

'Time of flight' temperature measurements[1,36,188-191] are performed in essence by quickly (< 100 μs) turning off the trapping beams, leaving the cloud of atoms to fall whilst it simultaneously expands owing to its thermal velocity distribution. The expanding cloud of atoms falls through a narrow resonant probe beam and the time-varying fluorescence signal is detected with a photodiode or photomultiplier. Bearing in mind the geometry of the probe beam, the probe intensity profile and the distance of the probe region from the trap site, a

---

[7] *Alternatively, a displacement of the cloud may be produced by an extra, seventh 'pushing' beam.*

calculation can then be performed to give the cloud temperature. Variations on the geometries include using the original trapping beams as a probe in the 'release and recapture' method, i.e. seeing how many atoms are left after the beams have been switched off for small variable times[1,28]. The paper [36] describes use of the release and recapture method and three other time of flight variations: a method with the probe directly beneath the molasses cloud, a method with the probe below and displaced to one side of the molasses, and a method with the probe above the molasses. In some recent experiments e.g.[189], the atoms themselves have been detected as they fell onto a micro-channel plate directly below the trap. This technique gives a time-resolved spatial distribution of the falling cloud and allows determination of the (non-Gaussian) velocity distribution and calculation of an effective temperature.

The first measurements of molasses temperatures made in 1985 by time of flight[1] were published with experimental error bars which embraced the Doppler cooling limit, i.e. the results appeared to confirm the then current theory. However, two years after molasses were first observed, a research group[36] reported that precise measurement of molasses temperature by time of flight gave molasses temperatures much lower than the Doppler limit. These low temperatures were measured when any stray magnetic fields in the molasses region were nulled. It was also observed that the longest molasses lifetime was obtained when the laser detuning was much greater than the optimal detuning predicted by Doppler theory. These contradictions were no doubt a major reason for the group [36] to use four different variations on the time of flight technique in order to be confident of their unexpected results. Other groups later confirmed the low temperature results [37,38]. Temperatures below the Doppler limit were also measured in an MOT[187] using the spring constant method. A revision of the theory of laser cooling was clearly called for and the new theories are the subject of the following chapter.

Chapter 4
Sub-Doppler cooling

Chapter 3 ended by pointing out that experimental results published in 1989/90 showed measured temperatures in molasses which were one or two orders of magnitude lower than those predicted by the extant Doppler-cooling theory. Clearly some undiscovered mechanism was involved, and new theories were required. These were swiftly supplied, by groups at the Ecole Normale Supérieure in Paris[39] and Stanford University in California[40]. The new mechanisms are known collectively as 'sub-Doppler cooling' mechanisms. Three new and differing mechanisms appeared in those papers and are known as 'sisyphus cooling', 'motion-induced orientation' and 'magnetically-induced orientation'. Although the three mechanisms are different in detail, they each depend on one common factor. The cooled atoms must be multilevel atoms; specifically, the ground state must be Zeeman degenerate, which allows 'optical pumping ' to occur. An important factor in two of these mechanisms is that the cooling light field exhibits spatial polarisation gradients, hence they are sometimes referred to as 'polarisation gradient cooling'. Section 4.1 of this chapter explains the terms 'optical pumping' and 'polarisation gradients' and also introduces the idea of 'light shifts'. Sections 4.2 to 4.4 discuss each of the three mechanisms in turn. The explanations of the sisyphus and motion-induced orientation mechanisms are given in more detail because of their connection with optical molasses and the MOT, and this connection is made in section 4.5. Section 4.6 discusses the important idea of localisation of atoms in optical potential wells.

Since 1988, the field of laser cooling has seen continued development, and several new mechanisms such as 'velocity selective coherent population trapping' (VSCPT), 'Raman cooling' and others (bearing even more imaginative acronyms) have appeared which are also

capable of yielding temperatures below the Doppler limit. The last section, 4.7, is a brief overview of such developments, intended to give a picture of the current 'state of the art'.

4.1 Optical pumping, polarisation gradients and light shifts

4.1.1 Optical pumping

Before proceeding to the detailed descriptions, it is worth pointing out that there are no new 'forces' involved in these new mechanisms; the dipole force and the scattering force as described in chapter 2 are all[1]. Rather, it is the way that these forces operate in multilevel atoms which undergo 'optical pumping' that gives rise to a new cooling effect. Optical pumping is the name given to the mechanism by which the distribution of a ground state atomic population over its Zeeman substates is determined by the polarisation of a local resonant light field. As a simple example, consider the $J_g = 1$ to $J_e = 2$ transition depicted in figure 4-1.

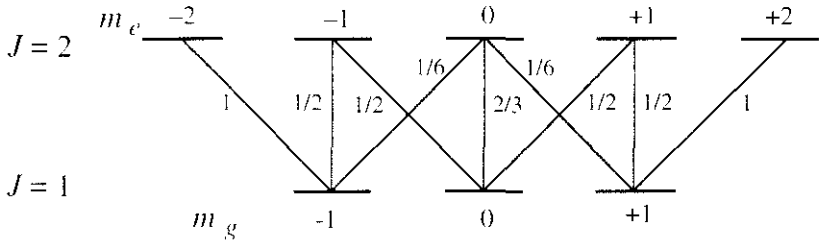

Figure 4-1 The Zeeman structure of a $J = 1 \rightarrow J = 2$ transition (with Clebsch-Gordan coefficients squared)

In the absence of a light field, the atomic population will be equally distributed over the Zeeman-degenerate ground states. If a resonant light field with σ^+ polarisation is then switched on, the population will undergo absorption and emission cycles as allowed by the selection rules. For an atom in σ^+ polarised light, absorption events always increase the angular momentum of the atom by $+\hbar$, and subsequent spontaneous emissions can change the angular momentum by $-\hbar$, 0 or $+\hbar$. On average each absorption-emission cycle increases the angular momentum of the atom and so eventually after several cycles all the population will be in the m_e= +1 ground state (apart from those which are temporarily in the excited m_e = +2 state). The average time for reaching this final steady state is known as the 'optical pumping time' τ_p, and is an important parameter for all sub-Doppler mechanisms. Generally, τ_p depends inversely on the mean scattering rate Γ_s, $\tau_p \approx 1/\Gamma_s$, where

$$\Gamma_s = \frac{s\Gamma}{2} = \frac{\Omega_0^2 \Gamma}{\Gamma^2 + 4\Delta^2} \qquad (4\text{-}0)$$

and τ_p is consequently large for large detunings and low intensities of the driving light field. The steady state population distribution of the atoms over the Zeeman substates is determined by the Clebsch-Gordan coefficients belonging to the particular $J_g \rightarrow J_e$ transition

[1] *Further categorisation, however, is possible for multilevel atoms, e.g. the 'redistribution force' in [140].*

concerned and by the local light polarisation. The Clebsch-Gordan coefficients are sets of numbers whose squares determine the relative coupling strengths of the various $m_g \rightarrow m_e$ transitions, and have their origins in the laws governing addition of angular momenta. They may be either calculated or obtained from the tabulations in standard spectroscopic texts.

It was pointed out in chapter 2 that a simple way of understanding the lowest temperature achievable by a cooling mechanism is to apply Heisenberg's uncertainty principle to the slowest timescale appearing in the cooling process. For Doppler cooling, this was $\tau = 1/\Gamma$, the natural lifetime of the transition. For sub-Doppler cooling processes, the longest relevant time is the optical pumping time $\tau_p = 1/\Gamma_s$, which can be up to two orders of magnitude longer than τ. Applying the uncertainty principle, $\Delta E \Delta t > \hbar / 2$, gives the condition $k_B T > \hbar \Gamma_s / 2$ for sub-Doppler cooling, which allows considerably lower temperatures than the corresponding condition for Doppler cooling.

4.1.2 Polarisation gradients

For a single plane wave of monochromatic light, the polarisation vector $\boldsymbol{\epsilon}$ is the same everywhere in the wave. If, however, two or more plane waves with differing wave vectors interefere, the polarisation vector of the resultant standing wave may vary spatially. Thus there are 'polarisation gradients' in the light field, and they play a vital role in some sub-Doppler cooling mechanisms. A first classification of polarisation gradients may be made by considering only those 1-D standing waves which are formed by two plane waves of equal amplitude and wavelength counterpropagating along the z-axis. There are then four basic patterns, with the following designations and prototype formulae:

1) 'Parallel linear' or 'lin // lin' or $\pi^x\pi^x$.

$$\mathbf{E} = E_0\hat{\mathbf{x}}\cos(kz - \omega t) + E_0\hat{\mathbf{x}}\cos(kz + \omega t)$$

which simplifies to $$\mathbf{E} = 2E_0\hat{\mathbf{x}}\cos kz\cos\omega t$$

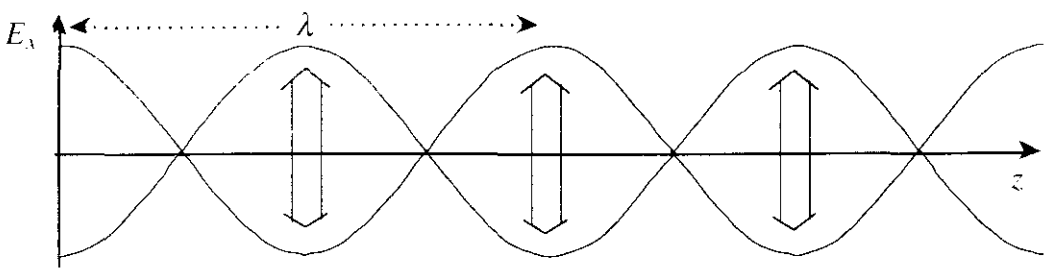

Figure 4-2a A $\pi^x\pi^x$ or parallel linear 1-D standing wave

2) 'Orthogonal linear' or 'sisyphus' or 'lin-perp-lin' or $\pi^y\pi^x$

$$\mathbf{E} = E_0\hat{\mathbf{y}}\cos(kz-\omega t) + E_0\hat{\mathbf{x}}\cos(kz+\omega t)$$

which simplifies to $$\mathbf{E} = E_0\left((\hat{\mathbf{x}}+\hat{\mathbf{y}})\cos kz\cos\omega t - (\hat{\mathbf{x}}-\hat{\mathbf{y}})\sin kz\sin\omega t\right)$$

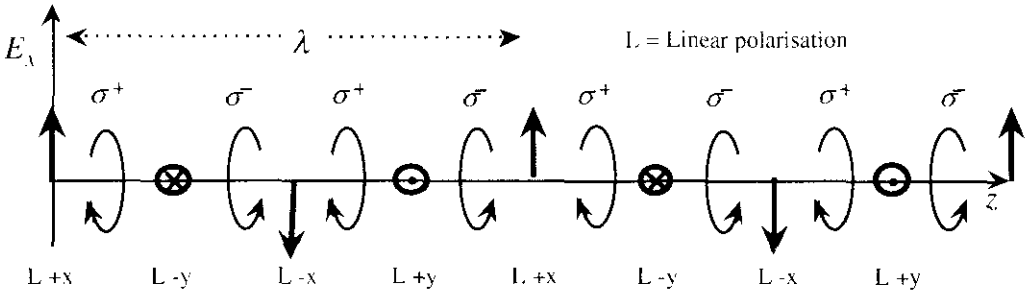

Figure 4-2b A $\pi^y\pi^x$ or sisyphus 1-D standing wave

3) 'Circularly polarised standing wave' or $\sigma^+\sigma^+$ (associated with 'MASE')

$$\mathbf{E} = \frac{E_0}{\sqrt{2}}\left[\hat{\mathbf{x}}\cos(kz-\omega t) - \hat{\mathbf{y}}\sin(kz-\omega t)\right] + \frac{E_0}{\sqrt{2}}\left[\hat{\mathbf{x}}\cos(kz+\omega t) + \hat{\mathbf{y}}\sin(kz+\omega t)\right]$$

which simplifies to $$\mathbf{E} = \sqrt{2}E_0\cos kz\left[\hat{\mathbf{x}}\cos\omega t - \hat{\mathbf{y}}\sin(\omega t)\right]$$

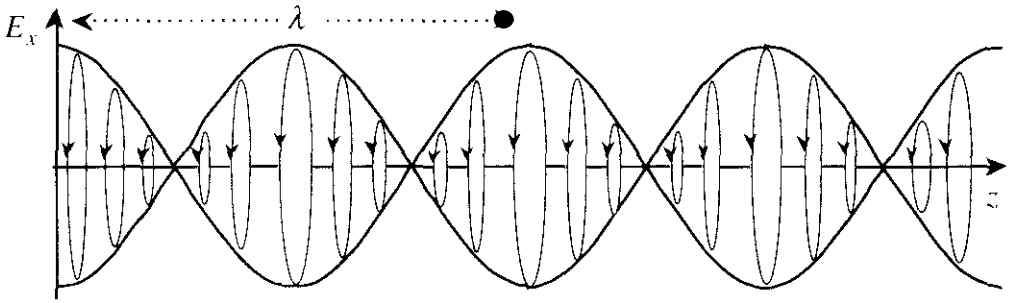

Figure 4–2c A $\sigma^+\sigma^+$ or circularly polarised 1-D standing wave

4) 'Corkscrew standing wave' or $\sigma^+\sigma^-$

$$\mathbf{E} = \frac{E_0}{\sqrt{2}}\left[\hat{\mathbf{x}}\cos(kz-\omega t) - \hat{\mathbf{y}}\sin(kz-\omega t)\right] + \frac{E_0}{\sqrt{2}}\left[\hat{\mathbf{x}}\cos(kz+\omega t) - \hat{\mathbf{y}}\sin(kz+\omega t)\right]$$

which simplifies to $$\mathbf{E} = \sqrt{2}E_0\cos\omega t\left[\hat{\mathbf{x}}\cos kz - \hat{\mathbf{y}}\sin kz\right]$$

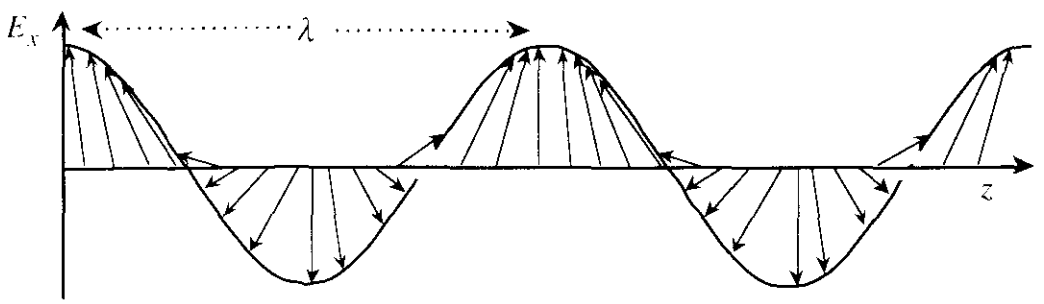

Figure 4-2d A $\sigma^+\sigma^-$ or corkscrew 1-D standing wave

It can be seen from the diagrams and equations of figure 4-2a to 4-2d that in the sisyphus and corkscrew configurations the polarisation vector changes on a spatial scale of ~ $\lambda/4$, whilst the wave amplitude is constant in space. In the case of the parallel linear and circularly polarised configurations, the polarisation vector is constant in space, whilst the amplitude of the standing wave varies as $\cos^2 kz$. The theory of sub-Doppler cooling, including calculation of friction and diffusion coefficients, was first worked out for a hypothetical atom travelling along the axis of a one-dimensional standing wave. Extension of the theory to three dimensional light fields is difficult; a first approximation may be obtained by assuming that the 1-D results for the x, y and z axes may be added vectorially. This is discussed further in section 4.5. One of the reasons why the development of a 3-D theory is difficult is due to the need to account for the many possible polarisation gradient configurations which can exist when the six orthogonal plane waves of molasses and MOTs interfere. Some theoretical studies which I carried out on polarisation gradients in 3-D standing waves form the subject matter of chapter 5.

4.1.3 Light shifts

Consider for the moment a two level atom. The ground and excited states are, strictly speaking, eigenstates of the unperturbed atomic Hamiltonian only. When the atom is subject to a weak static external field, by usual perturbation theory, the new Hamiltonian has new eigenstates whose energy levels may be shifted. These new eigenstates are mixtures of the unperturbed eigenstates. Examples are the Zeeman shift in a constant magnetic field and the Stark shift in a constant electric field. Analogously, in the case of perturbation by time-varying electromagnetic fields which are close to resonance, the resulting energy level shifts are known as A.C. Stark shifts. They can be calculated by diagonalising the Hamiltonian matrix of the whole system (atom + light field), as in the 'dressed state' approach [41,130,150]. For the case of a two level atom in a light field of detuning Δ ($=\omega_L - \omega_0$) and Rabi frequency Ω_0, the light shifts δ are $\delta = \pm\frac{\hbar}{2}\left[\left(\Omega_0{}^2 + \Delta^2\right)^{\frac{1}{2}} - \Delta\right]$. For large detunings when $\Delta >> \Omega_0$, the square root may be expanded in a Taylor series to give a good approximation:

$$\delta_g = \hbar\frac{\Omega_0{}^2}{4\Delta}, \qquad \delta_e = -\hbar\frac{\Omega_0{}^2}{4\Delta} \qquad\qquad \Delta >> \Omega_0 \qquad\qquad (4\text{-}1)$$

The light shift δ_g of the ground state is important in sub-Doppler cooling, and two points should be noted. Firstly, it is a negative shift when the laser detuning is negative. Secondly, the magnitude of the shift is proportional to the coupling strength $\Omega_0{}^2$ of the transition, which may vary spatially, allowing potential energy gradients (i.e. dipole forces) to exist.

Returning to the case of a multilevel atom, the selection rules allow three possible transitions starting from each of the Zeeman ground states. The relative coupling strengths of

these transitions are given by the squares of the corresponding Clebsch-Gordan coefficients and are generally different. Consequently, at each point in a light field of given polarisation, the light shifts of the individual Zeeman ground states are also generally different.

4.2 Sisyphus cooling

4.2.1 The sisyphus mechanism

This section examines sisyphus cooling in more detail. The important elements are shown schematically in figure 4-3. The simplest transition scheme which has the ground state degeneracy necessary for sisyphus cooling is a $J_g = 1/2 \rightarrow J_e = 3/2$ transition, shown with its relative coupling strengths (Clebsch-Gordan coefficients squared) in figure 4-3a. The light field consists of two plane waves counterpropagating along the z-axis, with orthogonal linear ($\pi^y\pi^x$) polarisations. The spatial variation of the polarisation over a wavelength of the resultant standing wave is shown in figure 4-3b. The spatially varying polarisation produces a spatial variation of the light shifts of the two ground states with magnitudes determined by the Clebsch-Gordan coefficients.

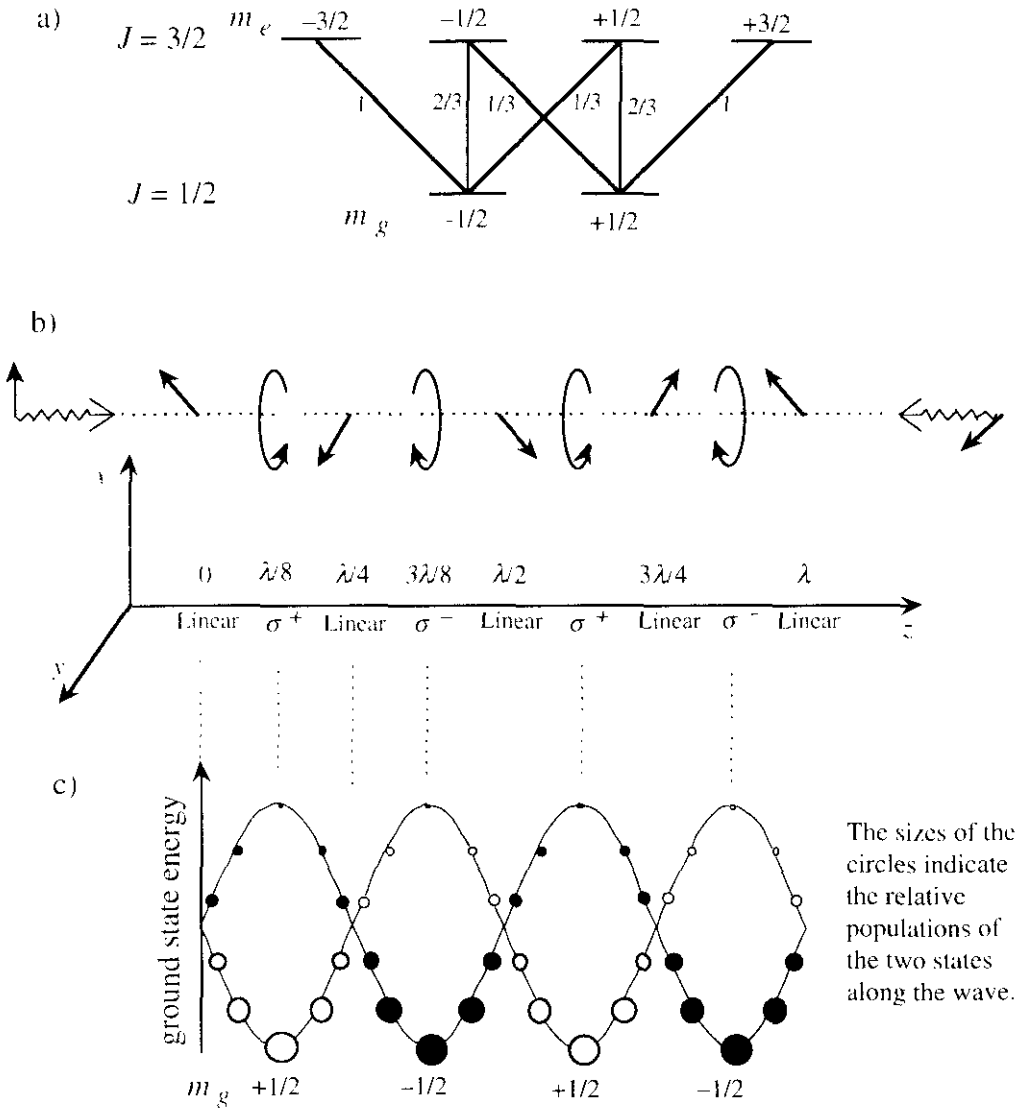

Figure 4-3 The essentials of sisyphus cooling

Figure 4-3c shows the spatial variation[2] $\pm\sin 2kz$ of both the light shifts and the steady-state populations for stationary atoms of the $g_{-1/2}$ and $g_{+1/2}$ states, i.e. the populations after optical pumping. It can be seen that the spatial variation of the light shifts gives rise to two intertwined series of hills and valleys of potential energy for the two ground states.

Consider an atom in the $g_{+1/2}$ state at $z = \lambda/8$ and moving in the $+z$ direction. As the atom moves towards $z = 3\lambda/8$, it climbs the potential energy hill at the expense of its own kinetic energy. This can also be thought of as deceleration due to the dipole force. At $z = 3\lambda/8$, the atom is likely to be optically pumped by the σ^- polarisation into the $g_{-1/2}$ state, which at that point has a lower potential energy. The excess potential energy is lost to the light field. A new cycle then begins, in which the atom climbs the potential hill towards $z = 5\lambda/8$, only on arrival to be optically pumped back to $g_{+1/2}$ and the bottom of the hill..."Thus, like Sisyphus, the atom is forever doomed to be climbing hills".

For this mechanism to be effective, the atom must be moving slowly enough to allow it to be optically pumped whilst near the top of a potential hill, i.e. it should not travel more than $\sim\lambda/4$ in the optical pumping time τ_p. A critical velocity v_c is defined by $v_c = 1/2k\tau_p$ such that v_z must be $\leq v_c$ for efficient sisyphus cooling. This condition is met by the coldest atoms in an optical molasses velocity distribution. Hence, in an optical molasses which also exhibits sisyphus cooling, i.e. which uses linear orthogonal beams and atoms with $J_g \geq 1/2$, the initial cooling of a fast atom is due to Doppler cooling and then, when $v \approx v_c$, sisyphus cooling takes over. It is predominantly this mechanism which was responsible for the low temperatures measured by the groups mentioned at the end of the previous chapter. The fact that the sisyphus mechanism was found to be effective only in a magnetic field free region may now be explained. Any stray magnetic fields cause Zeeman shifts which may swamp the light shifts and disrupt the sisyphus mechanism. An estimate of the maximum tolerable magnetic field is given by the condition Zeeman shift ≈ light shift, or $g_j\mu_B B \approx \hbar\Omega_0^2/4\Delta$, which implies for typical values of $\Omega_0 = \Gamma$ and $\Delta = 5\Gamma$ that $B_{max} \approx 0.4$ gauss, i.e. of the same order as the Earth's magnetic field.

4.2.2 Friction and diffusion coefficients for sisyphus cooling

Sub-Doppler cooling, like Doppler cooling, is a stochastic process and the steady-state 1-D temperature is determined by equation 2-36, $k_B T = \frac{D_p}{\beta}$, where D_p and β are the sisyphus momentum diffusion and sisyphus friction coefficients respectively. These coefficients are calculated in[39,41,150] using a semiclassical theory in the low intensity regime $\Omega_0 << \Gamma$ and for small velocities $kv_z << \Gamma$. The calculations proceed much as for Doppler cooling (chapter 2) but with the added complication of a multilevel atom. First, the steady-state

---

[2] *This spatial variation appears as $\sin^2 kz$ and $\cos^2 kz$ in a coord. system with different space / energy origin.*

solutions of the Bloch equations for the multilevel atom in the spatially varying light field are found. The resulting steady state ground state populations and optical coherences can then be substituted into the gradient of the atom-field interaction energy, which gives the force on the atom. The two most important results are[39,41]:

1) The force, spatially averaged over a wavelength is $\bar{f}_z = \dfrac{-\beta v_z}{1+(v_z^2/v_c^2)}$, where

$$\beta = -3\hbar k^2 \frac{\Delta}{\Gamma} \quad \text{and} \quad kv_c = \frac{1}{2\tau_p} \approx \frac{\Omega_0^2 \Gamma}{8\Delta^2} \tag{4-2}$$

Thus the friction coefficient β is independent of the laser intensity, whereas the capture velocity v_c is directly proportional to the intensity. This situation is the reverse of that in Doppler cooling, where the friction coefficient is proportional to the laser intensity and the capture velocity is independent of laser intensity. The maximum sisyphus friction coefficient is bigger than the maximum Doppler friction coefficient (eq. 2-26) by a factor $\approx 6\Delta/\Gamma$.

2) The momentum diffusion coefficient D_p is calculated to have a spatial average $D_p \approx \dfrac{3\hbar^2 k^2 \Omega_0^2}{8\Gamma}$ when the detuning is large ($\Delta >> \Gamma$), which is the regime of interest. There are three contributions to the diffusion coefficient: fluctuations of the momenta of spontaneously emitted photons, Poissonian fluctuations in the absorption rate and fluctuations of the instantaneous dipole force. The first two contributions account for most of the diffusion in the case of Doppler cooling. In sisyphus cooling, however, the third contribution can be far larger than the first two, and when $\Delta >> \Gamma$ it accounts for most of the diffusion[41]. These fluctuations in the dipole force are due to the atom being pumped at random times between the $g_{+1/2}$ and $g_{-1/2}$ states, which have differing potential energy curves. Such transfers are most likely at points where the $g_{+1/2}$ and $g_{-1/2}$ energies cross, i.e. at $z = 0, \lambda/4, \lambda/2, \ldots$ etc on figure 4-3c.

Putting the above expressions for the friction and diffusion coefficients into equation 2-36 gives, for the temperature of sisyphus-cooled atoms,

$$k_B T = \frac{\hbar \Omega_0^2}{8\Delta} \tag{4-3}$$

Note that this has the form $\text{temperature} \propto \dfrac{\text{laser intensity}}{\text{laser detuning}}$

The thermal energy $k_B T$ is of the order of the light shift ($\hbar\Omega_0^2/4\Delta$) and is predicted by equation 4-3 to be proportional to the laser intensity, and inversely proportional to the laser detuning. This prediction has been beautifully confirmed by experiments[29,161,191]. This confirmation is somewhat surprising, because the experiments were on a fully 3- D molasses with Cs atoms on a $J = 4 \rightarrow J = 5$ transition, whereas the theory leading to equation 4-3 was for a 1-D molasses with a $J = 1/2 \rightarrow J = 3/2$ transition. This agreement of results may be used as justification for the simple additive method of extension from the 1-D theory to 3-D and from low J–value to high J -value transitions. The temperature of a sisyphus-cooled

sample depends on the two variable parameters, the intensity and detuning of the light field, so the question arises: what is the fundamental limit on the lowest achievable temperature? Each absorption and emission event involves exchange of one photon's momentum $\hbar k$ with the light field, and so on average an atom will have at least a kinetic energy E_R, known as the 'photon recoil energy', where $E_R = \hbar^2 k^2 / 2m$. Theoretically therefore, the lowest achievable temperature is the 'photon recoil temperature' T_R given by $k_B T_R = E_R$. The lowest temperature achieved for Cs in [191] was 2.5 μK, which may be compared with the Doppler limit temperature of Cs, 127 μK, and the photon recoil temperature of Cs, 0.1 μK.

When an atom has a kinetic energy equal to E_R, its de Broglie wavelength is exactly equal to the wavelength of the light field. Thus, as the kinetic energy and temperature of the atoms approaches the photon recoil limit, the assumption of a small classical atom which underlies semiclassical theory is no longer valid. A fully quantum mechanical approach[41,192,193] is required to study these very cold atoms, and reveals the existence of important new phenomena including 'localisation of atoms', 'optical potential wells' and 'atomic energy bands', which are discussed in section 4-6 of this chapter.

4.3 The magnetically assisted sisyphus effect (MASE)

The magnetically assisted sisyphus effect, or MASE as it is now known, was first predicted in the literature in 1989[40] under the name 'magnetically-induced orientation'. This mechanism has much in common with ordinary sisyphus cooling in that it relies on the existence of optical potential wells which give rise to dipole forces. Unlike sisyphus cooling, however, the mixing of atomic ground states is accomplished by Larmor precession of the atomic magnetic dipoles in a transverse magnetic field, rather than by optical pumping. MASE was first observed experimentally in 1990[194]. A brief description is as follows. The 1-D version takes place in a circularly-polarised standing wave ($\sigma^+\sigma^+$) and can be understood for atoms on a $J_g = 1/2 \rightarrow J_e = 3/2$ transition, as with sisyphus cooling. The spatial variation[3] of the light field is shown in figure 4-2c. Such a standing wave is produced simply by reflecting a circularly polarised laser beam in a high reflectivity mirror. A constant magnetic field is applied transverse to the beams' propagation direction. At the antinodes of the wave, atoms will be optically pumped into the $g_{+1/2}$ state, which has a greater negative light shift there than the $g_{-1/2}$ state. The light shifts of both $g_{+1/2}$ and $g_{-1/2}$ are zero at the nodes of the standing wave, so as the atom moves towards a node, it climbs a potential hill, i.e. is slowed by the dipole force. At the nodes, there is no optical pumping, but there is Larmor precession ω_{La} of the $g_{+1/2}$ state towards the $g_{-1/2}$ state, owing to the transverse

[3] *As the polarisation does not change, this mechanism is not 'polarisation gradient cooling', though it certainly is sub-Doppler cooling.*

magnetic field. Consider an atom which has optimally precessed into the $g_{-1/2}$ state in the time it takes to travel $\lambda/2$ from one antinode to the next. There it is optically pumped from the $g_{-1/2}$ state back into the $g_{+1/2}$ state, which has a greater negative light shift and the excess energy is lost to the light field. The cycle then repeats itself, so once again the atom is "forever climbing hills". The transverse magnetic field is of course also present at the antinodes, so it is important that the average optical pumping rate at the antinodes is greater than the Larmor precession rate $1/\tau_p > \omega_{La}$, which gives a condition on the magnetic field magnitude. A typical value is of order 200 milligauss.

In 1990, a new and closely related sub-Doppler cooling scheme called 'velocity-selective magnetic resonance cooling' (VSMRC) was reported in [195,196]. VSMRC can occur in both $\pi^x\pi^y$ and $\sigma^+\sigma^+$ standing waves with a transverse magnetic field of larger magnitude than that of MASE (typically in the range 200 milligauss to a few gauss). In this regime the Larmor precession rate ω_{La} is greater than the optical pumping rate $1/\tau_p$. In VSMRC atoms are cooled to either of two small but non-zero velocities $\pm v_r$, which have sub-Doppler velocity distributions. The combination of atomic motion in a standing wave with Larmor precession in a constant magnetic field results in velocity-selective magnetic resonances at $\pm v_r = \pm \omega_L / 2k$ where ω_L is the Larmor frequency and k the wavenumber of the light. The resonances may be understood in terms of stimulated Raman transitions between Zeeman ground states, which are resonant when the difference in energy of the two Doppler-shifted Raman photons (counter-propagating) is equal to difference in Zeeman energies of the ground states. The damping force then arises from the spatial dependence of the light shifts of the Raman-induced Zeeman coherences. The friction coefficients and capture range of MASE and VSMRC are of the same order as those of sisyphus cooling[195] and sub-Doppler temperatures were measured for both mechanisms in [195,196]. It was also shown[196] both theoretically and experimentally that VSMRC occurs in a $\sigma^+\sigma^-$ (corkscrew) standing wave with a longitudinal magnetic field.

4.4 Motion-induced orientation (corkscrew cooling)

4.4.1 The motion-induced orientation mechanism

This section discusses a third sub-Doppler cooling mechanism, 'motion-induced orientation cooling' or 'corkscrew cooling'[39-41]. It differs from the two previously discussed sub-Doppler mechanisms in that it depends on the scattering rather than the dipole force. The discussion here is based on [39] and is confined to the regime of low intensity ($\Omega_0 << \Gamma$) and low velocity ($kv << \Gamma$) in a 1-D standing wave. The light field is the 'corkscrew' ($\sigma^+\sigma^-$) configuration depicted in figure 4-2d. It consists of a pair of counterpropagating (z-axis) laser beams of the same handedness, which means that the photons in each beam have opposite angular momenta. The resultant polarisation is linear at each point, but the direction of the polarisation vector rotates in the x-y plane, its tip tracing out a helix with pitch λ. The

amplitude of the standing wave is constant in space. We consider a $J_g = 1 \rightarrow J_e = 2$ transition, which is the simplest transition scheme which exhibits this type of cooling; such a transition is shown with its Clebsch-Gordan coefficients (squared) in figure 4-4.

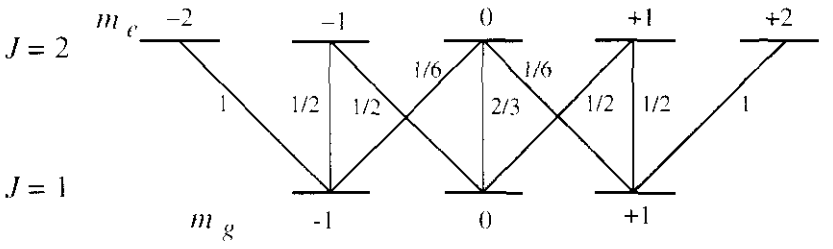

Figure 4-4 Clebsch-Gordan coefficients (squared) for a $J_g = 1 \rightarrow J_e = 2$ transition

Consider first a stationary atom at a point in the standing wave where the polarisation is linear along the y-axis. The field amplitude is spatially constant, so there are no light shift gradients and no forces on the stationary atom. At the same time, however, the populations of the ground state are optically pumped into a configuration known as an 'alignment' with respect to a y quantisation axis. This term applies to any configuration in which the population is distributed both unequally over the ground states and symmetrically about the centre of the ground states. See figure 4-5a, which shows examples of alignment.

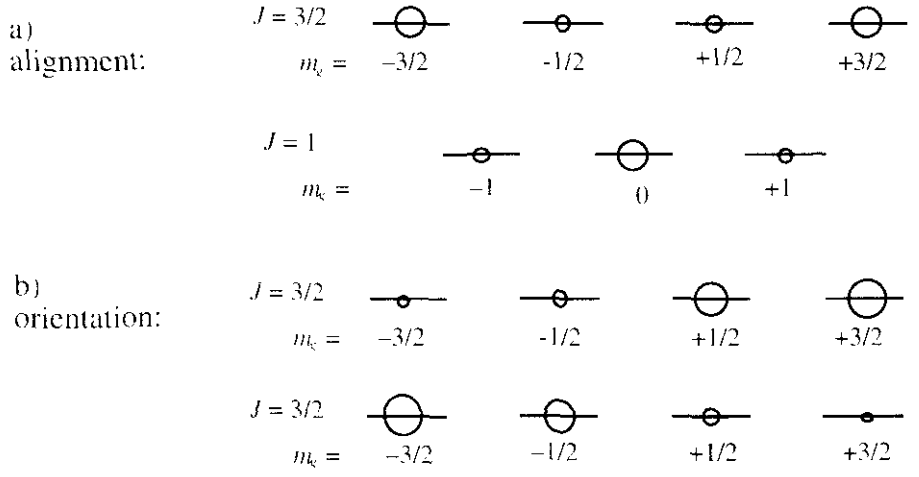

Figure 4-5 Examples of a) alignment b) orientation. The sizes of the circles indicate the relative population of each Zeeman ground state.

Consider now an atom moving slowly in the $+z$ direction with speed v_z. In the frame of the atom, the polarisation vector appears to rotate with angular speed $-kv_z$. Thus it is useful to transform to a reference frame rotating with this angular speed so that the polarisation of the light field is fixed (along the y-axis, say). This transformation to a rotating frame results in the appearance of an extra inertial term in the Hamiltonian equal to $kv_z\hat{J}_z$, where $\hat{J}_z$ is the operator for the z-component of angular momentum. This extra term is formally equivalent to one describing a constant magnetic field aligned along the z-axis and with a Larmor frequency equal to kv_z. It is shown in [39] that, to first order in kv_z/δ, this extra term does

not change the alignment of the ground states with respect to a y quantisation axis. However, this extra term does change the populations of the ground states (calculated to the same order) with respect to a z quantisation axis, so as to produce an 'orientation' of the ground states[4]. The term 'orientation' means that the relative populations of the ground states are distributed unequally but antisymmetrically over the ground states, i.e. they either increase or decrease as one goes from the state $m_g = -J_g$ to the state $m_g = +J_g$ (examples are shown in figure 4-5b). In the specific case of the $J_g = 1 \rightarrow J_e = 2$ transition, and for $\Delta >> \Gamma$, the 'motion induced orientation' is calculated to be[39]

$$\Pi_{+1} - \Pi_{-1} = \frac{120\Delta}{17\Omega_0^2} k v_z \tag{4-4}$$

where $\Pi_{\pm 1}$ are the populations of the $(m_g)_z = \pm 1$ ground states. Equation 4-4 shows that motion along the $+z$ axis in a negatively detuned corkscrew standing wave leads to an increase in the population of the $(m_g)_z = -1$ ground state. Looking at the Clebsch-Gordan coefficients in figure 4-4, one sees that there is a six times greater probability that an atom in $|g_{-1}\rangle_z$ will absorb a σ^- photon (propagating towards $z < 0$) than that it will absorb a σ^+ photon (propagating towards $z > 0$). Thus an atom moving in the $+z$ direction is more likely to absorb photons propagating in the $-z$ direction. A similar argument applied to an atom moving in the $-z$ direction shows that it is more likely to absorb photons propagating in the $+z$ direction. To summarise, the radiation pressures due to the two σ^+ and σ^- waves are unbalanced by the atom's motion, leading to the motion-induced orientation cooling force.

4.4.2 Friction and diffusion coefficients for corkscrew cooling

Reference[39] obtains $f_z = -\beta v_z$ where $\beta \equiv \frac{30}{17}\hbar k^2 \frac{\Gamma}{\Delta}$ and $\Delta >> \Gamma$. (4-5a)

A more detailed calculation[39] for the regime of low intensity and low velocity but for any detuning gives

$$\beta = \frac{120}{17} \frac{-\Delta\Gamma}{5\Gamma^2 + 4\Delta^2} \hbar k^2 \tag{4-5b}$$

As with sisyphus cooling, the corkscrew friction coefficient is independent of the laser intensity, and a corkscrew capture velocity can be found which is proportional to the laser intensity. There is however a difference in that for sisyphus cooling the capture velocity is proportional to the optical pumping rate $kv_c \approx 1/\tau_p$, whereas for corkscrew cooling, the capture velocity is proportional to the light shift $kv_c \approx \Omega_0^2/4\Delta$.

The momentum diffusion in the $\sigma^+\sigma^-$ configuration receives two contributions: fluctuations of the fluorescence photon momenta and fluctuations in the absorption rate. For large detunings, the two contributions are of the same order, though for small detunings, the second contribution becomes much larger owing to the likelihood of consecutive steps in

---

[4]*Sadly there does not appear to be any simple, physically intuitive picture to illustrate this effect.*

momentum space being in the same direction. Limiting this discussion, for simplicity, to the case of large detunings, the momentum diffusion coefficient is $D_p \approx \frac{29\hbar^2 k^2 \Gamma \Omega_0{}^2}{170\Delta^2}$ (equations 5.16 and 5.17 of [39]). Putting this expression for D_p and the expression 4-5a for the friction coefficient into the Einstein equation 2-36, gives the result for the equilibrium temperature

$$k_B T \approx \frac{\hbar \Omega_0{}^2}{10\Delta} \qquad \ldots\ldots\left(\propto \frac{\text{laser intensity}}{\text{laser detuning}}\right) \qquad \Delta > \Gamma \tag{4-6}$$

The dependence of the corkscrew cooling temperature on the ratio of laser intensity to laser detuning predicted by equation 4-6 has been confirmed experimentally[162,183,188,197].

Comparison of sisyphus and corkscrew cooling

For low intensities and large detunings, both the sisyphus and corkscrew cooling mechanisms lead to temperatures below the Doppler limit and are hence referred to as sub-Doppler mechanisms. Equations 4-3 and 4-6 for the sisyphus and corkscrew equilibrium temperatures respectively are very similar. Both the friction and diffusion coefficients of sisyphus cooling are larger than the corresponding coefficients of corkscrew cooling by a factor of ~ Δ^2/Γ^2. As the equilibrium temperature depends on the ratio of these two coefficients (equation 2-36), both mechanisms result in temperatures of the same order. In particular the equilibrium temperature is predicted to be proportional to the light intensity, inversely proportional to the detuning and of the order of the light shift. Although the sisyphus and corkscrew mechanisms have this feature in common and both involve a form of optical pumping, a fundamental difference is that the sisyphus mechanism involves the dipole force, or coherent redistribution of photons between the counterpropagating waves, whereas the corkscrew mechanism relies on the scattering force, or an imbalance in the radiation pressure due to each wave. For detunings $|\Delta| > \Gamma$, the corkscrew capture velocity is larger than the sisyphus capture velocity by a factor ~ Δ/Γ. Finally, comparing sisyphus and corkscrew forces with Doppler cooling forces, one finds that in the regime of detunings $|\Delta| > \Gamma$ and small velocities, the sub-Doppler friction coefficients are greater than the Doppler friction coefficient. However, as the capture range for the Doppler force is greater than that of the sub-Doppler forces, the maximum magnitude of the sub-Doppler forces is less than the maximum Doppler force.

4.5 Sub-Doppler cooling in 3-D optical molasses and the MOT

The explanations of the three sub-Doppler cooling mechanisms given above in sections 4.2, 4.3 and 4.4 followed the original papers in establishing the mechanisms in 1-D and for the simplest transitions ($J=1/2 \rightarrow J=3/2$ and $J=1 \rightarrow J=2$). Though there have been some 1-D experiments on atomic beams and using traps, most contemporary experimental work has been in the 3-D situations of optical molasses and the MOT, also on the alkali atoms sodium,

rubidium and caesium which have hyperfine structures with J or F values different from $J = 1/2 \rightarrow J = 3/2$ and $J = 1 \rightarrow J = 2$. These experimental arrangements therefore present difficulties to theorists aiming for accurate quantitative predictions. This section discusses such problems and possible solutions. A more detailed review of this area is in [56].

Extending the first 1-D calculations which were carried out for the simplest transitions ($J = 1/2 \rightarrow J = 3/2$ and $J = 1 \rightarrow J = 2$) to 1-D calculations for the actual hyperfine transitions employed in experiments (e.g. $F = 3 \rightarrow F = 4$ for ^{85}Rb and $F = 4 \rightarrow F = 5$ for Cs) is a first step towards a completely general theory. This has been carried out for the $\sigma^+\sigma^-$ configuration in [197], which studies $J \rightarrow J, J \pm 1$ for any J and gives quantitative results for the friction coefficient and capture velocity for $J \rightarrow J + 1$.

The extension of calculations to 3-D light fields brings a host of difficulties, mainly because the possible combinations of three orthogonal 1-D standing waves produce a large variety of '3-D standing waves' containing complicated polarisation gradients. It is, for instance, possible for both the sisyphus and corkscrew polarisation gradients to be present along different directions within the same 3-D molasses standing wave, thus allowing both forms of sub-Doppler cooling to be present simultaneously with the ordinary Doppler cooling. Another theoretical complication in real traps is due to the the long range forces e.g.[175,190] which occur as a result of absorption, radiation and reabsorption of light within the cloud (see section 3.6.2). These forces are important when the trap contains more than $\sim 10^5$ atoms, a condition satisfied by typical traps containing $\sim 10^7$ atoms. A method of numerical calculation[199] of friction and diffusion coefficients for any $J \rightarrow J'$ transition in a 3-D standing wave has been described and used to study the $J = 1 \rightarrow J = 2$ transition in four different 3-D laser configurations. The results show that there is a marked position dependence of the coefficients, but when they are spatially averaged, they lead to equilibrium temperatures which scale with intensity divided by the detuning[5], in agreement with experiments. For low intensities and large detunings, most of the friction coefficients and temperatures obtained in the 3-D calculations in [199] can be obtained to within 5% by multiplying the 1-D results for the corresponding light field by a scaling factor [115,140,169]. Paper [140] is a general treatment of light forces in a 3-D light field.

A particularly important experimental situation is the MOT, studied by Steane, Chowdhury and Foot[162]. They show that both sisyphus and corkscrew polarisation gradients are usually present in the 3-D $\sigma^+\sigma^-$ light field configuration used in the MOT, and thus that sisyphus cooling and motion-induced orientation cooling can occur. Also, because there is an inhomogeneous magnetic field in an MOT, there are regions where velocity-

---

[5] *Except in some special light field configurations where the 'relative phases' of the waves results in a big reduction in the friction coefficient[199]. The subject of the relative phases is discussed in chapter 5.*

selective magnetic resonance (VSMRC) cooling can occur. The latter is likely in the outer regions of the trap where the magnetic field magnitude is of the right order ($r > \sim 0.2$ mm for a magnetic field gradient of 10 G cm^{-1}). On the other hand, at the centre of the trap ($r < \sim 0.1$ mm), the magnetic field is small, and so both sisyphus and motion-induced orientation cooling are expected there. Steane et al[162] determined by 'intensity imbalance' experiments that, at the centre of the MOT, motion induced orientation provides the restoring force and sisyphus cooling provides the velocity-damping force. This explained the overdamping of the atomic motion in the trap which is found experimentally, as the sisyphus friction coefficient is greater than both the Doppler friction coefficient and corkscrew friction coefficient. Finally they suggest that it is sisyphus cooling which is responsible for the large scale interference fringes[179] seen in an MOT with misaligned beams. The misalignment of the beams gives rise to large scale (~ 0.05 to 0.5 mm) alternating zones of varied 'sisyphusness' (level of sisyphus polarisation gradients). In the zones where sisyphus cooling does occur, the friction coefficient is higher (the molasses is 'stickier') and this leads to the observed higher concentrations of atoms in those zones.

That the spring constant at the centre of the MOT is due to motion induced orientation can be understood in terms of the fictitious magnetic field (discussed in section 4.3) which appears in the frame rotating with an atom as it travels along a corkscrew polarisation gradient. The cooling force is proportional to this fictitious field which is in turn proportional to the velocity. It follows that if one introduces a real magnetic field parallel to the $\sigma^+\sigma^-$ light field and which is proportional to the distance from the trap centre, a restoring force due to motion-induced orientation will appear. This force is the subject of [200].

One conclusion to be drawn from this subsection is that the internal dynamics of the MOT are in reality considerably more complicated than those which appeared in its introductory description (section 3.3)! Atoms are captured by Doppler slowing and restoring forces in the outer regions of the trap, and also possibly experience velocity-selective magnetic resonance forces as they are 'Zeeman-slowed' (section 3.4.1) towards the trap centre. As the atom nears the trap centre, its velocity falls below the sisyphus and corkscrew capture velocities and consequently both the velocity damping and the restoring force become larger, as the sub-Doppler mechanisms take over. The equilibrium distribution of the atoms is determined by the damping and restoring forces and also by momentum diffusion, collisions and long range forces due to absorption and reabsorption of light.

4.6 Localisation of atoms and optical lattices

Atoms cooled in a 1-D sisyphus standing wave attain an equilibrium temperature given by equation 4-3. This temperature corresponds to a mean kinetic energy which is only a fraction of the depth of the 'optical potential wells' formed by the spatially varying light shifts. Therefore, in a simple classical picture, some atoms in the cold thermal distribution will have

insufficient energy to climb out of the wells and will, under the action of the dipole force, collect near the bottom of the wells. This phenomenon is known as 'localisation of atoms in optical potential wells'. The first evidence for this phenomenon was obtained in 1987 when caesium atoms in an atomic beam were channeled into the nodes or antinodes of a transverse 1-D standing wave of light[201]. Localisation of atoms has since been observed in 1-D, 2-D and 3-D light fields and is the subject of much study[49,50.76-86,192,193,201-210].

The kinetic energy of atoms slow enough to be trapped in the optical potential wells is only a few photon recoil energies and the de Broglie wavelength of the atoms is a significant fraction of an optical wavelength. Thus the atoms can no longer be regarded as points of matter in the standing wave, and a full quantum mechanical treatment of the atom as an extended wave packet is required. Such treatments[41,192,210] have been carried out for a 1-D light field and result in a new picture in which the atoms can exist in energy bands within the optical potential wells (figure 4-6). Near the bottom of the wells the potential profile is approximately that of a simple harmonic well. Thus the energy levels are given by $(n+1/2)\hbar\Lambda$, where $n = 0,1,2....$ and the oscillation frequency Λ of the harmonic well is given by[192]

$$\frac{1}{2}m\Lambda^2 = \frac{\hbar\Omega_0{}^2k^2}{3\Delta} \tag{4-7}$$

In a theoretical analysis[41] Cohen-Tannoudji finds that the quantum mechanical treatment is necessary when $\Lambda >> 1/\tau_p$, where τ_p is the optical pumping time (equation 4-0). If this inequality is satisfied, it implies that the atomic centre of mass is able to oscillate many times in the well between excitations. Conversely, when $\Lambda << 1/\tau_p$, the atom makes several absorption and emission cycles during one well oscillation period: in such circumstances, semiclassical theory is appropriate. Both regimes ($\Lambda >> 1/\tau_p$ and $\Lambda << 1/\tau_p$) are possible in laser cooling and trapping experiments, depending on the detuning and intensity of the light field. The quantum mechanical regime corresponds to large detunings and/or weak intensities.

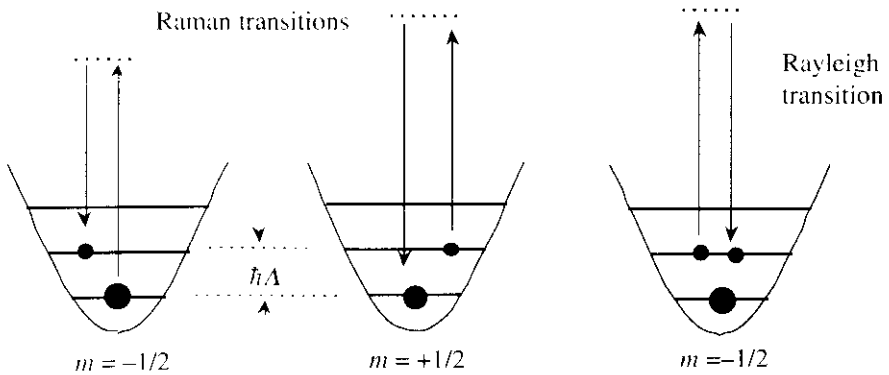

Figure 4-6 Optical potential wells

The energy levels are broadened into bands owing to the periodic structure of the many potential wells comprising the standing wave, but the lowest bands are very narrow owing

to the long relaxation times out of the bands. For example, for caesium with $\Delta = -20\Gamma$, $\Omega_0 = 1.5\ \Gamma$, one finds that the well depth is about 100 E_R which allows six bound bands spaced ~ 40 kHz apart, and the width of the lowest band is $10^{-6}E_R$[192]. The theory of this 1-D standing wave predicts that more than 50% of the atoms are trapped in the two lowest levels of the wells. A similar calculation[193] for a 2-D standing wave predicts a strongly modulated spatial distribution.

4.6.1 Continuous wave (CW) spectroscopy of localised atoms

Localisation of atoms has been studied experimentally mainly by the use of CW (continuous wave) probe spectroscopy, in which one obtains either the probe transmission spectrum or the probe reflection spectrum from a four wave mixing process. The first significant CW probe experiments[211-213] were performed in 1991 on cold atoms trapped in an MOT and both revealed Raman resonances at probe-pump detunings of several tens of MHz. These resonances are due to Raman transitions between Zeeman ground states with differing light shifts, and the observed spectral regions of probe amplification and attenuation reflect the differing populations of the ground states. A narrower central resonance with a dispersive line shape and a sub-natural linewidth (~ 400 kHz) was also observed; this was only properly understood in the light of later experiments. Another early experiment in 1990 involved the indirect observation of localisation of atoms by a different method[202]. Here, the fluorescence spectrum of optical molasses was obtained by a heterodyne technique and revealed the juxtaposition of two velocity distributions believed to be due respectively to free (but slow) atoms and those bound in optical wells.

Later CW probe experiments have been carried out with a higher frequency resolution, mainly by two groups; the group of Hemmerich and Hänsch[77-82] in Munich and the group of Grynberg[76,83-86,214] at the Ecole Normale Supérieure in Paris. These experiments showed that the narrow central dispersive resonance of the earlier experiments had a fine substructure, a typical example is shown in figure 4-7.

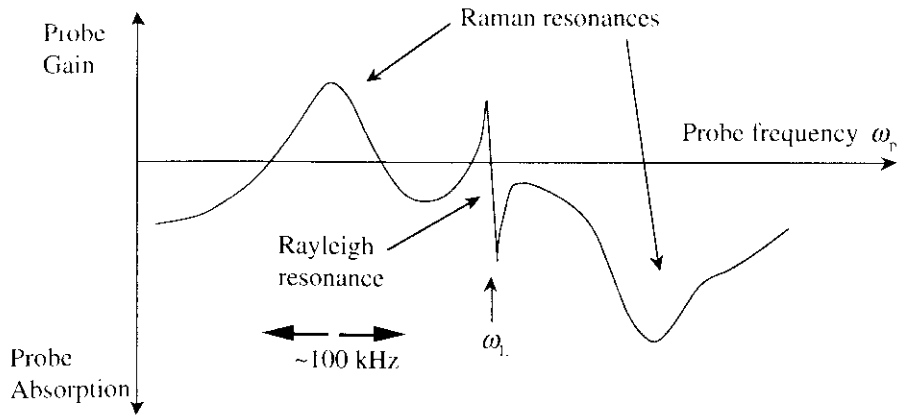

Fig 4-7 A typical C.W. probe transmission spectrum

With the higher frequency resolution, the probe transmission (or reflection) spectrum in the region defined by pump-probe detunings < ±500 kHz is seen to consist of regions of probe amplification when $\omega_p < \omega_L$ and attenuation when $\omega_p > \omega_L$, corresponding to Raman transitions (see figures 4-6 and 4-7) between adjacent energy bands of atoms bound within the optical potential wells. The high resolution experiments also revealed the presence of an extremely narrow (< 10 kHz) dispersive 'Rayleigh' resonance when $\omega_p \approx \omega_L$ which corresponds to transitions to and from the same bound levels. This resonance is discussed later. For the Raman resonances, the correspondence of probe amplification and attenuation with negative and positive probe detunings is due to there being a greater atomic population in the lower bound states. The width of the observed Raman resonances is less than that expected from the ground state decay rate (the inverse of the optical pumping time) alone. This is due to Lamb-Dicke narrowing[215], an effect in which the linewidth of atomic fluorescence becomes narrowed when the atoms are localised in a region smaller than the optical wavelength. Atoms in the lowest quantum vibrational state of a well are localised to around 1/25 of an optical wavelength and thus subject to strong Lamb-Dicke narrowing of their fluorescence. Lamb-Dicke narrowing in optical potential wells may be quantified in terms of the Lamb-Dicke parameter $g_{L\text{-}D} = \left(\hbar\Lambda/2E_R\right)^{\frac{1}{2}}$, where E_R is the recoil energy; Lamb-Dicke narrowing occurs when $g_{L\text{-}D}$ is > 1. This formulation yields a picture in which Lamb-Dicke narrowing occurs when the change in atomic energy due to one absorption-emission cycle is much smaller than the spacing of the bound energy levels in the potential wells. Thus many absorption-emission cycles are required for the atom to change between energy levels, resulting in a longer pumping time and consequent narrower linewidth.

The first experimental observation[203] of these stimulated Raman resonances due to quantised atomic motion was obtained in 1992 using probe transmission spectroscopy for cold caesium atoms in a $\pi^x\pi^y$ (sisyphus) 1-D standing wave. Almost simultaneously, an experiment[204] was reported which used resonance fluorescence spectroscopy of rubidium atoms in a sisyphus 1-D standing wave to observe well resolved sidebands due to spontaneous Raman transitions between quantised vibrational levels. Further experiments using probe transmission/reflection spectroscopy have observed the same pattern of Raman and Rayleigh resonances for cold atoms localised in various 1-D, 2-D and 3-D standing waves. In 1-D, localisation of atoms has been observed in the $\sigma^+\sigma^+$ MASE arrangement[76], but does not occur in the 1-D $\sigma^+\sigma^-$ arrangement[203,204]. In 2-D, however, localisation is observed for the $\sigma^+\sigma^-$ arrangement used in the MOT[77]. Localisation also occurs for various special 2-D and 3-D arrangements of laser beams which either generalise $\pi^x\pi^y$ 1-D standing waves to more dimensions[86,205] or represent new hybrid 2-D and 3-D light fields[78 – 82]. The exact shape of the probe transmission spectrum is strongly dependent on both the probe polarisation and on the angle between the

probe and pump beams. Studies of the variation of the spectra with respect to the above two parameters have been useful in understanding the nature of the resonances.

4.6.2 Optical lattices

When several non-collinear monochromatic laser beams intersect, the resulting 2-D or 3-D light field is known as an 'optical lattice' – a crystal-like light field with a periodic structure (topography) determined by the laser wavelength and the angles between the beams. Chapter 5 is concerned with the nature of these three-dimensional light fields. Two properties of 3-D light fields are relevant here. Firstly the light field topography generally contain periodic regions of high and low light intensity, and periodic regions of specific polarisation. If the lattice contains regions of strong circular polarisation alternating with regions of weak (low intensity or linear polarised) or differently-oriented circular polarisation, then it is a 3-D analogue of the 1-D sisyphus arrangement and localisation of the atoms in all three dimensions is expected and indeed observed. A second property of 3-D optical lattices made from three orthogonal 1-D standing waves is that their topography depends on two parameters, the 'relative time phases' of the three individual 1-D standing waves. The origins of relative time phases and their influence on experimental design are fully described in chapter 5. Here it is sufficient to point out that they may be either controlled, as in the experiments of the Hemmerich and Hänsch group, or eliminated from the experiment by using non-orthogonal beam arrangements as in the experiments conducted at E.N.S.

Optical lattices have been the object of considerable study[76–86]. Various beam geometries and beam polarisation schemes, designed to produce different optical lattices, have been proposed and tested. For instance there are lattices in which the localised atoms have differing periodicities in different spatial directions[83], or in which they exhibit ferromagnetic[81], antiferromagnetic[79] order and paramagnetic behaviour[84].

Much thought has been given to the origin of the extremely narrow linewidth of the dispersive Rayleigh resonance observed in the C.W. probe experiments, which cannot be explained by Lamb-Dicke narrowing alone[85]. Linewidths as small as 300 Hz FWHM have been observed[82]. Various explanations of the origin of this narrow resonance have been put forward in the period 1991 to 1994, including the following: the formation of a 'holographic' population grating by pump/probe interference[79], interference between the probe and a back-scattered pump beam (Bragg-diffracted from planes of atomic magnetisation)[203], a collective (Mossbauer-like) recoil of the whole atomic crystal when absorbing or emitting light[216] and 'recoil-induced' resonances[85,209]. This narrow resonance is still not totally understood, nevertheless all the above theories share the idea that the extreme narrowness of the resonance is related to the long range spatial order of the localised atoms. The long range order is relevant in directions parallel to the probe (backwards Bragg diffraction) and transverse to the probe (recoil-induced resonance). Some

connections between the various given explanations are clarified in [85] and in a recent paper[210] which calculates the four-wave mixing signal for a 1-D molasses. In [210] the magnitudes of both the Rayleigh resonances between the discrete motional bound states and the recoil-induced resonances between the transverse motional continuum states are determined. The results obtained agree with recent experiments[82] and suggest that both types of resonance contribute to the observed signal, but that in 3-D light fields the recoil-induced resonances may be the dominant factor.

Another recent development of likely future importance is that of so-called 'dark lattices'[49,50,217]. These are optical lattices in which cold atoms are optically pumped (on a spatial grid) into 'dark' (non-absorbing or nearly non-absorbing) ground states. Dark lattices have been recently observed[50] in both 2-D and 3-D. Because atoms trapped in dark states do not interact with the light field, there is no heating effect upon them and they do not interact with each other via dipole-dipole forces. Furthermore they are not subject to the long range repulsive forces due to reabsorption of fluorescence which occur in bright lattices. They may therefore enable the attainment of lower temperatures and higher atomic densities.

An interesting consequence of atoms being arrayed in a crystalline structure is that one could observe Bragg diffraction of light from the 'crystals'. This was suggested as a direct means of observing the localisation of the atoms, but it has been pointed out[205] that a similar directional signal would be given from a homogeneous (unlocalised) sample of atoms owing to four-wave mixing[206]. Subsequently, it was pointed out[207] that this ambiguity could be circumvented by performing the Bragg scattering after the molasses beams are turned off but before the atoms have moved significantly. However, even with the beams switched off, there remains an ambiguity which is due to the formation of a 'spin-grating'. A spin-grating is a residual spatial lattice of alternating magnetisation of the ground state atoms and can also give rise to Bragg scattering[218]. It is imprinted upon a uniform gas due to optical pumping associated with the local electric field polarisation prior to switching off the beams. Nevertheless, beam geometries are in theory possible[207] which allow unambiguous attribution of a Bragg reflected signal to atomic localisation rather than to a spin-grating. One such experimental result was very recently reported[172]. Bragg diffraction of light from atoms trapped in optical potential wells remains an appealing area of study, actively pursued by several groups[219] including our own (see chapter 7).

4.7 Review of recent trapping and cooling mechanisms

Since 1985 there has been continued growth of the laser cooling research area, bringing better understanding of Doppler and sub-Doppler cooling schemes and the invention of several new schemes which are capable of producing yet lower temperatures. This section gives brief descriptions of some of the other schemes. It is included to both show the current state of the art and to demonstrate that the field of laser cooling is still rapidly evolving.

4.7.1 Blue detuned stimulated molasses

The cooling mechanism of blue-detuned stimulated molasses[220] was touched upon earlier in the context of light forces on two-level atoms in strong light fields (section 2.3.5). In fact, it is another example of the sisyphus effect, and occurs for slowly moving atoms in a blue detuned standing wave. It has been described in terms of the stationary states of the atom-plus-radiation field (i.e. dressed states), perturbed by spontaneous decay. The dressed states of a two-level atom in a blue-detuned standing wave vary sinusoidally in energy and composition along the axis in such a way that the highest energy of each dressed state is when it has the largest admixture of the excited atomic state and the lowest energy is when it has the largest admixture of atomic ground state. Spontaneous decay is therefore most probable at positions where the dressed state energies are the highest. This is illustrated in figure 4-8.

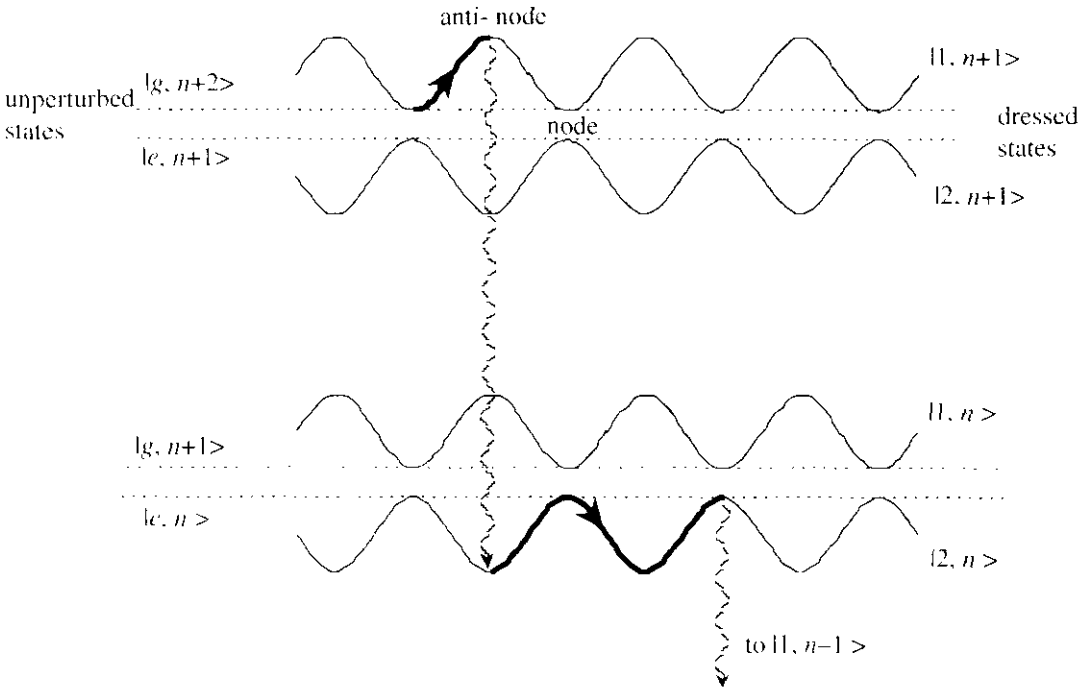

Figure 4-8 Dressed states for blue detuned stimulated molasses

Thus a slowly moving atom (represented by the thicker solid lines) which is initially in a dressed state at a position where its energy is lowest, experiences a deceleration phase as it moves towards a position of highest energy. Here it has a larger probability of undergoing spontaneous decay to another dressed state which is near its lowest energy at that position, and another cooling cycle begins. The effect was first observed in 1986[220], where a 1-D temperature of the same order as the Doppler limit was measured.

4.7.2 Velocity selective coherent population trapping

Much attention has been paid[41,42,221,222] to the cooling method called velocity selective coherent population trapping (VSCPT), which is capable of overcoming the photon recoil temperature limit, at least in one and two dimensions. So long as atoms are undergoing

absorption and emission cycles during a cooling process, the photon recoil limit remains the fundamental temperature limit. If however the atoms are optically pumped into a non-absorbing or 'dark' state, their momentum is no longer subject to diffusion and lower temperatures are theoretically possible. It is possible to create dark states which are perfectly non-absorbing for atoms with zero velocity along the axis of a counterpropagating pair of laser beams. Such dark states are superpositions of energy eigenstates. For instance, in the case of a $J_g = 1 \rightarrow J_e = 1$ transition in a $\sigma^+\sigma^-$ 1-D standing wave, the symmetric superposition of ground states $|g_{-1}\rangle + |g_{+1}\rangle$ is a non-absorbing state for zero velocity atoms. This follows from the Clebsch-Gordan coefficients of the transition (figure 4-9).

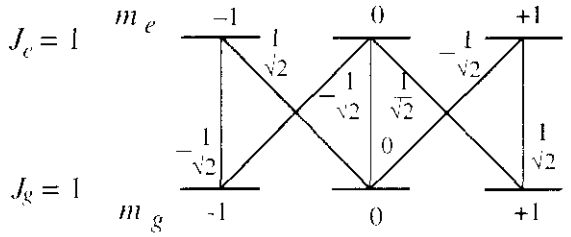

Figure 4-9 Clebsch-Gordan coefficients for a J=1 → J=1 transition

Thus if the atoms are cooled by some preliminary mechanism into a fairly narrow velocity distribution around zero, any atoms that fall 'accidentally' into the zero velocity dark state as a result of random momentum diffusion will then remain there. The very narrow velocity distribution thus obtained has a width Δp, in this case determined simply by the interaction time θ of the atoms with the light field so that $\Delta p \propto 1/\sqrt{\theta}$. Thus for long interaction times, Δp can become small enough that the atomic wavepacket is, by Heisenberg, of the order of the light wavelength and a full quantum treatment of the centre of mass motion of the atom is then required. In such a treatment, the dark state is not an eigenstate of the momentum operator, but a 50/50 superposition of two states with momenta $\pm\hbar k$. Thus the theory predicts that an experiment on VSCPT should reveal a momentum distribution with a peak on either side of zero, each with a width Δp. This has been clearly confirmed in both one[42] and two[58] dimensions. In the latter case, temperatures as low as 250 nK were obtained. Extensions of such experiments to 3-D have been proposed[222-225].

4.7.3 Raman cooling

Raman cooling[43,44,59] is a new (1992) mechanism which is also capable of producing atoms cooled below the photon recoil limit. The mechanism can be applied to any atoms having two long-lived ground states, for instance the alkali metals, which have two hyperfine ground states separated in energy by $\hbar\omega_{hfs}$. It relies on two-photon Raman transitions between the ground states via a third excited state (see figure 4-10). A series of short pulses (~200 μs) of laser light are applied to the atoms; each pulse consisting of two counterpropagating beams with frequencies ω_1 and ω_2 such that the 'Raman detuning' Δ_R given by $\Delta_R = \omega_1 - \omega_2 - \omega_{hfs}$ is approximately equal to $2kv$. This is the condition for an

atom with velocity v to be Doppler shifted into resonance with the Raman transition. Such atoms receive a decelerative momentum kick of $2\hbar k$ on being transferred from g_F to g_{F+1}. They are then optically pumped back into the state g_F by a third laser tuned to ω_3 and a spontaneous emission. This sequence may be repeated many times, with alternating directions for the beams with frequencies ω_1 and ω_2, and the Raman detuning Δ_R being gradually reduced to stay in step with the average atomic velocity as it decreases. The velocity distribution (temperature) can become arbitrarily narrow(small) so long as the pumping rate into the non-absorbing $v = 0$ state is larger than the loss rate due to non-resonant excitation. This requires that the pulse shapes should be specially tailored e.g. Blackman pulses and that the pulse widths should be decreased in step with the decreasing temperature. Experiments[43,44] using this or similar techniques have reached temperatures one order of magnitude less than the photon recoil limit in 1-D (23 nK for caesium) and around one to four times the photon recoil limit in 2-D and 3-D.

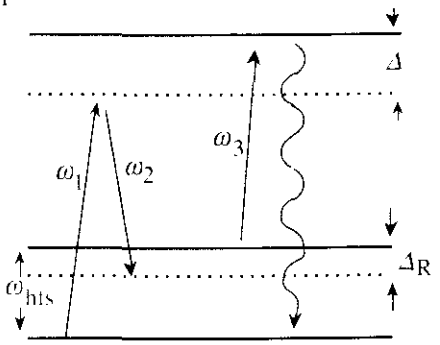

Figure 4-10 Raman cooling energy levels

4.7.4 The 'trap relying on optical pumping' (TROOP)

An interesting and very recent development is the 'trap relying on optical pumping' or 'TROOP' [226]. This is a 3-D radiation pressure trap which does not require any magnetic field. Thus it offers advantages in applications such as cold-atom frequency standards or sub-recoil cooling where small residual magnetic fields cause limitations. It employs six circularly polarised beams as in an MOT, but the beams are made divergent (±22°) by focusing each one at 3.5 cm from the trap centre with objective lenses. The divergence of the beams results, for atoms displaced from the trap centre, in an intensity imbalance between the counterpropagating beams of opposed circular polarisation. Thus a displaced atom 'sees' more of one polarisation than the other and is optically pumped into an orientation. Then the differing Clebsch-Gordan coefficients for σ^+ and σ^- transitions result in preferential absorption of photons from the two beams so that the atom is pushed back to the trap centre. This trap has a trapping efficiency about one order of magnitude lower than a conventional MOT: 3×10^7 atoms have been trapped with a temperature of ~40 μK. The TROOP is very sensitive to intensity imbalances between the opposed beams. The easy way to set up and load a TROOP is to start from an MOT and gradually reduce the magnetic field whilst tweaking the beam alignments and intensities.

4.7.5 The 45° trapping force (1992)

Somewhat confusingly called by its authors[227-229] the 'magneto-optical radiation force' or the 'rectified dipole force' the mechanism of the '45° trap' involves (in 1-D) two linearly polarised counterpropagating beams with the polarisation directions rotated 45° from each other. A static magnetic field is applied parallel to the beam propagation direction. This mechanism was used to construct a 3-D trap for caesium atoms[229], trapping ~10^8 atoms at a temperature around half the Doppler limit. As it depends on stimulated emission for its effect it may be possible to build traps with very large spring constants using this technique, by using very intense beams and large magnetic fields.

4.7.6 The spin-polarised spontaneous force trap and vortex-force atom trap (1992)

The spin-polarised spontaneous force trap[230,231] is a variation on the MOT in which trapping in two spatial dimensions is achieved exactly as in the MOT, but in the third dimension by a 'macroscopic vortex' force which is insensitive to light polarisations and magnetic fields. It has the advantage that if the light along this third direction is circularly polarised and a parallel magnetic field applied, the sample of cold atoms becomes spin polarised, which may be useful for certain experiments.

4.7.7 The far off resonance trap (FORT) (1993)

The 'far off resonance trap' [142] is basically a dipole trap made with a single focused laser beam of very high intensity (s ~ 10^8) and large detuning (4 to 60 nm). It offers long confinement times, low scattering rates and may be useful for obtaining high densities of trapped atoms. Typical parameters are 1300 atoms at a temperature of 400 μK and density of 8×10^{11} cm^{-3}.

4.7.8 Bichromatic cooling (1993)

Bichromatic cooling was first reported[232] in 1993, and the 1-D set up involves a three-level atom in two collinear 1-D standing waves of the same linear polarisation but different frequencies. Each of the standing waves is blue detuned with respect to a transition from a different hyperfine ground state to the same excited state. The mechanism is another example of the sisyphus effect and similarly cools atoms into the sub-Doppler temperature range.

4.7.9 The 'dark SPOT' trap (1993)

The dark spontaneous force optical trap[233], or 'dark SPOT' trap, is an adaptation of an MOT in which the intensity of the repumping light in the centre most region of the trap is much lower (~1/100) than that in outer regions where the repumping intensity is at the level normally required to maintain a sufficient trapping population. The result is that atoms are magneto-optically trapped normally in the outer regions, but then fall into the inner region where they are pumped into a 'dark' hyperfine ground state. Because these dark atoms are

no longer interacting with the trapping light, they may be trapped within this central dark region at densities around two orders of magnitude higher than would be achievable in a normal MOT.

4.7.10 The 'NOT' or 'not-a-trap' (1994)

It was recently reported in a paper[234] entitled 'Optical trapping with linearly polarised light at zero magnetic field' that $\sigma^+\sigma^-$ standing waves are not the only configuration for which an MOT will operate. In fact there is a continuous family of different linear polarisation geometries which also give rise to a trapping force in a quadrupole magnetic field. The configuration which is most stable and has the largest spring constant is that with orthogonal linear polarisations in each standing wave, but with the 'incoming' polarisations along each axis tilted at 45° (see figure 1 of [234]). Furthermore, this latter configuration can also trap atoms when there is no magnetic field. The number and number density of atoms in such traps are comparable with a conventional MOT and the temperature can be lower. An explanation for these results has not yet been published.

4.7.11 Evaporative cooling and the 'TOP' trap

Evaporative cooling[32-34,47,48,122,235] is a cooling method which has recently become important as it was the method employed to achieve the first Bose-Einstein condensation of a gas of ^{87}Rb[34]. It was also used shortly afterwards in the second observation of BEC in ^{7}Li[122]. The method involves a gradual lowering of the well depth of a potential well containing trapped atoms, so that the most energetic atoms in the thermal distribution are able to escape. The lowering must be performed slowly enough to allow the remaining atoms to rethermalise by elastic collisions. Evaporative cooling is possible in both magnetic and optical traps.

The 'TOP' (time-averaged orbiting potential) trap used to achieve B.E.C. is an adaptation of a quadrupole magnetostatic trap. In a conventional quadrupole trap using two anti-Helmholtz coils, atoms with a magnetic moment experience an axially symmetric potential which drops to zero at the centre of symmetry of the coil pair. The atoms collect near this zero-field point, but unfortunately this is exactly where the probability of making a spin-flip transition to another atomic state with opposite magnetic moment is most high. Such spin-flipped atoms are then repelled from the trap. In order to prevent this effect, in the TOP trap a small oscillating magnetic field is superimposed upon the quadrupole field so that the zero-field point rotates in a small circle. The rotation rate is set so that the atom's position always lags behind the position of the zero-field point. Then the atom's motion is effectively governed by the time average of the potential, which is an ellipsoidal harmonic whose minimum corresponds to a non-zero field. Thus the spin-flipping is greatly reduced and stable trapping of very cold atoms (<1 μK) is achievable.

To achieve B.E.C. a technique known as rf-driven evaporative cooling was used, in which a radiofrequency signal is tuned so as to excite only the most energetic atoms at the outermost edge of the trap, flipping their spins and ejecting them from the trap. The frequency is gradually ramped downwards, thus driving the evaporation process whilst maintaining a deep trap. This technique results in a denser sample of cold atoms and proved to be sufficient to reach the phase transition where B.E.C. begins. The condition for the phase transition is given[236] by $n\lambda_{dB}^3 > 2.612$, where n is the atomic number density and λ_{dB} is the atomic de Broglie wavelength. In the reported experiment, the critical condition was reached at a temperature of 200 nK, corresponding to a de Broglie wavelength of 620 nm and a density of 10^{13} cm^{-3}.

4.8 Summary of chapter 4

Chapter 4 described several sub-Doppler cooling mechanisms, concentrating on sisyphus cooling, the magnetically assisted sisyphus effect and motion induced orientation because they are all present in the magneto-optical trap. Important features of these three mechanisms are the independence of the friction coefficient from the laser intensity, the dependence of the capture velocity on the laser intensity and the dependence of the equilibrium temperature on the laser intensity divided by the detuning. It was shown that localisation of atoms in optical potential wells is possible and that in real 3-D cooling and trapping experiments, a combination of these mechanisms may be operating simultaneously.

Chapter 5
Polarisation gradients and three-dimensional standing waves of light

This chapter is devoted to original theoretical studies which I have made of the structure of three-dimensional (3-D) standing waves of monochromatic light, in particular of their electric field polarisation gradients. The work aims to give insight into the electromagnetic fields produced by the typical laser beam arrangements of molasses and trapping experiments. The work is restricted mainly to the arrangement of six plane-wave laser beams propagating parallel to each of the six cartesian axial directions. I refer to such an arrangement as a '6-beam standing wave'. Other types of arrangement are also discussed where relevant and some generally applicable results obtained.

Chapter four described several sub-Doppler cooling mechanisms which required the presence of specific types of polarisation gradients in the electric field: sisyphus cooling, corkscrew cooling (motion-induced orientation), the magnetically-assisted sisyphus effect and velocity-selective magnetic resonance cooling. The basic theoretical explanations of all of these cooling mechanisms have been given in the literature using a simple model of an atom moving in a one-dimensional (1-D) standing wave formed by two counterpropagating laser beams. Such 1-D models involve only one 'type' (see figure 4-2) of polarisation gradient and therefore allow a clear understanding of the mechanisms. Many actual cooling and trapping experiments, however, are carried out in three dimensions where the structure of the field polarisation becomes complicated and can simultaneously contain the polarisation gradients corresponding to different sub-Doppler mechanisms. Consequently the fully three-dimensional 'cooling and trapping problem', i.e. solving the equation of motion of the atom in a 3-D resonant light field is extremely difficult. This chapter does not attempt to study the

interaction of the atoms with the light field, but is confined to the interesting sub-problem of the structure of the light field itself, with the intention of gaining insight which may be useful as regards the larger dynamical problem.

The structure of this chapter is as follows. Section 5.1 sets out the mathematical notation and conventions which I have used to define different 3-D standing waves. Then, using specific examples, it discusses some salient physical features of '6-beam standing waves' and ways of categorising them. Section 5.2 describes work carried out with the objective of quantifying the degrees to which 3-D standing waves contain sisyphus or corkscrew polarisation gradients. Section 5.3 describes an attempt to make a connection between sisyphus and corkscrew polarisation gradients and fundamental field angular momentum properties. Finally section 5.4 is a 'compendium' of calculated field quantities for some common field configurations.

5.1 The physical and mathematical description of 3-D standing waves

5.1.1 Conventions and assumptions

For clarity, I list the conventions and assumptions behind the mathematical descriptions employed in this chapter.

i) Real, as opposed to complex, functions will be used to define the electric field. For example, a plane wave linearly polarised in $\hat{\mathbf{x}}$, and propagating along $\hat{\mathbf{z}}$ is written as $\mathbf{E} = E_0 \hat{\mathbf{x}} \cos(kz - \omega t + \psi)$, where E_0 is the electric field amplitude and ψ is a phase factor dependent on the chosen origin of the co-ordinate system. Plane waves propagating in the $\hat{\mathbf{z}}$ direction will always have argument $(kz-\omega t)$[1], and not $(\omega t-kz)$.

ii) Each of the component plane waves used to construct a 3-D standing wave will have the same wavenumber k, angular frequency ω and intensity I_0 $(= \frac{1}{2}\varepsilon_0 c E_0^{\,2})$.

iii) Following traditional optics convention, the two varieties of circularly polarised light are described as follows. When an observer looks towards a source of circularly polarised light, the electric field vector appears to rotate anti-clockwise for left-handed light, and is written as

$$\mathbf{E} = \frac{E_0}{\sqrt{2}}\left[\hat{\mathbf{x}}\cos(kz - \omega t + \psi) - \hat{\mathbf{y}}\sin(kz - \omega t + \psi)\right] \qquad (5\text{-}1a)$$

For right handed light, it appears to rotate clockwise and is written as

$$\mathbf{E} = \frac{E_0}{\sqrt{2}}\left[\hat{\mathbf{x}}\cos(kz - \omega t + \psi) + \hat{\mathbf{y}}\sin(kz - \omega t + \psi)\right] \qquad (5\text{-}1b)$$

iv) In spectroscopy, the terms σ^+ light and σ^- light refer to circularly polarised light carrying $+\hbar$ and $-\hbar$ of angular momentum per photon respectively, referred to the z quantisation axis

---

[1] *This facilitates consistent use of the formulae for right- and left-handed circular polarisation.*

used to describe atomic states. The relationship of σ^+ and σ^- light to the left-handed and right-handed description is shown in table 5-1.

	left-handed	right-handed
Light propagating in $+\hat{\mathbf{z}}$	σ^+	σ^-
Light propagating in $-\hat{\mathbf{z}}$	σ^-	σ^+

Table 5-1 Relationship between σ^+ (σ^-) and left-(right-)handed designations of circularly polarised light

v) The theory developed in this chapter is for 3-D standing waves constructed from plane waves with a constant intensity profile transverse to the propagation direction. The motivating laser cooling experiments generally use laser beams in the TEM_{00} mode which have a Gaussian radial intensity profile. At a transverse radius which is 25% of the $1/e^2$ beam waist, the electric field amplitude has fallen to ~94% of its peak on-axis value. Regarding such a 6% variation in amplitude as an acceptable approximation to a uniform plane wave, the following theory is directly applicable to the innermost part of the intersection volume of unapodised laser beams, and to all of an apodised beam.

vi) The phase factors (e.g. ψ in equation 5-1 above) are assumed to be constant. In any experiment, the total path length of a laser beam from its source to its action point is likely to be subject to small fluctuations due to acoustic vibrations of mirror mounts etc, leading to large fluctuations in the phase factors. The theoretical ideal of constant phase factor can be approximated by using mirrors mounted on piezo-driven translation mounts controlled by a servolock system, as in the experiments of A.Hemmerich and T.Hänsch, e.g.[78].

vii) It is assumed in this work that the two beams in each counter-propagating pair are perfectly aligned, i.e. parallel. Small misalignments can have important effects on the field structure, as was mentioned in chapter 4 and in [162].

viii) It is well established, e.g.[237], that for any arbitrary field which is exactly monochromatic the field must be fully polarised everywhere. The polarisation at each point must be elliptical, though the orientation and eccentricity of the ellipse may vary from point to point. The two extreme cases are when the eccentricity equals 1, in which case the light is linearly polarised, and when the eccentricity equals 0, in which case the light is circularly polarised.

5.1.2 Phase factors and the interference of several 1-D standing waves.

Four basic types of 1-D standing waves were introduced earlier in chapter four: 'parallel linear' $\pi^x\pi^x$, 'sisyphus' $\pi^y\pi^x$, 'circular standing-wave' $\sigma^+\sigma^+$ and 'corkscrew' $\sigma^+\sigma^-$. Illustrations and formulae for these standing waves may be found in section 4.1.2. Each of the four types manifests a distinct ' polarisation structure' (e.g. a helix for $\sigma^+\sigma^-$) which

repeats with periodicity λ along the axis of the standing wave. A first approach to the 3-D problem is to study the various ways in which these basic 1-D standing waves might be combined to construct 3-D standing waves. Qualitatively, one expects to find various distinct types of 3-D standing waves, each with a distinguishing polarisation structure or 'topography' repeated on a 'crystalline' cubic lattice with periodicity λ. Visualising these 3-D fields, however, is difficult and a mathematical analysis is needed. Then it becomes clear that it is important to consider the effect of the phase factors of the beams when they are added. This is conveniently explained with a specific example. Consider a 1-D $\pi^x\pi^x$ (parallel linear) standing wave whose components propagate along the z-axis:

$$\mathbf{E} = E_0\hat{\mathbf{x}}\left[\cos\left(kz' - \omega t + \psi^-\right) + \cos\left(kz' + \omega t + \psi^+\right)\right] \tag{5-2}$$

This can be partially simplified by a shift of the origin of the co-ordinate system along the z-axis.

$$z = z' + \frac{\psi^- + \psi^+}{2k}$$

which gives

$$\mathbf{E} = E_0\hat{\mathbf{x}}\left[\cos\left(kz - (\omega t + \psi)\right) + \cos\left(kz + (\omega t + \psi)\right)\right]$$

where $\psi = \dfrac{\psi^+ - \psi^-}{2}$ is a phase factor clearly related to the choice of the time origin of the (space-time) co-ordinate system. One can add to this standing wave two standing waves of the same amplitude 'propagating' along the x and y axes, having first performed similar shifts of the co-ordinate system origin along the x and y axes. The resultant field where these waves overlap is

$$\begin{aligned}\mathbf{E} = {} & E_0\hat{\mathbf{y}}\left[\cos(kx - (\omega t + \theta)) + \cos(kx + (\omega t + \theta))\right] \\ & + E_0\hat{\mathbf{z}}\left[\cos\left(ky - (\omega t + \phi)\right) + \cos\left(ky + (\omega t + \phi)\right)\right] \\ & + E_0\hat{\mathbf{x}}\left[\cos\left(kz - (\omega t + \psi)\right) + \cos\left(kz + (\omega t + \psi)\right)\right]\end{aligned} \tag{5-3}$$

Here, θ, ϕ and ψ are three 'time phases', associated with the 1-D standing waves propagating on the x, y and z axes respectively and determining their relative synchronisation. This association ($x \leftrightarrow \theta$, $y \leftrightarrow \phi$, $z \leftrightarrow \psi$) is retained throughout this chapter. By shifting the time origin of the co-ordinate system, one might eliminate one of the three time phases leaving just two 'relative time phases'. All four degrees of freedom relating to the choice of the co-ordinate system origin have then been 'used up', leaving the two relative time phases as necessary parameters determining aspects of the polarisation topography of the resultant 3-D standing wave. For most of the following discussion, it turns out to be more convenient to retain all three time phases, thus preserving the clear cyclical symmetry of equations such as 5-3. As an example of this, consider the next step in the simplification of equation 5-3:

$$\mathbf{E} = 2E_0\left[\hat{\mathbf{y}}\cos kx\cos(\omega t + \theta) + \hat{\mathbf{z}}\cos ky\cos(\omega t + \phi) + \hat{\mathbf{x}}\cos kz\cos(\omega t + \psi)\right] \tag{5-4}$$

This may conveniently be written as

$$\mathbf{E} = 2E_0\hat{\mathbf{y}}\cos kx\cos(\omega t + \theta) + \text{ cycle} \qquad (5\text{-}4)$$

where '+ cycle' indicates that two more terms are to be added, identical to the first apart from the changes $x \to y \to z \to x$ and $\theta \to \phi \to \psi \to \theta$.

The importance of these time phases when calculating the 3-D field due to three orthogonal 1-D standing waves was first recognised by Molmer[199], and has been subsequently studied by several groups[78,162,199,205]. To my knowledge the only workers who actively control the time phases in their experiments are A.Hemmerich and T.Hänsch[77-82,238,239]. They have shown theoretically, and confirmed in 2-D experiments[238,239], that the different field structures due to different time phases lead to different light forces on cold atoms. A recent Monte-Carlo simulation[115] of a 3-D molasses experiment also demonstrated the dramatic effect of different relative time phases in a 6-beam arrangement. The relative time phases might be deemed a 'problem' in that either experimentalists must control them, or, if they are left to fluctuate in experiments, then the theoretical analysis must use an average over all possible values.

An ingenious alternative approach to the 'time phase problem' was proposed by a group at L'Ecole Normale Supérieure[205]. It is based on a degrees of freedom argument. Consider the common example of the field due to the intersection of six plane waves. Before any simplifying co-ordinate shifts are made, each plane wave contributes one phase factor to the expression for the resultant 3-D field, giving six phase factors in all. The space-time origin of the co-ordinate system is arbitrary and may be chosen to eliminate four of the phase factors, as there are four degrees of freedom in this choice (three spatial and one temporal). Two phase factors cannot be eliminated; their values determine the structure of the field. If one applies the same argument to the intersection of only four plane waves (non co-planar), all four phase factors can be eliminated by a suitable choice of origin[2]. The physical meaning of this is that there is only one possible polarisation structure for the field; phase fluctuations merely cause a spatial translation of this structure. An example of such a field is that created at the intersection of four travelling waves aligned in the 'tetrahedral beam' arrangement, where each beam enters an imaginary tetrahedron normal to one of its faces. Tetrahedral beam arrangements have been successfully used in experiments[205,83,84,240]. It is not strictly necessary for the beams to be aligned with an exact tetrahedral symmetry, and in fact departures from such exact symmetry have been usefully exploited in experiments, e.g.[83], as they allow the creation of field structures with different spatial periodicities along different axes. As well as allowing this extra degree of freedom as regards the periodicities, the tetrahedral 4-beam field arrangment has the advantage of eliminating the need for phase

[2] *Similar arguments can be made for 1-D and 2-D beam arrangements.*

control in experiments. Nevertheless, many groups use the orthogonal 6-beam arrangement as studied in this chapter. Orthogonal beam arrangements allow optical lattices to be 'customised' to provide desirable experimental properties e.g.[77-82,238,239].

5.1.3 Describing '6-beam' standing waves

In general, 3-D standing waves may be constructed in many ways, using any number of monochromatic plane waves with arbitrary propagation directions, polarisations and relative time phases. This subsection 5.1.3 is now restricted to the 6-beam fields generated by the usual arrangement of six intersecting orthogonal beams. I now introduce a concise notation for 6-beam standing waves which indicates how they are constructed from component 1-D standing waves. It consists of a series of six standard polarisation symbols, giving the polarisation of each of the component travelling waves, always in the order: propagation in $+\hat{\mathbf{x}}$, propagation in $-\hat{\mathbf{x}}$, propagation in $+\hat{\mathbf{y}}$, propagation in $-\hat{\mathbf{y}}$, propagation in $+\hat{\mathbf{z}}$, propagation in $-\hat{\mathbf{z}}$. Thus as examples, the standing wave given by equation 5-3 is designated $\pi^y\pi^y\pi^z\pi^z\pi^x\pi^x$ and a 3-D standing wave with all beams having left-handed circular polarisation is designated $\sigma^+\sigma^-\sigma^+\sigma^-\sigma^+\sigma^-$. The work in this subsection is also restricted, as is the case in many experiments, to those 6-beam standing waves whose three component 1-D standing waves are each of the same 'standard' type (e.g. $\sigma^+\sigma^-\sigma^+\sigma^-\sigma^-\sigma^+$ as used in the MOT). Thus there are four basic families of 6-beam standing waves to consider, corresponding to the four prototype 1-D standing waves from which they are constructed. It should be pointed out that some experiments involve interesting exceptions, e.g.[82], using a mixture of types of 1-D standing wave $\pi^y\pi^y\pi^x\pi^x\sigma^+\sigma^+$, or [229] which uses 1-D standing waves whose plane wave components are linearly polarised at 45° to each other.

Rotational and reflective symmetry and 'similarity' of fields

6-beam standing waves all have a periodic structure with a cubic unit cell of side λ, the wavelength of the laser light. The polarisation topography within the unit cell depends on the nature of the six constituent plane waves. The question arises as to whether two 6-beam standing waves formed from differing arrangements of beam polarisations and/or time phases have a 'similar' polarisation topography. For instance, is one related to the other by a spatial translation or change of handedness? 'Similar' in this context is taken to mean that 'test' atoms travelling randomly in the two fields traverse on average the same intensity and polarisation gradients and thus experience identical cooling and trapping forces. The laws of physics relating to the interaction of light and atoms are invariant with respect to the following types of coordinate transformations: space translations, time translations, rotations and parity inversion. Hence I define two standing waves to be technically **similar** if there is such a legitimate co-ordinate transformation between them.

A 6-beam standing wave may be 'self-**similar**', i.e. have a polarisation topography which is **similar** whether viewed along the $\pm x$, $\pm y$ or $\pm z$-axes. Mathematically, symmetry

with respect to rotation by 90° requires that the expression for the total field is unchanged by the cyclic substitutions $x \to y \to z \to x$ and $\theta \to \phi \to \psi \to \theta$ and reflective symmetry allows any one of $x \to -x$, $y \to -y$ and $z \to -z$. Consider the following two 3-D standing waves, each built with three parallel linear 1-D standing waves.

Standing wave A $\pi^z\pi^z\pi^z\pi^z\pi^x\pi^x$

Propagation axis	Polarisation axis
x	z
y	z
z	x

Standing wave B $\pi^y\pi^y\pi^z\pi^z\pi^x\pi^x$

Propagation axis	Polarisation axis
x	y
y	z
z	x

It can be seen from the above table that for standing wave A, two of the component 1-D standing waves contribute z polarisation, and there is no y polarisation. Its 3-D polarisation structure is not rotationally symmetric. Standing wave B, on the other hand, receives balanced contributions to x,y and z polarisation and corresponds to the field described by equation 5-3. It is 90° rotationally symmetric, fulfilling the required cyclic condition.

Whether 90 rotational symmetry is desirable may depend on experimental objectives. It could be desirable in experiments requiring nearly isotropic distributions of field properties or atomic properties like velocity or magnetisation. On the other hand, deliberate introduction of asymmetry in the field/atom interaction might be useful in elucidating features of the interaction. The field used in the magneto-optical trap is not rotationally symmetric, the two beams aligned along the magnetic field coils having opposite handed circular polarisation to the other four beams, in order that the light field structure 'match' the quadrupole magnetic field. Four specific examples of 6-beam standing waves are now selected and examined in order to illustrate a number of key points. The four examples are each a 3-D extension of the four prototype 1-D standing waves ($\pi^x\pi^x$, $\sigma^+\sigma^-$, $\sigma^+\sigma^+$, $\pi^y\pi^x$).

5.1.4 Parallel Linear 6-beam standing waves

As a first example, consider 90° rotationally symmetric, parallel linear, 6-beam standing waves. Such a field was used in one of the earliest optical molasses experiments[36]. Firstly, there are only two possibilities: $\pi^y\pi^y\pi^z\pi^z\pi^x\pi^x$ and $\pi^z\pi^z\pi^x\pi^x\pi^y\pi^y$; they are related by a parity inversion and a 90° rotation. (There are also six asymmetric possibilities, also inter-related by rotations etc). As both arrangements are **similar**, I may use $\pi^y\pi^y\pi^z\pi^z\pi^x\pi^x$ as the prototype for further discussion. Its six components are described by equation 5-3, which was simplified to equation 5-4:

$$\mathbf{E} = 2E_0\left[\hat{\mathbf{y}}\cos kx\cos(\omega t+\theta) + \hat{\mathbf{z}}\cos ky\cos(\omega t+\phi) + \hat{\mathbf{x}}\cos kz\cos(\omega t+\psi)\right] \qquad (5\text{-}4)$$

One now considers the effect of various values of the time phases on the standing wave. An obvious place to start is with $\theta = \phi = \psi = 0$, which I call the 'synchronised configuration'. The equation becomes

$$\mathbf{E} = 2E_0 \cos\omega t\left(\hat{\mathbf{y}}\cos kx + \hat{\mathbf{z}}\cos ky + \hat{\mathbf{x}}\cos kz\right) \qquad (5\text{-}5)$$

which can be easily interpreted. It represents a 6-beam standing wave which

- is linearly polarised and in phase everywhere.
- has eight field nodes and eight antinodes (amplitude $2\sqrt{3}E_0$) per unit cell. At each antinode, the field is linearly polarised parallel to one of the unit cell diagonals
- contains polarisation gradients with corkscrew-like properties, i.e. linear polarisation which rotates in space.

Thus in the synchronised configuration, motion induced orientation is possible, but sisyphus cooling is not, owing to there being no regions of circular polarisation.

An important question is: what is the effect of different values of the time phases on this polarisation topography? A first approach to this question is simply to try substitution of various values for θ, ϕ and ψ in equation 5-4. For instance, starting from the synchronised configuration, putting any one of θ, ϕ or ψ equal to π radians gives a **similar** standing wave; in fact it is just the original synchronised configuration translated spatially by $\lambda/2$. Contrastingly, putting any one of θ, ϕ or ψ equal to $\pi/2$ radians produces a standing wave with different topography and which cannot be converted to the synchronised configuration by any co-ordinate transformation. It turns out that the most dramatic change in polarisation topography from the synchronised configuration is obtained with time phases such as $\theta = 0$, $\phi = \pi/3$, $\psi = -\pi/3$, or a similar permutation, which I call the 'three-phase configuration'. This assertion is backed by a mathematical argument which is given later in subsection 5.1.8. Meanwhile it may be visualised as in figure 5-1. Note that a change of any of the time phases by $\pm\pi$ merely reproduces the same topography, spatially shifted by $\lambda/2$.

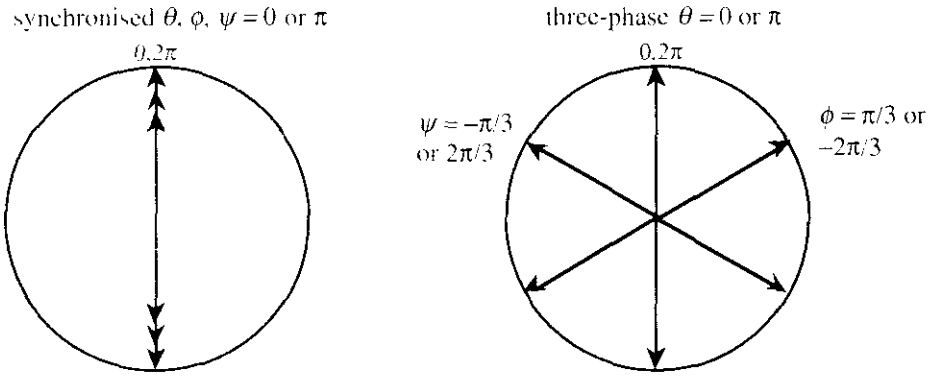

Figure 5-1 Time phase diagram for the synchronised and three-phase configurations

In changing from the synchronised to the three-phase configuration, the most significant change in the polarisation topography is that the polarisation at almost every point in the cell changes from linear to elliptical. Thus in the three-phase configuration, sisyphus polarisation gradients involving circular polarisation may be present.

5.1.5 Corkscrew 6-beam standing waves

As a second example, there are two basic polarisation structures for 6-beam corkscrew standing waves built from three $\sigma^+\sigma^-$ 1-D standing waves. For a $\sigma^+\sigma^-$ ($\sigma^-\sigma^+$) 1-D standing wave, both beams must be left (right) -handed. Using L(R) to denote a left (right)-handed 1-D standing wave, there are eight possible ways to make a 3-D standing wave, which divide into two groups, each group having a distinct polarisation structure. The first group contains the 90° rotationally symmetric combinations LLL ($\sigma^+\sigma^-\sigma^+\sigma^-\sigma^+\sigma^-$) and RRR ($\sigma^-\sigma^+\sigma^-\sigma^+\sigma^-\sigma^+$), which have a **similar** polarisation structure related by a parity inversion, and the second group consists of LLR, LRL, RLL, RRL, RLR, LRR which have a **similar** polarisation structure related by parity inversion and/or a 90° rotation. The field used in a magneto-optical trap belongs to the second group (not rotationally symmetric). I use LLR ($\sigma^+\sigma^-\sigma^+\sigma^-\sigma^-\sigma^+$) as an example. The field is given as the sum of six plane waves by

$$\mathbf{E} = \frac{E_0}{\sqrt{2}}\left[\hat{\mathbf{y}}\cos(kx-\omega t-\theta)-\hat{\mathbf{z}}\sin(kx-\omega t-\theta)\right]+\frac{E_0}{\sqrt{2}}\left[\hat{\mathbf{y}}\cos(kx+\omega t+\theta)-\hat{\mathbf{z}}\sin(kx+\omega t+\theta)\right]$$
$$+\frac{E_0}{\sqrt{2}}\left[\hat{\mathbf{z}}\cos(ky-\omega t-\phi)-\hat{\mathbf{x}}\sin(ky-\omega t-\phi)\right]+\frac{E_0}{\sqrt{2}}\left[\hat{\mathbf{z}}\cos(ky+\omega t+\phi)-\hat{\mathbf{x}}\sin(ky+\omega t+\phi)\right]$$
$$+\frac{E_0}{\sqrt{2}}\left[\hat{\mathbf{x}}\cos(kz-\omega t-\psi)+\hat{\mathbf{y}}\sin(kz-\omega t-\psi)\right]+\frac{E_0}{\sqrt{2}}\left[\hat{\mathbf{x}}\cos(kz+\omega t+\psi)+\hat{\mathbf{y}}\sin(kz+\omega t+\psi)\right.$$

which simplifies to the column vector

$$\mathbf{E} = \sqrt{2}E_0\begin{bmatrix}\cos kz\cos(\omega t+\psi)-\sin ky\cos(\omega t+\phi)\\ \cos kx\cos(\omega t+\theta)+\sin kz\cos(\omega t+\psi)\\ \cos ky\cos(\omega t+\phi)-\sin kx\cos(\omega t+\theta)\end{bmatrix} \tag{5-6}$$

In the synchronised configuration this becomes

$$\mathbf{E} = \sqrt{2}E_0\cos\omega t\begin{bmatrix}\cos kz-\sin ky\\ \cos kx+\sin kz\\ \cos ky-\sin kx\end{bmatrix} \tag{5-7}$$

The properties of the synchronised configuration include

- It is linearly polarised everywhere with a polarisation axis which varies throughout the unit cell.
- It has eight nodes per unit cell, e.g. at [$\lambda/8$, $\lambda/8$, $-\lambda/8$]. Note that the component $\sigma^+\sigma^-$ 1-D standing waves do not have nodes themselves.
- It has eight antinodes of amplitude $2\sqrt{3}E_0$ per unit cell, e.g.at [$-\lambda/8$, $-\lambda/8$, $\lambda/8$].

Once again, motion induced orientation is possible in the synchronised configuration, but sisyphus cooling is not.

The field in the three-phase configuration ($\theta = 0$, $\phi = 2\pi/3$, $\psi = -2\pi/3$) may be calculated, and has the following properties

- There are no longer any nodes

- The polarisation is elliptical almost everywhere, and in particular is exactly circular at the positions which were nodes and antinodes for the synchronised configuration.
- The field amplitude is now greater ($=3E_0/\sqrt{2}$) at the original nodal positions than at the original antinodal positions ($=\sqrt{3}E_0/\sqrt{2}$).

The key points to be made are firstly that the change of relative time phases from the synchronised to the three-phase configuration has again entirely changed the polarisation topography of the field. Secondly, the change has produced elliptical and circular polarisation, thus allowing the possibility of sisyphus polarisation gradients which are not present in the synchronised configuration.

I have carried out similar examinations of two other types of 6-beam standing wave. I briefly summarise the most important results below.

5.1.6 Circularly polarised 6-beam standing waves

There are eight ways to construct circularly polarised 6-beam standing waves, $\sigma^+\sigma^+\sigma^+\sigma^+\sigma^+\sigma^+$ and $\sigma^+\sigma^+\sigma^+\sigma^+\sigma^-\sigma^-$ are two examples. The light in each of the three 1-D standing waves has a definite angular momentum, parallel or anti-parallel with its propagation axis. The three angular momentum vectors (spatially averaged) will add to give a resultant vector pointing along one of the eight unit cell diagonals, depending on the individual 1-D standing waves. The polarisation topographies of all eight arrangements are **similar** in the technical sense. Once again, there are eight nodes and eight antinodes per unit cell. Two of the eight antinodes are linearly polarised, the other six are elliptically polarised with various orientations. The polarisation structure is dramatically changed in the three-phase configuration.

5.1.7 Sisyphus 6-beam standing waves

For sisyphus 6-beam standing waves there appear to be eight basic ways to combine three 1-D sisyphus standing waves, examples are $\pi^y\pi^z\pi^z\pi^x\pi^x\pi^y$ and $\pi^z\pi^y\pi^z\pi^x\pi^x\pi^y$. Again these are all technically **similar**, i.e. related by rotations and parity inversions. Interestingly, in the synchronised configuration, there are only two nodes and two antinodes per unit cell, as opposed to the eight of each found for the three beam arrangements described previously. The antinodes are linearly polarised, but the polarisation is elliptical with spatially varying orientation at most points in the unit cell. The topography is self-similar with a periodicity of $\lambda/4$, rather than the $\lambda/2$ found in the three previous arrangements. Correspondingly, time phase changes of $\pi/2$ in any of θ, ϕ or ψ change the polarisation topography to one which is **similar**. This is not surprising, in view of the $\lambda/4$ variation evident in the 1-D sisyphus standing wave. Once again, the polarisation structure is dramatically changed in the three-phase configuration.

5.1.8 Electromagnetic field properties of 6-beam standing waves

My first approach to studying 6-beam fields was, as illustrated by subsections 5.1.3 to 5.1.7 above, to calculate the resultant electric vector field (polarisation) and study its mathematical form. My second approach consisted of calculating general algebraic expressions for electromagnetic field quantities of potential interest in order to examine their spatial variation and dependence on time phases. Interesting properties, for instance, are the electric field energy density and its gradient as, in a simple two-level theory, these determine the dipole forces on atoms. Another interesting quantity is the Poynting vector, which is sometimes associated with the scattering force[3], for instance in the radiation pressure vortices reported in [238], or in simple atomic beam deceleration by a plane wave. The set of field properties which I calculated and examined is listed in table 5-7. Some results of these calculations are tabulated in section 5.5 of this chapter. The algebraic expressions for electromagnetic properties of these 1-D and 3-D standing waves possess fascinating mathematical symmetries.

In parallel with these calculations, a computer programme was used to display the spatial variation of the field quantities. Such computer pictures are of some use in understanding the structure of the fields. Their usefulness however is limited owing to the complexity of the fields, combined with the difficulty of reducing a 3-D field to an informative 2-D or 1-D image. For the record, an example of such a plot is included as figure 5-2, overleaf.

The idea that the 'three-phase configuration' of time phases represents a kind of polar opposite to the 'synchronised configuration' was depicted in figure 5-1. This idea gains weight from the results of calculations of field quantities. For instance, consider the example of the time-averaged Poynting vector, $\langle \mathbf{S} \rangle$, for a $\pi^y\pi^y\pi^z\pi^z\,\pi^x\pi^x$ standing wave:

$$\langle \mathbf{S} \rangle = 2E_0H_0 \begin{bmatrix} \cos ky \sin kz \sin(\phi - \psi) \\ \cos kz \sin kx \sin(\psi - \theta) \\ \cos kx \sin ky \sin(\theta - \phi) \end{bmatrix} \tag{5-8}$$

The minimum value of $\langle \mathbf{S} \rangle$ is zero when $\theta = \phi = \psi = 0$, i.e. in the synchronised configuration. The maximum possible value for $\langle \mathbf{S} \rangle$ may be found by study of the symmetry of equation 5-8, which leads to the conclusion that the maximum will occur when each of the three components is equal in magnitude. This requires that

$$\sin(\phi - \psi) = \sin(\psi - \theta) = \sin(\theta - \psi) \tag{5-9}$$

---

[3] *Our paper on light forces[133] showed that the scattering force and the Poynting vector are not necessarily always collinear, even for 2-level atoms.*

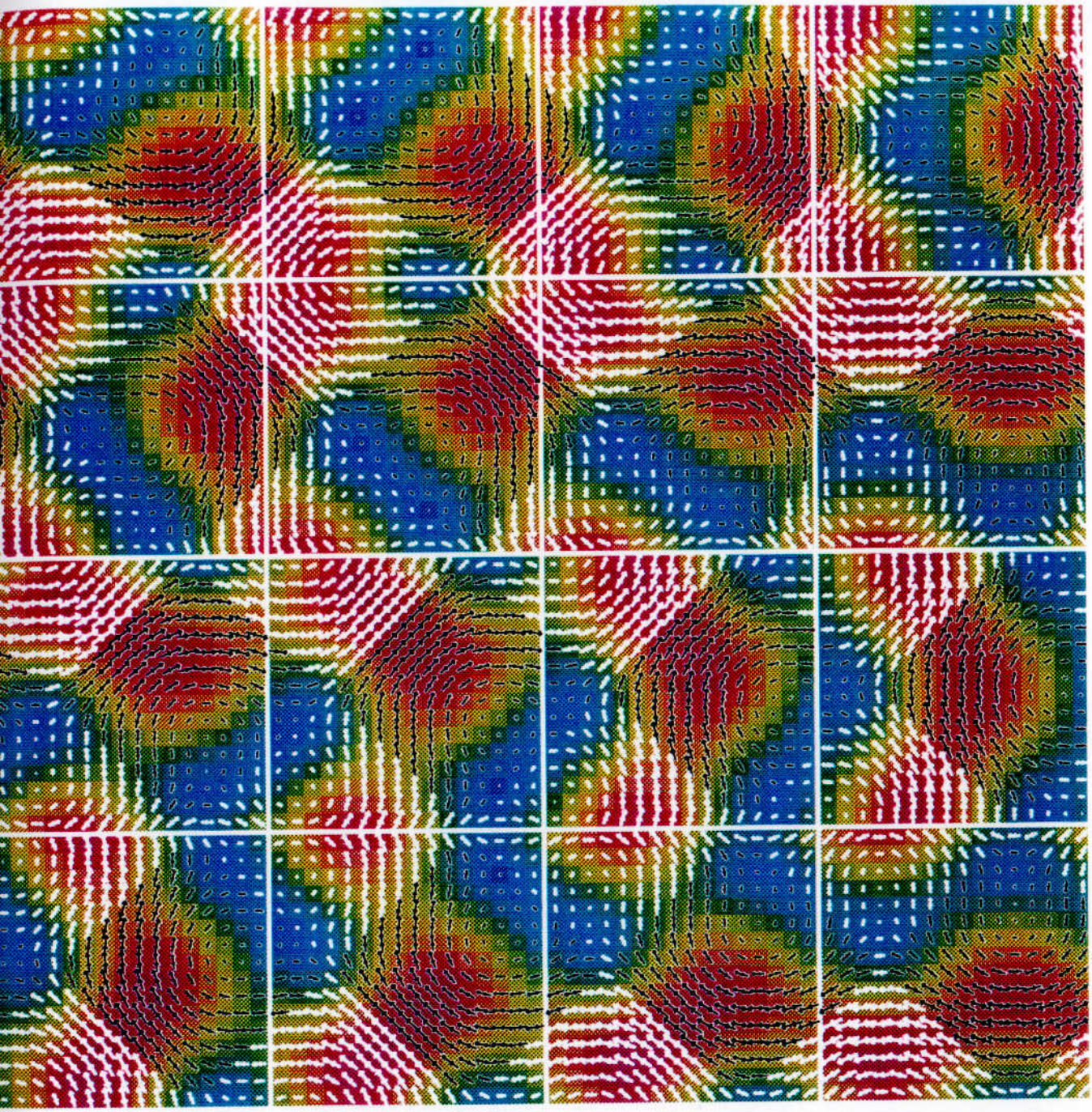

Figure 5-2 The electric field vector $\mathbf{E}$ *in a unit cell of a 6-beam* $\sigma^+\sigma^-\sigma^+\sigma^-\sigma^+\sigma^-$ *standing wave in the synchronised configuration, visualised as colour-coded 2-D slices through the field. The magnitude (intensity) is colour coded, red for high and blue for low. The* $\mathbf{E}$*-field polarisation in the x-y plane is indicated by the arrows. White arrows have a z-component out of the page, and black arrows into the page. Each small square represents a slice in the x-y plane of size* λ *by* λ*. Reading left to right and then down as usual, each square is displaced by* $\lambda/16$ *in the z-direction to build up a picture of the complete unit cell.*

We are free to choose $\theta = 0$, which is equivalent to fixing the time origin of the co-ordinate system, and then the three solutions in the range $-\pi$ to $+\pi$ are

$$\begin{aligned} &\theta = 0, \quad \phi = 0, \quad \psi = 0 \\ &\theta = 0, \phi = \pi/3, \psi = -\pi/3 \end{aligned} \tag{5-10}$$

Thus for this particular case (field type and field quantity), the three-phase configuration is shown to be special. It turns out that similar calculations of the field quantities listed in table 5-7 for the four types of 6-beam standing waves considered in this chapter always result in mathematical expressions whose stationary points are determined by equations either of the form

$$\begin{aligned} &\sin(\phi - \psi) = \pm\sin(\psi - \theta) = \pm\sin(\theta - \psi), \text{ which is equivalent to} \\ &\cos(\phi - \psi) = \pm\cos(\psi - \theta) = \pm\cos(\theta - \psi) \end{aligned} \tag{5-11}$$

or of the form

$$\begin{aligned} &\cos(\phi - \psi) = \pm\sin(\psi - \theta) = \pm\sin(\theta - \phi), \text{ which is equivalent to} \\ &\sin(\phi - \psi) = \pm\cos(\psi - \theta) = \pm\cos(\theta - \phi) \end{aligned} \tag{5-12}$$

The solutions to equations 5-11 are permutations of

$$\begin{aligned} &\theta = 0, \ \phi = 0, \ \psi = 0 \\ &\theta = 0, \ \phi = \pi/3, \ \psi = -\pi/3 \end{aligned} \tag{5-13}$$

which correspond to the synchronised and three-phase configurations. One solution gives the minimum of the particular field quantity under consideration and the other its maximum. The solutions to equation 5-12 are

$$\begin{aligned} &\theta = 0, \ \phi = \pi/2, \ \psi = -\pi/2 \\ &\theta = 0, \ \phi = \pi/6, \ \psi = -\pi/6 \end{aligned} \tag{5-14}$$

Again, the two solutions correspond to the minimum and maximum values of the particular field quantity under consideration.

The overall conclusions are as follows. All the field quantities listed in table 5-7 have their stationary points determined by either equation 5-11 or 5-12. Whichever equation applies, if one starts from a time phase configuration such that the field quantity has its minimum (maximum) value, then the maximum (minimum) will be produced by shifting any two of the time phases by $+\pi/3$ and $-\pi/3$ respectively. Although I am not aware of any formal publication of the above result, the three-phase configuration was used as one choice of time phases for a recent numerical simulation of 3-D laser cooling[115]. Figure 5-1 is the time phase diagram for those fields quantities whose stationary points are given by equations 5-11 and 5-13. To complete the diagrammatic picture, another time phase diagram is necessary. Figure 5-3 is therefore the time phase diagram for those field quantities whose stationary points are given by equations 5-12 and 5-14.

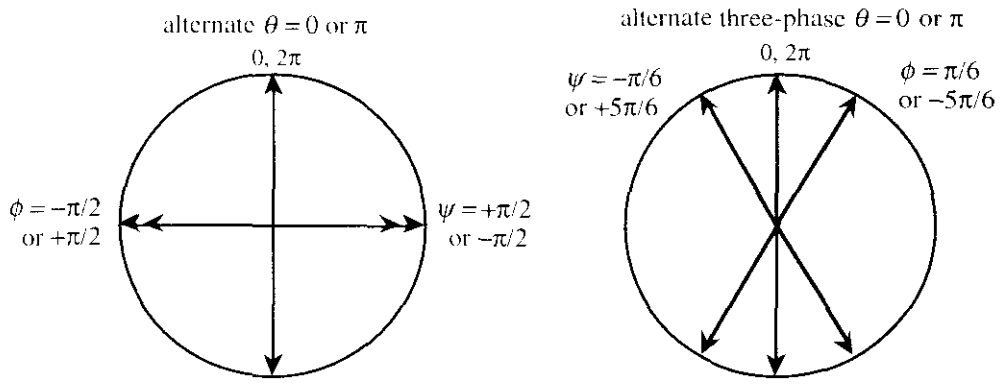

Figure 5-3 Time phase diagram for field quantities with stationary points determined by alternate equations 5-12 and 5-14

5.2 Measuring sisyphus and corkscrew polarisation gradients

Doppler cooling occurs in all 6-beam standing waves with red detuning and saturation parameter $s \leq 1$. The interesting question therefore is as to which 6-beam standing waves give rise to sub-Doppler cooling, in particular to sisyphus and corkscrew cooling as those mechanisms do not require the presence of a magnetic field. It is a reasonable assumption that if a particular sub-Doppler polarisation gradient is present in a 3-D field then the corresponding cooling mechanism is also present. Hence by measuring the amount of 'ellipticity' (degree of circular polarisation) or 'helicity'(corkscrewness) in a given standing wave one obtains a measure of the corresponding cooling mechanism. Following on from work published by Steane and Foot[162], I developed two parameters which measure the properties of ellipticity and helicity. These parameters were then used in a numerical simulation to measure the amounts and variation of ellipticity and helicity in various 6-beam standing wave arrangements with variable time phase settings. This work is described in sections 5.2.2 and 5.2.3. It is preceded by a review of established descriptions of polarisation in fields.

5.2.1 Established descriptions of light polarisation

There are several well established systems for describing light polarisation, including the Stokes parameters and associated Mueller matrices, the Jones vectors and Jones matrices and the coherency matrix. Full descriptions may be found in references[237,241,242]. These systems share the limitation of describing the polarisation state of only a single travelling wave, as opposed to a general field containing different wave vectors. For that reason they are not very useful for this work. As background information only, I briefly describe these systems below, and then consider ways in which they might be extended to arbitrary monochromatic 3-D fields.

The four Stokes parameters were originally defined in 1852 in terms of four field observables obtained by measuring the intensity of a travelling wave after it passed through each of a set of four polarisation filters. In general they are defined for both light which is quasi-monochromatic, (i.e. narrow bandwidth), and light which is exactly monochromatic. For the purposes of this chapter, the case of an exactly monochromatic plane wave is sufficient. Then, for a wave travelling in the $\hat{\mathbf{z}}$ direction with field $\mathbf{E}$ given by

$$\mathbf{E} = \hat{\mathbf{x}} E_{0x} \cos\left[(kz - \omega t) + \psi_x\right] + \hat{\mathbf{y}} E_{0y} \cos\left[(kz - \omega t) + \psi_y\right] \tag{5-15}$$

the Stokes parameters are

$$\begin{aligned} s_0 &= {E_{0x}}^2 + {E_{0y}}^2 \\ s_1 &= {E_{0x}}^2 - {E_{0y}}^2 \\ s_2 &= 2E_{0x}E_{0y}\cos(\psi_x - \psi_y) \\ s_3 &= 2E_{0x}E_{0y}\sin(\psi_x - \psi_y) \end{aligned} \tag{5-16}$$

which are related by

$${s_0}^2 = {s_1}^2 + {s_2}^2 + {s_3}^2 \tag{5-17}$$

s_0 is proportional to the intensity of the wave, and s_1, s_2 and s_3 specify the polarisation state; s_1 measures linear polarisation in the $\hat{\mathbf{x}}$ and $\hat{\mathbf{y}}$ directions, s_2 measures linear polarisation in the directions at $\pm 45^\circ$ to the $\hat{\mathbf{x}}$ direction and s_3 measures the degree of circular polarisation (or ellipticity). It is useful to normalise the Stokes parameters by dividing each one by s_0, and to write the four parameters as a vector. As examples, a right-handed circular polarised beam is then [1,0,0,1], a left-handed beam [1,0,0,-1], an $\hat{\mathbf{x}}$ linearly polarised beam [1,1,0,0] etc. The Stokes parameters offer two advantages. Firstly, they may be added like pseudovectors, but only for beams that are incoherent. Secondly, they may be combined with the 4 x 4 'Mueller matrices', which represent the effect of various optical components like wave-plates on the beams.

The coherency matrix is closely related to the Stokes parameters. As a matter of passing interest only, the relationship is mathematically analogous to that between the elements of a two-level atom density matrix and the Bloch vector. However, the Stokes parameters and coherency matrix are not very useful for this work, because they can only be added for incoherent beams. Nevertheless the parameter s_3 is of some interest here, because it measures the ellipticity of a plane wave.

The Jones vectors, invented by R.Clark Jones in 1941, are another representation of polarised plane waves. For the plane wave described by equation 5-15 above, the Jones vector is simply

$$\mathbf{E} = \begin{bmatrix} E_{0x} e^{i(kz+\psi_x)} \\ E_{0y} e^{i(kz+\psi_y)} \end{bmatrix} \tag{5-18}$$

which is the complex representation of the field with implicit time dependence $e^{-i\omega t}$. Such vectors can be added for coherent monochromatic beams. It is also possible to normalise the

Jones vectors to obtain prototype expressions for polarisation states. For instance, $\hat{\mathbf{x}}$ linearly polarised light becomes $\begin{bmatrix}1\\0\end{bmatrix}$, $\hat{\mathbf{y}}$ linearly polarised light becomes $\begin{bmatrix}0\\1\end{bmatrix}$ and left and right circularly polarised light become $\frac{1}{\sqrt{2}}\begin{bmatrix}1\\i\end{bmatrix}$, $\frac{1}{\sqrt{2}}\begin{bmatrix}1\\-i\end{bmatrix}$ respectively. When a polarised beam passes through a particular optical element, its Jones vector is transformed. The transformation may be described by the corresponding 2 x 2 'Jones matrix'. The Jones vector notation may be easily extended to include arbitrary 3-D monochromatic fields simply by adding a third component giving the $\hat{\mathbf{z}}$ electric field component to each plane wave. Then the Jones' vectors of each of the plane waves comprising the 3-D field may be added to give $\mathbf{J}$, a spatially varying 'generalised Jones vector'.

5.2.2 Parameters for ellipticity and helicity

This subsection starts by considering methods of calculating the magnitude and orientation of circular polarisation (ellipticity) at any point in an arbitrary monochromatic light field. I find four equivalent formulations, including a new and efficient 'vector' method. Then I proceed to develop complimentary methods for calculating the magnitude and orientation of corkscrewness or 'helicity' in the field.

Ellipticity

Formulation i) In their paper [162] on the magneto-optical trap, Steane, Chowdhury and Foot develop a parameter p_l which measures the degree of circular polarisation in the x-y plane at each point of an arbitrary monochromatic field. If the real field is $\mathbf{E}(\mathbf{r},t) = \mathrm{Re}\{\mathbf{E}_C(\mathbf{r},t)\}$, their prescription is

$$p_l = \left(\xi^+\right)^2 - \left(\xi^-\right)^2 \tag{5-19}$$

where $\xi^{\pm} = \frac{1}{\sqrt{2}}\left(\hat{\mathbf{x}} \pm i\hat{\mathbf{y}}\right)^* \cdot \mathbf{E}_C$.

Formulation ii) It can be shown that, for a monochromatic plane wave propagating along the z-axis, p_l is equal to the Stokes parameter s_3, which can be calculated with equations 5-15 and 5-16. The Stokes parameter s_3 is only defined for plane waves and is equal to +1 (−1) for a left (right)-handed beam. The parameter p_l applies to arbitrary fields including standing waves, where right-handed and left-handed are no longer appropriate terms as the propagation direction is not defined. The σ^+ and σ^- designation referred to the $\hat{\mathbf{z}}$ axis is well defined, and thus $p_z = +1$ for σ^+ light, $p_z = -1$ for σ^- light and $p_z = 0$ for linearly polarised light.

Formulation iii) Two alternative but equivalent ways of writing the field $\mathbf{E}(\mathbf{r},t)$ are

$$\begin{aligned}\mathbf{E} &= \mathrm{Re}\left\{\mathbf{J}e^{-i\omega t}\right\}\\ \mathbf{E} &= \mathbf{E}_1\cos\omega t + \mathbf{E}_2\sin\omega t\end{aligned} \tag{5-20}$$

Here **J** is the 'generalised Jones vector' extended to include arbitrary 3-D fields. **J**, $\mathbf{E}_1$, and $\mathbf{E}_2$ are related by $\mathbf{J} = \mathbf{E}_1 + i\mathbf{E}_2$. It can be shown that an alternative method of calculating the *parameter* p_z is

$$p_z = 2\hat{\mathbf{z}} \cdot (\mathbf{E}_1 \times \mathbf{E}_2) \tag{5-21}$$

Formulation iv) This is a new 'vector method' which I have developed as follows. Consider the arbitrary monochromatic field $\mathbf{E}(\mathbf{r},t)$ at any point. The polarisation must be elliptical, and so one can imagine the tip of the electric field vector tracing out the ellipse with period $2\pi/\omega$, as illustrated in figure 5-4. The 'velocity' of the tip is $\frac{\partial \mathbf{E}}{\partial t}$ and this is parallel to **E** in the case of linear polarisation and orthogonal to **E** in the case of circular polarisation. Defining a vector $\mathbf{M} = \mathbf{E} \times \frac{\partial \mathbf{E}}{\partial t}$, **M** points in the direction normal to the plane of rotation and has a magnitude which gives a measure of the degree of circularity. Note that $\mathbf{M} = \mathbf{0}$ for linearly polarised light. The **ellipticity** with respect to an arbitrary axis defined by unit vector $\hat{\mathbf{n}}$ is then defined by

$$p = \frac{2}{\omega}\hat{\mathbf{n}} \cdot \mathbf{M} = \frac{2}{\omega}\hat{\mathbf{n}} \cdot \left(\mathbf{E} \times \frac{\partial \mathbf{E}}{\partial t} \right) \tag{5-22}$$

where the factors of 2 and ω are introduced to make this parameter consistent with the three previous measures of ellipticity. For instance when $\hat{\mathbf{n}} = \hat{\mathbf{z}}$, then $p = p_z$. A useful feature of the parameter p is its simple formulation as the product of two distinct factors: a property dependent only on the electric field ($2\mathbf{M}/\omega$), and an arbitrary direction of interest $\hat{\mathbf{n}}$.

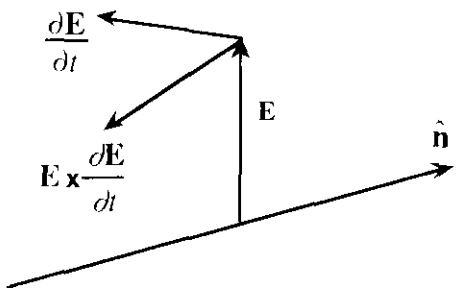

Figure 5-4 The 'vector' method of calculating ellipticity

Helicity

I found that it is possible to develop four helicity[4] parameters, which measure the 'corkscrewness' of a light field, corresponding respectively to the four formulations ***i*** to ***iv*** of the ellipticity parameter. In the formulations **i**, **ii** and **iii**, their mathematical constructions are somewhat artificial and they are only defined for 3-D fields built from 1-D standing waves with mutually orthogonal propagation directions, as is the case for 6-beam standing waves. Consequently I do not discuss them further. Corresponding to formulation **iv**,

[4] *Note that helicity here does not have the same meaning as that used by particle physicists.*

however, I found a helicity parameter r which is defined as follows for arbitrary monochromatic fields. Consider the arbitrary monochromatic field $\mathbf{E}(\mathbf{r},t)$ at any point. If one imagines that time is frozen, one can ask how $\mathbf{E}$ changes for a small displacement in an arbitrary direction $\hat{\mathbf{n}}$. The answer is $\frac{\partial \mathbf{E}}{\partial \mathbf{n}}$, where the differentiation with respect to a vector is an intuitive shorthand for $(\hat{\mathbf{n}} \cdot \nabla)\mathbf{E}$. See figure 5-5. The direction of $\frac{\partial \mathbf{E}}{\partial \mathbf{n}}$ may be parallel to $\mathbf{E}$, as it would be for instance in a linearly polarised 1-D standing wave, or it may be orthogonal to $\mathbf{E}$, as in a corkscrew 1-D standing wave along the z-axis when $\hat{\mathbf{n}} = \hat{\mathbf{z}}$, or it may be between those extremes. The vector $\mathbf{N} = \mathbf{E} \times \frac{\partial \mathbf{E}}{\partial \mathbf{n}}$ then defines the rotation direction of the field with respect to small displacements in the $\hat{\mathbf{n}}$ direction. The **helicity** r with respect to the arbitrary direction $\hat{\mathbf{n}}$ is then defined by

$$r = \frac{2}{k}\hat{\mathbf{n}} \cdot \mathbf{N} = \frac{2}{k}\hat{\mathbf{n}} \cdot \left(\mathbf{E} \times \frac{\partial \mathbf{E}}{\partial \mathbf{n}} \right) \tag{5-23}$$

where the k is introduced so as to give r the same dimensions as p, namely $[E^2]$, and the '2' is introduced to maintain mathematical symmetry with the ellipticity p.

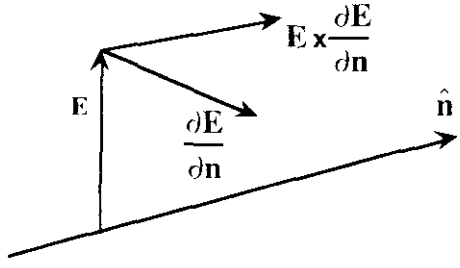

Figure 5-5 The 'vector' method of calculating helicity

If one rewrites equation 5-23 using tensor notation, it is seen to be a product of a tensor depending only on the electric field, a tensor depending only on $\hat{\mathbf{n}}$, and the Levi-Civita alternating tensor[143] ϵ_{ijk}.

$$r = \frac{2}{k}\left(n_j n_l\right)\left(E_{t,l} E_k\right)\left(\epsilon_{ijk}\right) \tag{5-24}$$

Written out in full vector component notation, equation 5-23 (5-24) is

$$\begin{aligned}
\frac{k}{2} r = {} & n_x^2 \left(E_y \frac{\partial E_z}{\partial x} - E_z \frac{\partial E_y}{\partial x} \right) + n_y^2 \left(E_z \frac{\partial E_x}{\partial y} - E_x \frac{\partial E_z}{\partial y} \right) + n_z^2 \left(E_x \frac{\partial E_y}{\partial z} - E_y \frac{\partial E_x}{\partial z} \right) \\
& + n_y n_x \left(E_z \frac{\partial E_x}{\partial x} - E_x \frac{\partial E_z}{\partial x} \right) + n_x n_y \left(E_y \frac{\partial E_z}{\partial y} - E_z \frac{\partial E_y}{\partial y} \right) \\
& + n_z n_y \left(E_x \frac{\partial E_y}{\partial y} - E_y \frac{\partial E_x}{\partial y} \right) + n_y n_z \left(E_z \frac{\partial E_x}{\partial z} - E_x \frac{\partial E_z}{\partial z} \right) \\
& + n_x n_z \left(E_y \frac{\partial E_z}{\partial z} - E_z \frac{\partial E_y}{\partial z} \right) + n_z n_x \left(E_x \frac{\partial E_y}{\partial x} - E_y \frac{\partial E_x}{\partial x} \right)
\end{aligned} \tag{5-25}$$

Note that in a simple case such as $\hat{\mathbf{n}} = \hat{\mathbf{z}}$, this simplifies to

$$r = \frac{2}{k}\left(E_x \frac{\partial E_y}{\partial z} - E_y \frac{\partial E_x}{\partial z} \right) \qquad (5\text{-}26)$$

The values of the parameters p and r for some simple fields, namely travelling waves and the four basic 1-D standing waves propagating along the z-axis are shown in table 5-2.

Light field	p	r
Linearly polarised plane wave	0	0
R.H. circ. polarised plane wave	−1	+1
L.H. circ. polarised plane wave	+1	−1
$\pi^y\pi^x$ 1-D standing wave	0	0
$\pi^y\pi^x$ 1-D standing wave	$2\sin 2kz$	$2\sin 2\omega t$
$\sigma^+\sigma^-$ 1-D standing wave	0	$-4\cos^2\omega t$
$\sigma^+\sigma^+$ 1-D standing wave	$+4\cos^2 kz$	0
'Hybrid' 1 – D standingwave	$\sqrt{2}\sin 2kz$	$\sqrt{2}\sin 2\omega t - 2\sqrt{2}\cos^2\omega t$

Table 5-2 Values of the un-normalised parameters ellipticity p and helicity r tabulated for several basic light fields. Each plane wave has an electric field amplitude equal to 1, wavenumber k and propagates in the +z or −z direction

The parameters p and r are clearly complementary in some ways, which is not surprising in view of the complementary nature of their derivation: one involves the derivative of **E** with respect to time, the other with respect to space. Interesting features of the parameters for 1-D standing waves are:

- In a $\pi^y\pi^x$ sisyphus standing wave, the ellipticity oscillates with a spatial frequency $2k$, whilst the helicity oscillates with a temporal frequency 2ω.
- In a $\sigma^+\sigma^+$ standing wave, the (un-normalised) ellipticity varies as $\cos^2 kz$, and the helicity is zero. Its 'complement' is a $\sigma^+\sigma^-$ standing wave, where the (un-normalised) helicity varies as $\cos^2\omega t$, and the ellipticity is zero.
- In a $\pi^y\pi^x$ lin-parallel-lin standing wave, the ellipticity and helicity are both zero.
- For amusement, I calculated a 'hybrid' 1-D standing wave which has equal degrees of the sisyphus and corkscrew polarisation gradients. This is done by simply superimposing sisyphus and corkscrew 1-D standing waves along the z axis, but it is important to use the correct relative time phase. The electric field may be visualised as two counterpropagating elliptically polarised plane waves, with opposite handed polarisations and with orthogonal major axes. The resultant 'hybrid' electric field is given by

$$\mathbf{E} = \frac{E_0}{\sqrt{2}} \left\{ \begin{array}{l} \hat{\mathbf{x}}\cos(kz - \omega t) + \hat{\mathbf{y}}\cos(kz - \omega t + \pi/4) \\ +\hat{\mathbf{x}}\cos(kz + \omega t) + \hat{\mathbf{y}}\cos(kz + \omega t + 3\pi/4) \end{array} \right\}$$

5.2.3 Computer searches for field configurations

I have made use of the ellipticity p and helicity r to search 6-beam standing waves for sisyphus and corkscrew polarisation gradients. The method consists of a numerical simulation in which a test atom travels along many straight line trajectories of length λ through the light field. The starting point and direction of each trajectory are both randomised. The normalised values of the ellipticity and helicity seen by the atom as it travels each trajectory are used to generate two further parameters $\overline{\Xi(p)}$ and $\overline{\Xi(r)}$, which are good indicators of the average 'sisyphusness' and 'corkscrewness' of the light field respectively, and defined as follows.

First, cycle-averaged[5] and normalised versions of p and r are defined:

$$p_N = \frac{\langle p \rangle}{2I} \tag{5-27a}$$

$$r_N = \frac{\langle r \rangle}{2I} \tag{5-27b}$$

where the $\langle\ \rangle$ denote a cycle average, and $I = \langle \mathbf{E} \cdot \mathbf{E} \rangle$ is the local field 'intensity'. Then for each of the straight line trajectories, $\Xi(p)$ is defined as $\sqrt{2}$ times the standard deviation of p_N along the trajectory

$$\Xi(p) = \sqrt{2}\sigma(p_N)$$

and $\Xi(r)$ is defined as the root mean square value of r_N along the trajectory

$$\Xi(r) = \left(\overline{r_N^2}\right)^{1/2}$$

To help demonstrate why the parameters p_N, r_N, $\Xi(p)$ and $\Xi(r)$ are useful, their values calculated along lines parallel to each of the four prototype 1-D standing waves are listed in table 5-3.

Light field	p_N	r_N	$\Xi(p)$	$\Xi(r)$
$\pi^x\pi^y$ 1-D standing wave	0	0	0	0
$\pi^y\pi^y$ 1-D standing wave	$\sin 2kz$	0	1	0
$\sigma^+\sigma^-$ 1-D standing wave	0	−1	0	1
$\sigma^+\sigma^+$ 1-D standing wave	+1	0	0	0
Hybrid 1-D standing wave	$(1/\sqrt{2})\sin 2kz$	$-1/\sqrt{2}$	$1/\sqrt{2}$	$1/\sqrt{2}$

Table 5-3 Values of p_N, r_N, $\Xi(p)$ and $\Xi(r)$ for the four prototype 1-D standing waves

Out of the set of the four basic 1-D standing waves, only the sisyphus standing wave has a non-zero standard deviation of the parameter p_N along its axis. Hence I calculate the parameter $\Xi(p)$ for each of many random trajectories through the 6-beam standing wave under study and then average $\Xi(p)$ over all the trajectories to obtain an indicator $\overline{\Xi(p)}$ of

[5] *In fact it is unnecessary to cycle-average p: p is always independent of time for a monochromatic light field.*

the sisyphusness of the field. Similarly, of the set of four basic standing waves, only the corkscrew standing wave has a non-zero value of the parameter $\Xi(r)$. Hence I calculate $\Xi(r)$ along each random trajectory through the 6-beam standing wave, and then average the result over all the trajectories to obtain an indicator $\overline{\Xi(r)}$ of corkscrewness. I use the root mean square of r_N because I wish to include the possibility of cooling by corkscrews which change handedness along a trajectory. Opposite-handed helices generate positive and negative values of r_N, which would otherwise cancel. Squaring also avoids the mutual cancellation of positive and negative corkscrews on different trajectories. The values of $\overline{\Xi(p)}$ and $\overline{\Xi(r)}$ are then plotted as a function of the (relative) time phases θ and ϕ. (ψ is assumed to be zero for simplicity).

To cover the full range of possibilities, θ and ϕ must each range from 0 to π. To put a reasonable constraint on computation time, θ and ϕ were increased in steps of $\pi/12$. Along each trajectory, p_N and r_N were calculated at 13 points spaced by $\lambda/12$ in order to generate $\overline{\Xi(p)}$ and $\overline{\Xi(r)}$. I found that 100,000 trajectories per θ, ϕ pair were sufficient to reduce run-to-run fluctuations in the values of $\overline{\Xi(p)}$ and $\overline{\Xi(r)}$ to $\leq 1\%$. The validity of each of these time-saving steps was carefully checked by comparing the programme output with that of adapted programmes using for instance, a finer mesh of θ, ϕ points, smaller steps of $\lambda/24$ along each trajectory and repeated runs of 100,000 trajectories at selected data points. The programme used to generate the final results, written in C, is reproduced in Appendix A7. The simulation takes about 36 hours to run on a "Digital" DEC 3000 workstation.

Results of the computer search for polarisation gradients

The simulations were carried out for four types of 6-beam standing wave and are now displayed as surface plots in figures 5-6A to 5-6D. Note that the vertical scales are 'normalised' in the sense that, for an atom travelling along the z axis of a $\pi^y\pi^x$ 1-D standing wave, $\overline{\Xi(p)}$ has a value of 1, and, for an atom travelling along the z axis of a $\sigma^+\sigma^-$ 1-D standing wave, $\overline{\Xi(r)}$ also has a value of 1. However, in simulations in which the test atoms travel on random 3-D trajectories in a 1-D standing wave, the corresponding values are $\overline{\Xi(p)} = 0.49$ for $\pi^y\pi^x$ and $\overline{\Xi(r)} = 0.33$ for $\sigma^+\sigma^-$.

A point of interest is that I also produced a second set of plots, not reproduced here, which used the same method as outlined above, except that un-normalised versions of the parameters p and r were used at each point on each trajectory. This was primarily to check whether normalisation had a large influence on the results. After scaling the un-normalised results (by dividing by the spatially averaged intensity $6I$, where I is the intensity of each plane wave), the shapes and absolute values of the plots produced by the two alternate versions of the programme were virtually indistinguishable in all cases.

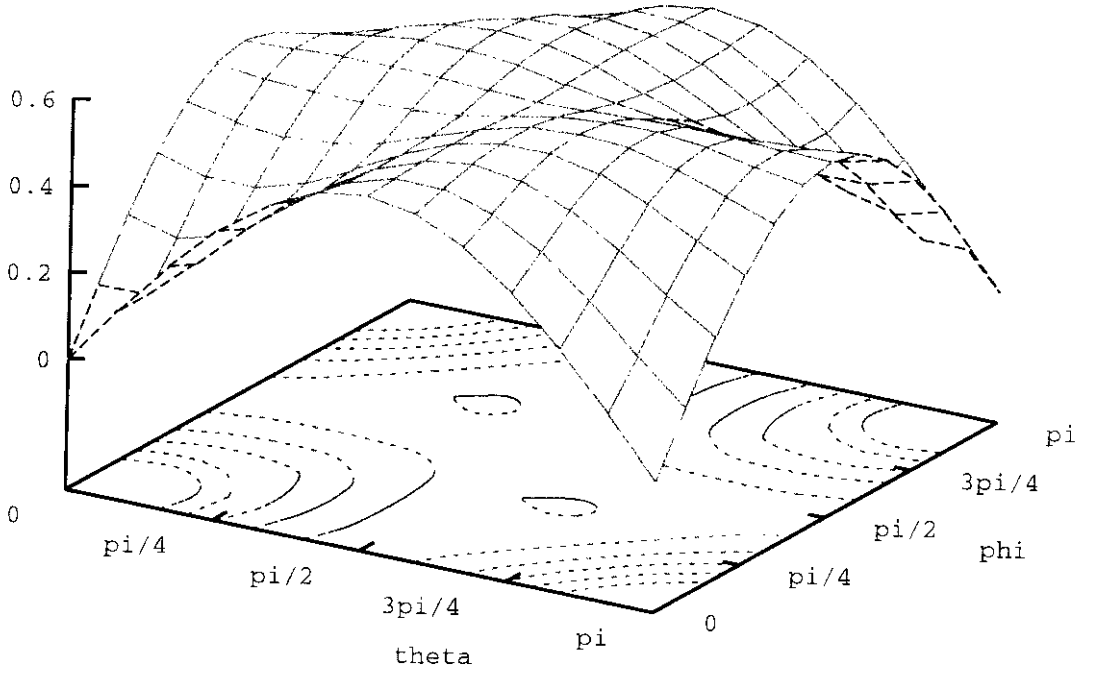

$\overline{\Xi(p)}$

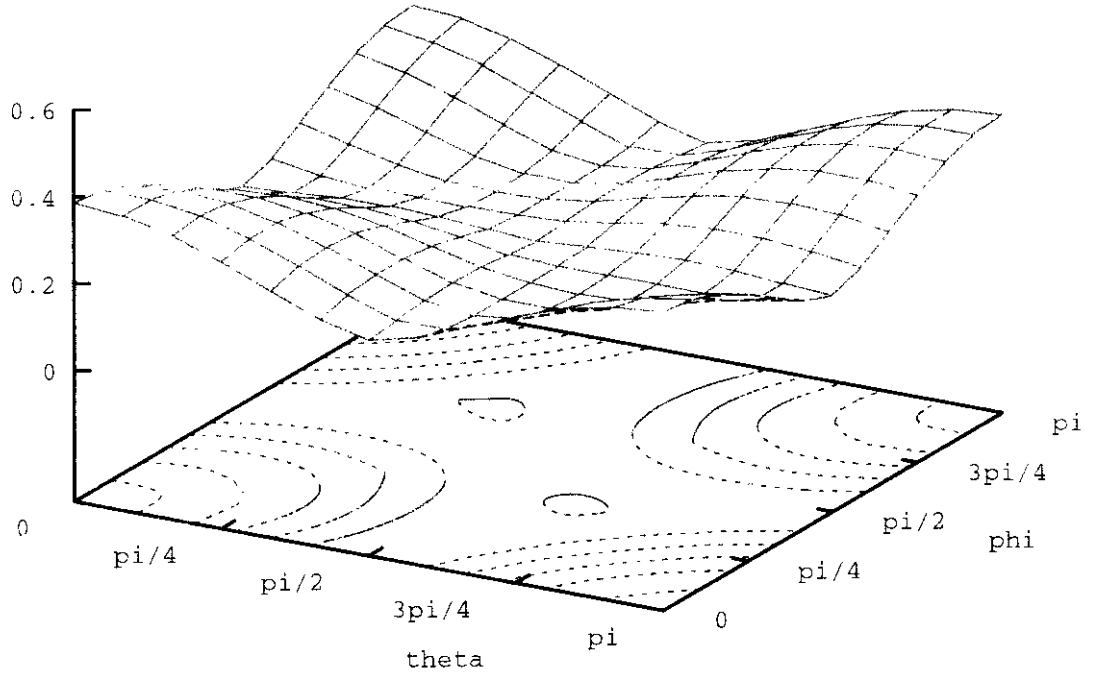

$\overline{\Xi(r)}$

Figure 5-6A Surface plots showing variation of $\overline{\Xi(p)}$ and $\overline{\Xi(r)}$ with θ and ϕ for a $\pi^y\pi^y\pi^z\pi^z\pi^x\pi^x$ standing wave (3D lin-parallel-lin)

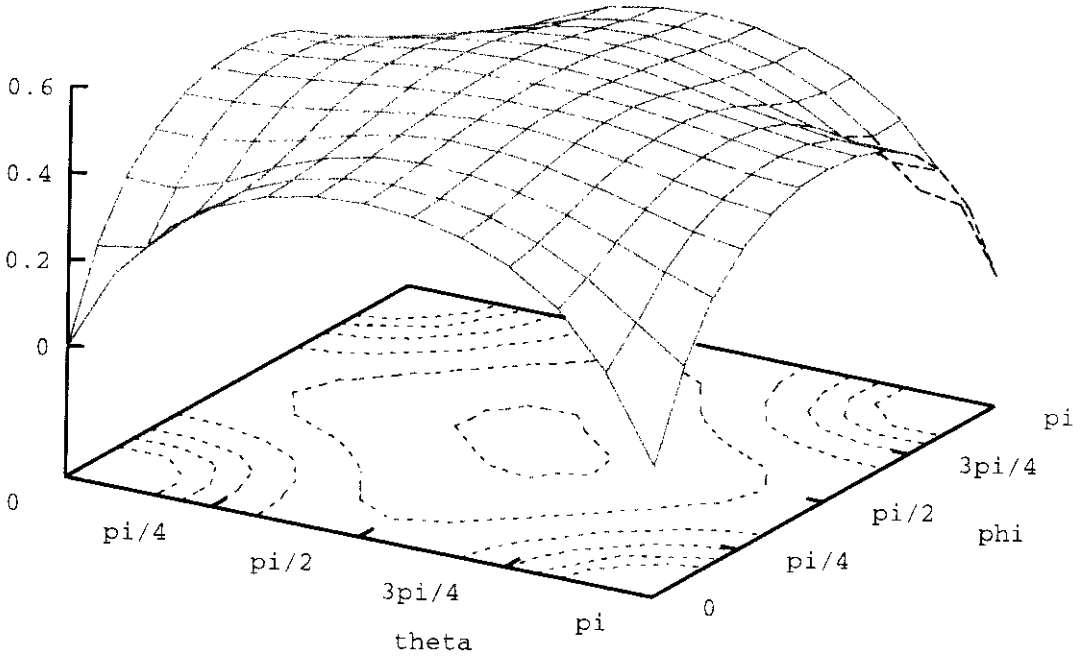

$\overline{\Xi(p)}$

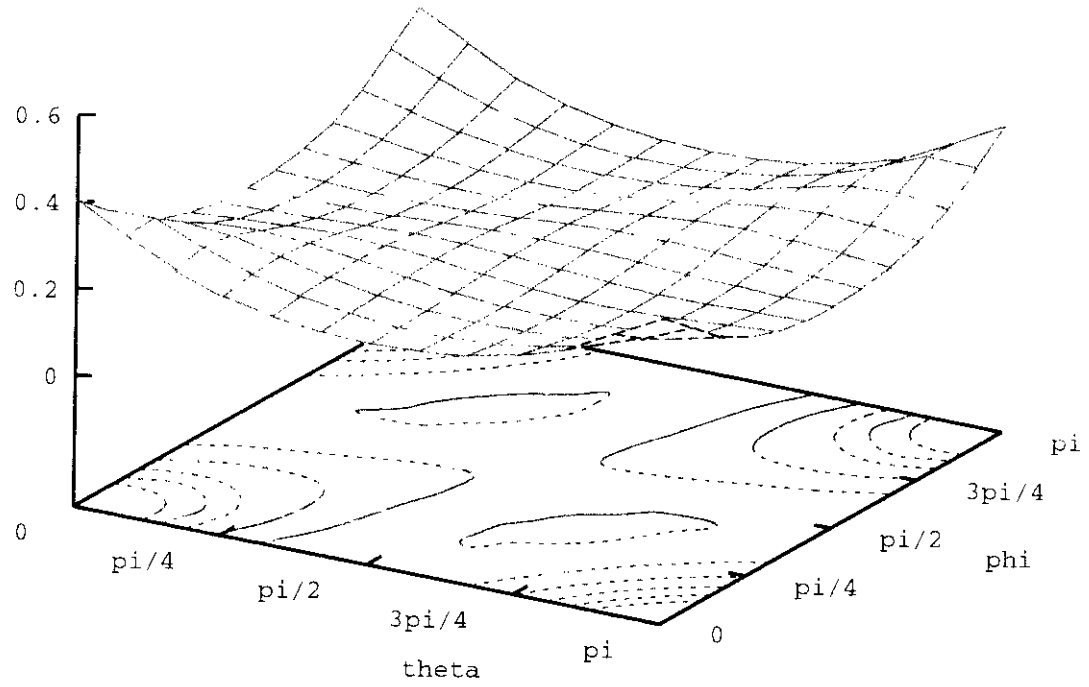

$\overline{\Xi(r)}$

Figure 5-6B Surface plots showing variation of $\overline{\Xi(p)}$ *and* $\overline{\Xi(r)}$ *with* θ *and* ϕ *for a* $\sigma^+\sigma^-\sigma^+\sigma^-\sigma^-\sigma^+$ *standing wave (3D* $\sigma^+\sigma^-$ *as in an MOT)*

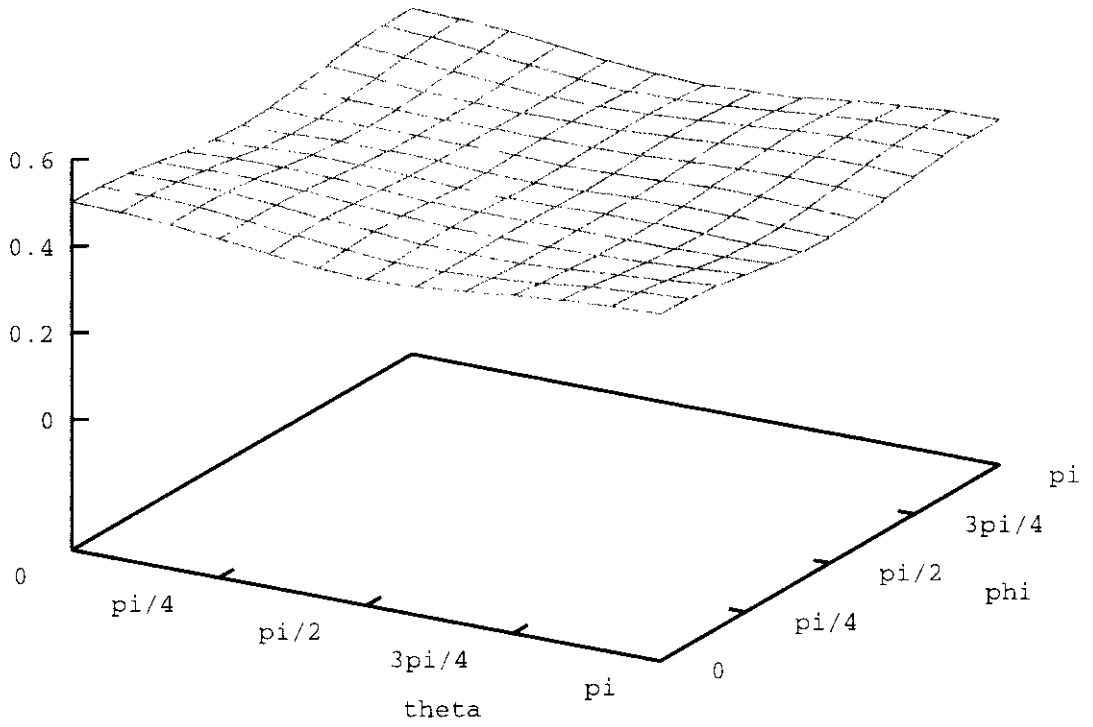

$\overline{\Xi(p)}$

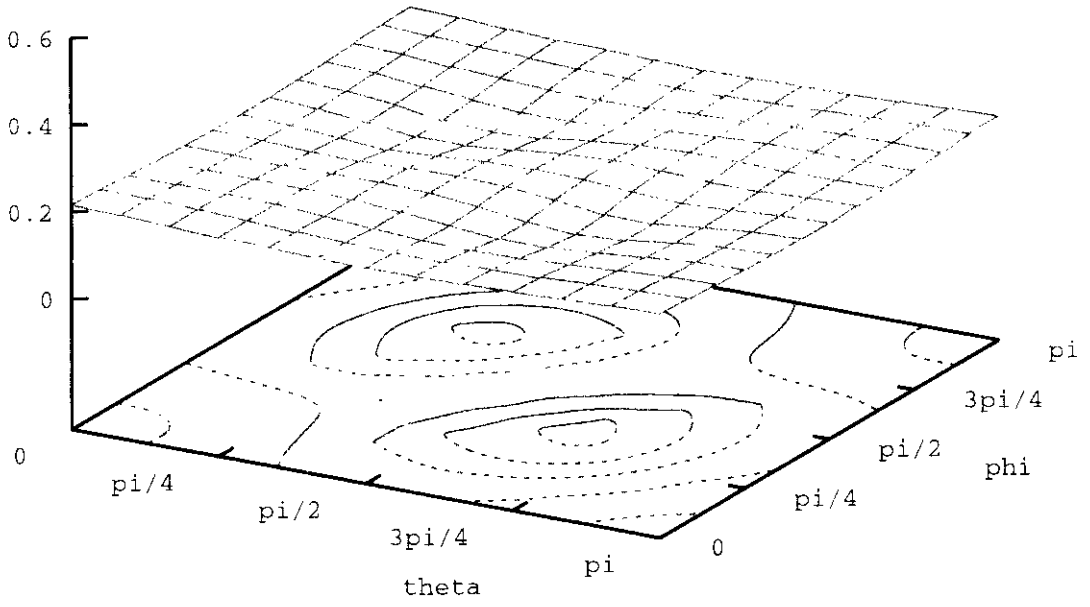

$\overline{\Xi(r)}$

Figure 5-6C Surface plots showing variation of $\overline{\Xi(p)}$ and $\overline{\Xi(r)}$ with θ and ϕ for a $\pi^{\prime}\pi^{y}\pi^{x}\pi^{z}\pi^{y}\pi^{x}$ standing wave (3D sisyphus or lin-perp-lin)

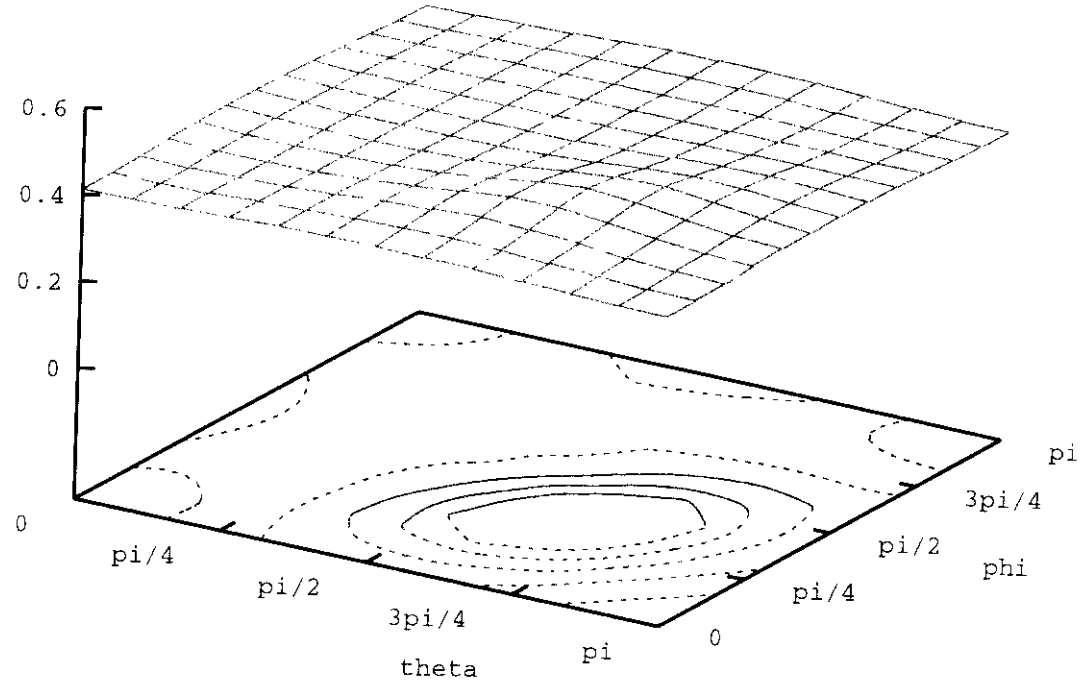

$\overline{\Xi(p)}$

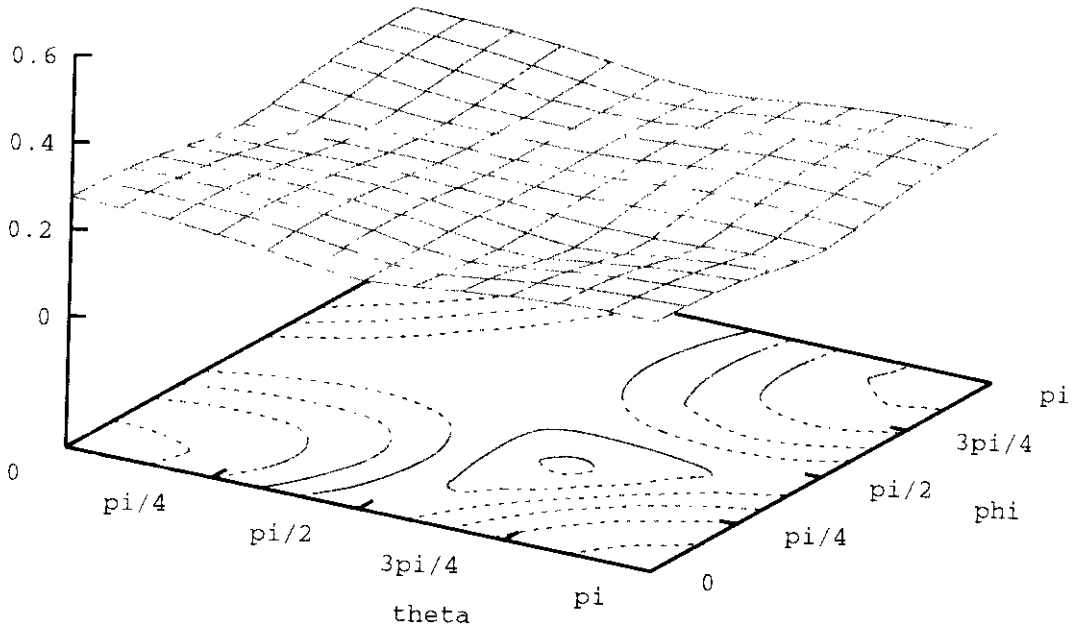

$\overline{\Xi(r)}$

Figure 5-6D Surface plots showing variation of $\overline{\Xi(p)}$ *and* $\overline{\Xi(r)}$ *with* θ *and* ϕ *for a* $\sigma^+\sigma^+\sigma^+\sigma^+\sigma^+\sigma^+$ *standing wave (3D* $\sigma^+\sigma^+$*)*

Discussion of results of the computer search for polarisation gradients

The numerical simulation provides quantitative measures $\overline{\Xi(p)}$ (sisyphusness) and $\overline{\Xi(r)}$ (corkscrewness) of the degrees to which sisyphus and corkscrew polarisation gradients are present in each light field studied. For convenience I refer to each of the four light fields studied and their corresponding plots by the letters A, B, C and D used to label figures 5-6A to 5-6D. The surface plots for each of the above four 6-beam standing waves show that sisyphus gradients can occur, for most time phase settings, in all four of the light fields, and corkscrew gradients occur for all time phases. There are only two arrangements which are sisyphus-free, these are fields A and B in the synchronised configuration of time phases; this result is similar to results found in a study of 2-D light fields[199]. There is evidence in the plots, particularly for field A, that the synchronised and three-phase configurations of time phases are associated with the minima and maxima of $\overline{\Xi(p)}$ and $\overline{\Xi(r)}$. However this is generally a weak effect except for fields A and B in the synchronised configuration, where there are no sisyphus gradients. The sisyphus plots of fields A and B shows a marked dependence on the time phases, whereas the sisyphus plots for fields C and D and the corkscrew plots for all four fields are suprisingly flat.

In order to aid comparison of the four field configurations, table 5-4 gives the maximum and minimum values of $\overline{\Xi(p)}$ and $\overline{\Xi(r)}$ for each field (obtained for specific time phases). It also gives the values of $\overline{\Xi(p)}$ and $\overline{\Xi(r)}$ averaged over the entire θ by ϕ grid of time phases. These average values give a measure of the presence of sub-Doppler polarisation gradients when the time phases fluctuate randomly, as expected in many experimental arrangements.

Light Field	$\overline{\Xi(p)}$ max	$\overline{\Xi(p)}$ min	$\overline{\Xi(p)}$ ave.	$\overline{\Xi(r)}$ max	$\overline{\Xi(r)}$ min	$\overline{\Xi(r)}$ ave.
A: 3D $\pi^x\pi^y$	0.57	0	0.44	0.39	0.19	0.26
B: 3D $\sigma^+\sigma^-$	0.53	0	0.44	0.40	0.20	0.24
C: 3D $\pi^y\pi^x$	0.50	0.45	0.47	0.21	0.16	0.19
D: 3D $\sigma^+\sigma^+$	0.47	0.41	0.43	0.27	0.20	0.24

Table 5-4 Values of $\overline{\Xi(p)}$ and $\overline{\Xi(r)}$ for four 6-beam standing wave arrangements

Some qualitative deductions may be made from the data in table 5-4. The values of $\overline{\Xi(p)}$ and $\overline{\Xi(r)}$ are always less than 0.6 in the 3-D light fields studied. Comparing these values with the maximum possible value of 1 (obtained for atoms moving parallel to either $\pi^x\pi^y$ or $\sigma^+\sigma^-$ 1-D standing waves) shows that these 3-D standing waves contain lower levels of polarisation gradients. Furthermore, the phase-averaged values of $\overline{\Xi(r)}$ are generally lower than the phase-averaged values of $\overline{\Xi(p)}$. The (time-phase) averaged values of $\overline{\Xi(p)}$ and $\overline{\Xi(r)}$ show that all four light field arrangements contain roughly similar degrees of sisyphus and corkscrew polarisation gradients when the time phases are fluctuating (uncontrolled).

The time phase averaged values for the 3-D field A show that it contains a high degree of both helicity and ellipticity, despite the fact that it is built from 1-D standing waves with zero helicity and ellipticity. In fact, the maximum variance of ellipticity (0.57) over all the fields studied here is found in field A in the synchronised configuration, and not in field C (3-D sisyphus) as might be expected. This demonstrates that the polarisation gradient properties of 6-beam standing waves can be entirely different from the polarisation properties of their constituent 1-D standing waves.

Connection of the simulation with sub-Doppler cooling

The following comments describe some possible implications of the simulation for laser cooling. The parameters $\overline{\Xi(p)}$ and $\overline{\Xi(r)}$ measure only the average polarisation gradients seen by an atom, and the actual atom-light dynamical problem has not been addressed. However the parameters may in future prove useful in the development of scaling factors[115,169] which relate 3-D results (for friction coefficients and temperatures) to the 1-D results for the corresponding light field.

Examination of the polarisation topography of the 6-beam standing waves studied showed (actually by building some 3-D models) that they can all contain helices which switch handedness along a trajectory with a spatial period of $\sim\lambda/2$. These alternating helices occur along many different trajectories in the light fields studied and contribute most[6] of the value of $\overline{\Xi(r)}$ (helices which do not change handedness along a trajectory are rare in 3-D fields). Along a typical 'alternating helix' trajectory, the linear polarisation rotates through 90° in $\lambda/2$ and then reverses direction back to its original orientation from $\lambda/2$ to λ. One would expect motion-induced orientation cooling to be present in alternating helices for atoms which move less than $\lambda/2$ in the optical pumping time ($kv < 1/\tau_p \approx \Omega_0^2\Gamma/4\Delta^2$). This condition on the velocity can be of the same order as the capture velocity condition ($kv < \Omega_0^2/4\Delta$) for the corkscrew cooling mechanism, and when $\Delta \approx \Gamma$, does not represent a new constraint. Speculatively, there is also the possibility of a localisation effect on a $\lambda/2$ lattice due to motion-induced orientation. This is because the helicity varies regularly in space from zero to some maximum value with a period $\sim\lambda/2$ along many alternating-helix trajectories; this may lead to regions of zero damping alternating with high corkscrew damping.

A final comment is that $\overline{\Xi(p)}$ is also a good qualitative measure of the existence of optical potential wells in a light field. It measures the average standard deviation of ellipticity over all possible straight lines in the unit cell of the light field. It will be maximal in light fields which have a distribution throughout the unit cell of regions with differently orientated circular polarisation, i.e. containing optical potential wells. The results in table 5-4 thus

---

[6] *This was ascertained by using the computer programme to also calculate the variance of r along many trajectories through the light fields.*

imply that optical potential wells are present in each of the above four types of 6-beam standing waves for appropriate time phases[7], and that for fluctuating time phases, the wells also fluctuate. It follows that temporary localisation of atoms will occur in all the fields A to D for fluctuating time phases, provided that the time phase fluctuations are much slower than the optical pumping rate.

5.3 The physical significance of the parameters *p* and *r*

There is a pleasing symmetry between the two parameters p and r which measure ellipticity and helicity respectively. The definitions of p and r are the same apart from the fact that p involves the electric field derivative with respect to time, whereas r involves the derivatives with respect to spatial directions. This fact and the fact that p and r are each connected with a sub-Doppler cooling mechanism led me to search for a relationship between the two parameters. I found that there is a fundamental physical relationship between p and r, in that they are related respectively to the density and flux of intrinsic angular momentum (or spin) of the electromagnetic field. This relationship is explained in detail in the rest of this section 5.3. As well as being interesting in its own right, this relationship may provide new insight into sub-Doppler cooling mechanisms in general. At present however, that is a speculation which will require further work.

5.3.1 Special relativity electrodynamics

This section 5.3 makes use of the Minkowski four-dimensional representation of the electromagnetic field, as is standard in many textbooks[143, 243]. For convenience, table 5-5 here summarises the definitions used in this work. The indices i, j etc scan the four dimensions x, y, z and ict and follow the usual Einstein summation rules. A comma in the indices row indicates differentiation with respect to the following index.

Table 5-5 Symbols used for the 4-D representation of the electromagnetic field

Symbol	Physical quantity	Component form
X_i	Spacetime coordinates	$[x, y, z, ict]$
Ω_i	Electromagnetic potential	$[A_x, A_y, A_z, i\phi/c]$
J_i	4-D Current density	$[j_x, j_y, j_z, ic\rho]$
F_{ij}	The electromagnetic field tensor	$\begin{bmatrix} 0 & \mu_0 H_z & -\mu_0 H_y & -iE_x/c \\ -\mu_0 H_z & 0 & \mu_0 H_x & -iE_y/c \\ \mu_0 H_y & -\mu_0 H_x & 0 & -iE_z/c \\ iE_x/c & iE_y/c & iE_z/c & 0 \end{bmatrix}$

[7] *Localisation of atoms in a 2-D $\sigma^+\sigma^-\sigma^+\sigma^-$ light field has been experimentally demonstrated[77].*

S_{ij}

The electromagnetic energy-momentum tensor

$U - \mu_0 H_x^2 - \varepsilon_0 E_x^2$	$-\mu_0 H_x H_y - \varepsilon_0 E_x E_y$	$-\mu_0 H_x H_z - \varepsilon_0 E_x E_z$	$-S_x/ic$
Symmetric	$U - \mu_0 H_y^2 - \varepsilon_0 E_y^2$	$-\mu_0 H_y H_z - \varepsilon_0 E_y E_z$	$-S_y/ic$
Symmetric	Symmetric	$U - \mu_0 H_z^2 - \varepsilon_0 E_z^2$	$-S_z/ic$
Symmetric	Symmetric	Symmetric	U

5.3.2 Intrinsic angular momentum in the electromagnetic field

Many textbooks on classical electrodynamics, e.g.[143], include a section on special relativity electrodynamics, and usually develop the theory as far as deriving the 4-D electromagnetic energy momentum tensor S_{ij} for fields in a vacuum (Table 5-4). The dual interpretation of the Poynting vector **S** (=**E** x **H**), as both the flow of field energy and the density of electromagnetic momentum is usually included and the continuity equations for energy and momentum are usually given. These are

$$\nabla_j S_j + \frac{\partial U}{\partial t} = 0$$
$$\nabla_j T_{ij} - \frac{1}{c^2}\frac{\partial S_i}{\partial t} = 0 \qquad (5\text{-}27)$$

where U is the field energy density (= $\frac{1}{2}\varepsilon_0 E^2 + \frac{1}{2}\mu_0 H^2$), S_i the Poynting vector and T_{ij} is Maxwell's stress tensor.

A further result[243] concerns the angular momentum of the field. For localised fields in a charge free region the density of intrinsic angular momentum $\mathbf{L}_I$, or spin density, of the field is given by the classical expression:

$$\mathbf{L}_I = \varepsilon_0 \mathbf{E} \times \mathbf{A} \qquad (5\text{-}28)$$

Here **A** is the vector potential of the field and the symbols $\mathbf{L}_I$ and $\mathbf{L}_O$ will be used to distinguish the intrinsic and orbital aspects of the total angular momentum. An outline proof of equation 5-28 is given in Appendix A6.

5.3.3 Relationship between spin density and ellipticity *p*

To find a relationship between the spin density and the ellipticity p, consider an arbitrary monochromatic field for which $\mathbf{A} = \mathbf{A}_0(\mathbf{r})e^{-i\omega t}$. Then it follows that

$$\frac{\partial^2 \mathbf{A}}{\partial t^2} = -\omega^2 \mathbf{A} \qquad (5\text{-}29)$$

For fields in charge-free space $\mathbf{E} = -\frac{\partial \mathbf{A}}{\partial t}$ and hence $\frac{\partial \mathbf{E}}{\partial t} = -\frac{\partial^2 \mathbf{A}}{\partial t^2}$. Substitution into equation 5-29 gives $\mathbf{A} = \frac{1}{\omega^2}\frac{\partial \mathbf{E}}{\partial t}$ and substitution of **A** in equation 5-28 gives

$$\mathbf{L}_I = \frac{\varepsilon_0}{\omega^2}\left(\mathbf{E} \times \frac{\partial \mathbf{E}}{\partial t}\right) \tag{5-30}$$

Finally, comparison of equations 5-30 and 5-22 (page 102) shows that

$$p = \frac{2\omega}{\varepsilon_0}\hat{\mathbf{n}} \cdot \mathbf{L}_I \tag{5-31}$$

Thus the ellipticity parameter p is, apart from a constant factor, measuring the projection of the field's spin density onto the chosen axis $\hat{\mathbf{n}}$. Though this is not entirely surprising, it is nevertheless gratifying to know that a geometric feature of the field, namely a sisyphus polarisation gradient, is directly related to a physical feature, namely the spin density of the electromagnetic field.

5.3.4 Physical meaning of the helicity parameter *r*

Having been successful in attributing physical significance to the ellipticity parameter p in equation 5-31, and mindful of the space-time symmetry of p with r, the helicity parameter, it seemed reasonable to examine the physical significance, if any, attached to r. Examination of the values of r which I had calculated for travelling waves and for the four basic 1-D standing waves suggested that r was associated with a flow of intrinsic angular momentum. The time average of r is non-zero in two of these cases: for a circularly polarised travelling wave, and for a 1-D $\sigma^+\sigma^-$ standing wave, and the signs and magnitudes are consistent with the interpretation that r measures the flux of spin (per unit area per unit time) in the field. Hence I carefully investigated the hypothesis that r as defined by equation 5-23 is proportional to the flux of spin in an arbitrary direction $\hat{\mathbf{n}}$. I found that the hypothesis is almost the whole truth. In fact the cycle average of r is proportional to the cycle averaged spin flux, but r is $\pi/2$ out of phase with the spin flux[8]. The detailed method leading to proof of this assertion is now described below.

The 4-D generalisation of angular momentum for the electromagnetic field[243] is a rank 3 tensor M_{ijk}, given by

$$M_{ijk} = S_{ij}X_k - S_{ik}X_j \tag{5-32}$$

where S_{ij} is the Belinfante-Rosenfeld[246] symmetric energy momentum tensor given in table 5-5. The tensor M_{ijk} has 24 independent terms of which three (M_{432}, M_{413}, M_{421}) are the conventional 3-D angular momentum (multiplied by ic), nine are the tensor components of angular momentum flow, and the other twelve are related to the centre of mass motion of the field. There are six independent continuity equations derivable from the tensor M_{ijk} and each is associated with a conserved quantity. They are

$$M_{ijk,i} = 0 \quad \text{for } jk = 32,13,21,14,24,34.$$

Thus in the case $jk = 21$, we have

---

[8] *The resolution of this slightly annoying phase shift is described in section 5.4, point v) on page 119.*

$$\frac{\partial M_{121}}{\partial x}+\frac{\partial M_{221}}{\partial y}+\frac{\partial M_{321}}{\partial z}+\frac{\partial M_{421}}{\partial(ict)}=0$$

which is the continuity equation for the $\hat{\mathbf{z}}$ component of angular momentum l_z. M_{421}/ic is the z component of angular momentum density and M_{121}, M_{221}, M_{321} are the flow of l_z in the x, y and z directions respectively.

In Appendix 6, as part of the derivation of equation 5-28, it is shown that the total (linear) momentum density $\mathbf{g}$ of an electromagnetic field can be divided into two parts $\mathbf{g}_1$ and $\mathbf{g}_2$ (where $\mathbf{g} = \mathbf{g}_1 + \mathbf{g}_2$) such that $\mathbf{r} \times \mathbf{g}_1$ and $\mathbf{r} \times \mathbf{g}_2$ correspond to the density of orbital and intrinsic angular momentum respectively. Here $\mathbf{g} = \mathbf{S} / c^2$, where $\mathbf{S}$ is the Poynting vector. In the light of the fact that $\mathbf{g}$ is just three of the components of the tensor S_{ij}, it seems desirable to generalise this splitting to all the ten independent components of S_{ij}. That generalised splitting might then lead, via equation 5-32, to a splitting of M_{ijk} into orbital and intrinsic parts. Such problems belong to the physics area of general relativistic field theories and there is a systematic technique for making such a splitting, involving the variational principle applied to an appropriate field Lagrangian[244]. The non-trivial question of finding the appropriate Lagrangian is addressed in [245] and leads into deeper theory than is necessary for this work (I required the solution only for the particular case of a monochromatic electromagnetic field). The important point is that in order to be a meaningful splitting, it must be covariant, i.e. a splitting agreed by all inertial observers. The physical test of a covariant splitting is that the two resulting parts, the intrinsic energy-momentum and the orbital energy-momentum, must be separately conserved. In mathematical terms, therefore, the two parts must each obey a continuity equation. Guided by these principles and by references [244,245], I devised my own splitting method, described as follows.

Splitting the energy-momentum tensor into intrinsic and orbital parts

The energy-momentum tensor S_{ij} can be split into intrinsic and orbital parts as follows. We require

i) the definition of the energy-momentum tensor

$$\mu_0 S_{ij} = F_{ik}F_{jk} - \tfrac{1}{4}\delta_{ij}F_{kl}F_{kl} \tag{5-33}$$

ii) Maxwell's equations for a charge free region

$$F_{ij} = \Omega_{j,i} - \Omega_{i,j}$$
$$\Omega_{k,jj} = 0 \tag{5-34}$$

iii) The Lorentz gauge condition

$$\Omega_{j,j} = 0 \tag{5-35}$$

Here, Ω_i is the 4-D field potential. $\Omega_i = (\mathbf{A}, ic\phi)$, where $\mathbf{A}$ is the vector potential and ϕ is the electric potential, which is zero in a charge free region. Substitution of 5-34 into 5-33 gives

$$\mu_0 S_{ij} = \left(\Omega_{k,i} - \Omega_{i,k}\right)\left(\Omega_{k,j} - \Omega_{j,k}\right) - \tfrac{1}{4}\delta_{ij}\left(\Omega_{l,k} - \Omega_{k,l}\right)\left(\Omega_{l,k} - \Omega_{k,l}\right)$$

Expanding the brackets, using $\Omega_{l,k}\Omega_{l,k} = \Omega_{k,l}\Omega_{k,l}$ and grouping the remaining terms as follows gives

$$\mu_0 S_{ij} = \underbrace{\left[\Omega_{k,i}\Omega_{k,j} - \tfrac{1}{2}\delta_{ij}\Omega_{l,k}\Omega_{l,k}\right]}_{\text{Orbital}} + \underbrace{\left[\Omega_{i,k}\Omega_{j,k} - \Omega_{k,i}\Omega_{j,k} - \Omega_{i,k}\Omega_{k,j} + \tfrac{1}{2}\delta_{ij}\Omega_{l,k}\Omega_{k,l}\right]}_{\text{Intrinsic}} \quad (5\text{-}36)$$

Denoting the two parts by $S_{ij} = S^{\mathrm{O}}_{ij} + S^{\mathrm{I}}_{ij}$, it may be shown that each of these parts separately has zero divergence: $S^{\mathrm{O}}_{ij,j} = 0$ and $S^{\mathrm{I}}_{ij,j} = 0$. This means that the orbital and intrinsic 4-D momenta are separately conserved quantities and therefore equation 5-36 is a covariant splitting. Note that both S^{O}_{ij} and S^{I}_{ij} are symmetric tensors.

This splitting established, equation 5-32 may be used to split M_{ijk} into two rank 3 angular momentum tensors, corresponding to orbital angular momentum M^{O}_{ijk} and intrinsic spin M^{I}_{ijk}, as will be proved shortly.

$$\begin{aligned} M^{\mathrm{O}}_{ijk} &= S^{\mathrm{O}}_{ij}X_k - S^{\mathrm{O}}_{ik}X_j \\ M^{\mathrm{I}}_{ijk} &= S^{\mathrm{I}}_{ij}X_k - S^{\mathrm{I}}_{ik}X_j \end{aligned} \quad (5\text{-}37)$$

It follows from the fact that S^{O}_{ij} and S^{I}_{ij} are symmetric tensors that both the tensors M^{O}_{ijk} and M^{I}_{ijk} have zero divergence with respect to X_i, and thus orbital angular momentum and spin are separately conserved quantities (for fields in a charge free region). Hence this splitting of M_{ijk} is also covariant. The proof is as follows. Taking M^{I}_{ijk} as an example, its divergence is obtained directly from its definition in equation 5-37.

$$M^{\mathrm{I}}_{ijk,i} = S^{\mathrm{I}}_{ij,i}X_k + S^{\mathrm{I}}_{kj} - S^{\mathrm{I}}_{ik,i}X_j - S^{\mathrm{I}}_{jk}$$

But the divergence of S^{I}_{ij} is zero: $S^{\mathrm{I}}_{ij,i} = S^{\mathrm{I}}_{ik,i} = 0$, and as S^{I}_{ij} is symmetric, $S^{\mathrm{I}}_{kj} = S^{\mathrm{I}}_{jk}$. Hence

$$M^{\mathrm{I}}_{ijk,i} = 0 \quad (5\text{-}38)$$

Equation 5-38 is the differential form of the continuity equation for the intrinsic angular momentum of an electromagnetic field in a charge free region. Applying the 4-D version of Gauss's theorem to 5-38 gives the integral form of the continuity equation $\iiint M^{\mathrm{I}}_{ijk}\,d\sigma_i = 0$ where the $d\sigma_i$ are 3-D hypersurfaces orthogonal to x, y, z and t, and which enclose a closed region of 4-D space-time. The continuity equation also takes the more familiar form

$$\iint_{\text{surface}} M^{\mathrm{I}}_{vjk}\,dydz + \iint_{\text{surface}} M^{\mathrm{I}}_{vjk}\,dxdz + \iint_{\text{surface}} M^{\mathrm{I}}_{zjk}\,dxdy + \frac{1}{ic}\iiint_{\text{volume}} \frac{\partial M^{\mathrm{I}}_{tjk}}{\partial t}\,dxdydz = 0 \quad (5\text{-}39)$$

It remains to prove that M^{I}_{ijk} does in fact correspond to the 4-D intrinsic angular momentum of the field, by showing that it can be recast in a form which is independent of the origin of the coordinate system. An outline of the proof is as follows. Each component of M^{I}_{ijk} can be rewritten in terms of the vector potential Ω_i, and then integrated by parts over a closed region of 4-D spacetime. The field is assumed to be localised, i.e. falls rapidly to zero at the boundaries of the closed 4-D region. For each of the components, one finds that after the integration by parts, most of the resulting terms either cancel each other via $\Omega_{i,i} = 0$ and $\Omega_{i,jj} = 0$, or are zero because they are evaluated on the boundaries where the field is zero.

The remaining uncancelled terms form the components of a tensor M^{Λ}_{ijk} whose elements are not dependent on **r**. i.e. are independent of the choice of origin.

$$M^{\Lambda}_{ijk} = \frac{1}{\mu_0}\left(\Omega_j \Omega_{k,i} - \Omega_k \Omega_{j,i}\right) \quad \text{with } \Omega_4 = 0 \text{ (charge-free region)} \tag{5-40}$$

Furthermore, the elements of M^{Λ}_{ijk} satisfy the continuity equations

$$M^{\Lambda}_{ijk,i} = 0 \quad \text{or} \quad \frac{\partial M^{\Lambda}_{1jk}}{\partial x} + \frac{\partial M^{\Lambda}_{2jk}}{\partial y} + \frac{\partial M^{\Lambda}_{3jk}}{\partial z} + \frac{\partial M^{\Lambda}_{4jk}}{ic\partial t} = 0 \tag{5-41}$$

thus confirming that the components correspond to conserved quantities. The facts that the tensor has been shown to represent an angular momentum which is both independent of the coordinate origin and conserved prove that it corresponds to the intrinsic angular momentum of the field. The elements of this '**spin tensor**' M^{Λ}_{ijk} (multiplied by μ_0) are given in full in table 5-6 below. The components of the spin density, which were given earlier as $\mathbf{L}_1 = \varepsilon_0 \mathbf{E} \times \mathbf{A}$ (equation 5-28) appear in the layer M^{Λ}_{4jk} of M^{Λ}_{ijk}. Thus that earlier result, proved within a 3-D formalism in appendix 6. is incorporated within this 4-D result.

Table 5-6 The components of the spin tensor $\mu_0 M^{\Lambda}_{ijk}$ (a-s signifies anti-symmetric)

111			
0	$A_x \frac{\partial A_y}{\partial x} - A_y \frac{\partial A_x}{\partial x}$	$A_x \frac{\partial A_z}{\partial x} - A_z \frac{\partial A_x}{\partial x}$	0
121			
a-s	0	$A_y \frac{\partial A_z}{\partial x} - A_z \frac{\partial A_y}{\partial x}$	0
a-s	a-s	0	0
0	0	0	0

211			
0	$A_x \frac{\partial A_y}{\partial y} - A_y \frac{\partial A_x}{\partial y}$	$A_x \frac{\partial A_z}{\partial y} - A_z \frac{\partial A_x}{\partial y}$	0
221			
a-s	0	$A_y \frac{\partial A_z}{\partial y} - A_z \frac{\partial A_y}{\partial y}$	0
a-s	a-s	0	0
0	0	0	0

311			
0	$A_x \frac{\partial A_y}{\partial z} - A_y \frac{\partial A_x}{\partial z}$	$A_x \frac{\partial A_z}{\partial z} - A_z \frac{\partial A_x}{\partial z}$	0
321			
a-s	0	$A_y \frac{\partial A_z}{\partial z} - A_z \frac{\partial A_y}{\partial z}$	0
a-s	a-s	0	0
0	0	0	0

411			
0	$\frac{A_x}{ic}\frac{\partial A_y}{\partial t} - \frac{A_y}{ic}\frac{\partial A_x}{\partial t}$	$\frac{A_x}{ic}\frac{\partial A_z}{\partial t} - \frac{A_z}{ic}\frac{\partial A_x}{\partial t}$	0
421			
a-s	0	$\frac{A_y}{ic}\frac{\partial A_z}{\partial t} - \frac{A_z}{ic}\frac{\partial A_y}{\partial t}$	0
a-s	a-s	0	0
0	0	0	0

The first three large squares correspond to the spin flux parallel to the x, y and z directions respectively, and the fourth square contains the components of the spin density. The specific components of the spin are addressed by the last two indices according to the following cyclic rule: $*21 \rightarrow z$, $*32 \rightarrow x$, $*13 \rightarrow y$ $\quad$ $*12 \rightarrow -z$, $*23 \rightarrow -x$, $*31 \rightarrow -y$. Thus as examples, M^{A}_{321} gives the flux of the z component of spin in the z direction, M^{A}_{113} gives the flux of the y component of spin in the x direction and M^{A}_{432} gives the density of the x component of the spin.

I have calculated some of the terms of $\langle M^{A}_{ijk} \rangle$ for travelling waves, 1-D standing waves, and four types of 6-beam standing waves, and tabulated them in section 5.5.

The relationship between spin flux and helicity *r*

The spin tensor M^{A}_{ijk} and the helicity parameter r (equation 5-23) are very closely related as is now explained. The flux of the spin component parallel to an arbitrary vector $\hat{\mathbf{n}}$ through a surface normal to $\hat{\mathbf{n}}$ may be calculated from M^{A}_{ijk} and is given by the scalar f_s:

$$f_s = \tfrac{1}{2} n_i n_l M^{A}_{ijk} \epsilon_{lkj} \qquad (5\text{-}42)$$

where ϵ_{lkj} is the alternating tensor. When written out in component form, this is almost identical to the helicity parameter r in its expanded form (equation 5-25). One trivial difference is that of a constant multiplier $(2\omega/\varepsilon_0 c)$; the main difference is that the spin flux f_s involves the vector potential **A**, whereas the helicity parameter r involves the electric field **E**.

However, by using the relation $\mathbf{E} = -\dfrac{\partial \mathbf{A}}{\partial t}$, it can be shown that, in the case of monochromatic fields, the spin flux f_s is related to r by a constant factor and a time phase shift of $\pi/2$. The time averaged $\langle\ \rangle$ versions are identical apart from the constant factor.

$$r(t) = \frac{2\omega}{\varepsilon_0 c} f_s(t + \pi/2\omega) \qquad \langle r \rangle = \frac{2\omega}{\varepsilon_0 c} \langle f_s \rangle \qquad (5\text{-}43)$$

Thus the 'corkscrewness' of a field along an arbitrary axis has been shown to be physically meaningful: the helicity parameter with respect to an arbitrary axis measures, to a multiplicative constant, the flow of the component of spin parallel to that axis along that same axis.

5.4 Conclusion to chapter 5

This chapter has discussed the polarisation properties of monochromatic standing waves, particularly 6-beam standing waves, and developed some techniques for studying those properties. There are many other possible 3-D standing waves which were not considered, for instance those using beams intersecting at angles other than 90°, or those using different polarisation schemes. It is likely that as the field of atomic optics develops further, other schemes will be invented, possibly with asymmetric properties which are experimentally useful. The techniques developed in this chapter may be useful in understanding the polarisation structure of such fields. The main results of this work are

i) Of the many possible topographies created by changing the relative time phases of a 6-beam standing wave, two are of particular importance because they produce 'polar-opposite' topographies. I called them the 'synchronised' and 'three-phase' time phase configurations, and their mathematical basis was demonstrated.

ii) Two parameters p and r were developed which measure **ellipticity** and **helicity**, which are geometric aspects of an electromagnetic field and which are associated with the polarisation gradients corresponding to sisyphus and corkscrew cooling. The parameters can be applied to polychromatic fields.

iii) The parameters p and r were used in a numerical simulation to quantify polarisation gradients in various 6-beam standing waves with variable time phases, allowing quantitative comparison of different field configurations. The simulations can provide qualitative insight into the effects of time phases on sub-Doppler cooling, and may lead to 3-D light field configurations of particular interest, such as the 'hybrid' 1-D field of section 5.2.1. The simulations can easily be extended to study other light fields used in experiments, such as tetrahedral arrangements[83,84], special fields[82] or fields due to misaligned beams[162].

iv) For monochromatic fields, the parameters for ellipticity p and helicity r were shown to be proportional to the density and flux of intrinsic electromagnetic field angular momentum respectively, thus showing that the geometric aspects of the field polarisation have fundamental significance.

v) An explicit expression for the 4-D spin tensor of a localised electromagnetic field was obtained, which is valid for polychromatic light fields. With hindsight, the spin tensor could be used as a superior, more general basis for studying polarisation gradients. Adapted versions of the ellipticity and helicity parameters may be constructed, based on the gradients of the electromagnetic vector potential **A** rather than the electric field **E**, such that the adapted versions are directly proportional to the density and flux of spin for polychromatic light fields (as opposed to being $\pi/2$ out of phase).

vi) Further work is necessary to determine whether the parameters $\overline{\Xi(p)}$ and $\overline{\Xi(r)}$ are useful as regards calculations of scaling factors[115,169] relating 3-D cooling parameters such as temperature and friction and diffusion coefficients to their corresponding 1-D values.

5.5 Results of electromagnetic field calculations

This section is a compendium containing various electromagnetic field quantities calculated for a few important field configurations. The quantities calculated are listed in table 5-7 below. Subsection 5.5.1 covers travelling waves, and therefore includes a linearly polarised wave and a circularly polarised wave. Subsection 5.5.2 covers the four basic 1-D standing waves. Subsection 5.5.3 gives calculations for four 6-beam standing waves including the two common experimental arrangements of the MOT and 3-D sisyphus molasses. Each of

these 6-beam standing waves is based on one of the 'archetypal' 1-D standing waves ($\pi^x\pi^x$, $\pi^y\pi^y$, $\sigma^+\sigma^+$, $\sigma^+\sigma^-$).

Symbol	Quantity
E	electric field
H	magnetic field
A	vector potential
U_E and $\langle U_E \rangle$	electric field energy density and its time-average
U_M and $\langle U_M \rangle$	magnetic field energy density and its time average
U and $\langle U \rangle$	total field energy density (or 'intensity') and its time average
S and $\langle \mathbf{S} \rangle$	Poynting's vector and its time-average
$\mathbf{L}_I$	electromagnetic spin density
$\langle M^A_{3jk} \rangle$	electromagnetic spin flux (cycle-averaged)

Table 5-7 A list of the electromagnetic field quantities calculated for light fields in section 5.5

Notes

i) There are 9 independent spin flux elements in the spin tensor M^A_{ijk}, however cycle-averages of only the three terms M^A_{3jk} (i.e. with $i = \hat{\mathbf{z}}$) are calculated, as the remaining six are cyclic. The given terms are $\langle M^A_{321} \rangle$, the flux of the z component of spin in the $\hat{\mathbf{z}}$ direction; $\langle M^A_{332} \rangle$, the flux of the x component of spin in the $\hat{\mathbf{z}}$ direction; and $\langle M^A_{113} \rangle$, the flux of the y component of spin in the $\hat{\mathbf{z}}$ direction. As an example of 'cycling', to find (say) the flux of the y component of spin in the $\hat{\mathbf{x}}$ direction, one must cycle $\langle M^A_{332} \rangle \rightarrow \langle M^A_{113} \rangle$. Thus one looks up $\langle M^A_{332} \rangle$ in section 5.5.3 and cycles $x \rightarrow y \rightarrow z \rightarrow x$ and $\theta \rightarrow \phi \rightarrow \psi \rightarrow \theta$ in the given trignometric expression to obtain $\langle M^A_{113} \rangle$.

ii) The **ellipticity** parameter p along $\hat{\mathbf{n}}$, can be obtained from the spin density $\mathbf{L}_I$ by using

$$p = \frac{2\omega}{\varepsilon_0} \hat{\mathbf{n}} \cdot \mathbf{L}_I \tag{5-31}$$

iii) The **helicity** parameter r along $\hat{\mathbf{n}}$, can be obtained from the spin flux tensor M^A_{ijk} by using equations 5-43. The cycle averaged version is

$$\langle r \rangle = \frac{2\omega}{\varepsilon_0 c} \langle f_s \rangle \tag{5-43}$$

where f_s is given by equation 5-42. In the case when $\hat{\mathbf{n}} = \hat{\mathbf{z}}$, this simplifies to

$$\langle r_z \rangle = \frac{2\omega}{\varepsilon_0 c} \langle M^A_{321} \rangle \tag{5-44}$$

5.5.1 Electromagnetic properties of travelling waves

Linearly polarised travelling wave	R.H. Circularly polarised standing wave
$\mathbf{E} = \hat{\mathbf{x}} E_0 \cos(kz - \omega t)$	$\mathbf{E} = \frac{1}{\sqrt{2}} E_0 \left[\hat{\mathbf{x}} \cos(kz - \omega t) + \hat{\mathbf{y}} \sin(kz - \omega t)\right]$
$\mathbf{H} = \hat{\mathbf{y}} H_0 \cos(kz - \omega t)$	$\mathbf{H} = \frac{1}{\sqrt{2}} H_0 \left[-\hat{\mathbf{x}} \sin(kz - \omega t) + \hat{\mathbf{y}} \cos(kz - \omega t)\right]$
$\mathbf{A} = -\hat{\mathbf{x}} \frac{E_0}{\omega} \sin(kz - \omega t)$	$\mathbf{A} = \frac{E_0}{\sqrt{2}\omega} \left[\hat{\mathbf{x}} \sin(kz - \omega t) - \hat{\mathbf{y}} \cos(kz - \omega t)\right]$
$\mathbf{S} = \hat{\mathbf{z}} \varepsilon_0 c E_0^2 \cos^2(kz - \omega t)$	$\mathbf{S} = \hat{\mathbf{z}} \frac{1}{2} \varepsilon_0 c E_0^2$
$\langle \mathbf{S} \rangle = \hat{\mathbf{z}} \frac{1}{2} \varepsilon_0 c E_0^2$	
$U_E = \frac{1}{2} \varepsilon_0 E_0^2 \cos^2(kz - \omega t)$	$U_E = \frac{1}{4} \varepsilon_0 E_0^2$
$\langle U_E \rangle = \frac{1}{4} \varepsilon_0 E_0^2$	
$U_M = \frac{1}{2} \varepsilon_0 E_0^2 \cos^2(kz - \omega t)$	$U_M = \frac{1}{4} \varepsilon_0 E_0^2$
$\langle U_M \rangle = \frac{1}{4} \varepsilon_0 E_0^2$	
$U = \varepsilon_0 E_0^2 \cos^2(kz - \omega t)$	$U = \frac{1}{2} \varepsilon_0 E_0^2$
$\langle U \rangle = \frac{1}{2} \varepsilon_0 E_0^2$	
$\mathbf{L}_I = \mathbf{0}$	$\mathbf{L}_I = -\hat{\mathbf{z}} \frac{\varepsilon_0 E_0^2}{2\omega}$
$M^A_{321} = 0$	$M^A_{321} = -\frac{\varepsilon_0 E_0^2}{2k}$

5.5.2 Electromagnetic properties of 1-D standing waves

i) prototype $\pi^x \pi^x$ 1-D standing wave

$$\mathbf{E} = \hat{\mathbf{x}} E_0 \left[\cos(kz - \omega t) + \cos(kz + \omega t)\right] = \hat{\mathbf{x}} 2E_0 \cos kz \cos \omega t$$

$$\mathbf{H} = \hat{\mathbf{y}} H_0 \left[\cos(kz - \omega t) - \cos(kz + \omega t)\right] = \hat{\mathbf{y}} 2H_0 \sin kz \sin \omega t$$

$$\mathbf{A} = \hat{\mathbf{x}} \frac{E_0}{\omega} \left[\sin(kz - \omega t) - \sin(kz + \omega t)\right] = -\hat{\mathbf{x}} \frac{2E_0}{\omega} \cos kz \sin \omega t$$

$$\mathbf{S} = \hat{\mathbf{z}} \varepsilon_0 c E_0^2 \sin 2kz \sin 2\omega t \qquad \langle \mathbf{S} \rangle = \mathbf{0}$$

$$U_E = 2\varepsilon_0 E_0^2 \cos^2 kz \cos^2 \omega t \qquad \langle U_E \rangle = \varepsilon_0 E_0^2 \cos^2 kz$$

$$U_M = 2\mu_0 H_0^2 \sin^2 kz \sin^2 \omega t \qquad \langle U_M \rangle = \mu_0 H_0^2 \sin^2 kz$$

$$U = \varepsilon_0 E_0^2 (1 + \cos 2kz \cos 2\omega t) \qquad \langle U \rangle = \varepsilon_0 E_0^2$$

$$\mathbf{L}_I = \mathbf{0}$$

$$M^A_{321} = 0$$

---

ii) prototype $\pi^y \pi^x$ 1-D standing wave

$$\mathbf{E} = E_0 \left[\hat{\mathbf{y}} \cos(kz - \omega t) + \hat{\mathbf{x}} \cos(kz + \omega t)\right]$$

$$\mathbf{H} = H_0 \left[-\hat{\mathbf{x}} \cos(kz - \omega t) - \hat{\mathbf{y}} \cos(kz + \omega t)\right]$$

$$\mathbf{A} = \frac{E_0}{\omega} \left[\hat{\mathbf{y}} \sin(kz - \omega t) - \hat{\mathbf{x}} \sin(kz + \omega t)\right]$$

$$\mathbf{S} = \hat{\mathbf{z}} \varepsilon_0 c E_0^2 \sin 2kz \sin 2\omega t \qquad \langle \mathbf{S} \rangle = \mathbf{0}$$

$$U_{\mathrm{E}} = \tfrac{1}{2}\varepsilon_0 E_0{}^2(1+\cos 2kz\cos 2\omega t) \qquad \langle U_E\rangle = \tfrac{1}{2}\varepsilon_0 E_0{}^2$$

$$U_{\mathrm{M}} = \tfrac{1}{2}\mu_0 H_0{}^2(1+\cos 2kz\cos 2\omega t) \qquad \langle U_M\rangle = \tfrac{1}{2}\mu_0 H_0{}^2$$

$$U = \varepsilon_0 E_0{}^2(1+\cos 2kz\cos 2\omega t) \qquad \langle U\rangle = \varepsilon_0 E_0{}^2$$

$$\mathbf{L}_{\mathrm{I}} = \hat{\mathbf{z}}\frac{\varepsilon_0 E_0{}^2}{\omega}\sin 2kz$$

$$M^{\mathrm{A}}_{321} = \frac{\varepsilon_0 E_0{}^2}{k}\sin 2\omega t$$

---

iii) $\sigma^+\sigma^+$ 1-D standing wave

$$\mathbf{E} = \tfrac{1}{\sqrt{2}}E_0\left[\hat{\mathbf{x}}\cos(kz-\omega t)-\hat{\mathbf{y}}\sin(kz-\omega t)+\hat{\mathbf{x}}\cos(kz+\omega t)+\hat{\mathbf{y}}\sin(kz+\omega t)\right]$$

$$= \sqrt{2}E_0\cos kz(\hat{\mathbf{x}}\cos\omega t+\hat{\mathbf{y}}\sin\omega t)$$

$$\mathbf{H} = \tfrac{1}{\sqrt{2}}H_0\left[\hat{\mathbf{x}}\sin(kz-\omega t)+\hat{\mathbf{y}}\cos(kz-\omega t)+\hat{\mathbf{x}}\sin(kz+\omega t)-\hat{\mathbf{y}}\cos(kz+\omega t)\right]$$

$$= \sqrt{2}H_0\sin kz(\hat{\mathbf{x}}\cos\omega t+\hat{\mathbf{y}}\sin\omega t)$$

$$\mathbf{A} = \tfrac{1}{\sqrt{2}\omega}E_0\left[\hat{\mathbf{x}}\sin(kz-\omega t)+\hat{\mathbf{y}}\cos(kz-\omega t)-\hat{\mathbf{x}}\sin(kz+\omega t)+\hat{\mathbf{y}}\cos(kz+\omega t)\right]$$

$$= \frac{\sqrt{2}E_0}{\omega}\cos kz(-\hat{\mathbf{x}}\sin\omega t+\hat{\mathbf{y}}\cos\omega t)$$

$$\mathbf{S} = \mathbf{0}$$

$$U_{\mathrm{E}} = \varepsilon_0 E_0{}^2\cos^2 kz$$

$$U_{\mathrm{M}} = \varepsilon_0 E_0{}^2\sin^2 kz$$

$$U = \varepsilon_0 E_0{}^2$$

$$\mathbf{L}_{\mathrm{I}} = \hat{\mathbf{z}}\frac{2\varepsilon_0 E_0{}^2}{\omega}\cos^2 kz$$

$$M^{\mathrm{A}}_{321} = 0$$

---

iv) $\sigma^+\sigma^-$ 1-D standing wave

$$\mathbf{E} = \tfrac{1}{\sqrt{2}}E_0\left[\hat{\mathbf{x}}\cos(kz-\omega t)-\hat{\mathbf{y}}\sin(kz-\omega t)+\hat{\mathbf{x}}\cos(kz+\omega t)-\hat{\mathbf{y}}\sin(kz+\omega t)\right]$$

$$= \sqrt{2}E_0\cos\omega t(\hat{\mathbf{x}}\cos kz-\hat{\mathbf{y}}\sin kz)$$

$$\mathbf{H} = \tfrac{1}{\sqrt{2}}H_0\left[\hat{\mathbf{x}}\sin(kz-\omega t)+\hat{\mathbf{y}}\cos(kz-\omega t)-\hat{\mathbf{x}}\sin(kz+\omega t)-\hat{\mathbf{y}}\cos(kz+\omega t)\right]$$

$$= \sqrt{2}H_0\sin\omega t(-\hat{\mathbf{x}}\cos kz+\hat{\mathbf{y}}\sin kz)$$

$$\mathbf{A} = \tfrac{1}{\sqrt{2}\omega}E_0\left[\hat{\mathbf{x}}\sin(kz-\omega t)+\hat{\mathbf{y}}\cos(kz-\omega t)-\hat{\mathbf{x}}\sin(kz+\omega t)+\hat{\mathbf{y}}\cos(kz+\omega t)\right]$$

$$= \frac{\sqrt{2}E_0}{\omega}\cos kz(-\hat{\mathbf{x}}\sin\omega t+\hat{\mathbf{y}}\cos\omega t)$$

$$\mathbf{S} = \mathbf{0}$$

$$U_{\mathrm{E}} = \varepsilon_0 E_0{}^2\cos^2\omega t \qquad \langle U_{\mathrm{E}}\rangle = \tfrac{1}{2}\varepsilon_0 E_0{}^2$$

$$U_{\mathrm{M}} = \varepsilon_0 E_0{}^2\sin^2\omega t \qquad \langle U_{\mathrm{M}}\rangle = \tfrac{1}{2}\varepsilon_0 E_0{}^2$$

$$U = \varepsilon_0 E_0{}^2$$

$$\mathbf{L}_{\mathrm{I}} = 0$$

$$M_{321}^{A} = \frac{2\varepsilon_0 E_0^{\,2}}{k}\sin^2\omega t$$

5.5.3 Electromagnetic properties of selected 6-beam standing waves

i) Parallel linear $\pi^y\pi^y\pi^z\pi^z\pi^x\pi^x$ 6-beam standing wave

$$\mathbf{E} = E_0\hat{\mathbf{y}}[\cos(kx-\omega t-\theta)+\cos(kx+\omega t+\theta)] \;+\; \text{cycle}$$

$$= 2E_0\hat{\mathbf{y}}\cos kx\cos(\omega t+\theta) \;+\; \text{cycle}$$

$$\mathbf{H} = H_0\hat{\mathbf{z}}[\cos(kx-\omega t-\theta)-\cos(kx+\omega t+\theta)] \;+\; \text{cycle}$$

$$= 2H_0\hat{\mathbf{z}}\sin kx\sin(\omega t+\theta) \;+\; \text{cycle}$$

$$\mathbf{A} = \frac{E_0}{\omega}\hat{\mathbf{y}}[\sin(kx-\omega t-\theta)-\sin(kx+\omega t+\theta)] \;+\; \text{cycle}$$

$$= -\frac{2E_0}{\omega}\hat{\mathbf{y}}\cos kx\sin(\omega t+\theta) \;+\; \text{cycle}$$

$$\langle\mathbf{S}\rangle = 2E_0H_0\hat{\mathbf{x}}\cos ky\sin kz\sin(\phi-\psi) \;+\; \text{cycle}$$

$$\langle U_{\mathrm{E}}\rangle = \varepsilon_0E_0^{\,2}\left(\cos^2 kx+\cos^2 ky+\cos^2 kz\right)$$

$$\langle U_{\mathrm{M}}\rangle = \varepsilon_0E_0^{\,2}\left(\sin^2 kx+\sin^2 ky+\sin^2 kz\right)$$

$$\langle U\rangle = 3\varepsilon_0E_0^{\,2}$$

$$\mathbf{L}_{\mathrm{I}} = \frac{4\varepsilon_0E_0^{\,2}}{\omega}\hat{\mathbf{x}}\cos kx\cos ky\sin(\theta-\phi) \;+\; \text{cycle}$$

$$\left\langle M_{321}^{A}\right\rangle = -\frac{2\varepsilon_0E_0^{\,2}}{k}\cos kx\sin kz\cos(\psi-\theta)$$

$$\left\langle M_{332}^{A}\right\rangle = 0 \qquad\qquad +\text{cycle}$$

$$\left\langle M_{313}^{A}\right\rangle = +\frac{2\varepsilon_0E_0^{\,2}}{k}\cos ky\sin kz\cos(\phi-\psi)$$

---

ii) Perpendicular Linear $\pi^z\pi^y\pi^x\pi^z\pi^y\pi^x$ 6-beam standing wave

$$\mathbf{E} = E_0\left[\hat{\mathbf{y}}\cos(kz-\omega t-\psi)+\hat{\mathbf{x}}\cos(kz+\omega t+\psi)\right] \;+\; \text{cycle}$$

$$\mathbf{H} = H_0\left[-\hat{\mathbf{x}}\cos(kz-\omega t-\psi)-\hat{\mathbf{y}}\cos(kz+\omega t+\psi)\right] \;+\; \text{cycle}$$

$$\mathbf{A} = \frac{E_0}{\omega}\left[\hat{\mathbf{y}}\sin(kz-\omega t-\psi)-\hat{\mathbf{x}}\sin(kz+\omega t+\psi)\right] \;+\; \text{cycle}$$

$$\langle\mathbf{S}\rangle = E_0H_0\hat{\mathbf{x}}\left[\sin(kx+ky)\sin(\theta-\phi)-\sin(ky-kz)\sin(\phi-\psi)-\sin(kz+kx)\sin(\psi-\theta)\right]$$

$$+\text{cycle}$$

$$\langle U_{\mathrm{E}}\rangle = \tfrac{1}{2}\varepsilon_0E_0^{\,2}\left[1+\cos(ky+kz-\phi+\psi)\right] \;+\; \text{cycle}$$

$$\langle U_{\mathrm{M}}\rangle = \tfrac{1}{2}\varepsilon_0E_0^{\,2}\left[1+\cos(ky+kz+\phi-\psi)\right] \;+\; \text{cycle}$$

$$\langle U\rangle = \varepsilon_0E_0^{\,2}\left[1+\cos(ky+kz)\cos(\phi-\psi)\right] \;+\; \text{cycle}$$

$$\mathbf{L}_{\mathrm{I}} = \frac{\varepsilon_0E_0^{\,2}}{\omega}\hat{\mathbf{x}}\left[\begin{array}{l}\sin 2kx+\sin(kx-ky+\theta-\phi)-\sin(kz-kx-\psi+\theta)\\ \qquad -\cos(ky-kz)\sin(\phi-\psi)-\sin(ky+kz)\cos(\phi-\psi)\end{array}\right]$$

$$+\text{cycle}$$

$$\left\langle M^{A}_{321} \right\rangle = -\frac{\varepsilon_0 {E_0}^2}{2k}\left[\sin(kz - kx + \psi - \theta) + \sin(ky - kz + \psi - \phi)\right]$$

$$\left\langle M^{A}_{332} \right\rangle = -\frac{\varepsilon_0 {E_0}^2}{2k}\left[\sin(ky + kz + \phi - \psi) + \sin(kz - kx - \psi + \theta)\right]$$

$$\left\langle M^{A}_{313} \right\rangle = -\frac{\varepsilon_0 {E_0}^2}{2k}\left[\sin(ky - kz + \phi - \psi) - \sin(kx + kz + \psi - \theta)\right]$$

---

iii) MOT corkscrew $\sigma^+\sigma^-\sigma^+\sigma^-\sigma^-\sigma^+$ 6-beam standing wave

Note that this field is not rotationally symmetric, and therefore cannot be written using the "+ cycle" abbreviation. The field **E** is

$$\mathbf{E} = \frac{E_0}{\sqrt{2}}\begin{bmatrix}\hat{\mathbf{x}}\cos(kz - \omega t - \psi) + \hat{\mathbf{y}}\sin(kz - \omega t - \psi) \\ +\hat{\mathbf{x}}\cos(kz + \omega t + \psi) + \hat{\mathbf{y}}\sin(kz + \omega t + \psi)\end{bmatrix}$$
$$+\frac{E_0}{\sqrt{2}}\begin{bmatrix}\hat{\mathbf{y}}\cos(kx - \omega t - \theta) - \hat{\mathbf{z}}\sin(kx - \omega t - \theta) \\ +\hat{\mathbf{y}}\cos(kx + \omega t + \theta) - \hat{\mathbf{z}}\sin(kx + \omega t + \theta)\end{bmatrix}$$
$$+\frac{E_0}{\sqrt{2}}\begin{bmatrix}\hat{\mathbf{z}}\cos(ky - \omega t - \phi) - \hat{\mathbf{x}}\sin(ky - \omega t - \phi) \\ +\hat{\mathbf{z}}\cos(ky + \omega t + \phi) - \hat{\mathbf{x}}\sin(ky + \omega t + \phi)\end{bmatrix}$$

which simplifies to

$$\mathbf{E} = \sqrt{2}E_0\begin{bmatrix}\hat{\mathbf{x}}\left(\cos kz\cos(\omega t + \psi) - \sin ky\cos(\omega t + \phi)\right) \\ +\hat{\mathbf{y}}\left(\cos kx\cos(\omega t + \theta) + \sin kz\cos(\omega t + \psi)\right) \\ +\hat{\mathbf{z}}\left(\cos ky\cos(\omega t + \phi) - \sin kx\cos(\omega t + \theta)\right)\end{bmatrix}$$

Similarly, **H** and **A** are, after simplification

$$\mathbf{H} = \sqrt{2}H_0\begin{bmatrix}\hat{\mathbf{x}}\left(\sin ky\sin(\omega t + \phi) + \cos kz\sin(\omega t + \psi)\right) \\ +\hat{\mathbf{y}}\left(\sin kz\sin(\omega t + \psi) - \cos kx\sin(\omega t + \theta)\right) \\ +\hat{\mathbf{z}}\left(\sin kx\sin(\omega t + \theta) - \cos ky\sin(\omega t + \phi)\right)\end{bmatrix}$$

$$\mathbf{A} = \frac{\sqrt{2}E_0}{\omega}\begin{bmatrix}\hat{\mathbf{x}}\left(-\cos kz\sin(\omega t + \psi) + \sin ky\sin(\omega t + \phi)\right) \\ +\hat{\mathbf{y}}\left(-\cos kx\sin(\omega t + \theta) - \sin kz\sin(\omega t + \psi)\right) \\ +\hat{\mathbf{z}}\left(-\cos ky\sin(\omega t + \phi) + \sin kx\sin(\omega t + \theta)\right)\end{bmatrix}$$

$$\langle \mathbf{S} \rangle = 2E_0H_0\sin(\theta - \phi)\left[\hat{\mathbf{x}}\cos kx\cos ky + \hat{\mathbf{y}}\sin kx\sin ky + \hat{\mathbf{z}}\cos kx\sin ky\right]$$

$$\langle U_{\mathrm{E}}\rangle = \varepsilon_0 {E_0}^2\left[\frac{3}{2} - \cos kz \sin ky \cos(\phi - \psi) + \cos kx \sin kz \cos(\psi - \theta) - \cos ky \sin kx \cos(\theta - \phi)\right]$$

$$\langle U_{\mathrm{M}}\rangle = \varepsilon_0 {E_0}^2\left[\frac{3}{2} + \cos kz \sin ky \cos(\phi - \psi) - \cos kx \sin kz \cos(\psi - \theta) - \cos ky \sin kx \cos(\theta - \phi)\right]$$

$$\langle U\rangle = \varepsilon_0 {E_0}^2\left[3 - 2\cos ky \sin kx \cos(\theta - \phi)\right]$$

$$\mathbf{L}_{\mathrm{I}} = \frac{2\varepsilon_0 {E_0}^2}{\omega}\left[\begin{array}{l} \hat{\mathbf{x}}\left(\cos kx \cos ky \sin(\theta - \phi) - \cos ky \sin kz \sin(\phi - \psi) - \sin kz \sin kx \sin(\psi - \theta)\right) \\ +\hat{\mathbf{y}}\left(\cos ky \cos kz \sin(\phi - \psi) + \cos kz \sin kx \sin(\psi - \theta) + \sin kx \sin ky \sin(\theta - \phi)\right) \\ +\hat{\mathbf{z}}\left(\cos kz \cos kx \sin(\psi - \theta) + \cos kx \sin ky \sin(\theta - \phi) - \sin ky \sin kz \sin(\phi - \psi)\right) \end{array}\right]$$

$$\left\langle M^{\mathrm{A}}_{321}\right\rangle = -\frac{\varepsilon_0 {E_0}^2}{k}\left[1 - \sin ky \cos kz \cos(\phi - \psi) + \cos kx \sin kz \cos(\psi - \theta)\right]$$

$$\left\langle M^{\mathrm{A}}_{332}\right\rangle = \frac{\varepsilon_0 {E_0}^2}{k}\left[\cos ky \cos kz \cos(\phi - \psi) - \cos kz \sin kx \cos(\psi - \theta)\right]$$

$$\left\langle M^{\mathrm{A}}_{313}\right\rangle = \frac{\varepsilon_0 {E_0}^2}{k}\left[\sin kz \cos ky \cos(\phi - \psi) - \sin kx \sin kz \cos(\psi - \theta)\right]$$

---

iv) circular polarised $\sigma^+\sigma^+\sigma^+\sigma^+\sigma^+\sigma^+$ 6-beam standing wave

$$\mathbf{E} = \frac{E_0}{\sqrt{2}}\left[\begin{array}{l} \hat{\mathbf{x}}\cos(kz - \omega t - \psi) - \hat{\mathbf{y}}\sin(kz - \omega t - \psi) \\ +\hat{\mathbf{x}}\cos(kz + \omega t + \psi) + \hat{\mathbf{y}}\sin(kz + \omega t + \psi) \end{array}\right]$$
$$+ \text{ cycle}$$

which simplifies to

$$\mathbf{E} = \sqrt{2}E_0\left[\begin{array}{c} \hat{\mathbf{x}}\left(\cos kz \cos(\omega t + \psi) + \cos ky \sin(\omega t + \phi)\right) \\ + \text{ cycle} \end{array}\right]$$

Similarly **H** and **A** are, after simplification

$$\mathbf{H} = \sqrt{2}H_0\left[\begin{array}{c} \hat{\mathbf{x}}\left(\sin kz \cos(\omega t + \psi) + \sin ky \sin(\omega t + \phi)\right) \\ + \text{ cycle} \end{array}\right]$$

$$\mathbf{A} = \frac{\sqrt{2}E_0}{\omega}\left[\begin{array}{c} \hat{\mathbf{x}}\left(-\cos kz \sin(\omega t + \psi) + \cos ky \cos(\omega t + \phi)\right) \\ + \text{ cycle} \end{array}\right]$$

$$\langle \mathbf{S}\rangle = E_0 H_0 \hat{\mathbf{x}}\left[\sin(kx - kz)\cos(\psi - \theta) + \sin(kz - ky)\sin(\phi - \psi) + \sin(ky - kx)\cos(\theta - \phi)\right]$$
$$+ \text{ cycle}$$

$$\langle U_{\mathrm{E}}\rangle = \varepsilon_0 {E_0}^2\left[\cos^2 kx + \cos ky \cos kz \sin(\phi - \psi)\right] + \text{ cycle}$$

$$\langle U_{\mathrm{M}}\rangle = \varepsilon_0 {E_0}^2\left[\sin^2 kx + \sin ky \sin kz \sin(\phi - \psi)\right] + \text{ cycle}$$

$$\langle U\rangle = \varepsilon_0 {E_0}^2\left[1 + \cos(ky - kz)\sin(\phi - \psi)\right] + \text{ cycle}$$

$$\mathbf{L}_1 = \frac{2\varepsilon_0 {E_0}^2}{\omega}\hat{\mathbf{x}}\begin{bmatrix}\cos^2 kx + \cos kx \cos ky \sin(\theta - \phi) \\ -\cos ky \cos kz \cos(\phi - \psi) + \cos kz \cos kx \sin(\psi - \theta)\end{bmatrix}$$

$$+ \text{cycle}$$

$$\left\langle M^{\mathrm{A}}_{321} \right\rangle = \frac{\varepsilon_0 {E_0}^2}{k}\left[\sin kz \cos ky \cos(\phi - \psi) - \sin kz \cos kx \cos(\psi - \theta)\right]$$

$$\left\langle M^{\mathrm{A}}_{332} \right\rangle = \frac{\varepsilon_0 {E_0}^2}{k}\left[\sin kz \cos ky \sin(\phi - \psi) - \sin kz \cos kx \cos(\psi - \theta)\right]$$

$$\left\langle M^{\mathrm{A}}_{313} \right\rangle = -\frac{\varepsilon_0 {E_0}^2}{k}\left[\sin kz \cos ky \cos(\phi - \psi) - \sin kz \cos kx \sin(\psi - \theta)\right]$$

Chapter 6
Experimental apparatus for a magneto-optical trap for rubidium atoms

Introduction

This chapter describes the construction of a magneto-optical trap (MOT) for rubidium atoms at the Open University physics department spectroscopy laboratory at Walton Hall, Milton Keynes. Work on laser cooling began in October 1991, requiring that the necessary apparatus be designed and built up from nothing during the years leading up to this thesis. From an experimental point of view, the MOT is composed of four elements: a set of resonant laser beams (described in section 6.1), a magnetic field gradient (section 6.2), a sample of rubidium atoms in a vacuum chamber (section 6.3) and finally a set of diagnostic tools (section 6.4). Relevant spectroscopic data for the rubidium atom may be found in Appendix A8.

6.1 Laser beams and optics

The cooling and trapping of atoms requires a stable source of narrow bandwidth laser light with a frequency which is detuned from an atomic transition. Good control is required of many properties of the laser beams: frequency, linewidth, power, diameter, spatial quality (mode structure), direction and polarisation. This section starts with an overview of the complete optical system before discussing each of the above laser beam properties in detail. Figure 6-1 is a schematic diagram of the necessary laser and optical components.

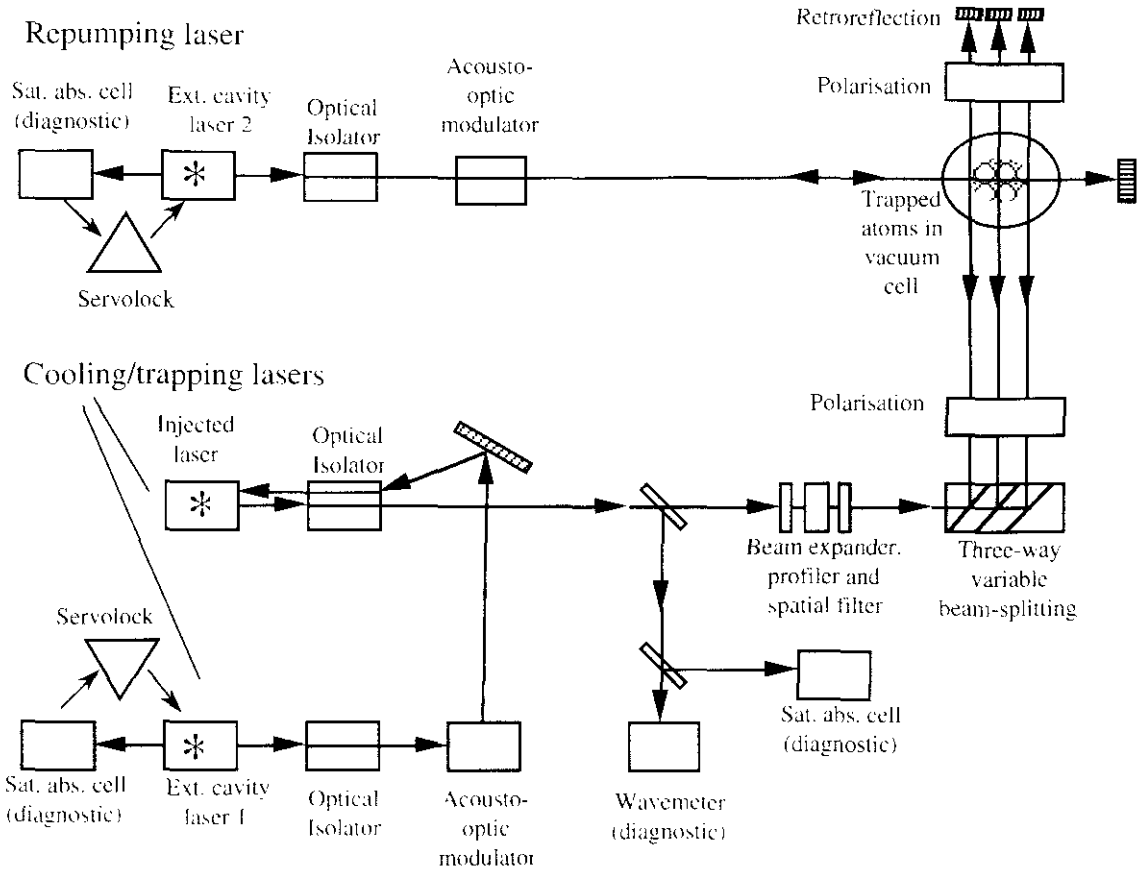

Figure 6-1 The optical bench configuration

The essential optical components are shown in the above figure. Laser light of the desired frequency and linewidth is produced in the 'external cavity laser 1' (section 6.1.1), whose output is monitored and controlled by a saturated absorption cell and electronic servolock system. The output of this laser is amplified by 'injection-locking' (section 6.1.3) a second more powerful 'injected' diode laser, whose output retains the spectral qualities of the external cavity laser. Optical isolators are necessary to prevent unwanted feedback effects due to retro-reflected light (section 6.1.2), and an acousto-optic modulator (section 6.1.5) is used for precise scanning and/or switching of the laser frequency. The beam from the injected laser is then spatially filtered, adjusted to have a circular profile of the desired diameter, split into three equal parts, circularly polarised and finally directed into the vacuum cell where atom trapping takes place. A second similar system consisting of external cavity laser 2, a saturated absorption cell, an optical isolator and an acousto-optical modulator (AOM) is used to create a 'repumping' beam with a different frequency. The purpose of the repumping beam was explained in section 3.1. The repumping beam may either be sent directly into the vacuum cell as shown above or may be combined with the trapping beams prior to the three-way splitting stage. An advantage of the latter arrangement is that it allows both trapping and repumping beams to be blocked simultaneously with a single shutter.

The external laser cavities are highly sensitive to acoustic vibrations and the performance of most of the above components is sensitive to small beam misalignments. To help overcome these problems, the experiment is mounted on a 1.2 x 3.0 m laminated steel 'floating' optical table (Ealing Optics) which provides a high degree of vibration isolation and long term positional stability for the optical components.

6.1.1 Laser frequency and linewidth.

The laser light for any cooling or trapping experiment must fulfil two important conditions. Firstly, it must have a linewidth narrower than the natural linewidth of the hyperfine atomic transitions used for cooling. Secondly, for stable trap operation, the frequency drift must be less than some fraction of that same natural linewidth during the time of the experiment. For rubidium cooled on the hyperfine transition $5S_{1/2}(F = 3)$ to $5P_{3/2}(F = 4)$ (see figure 6-2) the natural linewidth is $\Gamma/2\pi = 5.68$ MHz. Hence a suitable laser design should have a central frequency drift less than say 1 MHz in 5 minutes and a linewidth less than 1 MHz. Furthermore, if a part of the laser beam is to be used as a precise probe of narrow resonances e.g. the Rayleigh and Raman resonances described in chapter 4, an even smaller linewidth between 1 and 10 kHz is desirable. The repumping laser must also have a similarly small frequency drift of less than 1 MHz in 5 minutes, though it is not so important that it have a narrow linewidth. The above-mentioned conditions on linewidth and frequency drift are achieved in this work by using a technique[247] that has become common amongst laser-cooling research groups, namely that of an 'external cavity laser'. This consists of a laser diode in an external cavity with a diffraction grating, frequency-locked to an atomic transition by a saturated absorption technique. A description of our external cavity lasers is given shortly, following a brief description of laser diodes themselves.

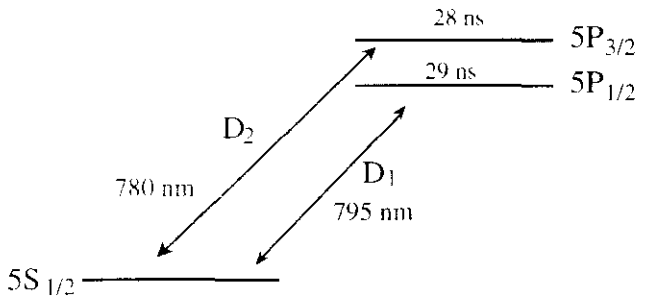

Figure 6-2 The D_1 and D_2 laser cooling transition(s) of rubidium

The gross structure of the electronic energy levels for rubidium may be found in Appendix 8 and the relevant hyperfine structure is shown in figure 6-6a. The D_1 and D_2 lines are at 794.76 and 780.027 nm respectively. These wavelengths are not normally considered visible, being at the extreme edge of the visible spectrum. Nevertheless one milliwatt of 780 nm laser light incident on a white card is sufficiently intense to produce a clearly visible red spot.

Laser diodes

The use of laser diodes in this work is possible because of the convenient coincidence of the wavelength of the rubidium D lines at 780 nm (and caesium lines at 852 nm) with the wavelength of commercially available laser diodes. Laser diodes have the advantage of being considerably cheaper than alternatives such as a titanium-sapphire laser or a continuous-wave dye laser. They were first used for laser cooling in 1986 to slow a caesium atomic beam[248] and later for 3-D cooling of caesium[249]. The fluctuations in the power output of laser diodes are small[249], typically ~1 in 10^5, and their wavelength is controllable via temperature or injection current. The frequency of diode laser light may be modulated via the injection current at rates[250] from zero up to 15 GHz per μs. These features enable relatively easy tuning, frequency locking and scanning.

An introduction to diode lasers per se can be found in Ohtsu[251] and to the use of diode lasers in atomic physics in Camparo[252]. Light is generated in a semiconductor chip when a direct current injected at a p-n junction in the chip produces electrons and holes which recombine to produce photons. The semiconductor material GaAlAs can be used to construct laser diodes with a wavelength in the range 750 to 830 nm. The energy of the photon corresponds to the band gap which in turn depends on the ratio of gallium to aluminium in the chip. The laser cavity is a Fabry-Perot resonator formed between two cleaved ends of the active (electron/hole recombination) region of the semiconductor crystal. The cleaved ends have a higher reflectivity (~0.3) than any adjacent semiconductor material and act as the cavity mirrors. This resonator may support several longitudinal and transverse modes and laser oscillation occurs at the mode(s) at the peak of the semiconductor gain curve. In the 'index-guided' type of laser diode used in these experiments, unwanted transverse modes are suppressed by confining the light to a long thin rectangular strip (waveguide) of dimensions around 300 x 2 x 0.1 μm. The waveguide is formed by surrounding the active region with cladding layers of different refractive index. See figure 6-3. The laser diode then operates on a single transverse mode. Furthermore, when the drive current is sufficiently above the lasing threshold, only one (temperature-selected) longitudinal mode is active.

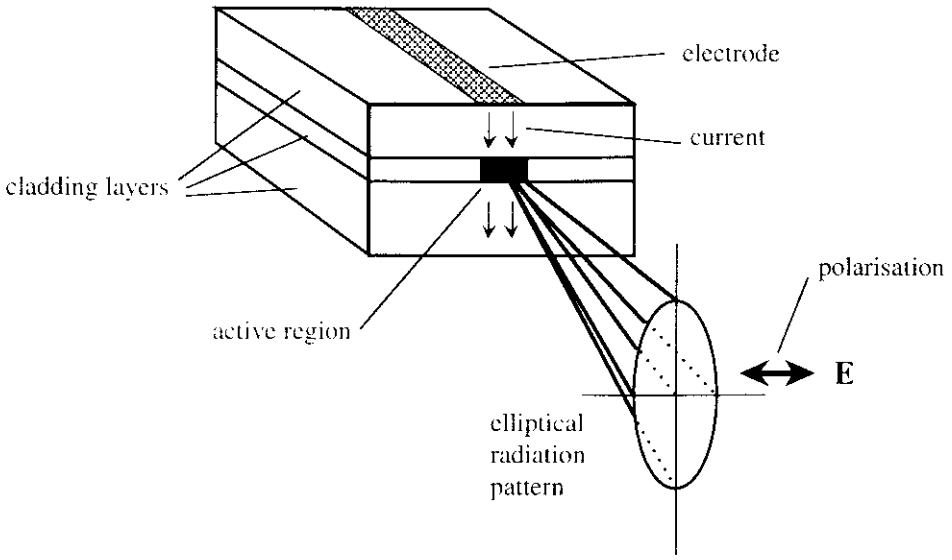

Figure 6-3 The simplified structure of a laser diode

The frequency of laser diode light may be controlled by altering their temperature and/or injection current. Changing the temperature changes both the peak of the gain curve and the frequency of the cavity modes, the latter through changes in the refractive index (which is around 3.5 for GaAlAs). Laser diodes can easily be damaged by spikes in the injection current and precautions for handling electrostatically sensitive devices must be observed[1].

The external cavity laser

The diodes used in our work are Sharp LTO24MDO and LTO25MDO, with nominal light output powers of 30 and 40 mW, and room temperature wavelengths in the range 781 - 789 nm. When running free, i.e. without any form of cavity feedback, their linewidth was measured with a spectrum analyser to be of the order of 80 MHz. This width could be randomly narrowed in the range 30 to 80 MHz by feedback from a glass plate in the path or from the entrance facet of the spectrum analyser itself. The wavelength may be controlled linearly over small ranges (a few nanometres) by changing the temperature (sensitivity 30 GHz K^{-1}) or by changing the driving current (sensitivity 7 GHz mA^{-1}). The linear response is interrupted by 'mode-hops', which are laser frequency jumps between preferred internal longitudinal cavity modes. The internal cavity modes of the Sharp lasers were measured to be ~0.26 nm (or 130 GHz) apart, by measuring the diffraction angles of different modes from a 600 lines per mm grating.

Our external cavity lasers were designed by Dr Eric Usadi, and are a variation on a design by Dr Andrew Steane[169]. They were built by the Open University machine shop and full technical specifications including technical drawings may be found in [253]. The

---

[1] *As I learnt after 'killing' several diodes myself! An earthed wristband should be worn when handling them directly, and all electrical connections must be secure, especially where the diode pins are held by friction.*

sensitivities of the frequency to temperature and current (given above for the bare diode) imply that for an ultimate frequency stability of $< \pm 0.5$ MHz, the temperature and current variations must be $< \pm 20$ μK and $< \pm 70$ nA respectively. This degree of current stability is achievable with a well designed current driver. Such precise control of the temperature, however, would be very difficult to achieve in practice and fortunately the requirement is not so severe when the external cavity laser is employed. This is because the output frequency of the external cavity laser is strongly dominated by the external cavity length, which is less sensitive to temperature fluctuations than the laser diode itself. A simple calculation of cavity length variation with temperature shows that, for frequency stability of $< \pm 0.5$ MHz, the temperature must be stable to around ± 1 mK, which is an achievable, though exacting requirement. Thus temperature and current control are key factors in the design of the external cavity laser and its control electronics.

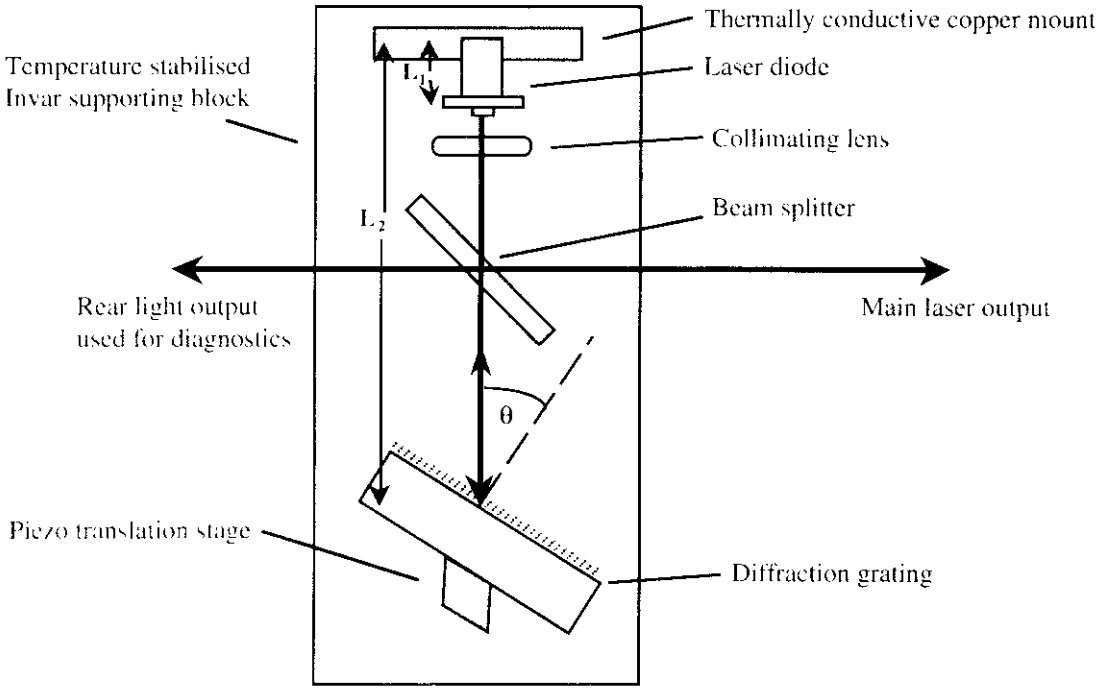

Figure 6-4 The external cavity laser

Figure 6-4 shows the main parts of the external cavity laser. The external cavity is formed by the rear facet of the laser diode and the face of a diffraction grating, which has 1200 lines mm^{-1}, is blazed for 780nm in first order and mounted in Littrow configuration (first order diffraction beam is retro-reflected). The mode spacing of the external cavity is 2.5 GHz. The front face of the laser diode is anti-reflection coated as supplied, an important feature as it allows enough of the reflected light from the grating to re-enter the laser-diode and produce a strong feedback loop. A collimating lens is placed close (4 mm) to the output facet of the laser diode and the collimated beam passes through a beamsplitter which results in two output beams. The diffraction grating is held by a mount rotatable about all three axes, to allow alignment and coarse wavelength tuning. This mount is itself attached to an Invar bar

via a piezo-electric crystal which allows small, smooth alterations in the external cavity length to be made under voltage control. Invar was used for the mounting base in order to minimise fluctuations of cavity length with temperature. The Invar bar is kept in thermal contact with a copper heat sink which is temperature stabilised by a negative feedback loop involving a thermistor (Fenwal standard bead 100 kΩ) buried in the copper and an 18W Peltier heat pump (Melcor CP-1.4-71-10L). The high-stability electronic controller for the temperature feedback loop was built by the Open University electronics workshop, following designs in [254]. The feedback is the sum of three contributions: one proportional to the difference between the actual and set temperatures (linear), one proportional to the rate of change of that difference (differential) and one proportional to the recent history of the difference (integral). The use of these three functions allows fast cooling when required but prevents large overshoot or oscillations about the set point. The system design is claimed[254] to be able to maintain a steady temperature to within ± 0.3 mK per hour, but we have measured the typical drift of our system to be ~±10 mK per hour, by monitoring the thermistor resistance. This corresponds to a laser frequency drift of ±0.5 MHz per 5 minutes, which meets the required specification. A second outer tier of temperature control, involving a similar feedback loop connected to the metal box surrounding the cavity was tried. It offered a small improvement in stability, but did not justify the extra complexity involved.

External cavity laser tuning

The external cavity laser is tuned to the desired frequency in stages as follows. First, the temperature is adjusted until the bare diode is lasing within < 2 nm of the target wavelength. An initial alignment of the grating is then made, which establishes operation of the laser diode with optical feedback. Then, by fine adjustment of the angle of the grating with respect to the laser diode beam via three fine pitched screws and some juggling of the temperature, the diode may be induced to lase on the desired mode of its internal cavity, which implies that the frequency is within ±70 GHz of the atomic transition frequency. The jumps between modes are monitored with a wavemeter. The temperature of the cavity may then be adjusted, typically within the range 10 to 20°C, to translate that mode frequency to within ~20 GHz of the desired point, this being the available resolution of our wavemeter. Finer adjustment is then obtained by altering the current to the laser diode, whilst watching for the fluorescence from a rubidium absorption cell to identify the transition frequencies. This visual monitoring of a rubidium absorption cell allows one to place the laser frequency within the Doppler width (400 MHz) of any of the four lines distinguished: two lines due to each of the two isotopes of natural rubidium (see figure 6-6b). The current driver was built by the O.U. electronics workshop, again following a design in [254]. For optimum stability the current drivers are powered by lead acid batteries (12 V, 9.5 A hr storage) and achieve a stability of

± 1 μA per hour, corresponding to a change of less than 7 MHz per hour. An important feature of the driver is that the current is ramped whenever switched on or off so as to avoid current transients which might damage the laser.

The fine tuning is achieved via small alterations to the length of the external cavity. The diffraction grating is mounted upon a piezo-electric crystal, enabling voltage controlled changes in the cavity length (46 nm per volt) with a resolution better than 1 nm. This allows the frequency to be scanned over a total range of 4 GHz corresponding to the 15 volt linear range of the piezo crystal. An absolute reference for the fine tuning of the laser is provided by a rubidium saturated absorption spectrum, described in the next section. A servolock system (negative feedback loop), in which the voltage to the piezo is controlled electronically by the saturation absorption signal strength, allows the laser to be locked anywhere on the slopes of the absorption profile due to the hyperfine lines (see figure 6-6c). The servolock circuit, based on a design in reference[247] was built by the O.U. electronics department. It can operate in either of two modes: a locked mode which eliminates any remaining slow frequency drift due to temperature drift of the laser cavity, or in a ramp mode which allows a chosen range of the saturated absorption signal to be viewed and identified on a Tektronix 2445 oscilloscope (150 MHz). In the ramp mode, the viewed frequency range may be varied from <1MHz to 4 GHz. In the locked mode, the 'jitter' noise in the laser frequency caused by environmental noise such as acoustic vibration is reduced to less than 1 MHz.

Saturated absorption spectroscopy

A saturated absorption spectroscopy arrangement is attached permanently as a frequency monitor to each of the external cavity lasers. This standard spectroscopic technique[255] is 'Doppler-free', and thus allows the hyperfine structure of the rubidium D lines to be resolved. Each external cavity laser provides two output beams, allowing one of the beams to be conveniently deployed as the saturated absorption pump. The optical arrangement for saturated spectroscopy is shown in figure 6-5. A commercial glass-blower pre-fabricated our saturated absorption cells to a design which incorporated a small tapered-neck entrance so that I could later load them with rubidium. The final sealing was then easily carried out by an O.U. technician, Mr G. Jeffs.

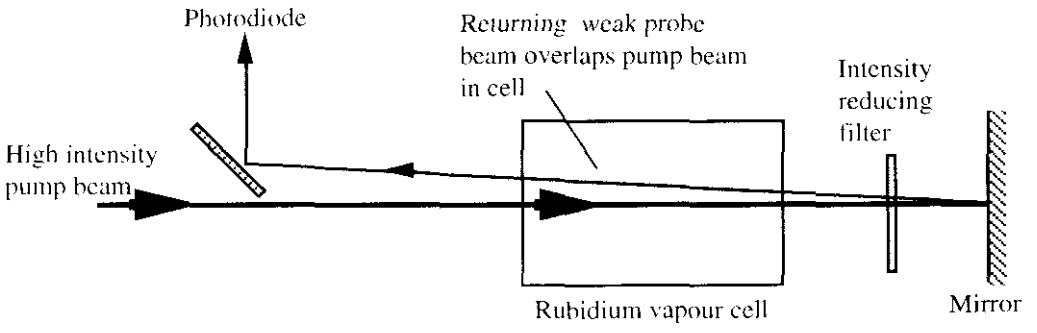

Figure 6-5 Optical arrangement for saturated absorption spectroscopy

The principle of saturated absorption is as follows. There is a certain velocity group of atoms in the vapour whose Doppler shift is equal and opposite to the pump laser detuning and this velocity group is therefore resonant with the high intensity pump beam. These resonant atoms are saturated, in other words only approximately half of them are in their ground state. The counterpropagating weak probe beam generally interacts with a different velocity group of atoms in the vapour. The exception is when the beam is exactly tuned to an atomic transition, in which case both pump and probe interact with the zero velocity group of atoms. In this case, the probe beam 'sees' fewer atoms as the number available for absorption has been depleted by the pump beam. This results in features appearing within the Doppler broadened absorption profile which are known as 'Lamb dips', and which have widths equal to the natural linewidths of the hyperfine transitions.

Saturated absorption profile of rubidium

Figure 6-6a shows the hyperfine transitions which make up the D_2 line for the two isotopes of natural rubidium. Figure 6-6b shows a plot of (unsaturated) absorption against frequency for a laser beam passing once through a rubidium vapour cell. Four broad peaks are resolved, each peak containing three hyperfine components which are not well resolved owing to Doppler broadening. The four peaks in the plot (figure 6-6b) are aligned below their corresponding transitions in figure 6-6a. Figure 6-6c shows the saturated absorption curve of three of the six hyperfine transition lines comprising the rubidium 85 D_2 line. Three 'crossover' lines are also obtained when using saturated absorption methods. They occur midway between the pairs of hyperfine lines and are often larger than the actual hyperfine lines. An analysis by Nakayama[256] shows that the shape of the saturated absorption spectrum is determined by a combination of optical pumping, laser polarisation and saturation effects. The line centres of the $F = 3 \rightarrow F' = 2$ and $F = 3 \rightarrow F' = 3$ lines are, respectively, 186 and 122 MHz below the $F = 3 \rightarrow F' = 4$ line[257].

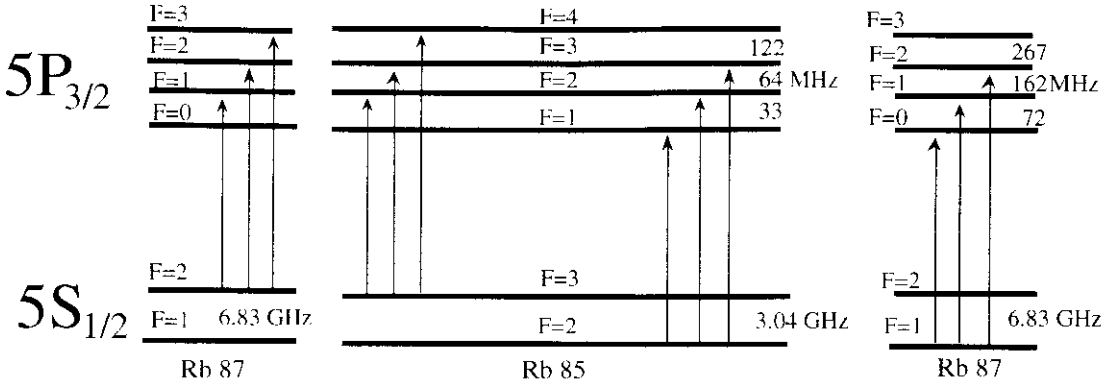

Figure 6-6a The hyperfine energy levels of the D_2 line of natural rubidium

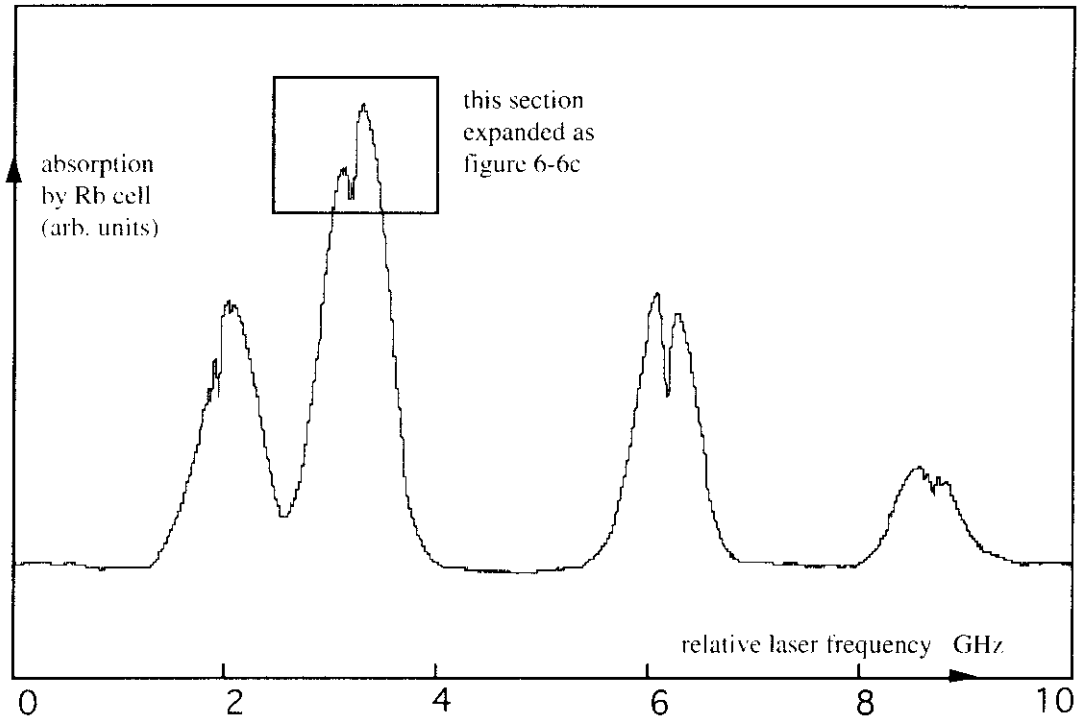

Figure 6-6b Absorption profile of the D_2 line of natural rubidium, recorded at the O.U.

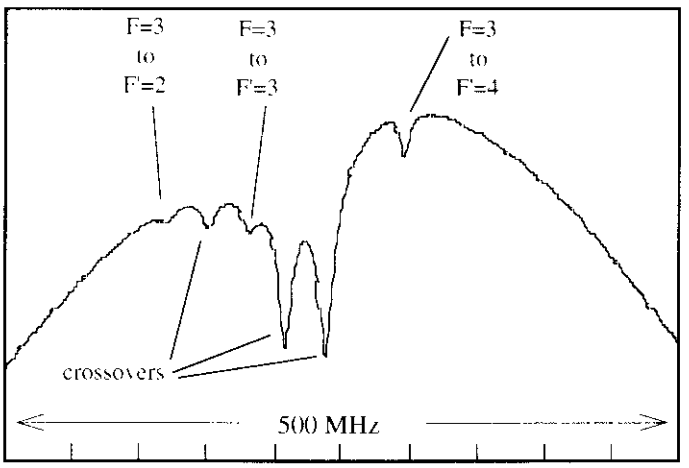

Figure 6-6c Expanded section of the saturated absorption curve of figure 6-6b, showing Lamb dips corresponding to hyperfine transitions

External cavity laser linewidth

The linewidth of a laser diode can be narrowed by controlled optical feedback, designated either 'weak' feedback (<0.01% of the laser power) in the case of feedback from a high Q Fabry-Perot etalon [249,258,259] or 'strong' feedback (>1% of the laser power) as is required in the case of feedback from a diffraction grating[169,260]. Reference[169] contains a theoretical argument showing that linewidth narrowing to widths less than 1/300 of the bare diode linewidth (i.e. < 100kHz in our case) is to be expected with the external cavity laser design. The linewidth of our lasers was found to be less than the 20 MHz resolution of our spectrum analyser. An exact measurement of the linewidth has not been made, but an upper limit may be deduced from the fact that our saturated absorption scans show hyperfine lines of known FWHM 6 MHz to be sharply resolved at the peak, although broadened to ~ 7.5 MHz. This implies that the linewidth is less than 1MHz. Later experiments to observe Raman and Rayleigh resonances which are ~100 kHz apart should give further information on this upper limit. Other workers[260,261] who have used external cavities with grating feedback have measured linewidths less than 100kHz, thus increasing our confidence that the linewidth of our external cavity laser is sufficiently narrow.

6.1.2 Optical isolators

Diode lasers are extremely sensitive to feedback of retro-reflected light, a feature which is used to advantage in the external cavity. However, retro-reflections from downline optical components lead to unwanted amplitude and frequency fluctuations ('jitter') of the laser output. Laser diode feedback of as little as 1 in 10^6 of the output has been shown to affect their frequency and amplitude stability[262]. These retro-reflections must therefore be prevented from returning to the laser diode by the use of optical isolators.

An optical isolator is simply a one-way light valve, allowing transmission in a forward direction, but high attenuation in the reverse direction. The attenuation is usually expressed in decibels and is typically in the range 30 to 50 db, with forward transmission better than 95%. The most effective isolators are magneto-optical isolators, which depend for their operation on 'Faraday rotation', the rotation of the plane of polarisation of a polarised light beam as it passes through a transparent solid in a magnetic field (see figure 6-7). In the forward mode, input light is first vertically polarised at A, then rotated through 45° by the Faraday rotator. The light then passes through the second polariser B, whose transmission axis is at 45° to the vertical. In the reverse mode, returning light is linearly polarised at 45° to the vertical as it passes through B. It is then rotated through 45° by the Faraday rotator and becomes horizontally polarised. Thus it is stopped by polariser A. The essential property of a Faraday rotator is that it rotates the plane of polarisation in the same sense regardless of the propagation direction of the light. The amount of rotation is given by

$$\theta = V\mathbf{B}\cdot\mathbf{l}$$

where θ is the rotation angle, **B** a uniform magnetic field, **l** the path of the light through the rotator and V is a constant for a given material known as the Verdet constant.

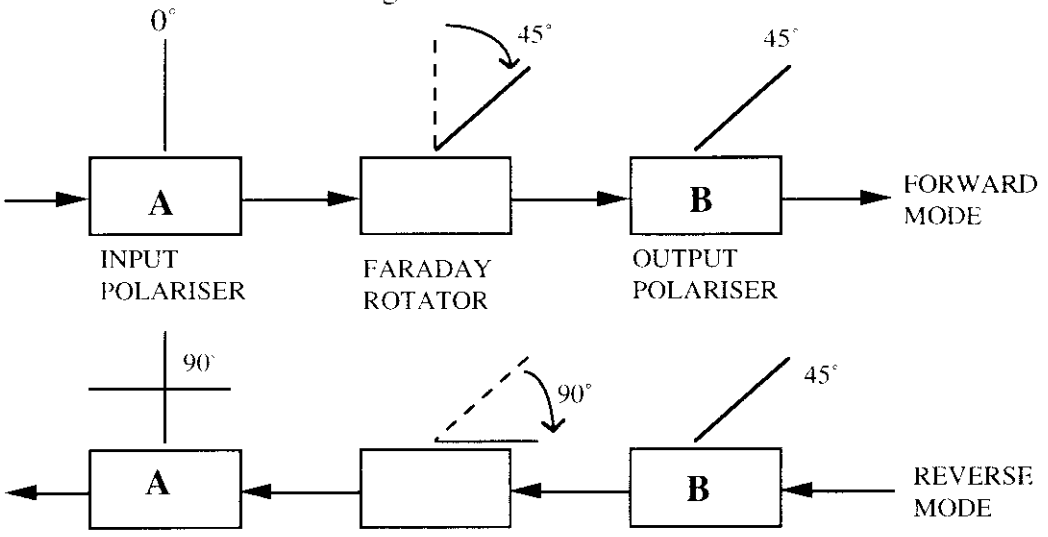

Figure 6-7 The operating principle of a magneto-optical isolator

The design of the Newport isolators used in the experiment is sketched in figure 6-8. The crystal material is YIG (yttrium iron garnet) in the shape of a cylindrical rod of 5 mm diameter and 20 mm length, housed along the drilled out axis of a cylindrical permanent magnet. The magnets are neodymium-iron-boron and produce a field of ~5000 gauss along the crystal axis. This field may be 'tuned' to give the optimum rotation of 45° and hence the optimum attenuation at a given wavelength by altering the distance between the inner (I) and outer (O) magnets, which are magnetised in the opposite sense. The polarisers are high quality (50 db attenuation) Rochon cube polarisers.

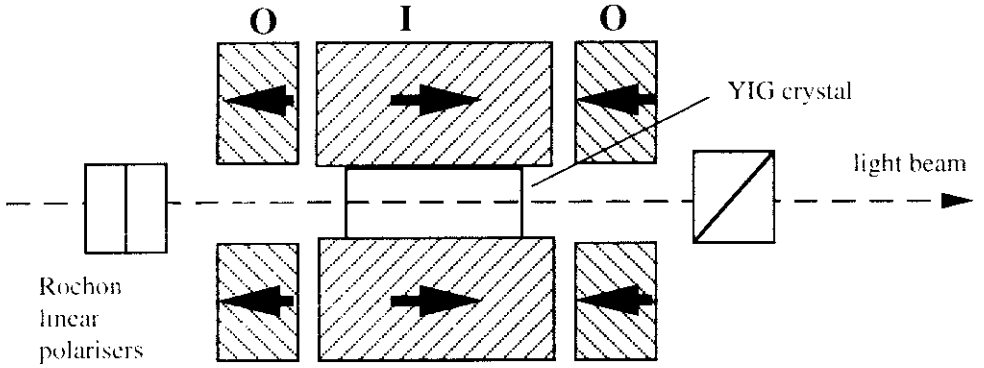

Figure 6-8 A practical magneto-optical isolator

6.1.3 Laser power and injection locking

The theory of chapters 2 and 3 (equation 3-1b) predicts that optimal Doppler cooling is obtained for a Rabi frequency $\Omega \approx \Gamma/\sqrt{6}$ in each of the six beams, therefore it is desirable to have at least enough laser power to achieve this. For the Rb D_2 line this is equal to 1.3 $mWcm^{-2}$ for each beam. The beam intensity can be adjusted, given a fixed available total power, by adjusting the diameter of the beam with a system of beam expanding lenses. However, other trap properties, such as loading-time, capture velocity and densities also

depend on the diameter and diameters ($1/e^2$) of at least 5 mm are generally preferable. It follows that it is necessary to have a total of at least 2 mW available after all frequency locking, line-narrowing and spatial filtering.

The light power output of a free-running diode laser nominally 30 mW may vary between 15 and 30 mW depending on the driving current. This is much reduced when the laser is subject to optical feedback in the external cavity and was measured to be 2.5 mW maximum. Passage through the subsequent optics results in a further reduction to less than the required 2 mW, hence it is necessary to amplify the beam by 'injection-locking' a second, more powerful laser diode (Sharp LT025MDO). The first external cavity laser (the 'injecting' laser) thus acts as a source of specific spectral qualities (frequency and linewidth) which are copied onto the more powerful 'injected' diode laser[263]. Injection locking has been satisfactorily achieved with the injection of as little as 0.1% of the total output power[169]. The maximum power of our injected laser when locked is 12 mW. The temperature and drive current of the injected laser are controlled by similar systems to those used for the external cavity laser.

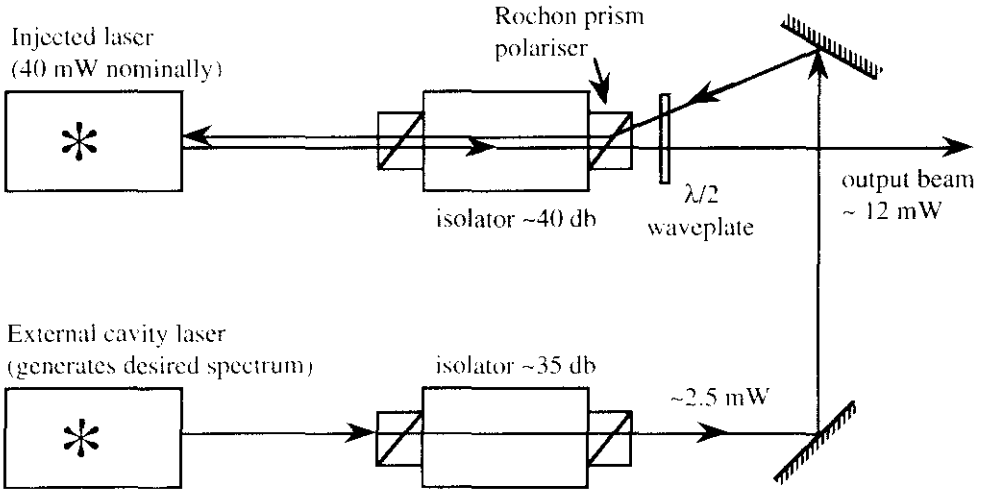

Figure 6-9 Injection locking scheme

For injection-locking, two optical isolators are necessary as shown to protect both lasers from retro-reflections. The external cavity output is injected into the the second laser by taking advantage of a 'backwards' light path through the isolator. The 'backwards' path is just the reverse of the path taken by that part of the injected laser light which is rejected by the output polariser of the isolator. The λ/2 waveplate is necessary to match the polarisations of the injecting beam and injected output beam at the diode output facet.

With our apparatus, injection-locking takes place when the injected laser has a free-running wavelength approximately 1.5 nm shorter than the injecting light wavelength. This is about five internal cavity modes away from the free-running wavelength. The procedure to obtain good injection-locking is as follows. A faint 'rejected' beam from the injected laser always marks out the backwards path, owing to the less than perfect performance of the

isolator. Precise alignment of the injecting beam with this 'rejected' beam is ensured by passing both beams through two small apertures (1 mm) separated by at least a metre. With the injecting laser temporarily blocked, the temperature of the injected laser is adjusted until the injected laser is free-running on the correct internal cavity mode (~788.65 ± 0.05nm in our case). The injecting laser is unblocked and the injected laser drive current adjusted until locking is obtained, as evidenced by the wavemeter jumping from ~788.65 to ~780.03 nm. The three 'parameters' of beam alignment, polarisation matching and drive current are then optimised by observing a saturated absorption spectrum obtained with the injection-locked output, and adjusting the parameters until the signal is as noise-free as possible. We have also observed the output of the injected laser with a spectrum analyser of resolution 20 MHz. This revealed that, at the edges of the 'good-locking' range of these parameters, locking was maintained, but strong sidebands[2] appeared in the output spectrum with a spacing ± ~1 GHz. An interesting observation is that we were able to trap atoms without a separate repumping laser when these sidebands were present in the trapping light. The hyperfine ground state splitting of ^{85}Rb is 3.04 GHz and I deduce that the higher frequency sidebands are able to provide sufficient repumping light. However, in normal operation, we use a separate repumping laser and an optimised injection-locking system.

6.1.4 Polarisation, spatial quality and other optics

Generally, the basic optics (mirrors, beamsplitters etc) are made to high specifications in order to preserve desirable beam characteristics such as spatial coherence, circularity of polarisation and to minimise power losses etc. Many of the optical surfaces are either reflection or anti-reflection coated at 780 nm, and meet exacting flatness and surface polish standards (better than $\lambda/10$ and 60/40 scratch/dig respectively). Many beam-processing operations require linearly polarised light, which is achieved by the use of various Glan-Thompson polarising cubes and polarising beamsplitter cubes (e.g. Meadowlark BP 0.5-785). The linear polarisation can be rotated into any angle by the use of half-wave plates or mirror pairs. Combining a half-wave plate with a polarising beamsplitter allows a variable ratio beamsplitter to be constructed. Circular polarisation is achieved where necessary by the use of quartz multi-mode quarter-wave plates. Three particular beam-processing operations are beam expansion, beam shaping and spatial filtering, described below.

Beam expansion and shaping

The laser diode output is naturally highly divergent, the divergence being around 10° and 30° in the two directions (see figure 6-3). The ellipticity is due to the shape of the gain medium which is that of a rectangular strip. The output light is collimated by a small lens with a high

[2] *I have not investigated the reason for the formation of these sidebands, but note that sidebands have been predicted and observed for light produced by injection-locking under certain circumstances[263].*

numerical aperture (0.47) placed one focal length (~4 mm) from the front facet of the diode itself. This collimation is not perfect, as the output is also slightly astigmatic, the focal points for light collimated in the two transverse directions being different by ~ 50 μm[264]. The collimated light has an elliptical profile and is strongly linearly polarised parallel to the short axis. The beam profile may be made circular either by use of of a pair of 'anamorphic prisms', figure 6-10a, or by use of two cylindrical lenses to make a one-dimensional beam expander, figure 6-10b. Both systems are used in our experimental set-up. The final size of the beam diameter is variable, but usually set within the range 5 to 10 mm by a normal beam expander consisting of two plano-convex circular lenses of different focal lengths.

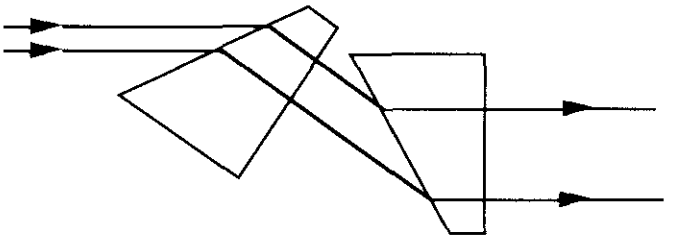

Figure 6-10a Beam shaping with anamorphic prisms

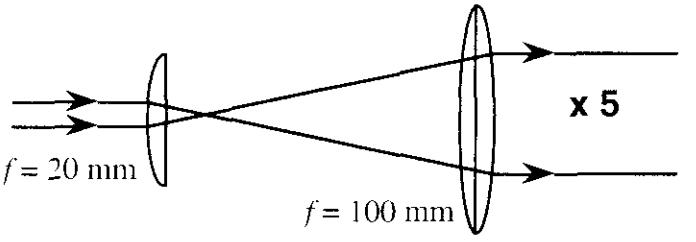

Figure 6-10b Beam expansion in one or two dimensions

Spatial filtering

Laser light diffracted from optical apertures (e.g. the collimating lens), small dust particles or slight imperfections in the optics may produce irregularities in the otherwise smooth irradiance distribution. The scattered light travels in different directions from the parallel laser beam, and is thus spatially separate at a lens focal plane. By the use of a spatial filter, consisting of two lenses f = 100mm and a pinhole of ~ 100 μm diameter centred around the focal spot of the direct beam, it is possible to block the scattered beams, whilst allowing the direct beam (TEM_{00} mode) to pass. The result is a collimated beam of light with a gaussian intensity distribution.

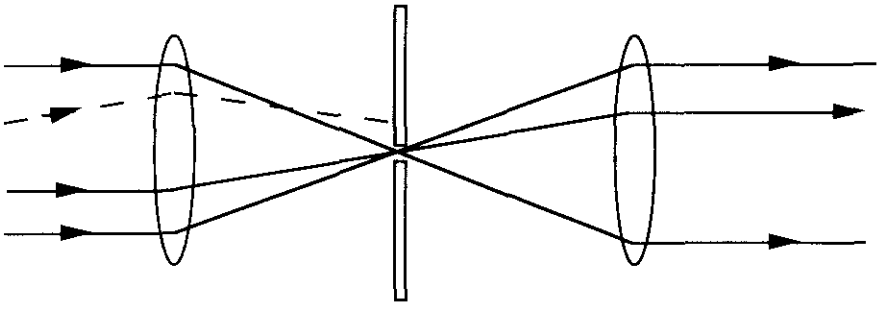

Figure 6-10c Spatial filtering

The exact profile of the trapping laser beams is not important for all MOT experiments, nevertheless we employ a spatial filter. One advantage of this is that it enables easy identification of problems due to slightly misaligned optical components, as deviations from a circular Gaussian profile are readily spotted. A disadvantage is that there is an associated power loss of ~15%, which is partly due to the different focal planes caused by the astigmatism of laser diode light.

6.1.5 Acousto-optic modulators (AOMs)

Acousto-optic modulators are devices which allow the shifting of the frequency of monochromatic light which passes through them by relatively small amounts, typically between 60 and 100 MHz.

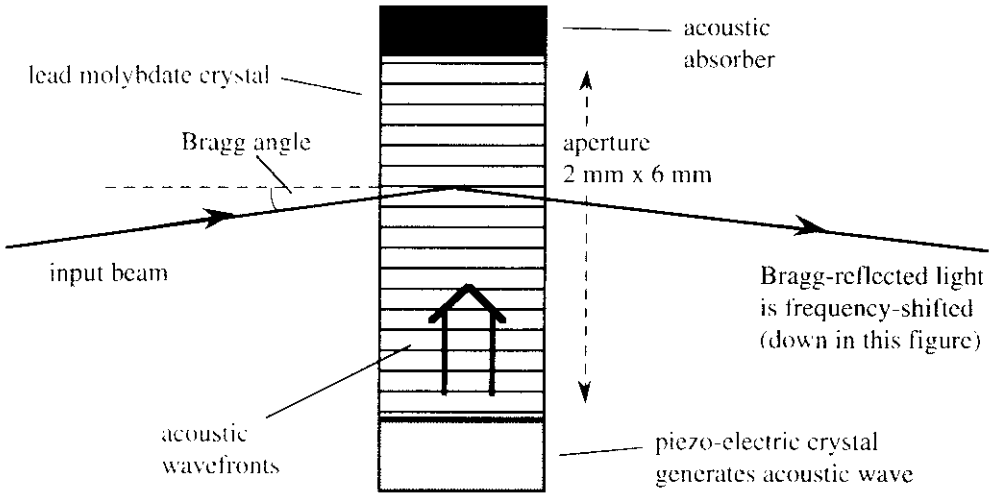

Figure 6-11 The acousto-optic modulator

The operating principle of an AOM is as follows. An acoustic travelling wave of typically 80 MHz and wavelength ~45 μm is set up in a crystalline material; in the case of our AOMs it is lead molybdate ($PbMbO_4$). The acoustic wave propagates in a direction transverse to the propagation direction of the laser light through the crystal. The acoustic wave is produced by a piezo-electric crystal driven by a radio-frequency source and the wave is efficiently absorbed after passing once through the crystal. The acoustic wave transforms the crystal into a Bragg diffraction grating (see figure 6-11) owing to the variation of the material's index of refraction between the planes of compression and rarefaction. The grating, however, is moving at the speed of the acoustic wave. Consequently, light beams incident at the Bragg angle are diffracted and the frequency of the diffracted beam is shifted up or down by the frequency of the acoustic wave. The Bragg angle is typically a few mrad. Up to 90% of the output energy is in the frequency-shifted Bragg reflection, the balance of the energy being in the straight-through (zeroth) order. The intensity of the diffracted beam increases with the intensity of the acoustic wave and this relationship can be exploited to make a fast light switch. If the acoustic wave is switched off, the first order Bragg reflection disappears and the light is transmitted in the zeroth order. This takes place in ≤ 200 ns (depending on beam diameter), which is much faster than any mechanical shutters, which typically take ~1

ms to operate. As the zeroth order is at an angular separation of about 1°, it is easily blocked. The frequency of the acoustic wave may be scanned over a range from 60 to 100 MHz, allowing corresponding scanning of the output light frequency. This allows very precise voltage-controlled shifting of the laser frequency, with a resolution of ~ 4 kHz.

The spatial quality of a beam passing through an AOM may suffer owing to a lensing effect caused by a temperature gradient which appears in the crystal. Where necessary, we minimise this effect by contracting the beam diameter before it passes through the AOM. Because a single AOM cannot produce light frequency shifts less than 60 MHz, two AOMs are needed to produce small shifts. The first gives a fixed detuning of, for instance, –80 MHz and the second gives a variable 'retuning' of +80 ± 20 MHz. The nett result is a tuning range of ± 20 MHz about zero. The effective frequency shift of an AOM may be increased by using it in a 'double-pass' arrangement, as shown in figure 6-12.

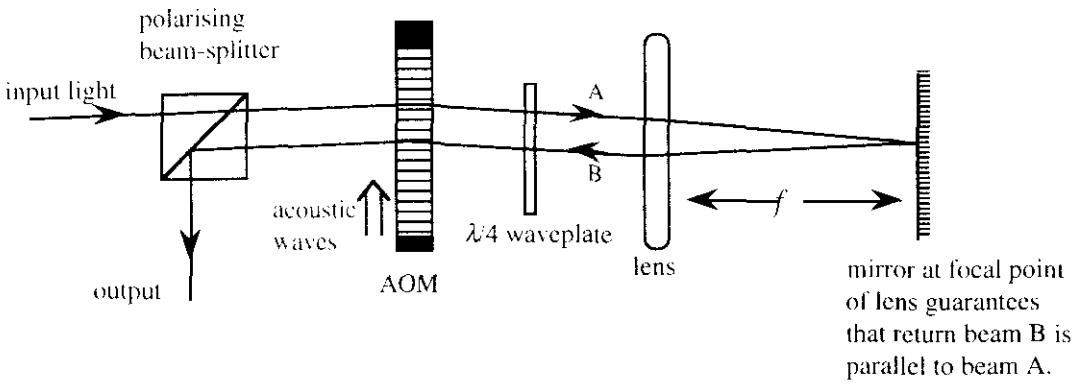

Figure 6-12 An AOM double -pass arrangement

In the double-pass arrangement, the light passes twice through the AOM and its frequency is down(up)-shifted twice, thus allowing shifts in the range 120 - 200 MHz. The two passes through the quarter-wave plate give a total rotation of the input linear polarisation through 90°, so that the light follows a different path on its return to the beamsplitter.

The makes and specifications of the AOMs used in our set-up are:

Crystals:	Isomet 1205C-2-804	
Drivers:	Isomet 232A 2	(fixed frequency)
	Isomet D322B-805	(variable frequency)

They have three main uses in the experiment, as follows. Firstly, they may be used as a fast on-off switch for the laser beams using either the technique described above, or alternatively by rapidly shifting the trapping frequency by 200 MHz. Secondly, they may be used to scan the frequency of spectroscopic probe beams with a high resolution ≤ 10 kHz, and at variable rates. Thirdly, they are useful when servo-locking the external cavity laser frequency to the atomic absorption lines. The external cavity laser gives the best frequency stability (both long and short term) when locked at a frequency corresponding to an extensive section of steep slope on the saturated absorption versus frequency curve. However, such locking

points do not usually coincide with the desired trapping frequency range, so we use an AOM to shift the well-locked frequency to the desired trapping frequency. In our specific case, for ^{85}Rb at 780 nm, we lock at a point ~140 MHz higher than the $F = 3$ to $F' = 4$ hyperfine transition, and use a double pass AOM to downshift by 160 ± 40 MHz, resulting in a range of detunings from -10Γ to $+3\Gamma$.

6.2 Magnetic fields in the experiment

6.2.1 Anti-Helmholtz coils

The magneto-optical trap (MOT) requires a uniform magnetic field gradient along each of three orthogonal axes, with a zero field at the centre. Such a field is the quadrupole field provided by an 'anti Helmholtz' coil pair (see figure 6-13), which have the same geometry as a Helmholtz pair but with opposed current circulation in each coil.

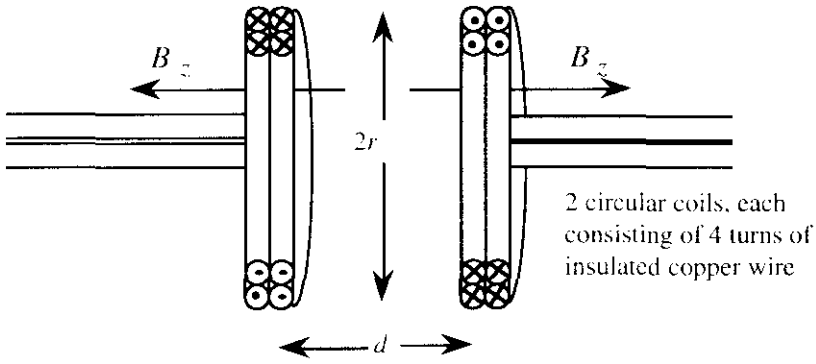

Figure 6-13 Anti-Helmholtz coils, as fitted to the 'metal' vacuum cell

For a given radius r, the maximum gradient at the centre of the axis is obtained when the separation $d = r$, and is given by $\partial B_z/\partial z = 0{\cdot}86\mu_0 NI/r^2$, where N is the number of turns on each coil and I is the current. The gradient at the centre along the other two axes has half this value, which follows from div $\mathbf{B} = 0$. The most uniform gradient is obtained when $d = \sqrt{3}r$, but has only 75% of the magnitude obtained for coils of the same radius r and $d = r$. If required, field gradients at positions off the central axis may be calculated numerically by a computer programme. Because the wire diameter itself occupies a significant proportion of the coil separation, a more accurate value for the gradient is obtained by calculating the field due to each individual turn and summing the results. When designing the MOT anti-Helmholtz coils, the exact ratio of d to r adopted is not a critical factor and is likely to be determined by other considerations such as the available space.

Typical values for field gradients in an MOT vary in the range $\partial B_z/\partial z = 2$ - 15 Gauss cm^{-1}, which can be achieved in practice either by using a small coil (radius ~2 cm) with around $N = 4$ turns and currents between 5 -10 A, or by using larger coils with more turns (N scales as r^2 for a given field gradient). In the latter case, resistive heating may necessitate the use of water-cooled coils. Furthermore, large radius coils need many turns to achieve the

required field strengths, and as coil inductance is proportional to N^2, the consequence is a larger time constant when the magnetic field is switched on or off. In order to allow fast switching of the magnetic field, the small coil option has been adopted in this work in all three designs of MOT vacuum cell. The O.U. electronics workshop designed and built a computer controlled current driver for our anti-Helmholtz coils which switches the current from 10 A to zero with a time constant of 5 μs. The specifications of the coils in the two cells used in our experimental set-up are given in table 6-1.

	Coils in the glass cell	Coils in the metal cell
Radius	10.5 mm	19 mm
Separation	From 23 to 31 mm	From 26 to 30 mm
Number of turns	4	4
Wire	0.8 mm^2 c.s.a enamel-coated copper wire, outside cell	0.6 mm^2 c.s.a Kapton insulated copper wire, inside cell
Axial magnetic field gradient	1.75 $GA^{-1}cm^{-1}$ over current range 0 – 10A	1.32 $GA^{-1}cm^{-1}$ over current range 0 – 10A

Table 6-1 Anti-Helmholtz coil specifications

6.2.2 Nulling coils

Stray magnetic fields in the laboratory may be due to instruments, magnetised metal and plastic and of course the Earth's field. Though a small stray field (< 1gauss) will not interfere significantly with the operation of a MOT as a tool for collecting a sample of cold atoms, there are other experimental arrangements where stray fields must be eliminated in the trapping region. This is vital, for instance, to observe sub-Doppler cooling in molasses, where a small Zeeman shift in the transition energy can swamp the light shifts which give rise to sub-Doppler cooling. In such a case, a typical requirement is for a spherical zone of radius at least 3 mm in which the field is less than 10 mG. Such a zone of near zero magnetic field is achieved by the use of three Helmholtz pairs, one to cancel each of the three components of the stray field. For a circular Helmholtz coil pair, the ratio of the coil separation to the coil diameter is 0.5; for a square Helmholtz coil pair, the ratio of the separation to the side of the square is 0.54.

The sizes of the coils and currents used in this work are shown in figure 6-14. The coils are wound onto a sturdy aluminium frame designed to double as a mount for other apparatus such as optical components. Precautions are also taken to avoid stray magnetic fields due to parts of the apparatus, by using non-magnetic material wherever possible, by keeping magnetised material at a suitable distance and by demagnetising objects such as the steel top of the optical table. With these precautions, the only significant stray field to be nulled is the

Earth's magnetic field (≈0.4 G) and this was measured to vary by less than 5mG cm^{-1} over the volume enclosed by the nulling coils. For a square Helmholtz pair of coil side $2r$, the fractional magnetic field variation for small displacements z from the centre of symmetry is of the order of $(z / r)^4$. It follows that the magnetic field at the centre of our nulling coils is uniform to within < 0.1% of the Earth's field over a sphere of ~ 2 cm radius, when the coil currents are optimal.

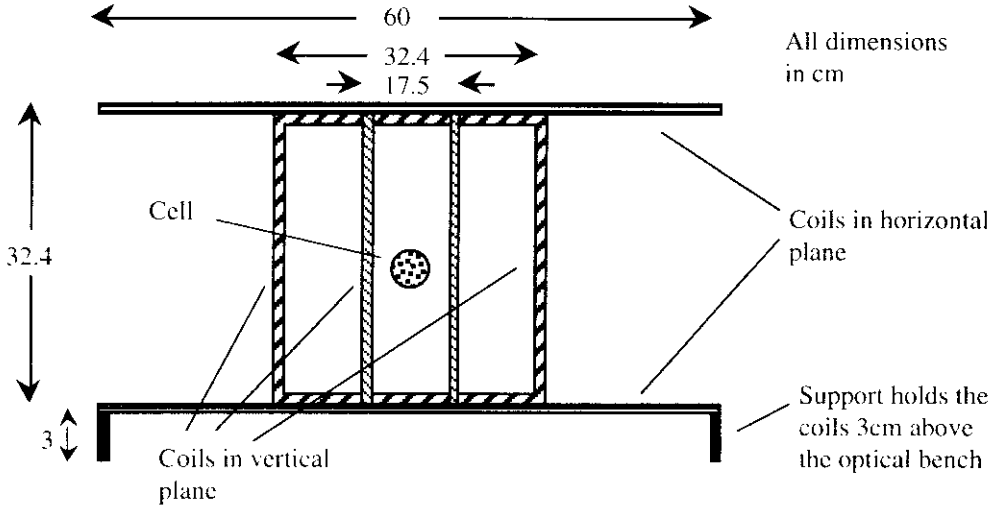

Figure 6-14 Helmholtz coils to null the Earth's magnetic field

The current settings giving a central zero-field were initially obtained to within ± 3 mgauss by use of a Hall probe. Another method is possible when the MOT is fully operational. For well-balanced beam intensities, the MOT atom cloud always forms at the magnetic field zero, which has a position determined by the anti-Helmholtz coils plus any residual, uncancelled field due to the Earth. When the anti-Helmholtz gradient is high, any shift in the field zero position due to the (relatively small) residual field is also small. As the anti-Helmholtz gradient is reduced, the shift in the zero field position due to the residual field becomes relatively larger, resulting in a visible movement of the cloud position. When the residual field is itself zero, however, the cloud position does not move as the anti-Helmholtz gradient is changed, and thus the correct setting for the nulling coils may be identified. We are not presently able to use this method, as our current set-up with the 'glass' cell has a beam intensity imbalance due to the surfaces of our glass cell not being anti-reflection coated at 780 nm. This results in the retro-reflected beam in each counter-propagating pair having an intensity estimated to be 78% (at the trap position) of the ingoing beam.

6.3 Vacuum cell design and operation for an MOT

Several factors influence the design of a vacuum cell for laser cooling and trapping of rubidium, and are discussed in the following subsections. Important factors include the need for: an ultra-high vacuum in the cell, control of the rubidium vapour pressure in the cell, space for magnetic field coils and good optical access to the cell.

6.3.1 Vacuum cell design

Ultra-high vacuum and the MOT

An ideal vacuum cell for an MOT would contain only a 'background' vapour of alkali metal atoms at a saturated vapour pressure that can be varied between ~10^{-9} and ~10^{-7} torr (see figure 6-15). Lower pressures than 10^{-9} torr result in a loading rate into the trap which is very slow. Greater pressures than 10^{-7} torr result in a background number density (of hot atoms) greater than ~ 10^{10} atoms cm^{-3}, which is a typical number density for cold atoms in the trap, and the trap is 'swamped'. Ideally, the number of 'foreign' atoms such as water and hydrogen in the cell would be zero, but in practice, even with the best vacuum technology, a partial pressure due to foreign gases is inevitable. The foreign gases are acceptable provided their partial pressure is less than the desired rubidium background vapour pressure. Thus the vacuum system should be capable of achieving a vacuum of ~10^{-9} torr or better. This pressure region is known as the ultra-high vacuum region (UHV) and its production entails the use of specialised vacuum hardware. Good sources of information about vacuum science and system design are listed in [265].

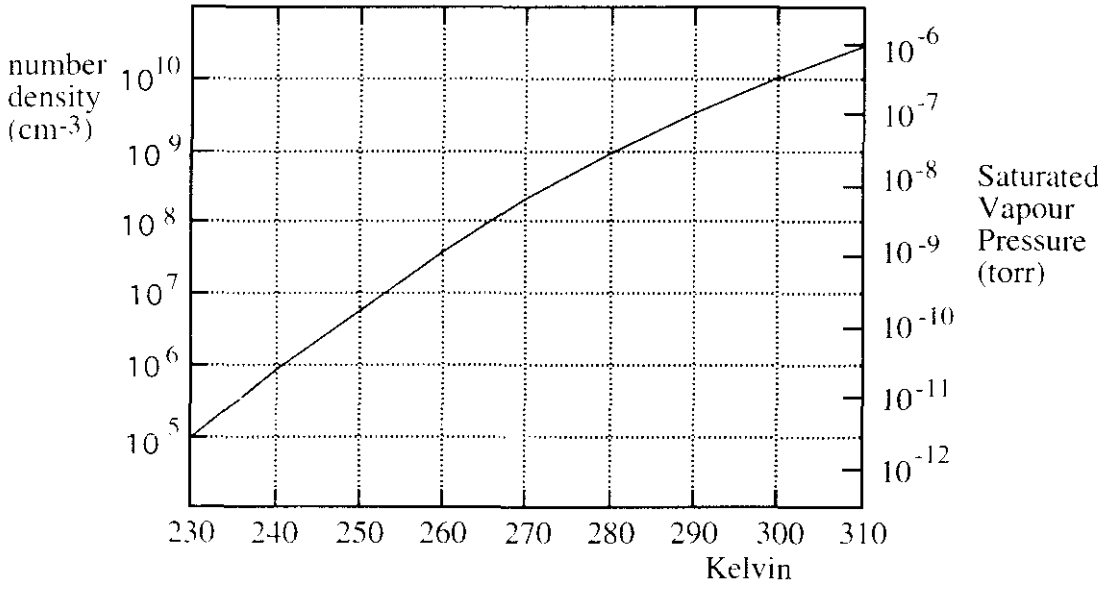

Figure 6-15 Saturated vapour pressure of rubidium, taken from [266]

The UHV region is characterised by molecular flow rather than viscous flow, meaning that the molecules rarely interact with each other, each molecule bouncing around inside the vacuum chamber at random until it enters the pump inlet and is removed. Once the bulk of the atmospheric gases have been pumped out of a system and the residual gases adsorbed on the walls have become 'unstuck' and pumped away, the main obstacle to achieving UHV pressures is 'outgassing', whereby gas molecules absorbed within the material of the vacuum system walls diffuse into the chamber. The choice of suitable construction materials for UHV systems is limited to those with sufficiently low outgassing rates and there are just three in common use: glass, ceramics or stainless steel. Very small areas of oxygen-free

copper and some special materials, e.g. Kapton, are also usable inside the vacuum system. Stainless steel is a commonly used material for the body of UHV systems because most shapes are easily fabricated, but it outgasses hydrogen at a rate which must be taken into account in vacuum system design. (The outgassing rate for a stainless steel after a 4 hour bake-out at 200 C° is of order 5×10^{-11} torr ls^{-1} cm^{-2}). In stainless steel UHV systems, the residual pressure is due almost entirely to H_2 molecules outgassed from the surfaces of the system walls, valves and connectors. There may also be permeation of helium through any glass walls or windows, but the helium inflow (per second per unit area) via such routes is usually one or two orders of magnitude less than that the inflow of hydrogen due to stainless steel outgassing[265]. Because of their low outgassing and permeation rates, glass and ceramics are ideal vacuum materials, but present difficulties in the fabrication of exact shapes. For instance, perfectly flat glass windows are not possible owing to the thermal stresses introduced when the windows are fused to the structure at temperatures around 800°C. Such high temperatures would also damage any optical coatings previously applied to the windows and thus optical coating of only the outer window surfaces (after fabrication) is possible. Wieman et al [267] have experimented with all-glass arrangements including glass valves and non-stick coatings on the internal surfaces in relation to the trapping of rare isotopes.

Thus the first design choice to be made is whether to build the cell body from glass or stainless steel, each of which has advantages and disadvantages. In our case, two cells were designed and built, one from glass and the other from stainless steel. These are described shortly. Owing to outgassing from the internal surfaces, an ultra-high vacuum system must be pumped on continuously, and a second choice to be made is which type of vacuum pump to use, the options being: oil diffusion pumps, turbo pumps or ion pumps. Both diffusion and ion pumps are used in our vacuum system designs and described in sections 6.3.3 and 6.3.4.

A final necessity is some means of loading the cell with rubidium vapour and then controlling its partial pressure. Loading is accomplished by attaching a small reservoir (~ 1 gm) of rubidium to the cell via an UHV valve. The trap is loaded by gentle heating of the reservoir whilst the valve is open, resulting in flow of rubidium atoms into the cell where they immediately condense onto the ultra-clean surfaces inside the cell. As the vacuum cell must be continuously pumped, the background alkali metal atoms are also continuously pumped away. In theory, a steady state background pressure may be obtained by judicious balancing of the input rate from the reservoir against the pump extraction rate, achievable by adjusting the reservoir or 'cold finger' temperature. In practice, we initially load the cell with enough rubidium to enable resonance fluorescence to be observed and then shut off the reservoir. The rubidium partial pressure in the cell then gradually falls as the atoms are

pumped away; this happens sufficiently slowly for the pressure to be regarded as steady state for most experimental purposes.

Optical access to a vacuum cell

Another design requirement is that there should be good optical access to the cell interior for the trapping beams, usually in an orthogonal arrangement, but possibly also for beams in a tetrahedral arrangement[205]. Access is also required for probe beams at various angles and other diagnostic instruments, for instance a CCD camera to view the cloud. The cell windows must be strong enough to withstand the pressure of the atmosphere across their surface and must have good transmission properties at all wavelengths of interest. Also, depending on the experiment, the cell windows may be required to be optically flat, anti-reflection coated or made of special material etc. For normal MOT trapping, optical flatness is not important[29]. However, the optical flatness of windows is important in any studies of localisation of atoms in optical potential wells, because distortion of the laser beam wavefronts changes the relative optical phases of the beams and may distort the structure of the 3-D interference pattern which gives rise to the atomic lattice. Such distortions may be caused by either small scale pits and scratches, or by large scale deviations from a perfectly flat surface. For such experiments, the acceptable degree of distortion may be calculated for pits and scratches by diffraction considerations and for large scale irregularities by calculating the wavefront deviations produced by the lensing effect of non-planar window surfaces. I carried out such calculations with the following conclusions. For distortions due to scratches and digs, I used the criterion that no more than 1% of the incident beam energy may be subject to diffraction by small scale surface imperfections. The result of my calculation was that spot sizes up to 0.3 mm are then acceptable, so long as they are rare. This corresponds to a standard Melles-Griot scratch/dig specification[268] of "50/30". For distortion due to large scale deviations from flatness, I used the criterion that across a 5 mm cross-section of the laser, chosen to correspond to the size of a typical molasses cloud, wavefront distortion should be less than $\lambda/10$. Thus to satisfy the criterion, a typical window of clear diameter 25 mm must be flat to better than $\lambda/2$ across its surface.

Vacuum cell design and anti-Helmholtz magnetic field coils

There must be space for the anti-Helmholtz coils either inside or outside the vacuum system. The shape and size of the vacuum cell are constrained if the coils are to be kept both small and on the outside of the vacuum cell. On the other hand, the positioning of the coils inside the cell necessitates the use of specialised UHV compatible materials. In either case, all the materials near the trapping region should be non-magnetic, so as to avoid remanent fields induced by the coil fields when the coils are switched off.

Combining all the considerations described in the previous subsection (6.3.1) into a practical vacuum cell design presents a tricky problem and inevitably involves some

compromise. We have three vacuum cells, representing different solutions to the design problem; they are now described below.

6.3.2 The preliminary vacuum cell

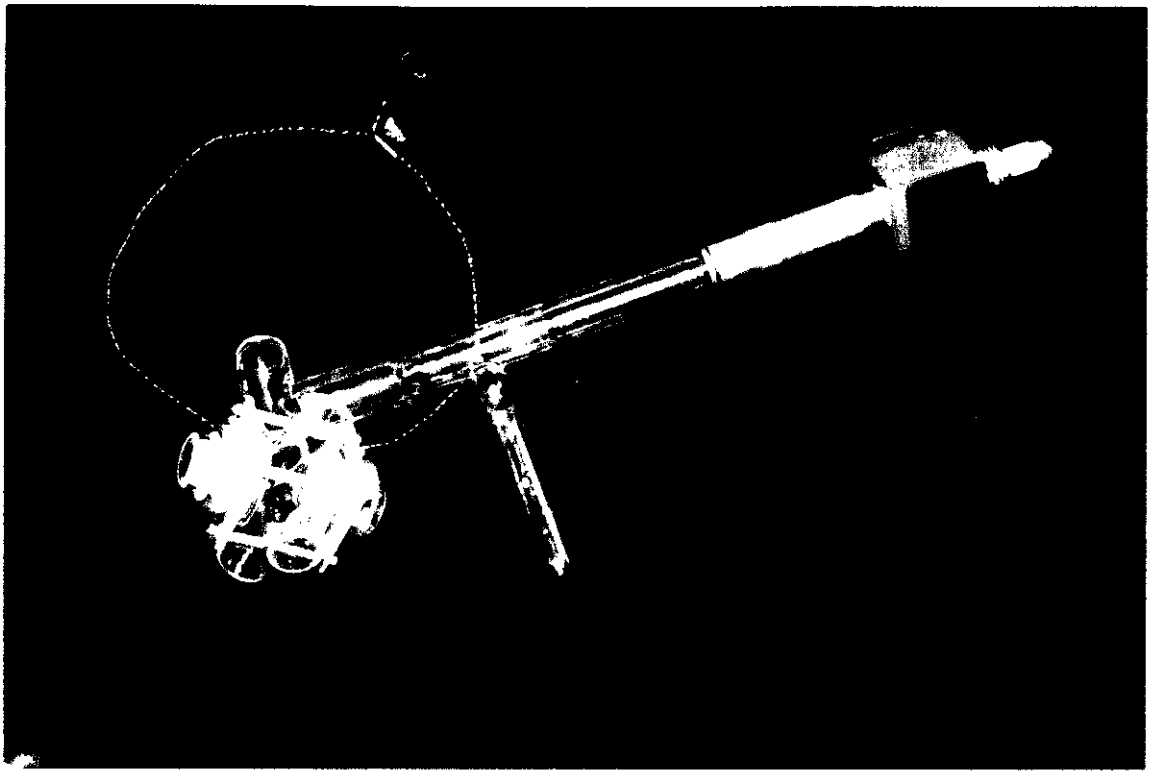

Figure 6-16 Photograph of the preliminary vacuum cell

Our first vacuum cell, in which we obtained our first MOT, was a small and simple cell consisting of a three-way cross of glass tubing (figure 6-16) with optical windows on each tube end. This cross was attached permanently and without valves to a rubidium cold finger and a 2 ls^{-1} (litres per second) ion pump. Anti-Helmholtz coils were attached on the outside of the glass cross. The glass-blowing was carried out by Mr S. Giles of the Clarendon laboratory, Oxford. The rubidium background vapour pressure was controlled by immersing the cold finger in either a water–ice mixture (0°C), or a methanol–dry ice mixture (-72°C).

The preliminary cell fulfilled its purpose, which was simply to allow magneto-optical trapping to be observed as a confirmation that all the laser controls and optics were operating according to their design. This was achieved twenty-two months after the inception of the project. This cell was not ideal for quantitative measurements for two reasons. Firstly, undistorted optical access was limited to zones of 15 mm diameter at the centres of the windows, and this space was used by the trapping beams. Pictures of the cloud had to be obtained through the curved contours of the tubes and were badly distorted. Secondly, after two months usage, the ion pump current gauge began to give erratic readings, causing us to doubt its pumping efficacy. As this was a sealed system, the only remedy would have been to start again with a new ion pump. However, we were meanwhile designing two new

vacuum cells with specific experiments in mind. These two designs, referred to as the 'glass' cell and the 'metal' cell, are now described.

6.3.3 The glass vacuum cell

The 'glass' vacuum cell, which we have been using for magneto-optical trapping in the laboratory since September 1994, consists mainly of a custom-made piece of 'Duran' glassware, in which two of the windows are mounted on the ends of glass tubes which intrude into central volume of the cell (figures 6-17, 6-18). The design has one large pair of windows to provide good optical access, whilst the small intruding windows allow small radius anti-Helmholtz coils to be fitted close to the trapping region, but outside the vacuum system. The third pair of windows are on the ends of two extruding glass tubes. The large windows facilitate viewing and probing of the trapped atom cloud over a wide range of angles (from 0° to 45° relative to the trapping beams) and also allow probe beams and detectors for time of flight measurements to be directed into the region directly below the trap.

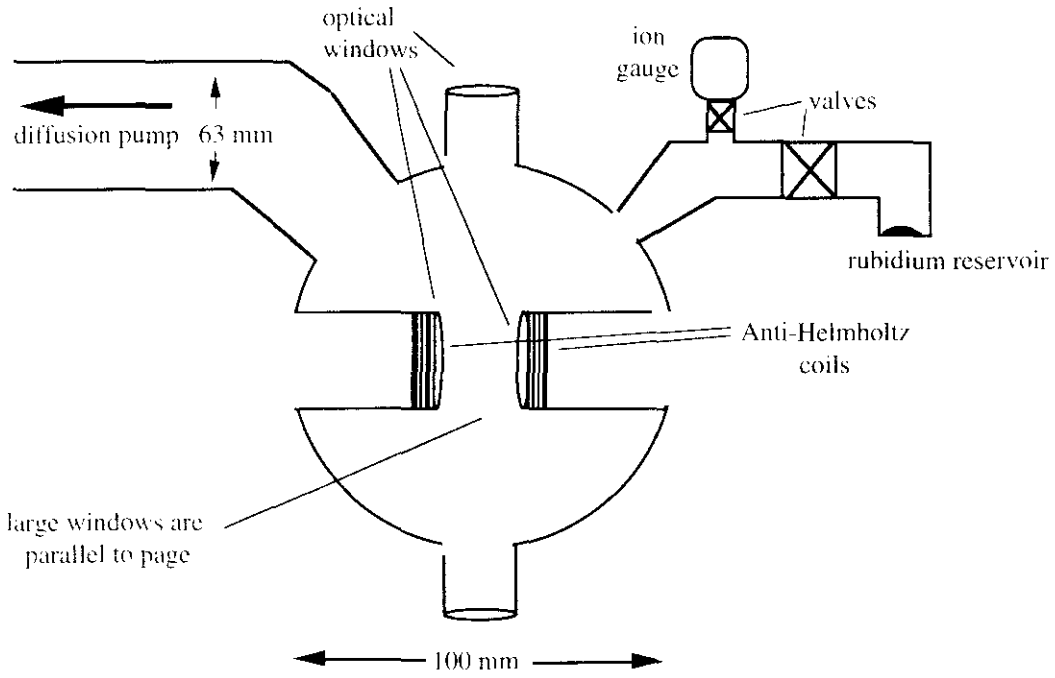

Figure 6-17 The shape of the glass cell

I tested the flatness of the windows of the glass cell after cell construction, using a laboratory-built Mach-Zender interferometer. The peripheral regions of the windows were strongly distorted owing to the glass-blowing process when they were sealed onto their tubes. I found that the central regions of all the windows were flat to better than 2λ (780 nm) for a 1 cm lateral translation across the window surface. (By central regions I mean within a diameter of 60 mm for the large windows and 15 mm for the small windows.) As the windows had been flat to within $\lambda/12$ per cm prior to the glass-blowing, this indicates that permanent distortions are produced within glass structures fabricated in this way, despite the

best efforts of the glass-blower. The measured flatness of $< 2\lambda$ per cm does not meet the criterion defined earlier for optical lattice experiments requiring wavefront preservation across a 5 mm molasses cloud. However, the measured flatness is sufficient to preserve a wavefront to within $\lambda/10$ over a 0.5 mm MOT cloud. I also measured the scratches and digs, and found that the cell fusing process had not changed them from their original manufacturer's specification of 40/20.

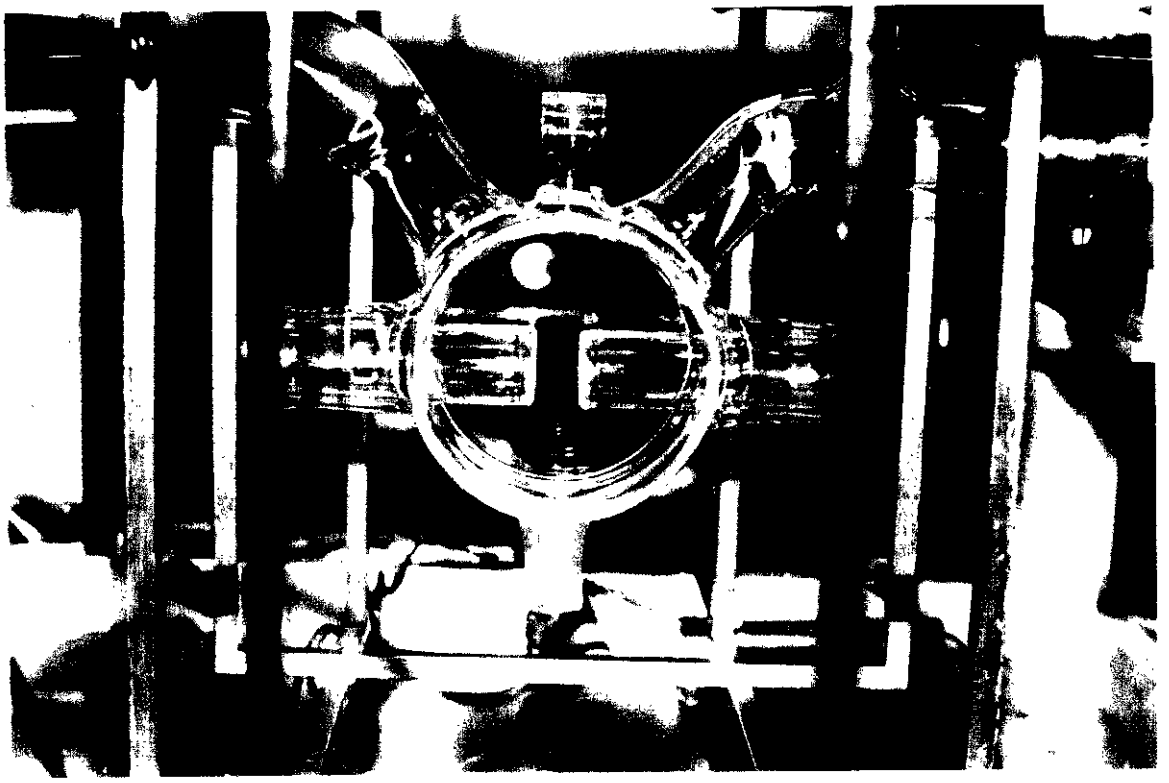

Figure 6-18 Photograph of the glass cell

Vacuum in the glass cell

The glass cell and pumping system were carefully designed with the object of attaining a vacuum of 10^{-9} torr or better. Though the internal surface area of the cell is large, as it is mainly glass (Duran), the outgassing is low and the helium permeation is negligible. The pressure is limited by the hydrogen outgassing from the steel in the valves and connecting pipes. The surface area of stainless steel was therefore kept to a minimum, although some steel has to be used, as the necessary UHV valves are only available in this material. The vacuum system is shown schematically in figure 6-19.

The pumping system for the glass cell consists of a water-cooled Edwards E02 oil diffusion pump, with pumping speed 150 ls^{-1}. It uses Santovac 5 oil (room temperature S.V.P. of 5×10^{-10} torr) and a backing pressure of 0.1 torr is provided by an Edwards rotary pump, model ES50. The critical backing pressure is 0.4 torr. The diffusion pump incorporates a liquid nitrogen trap, whose use is optional.

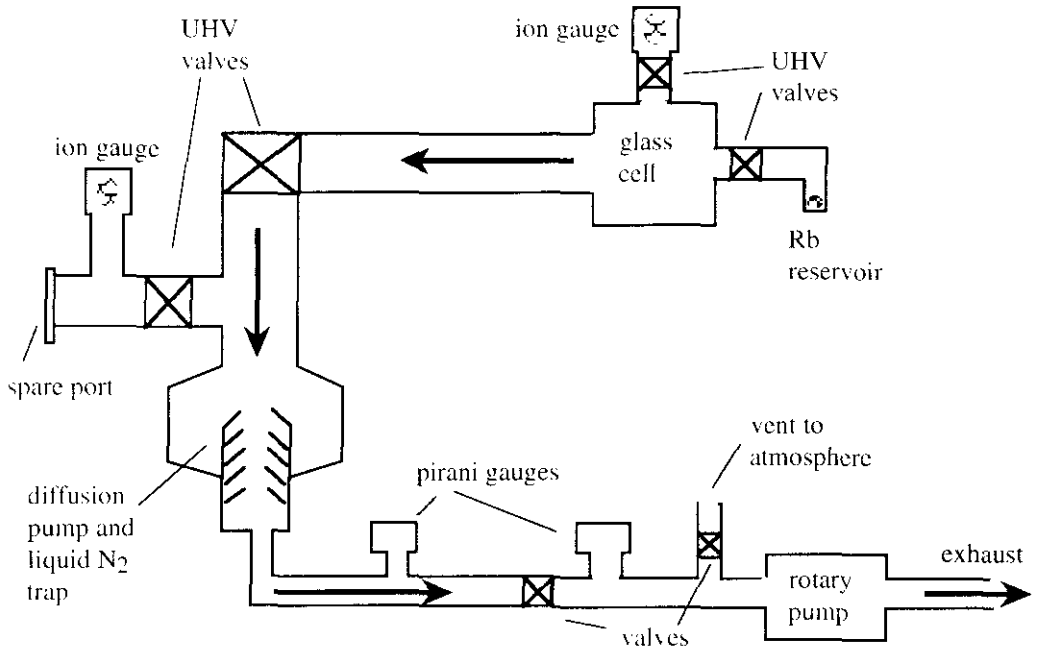

Figure 6-19 The vacuum pumping system

The cell is connected to the pump via a 63 mm diameter glass tube and bakeable all-metal UHV valve, sealed to the diffusion pump with a gold wire seal. Other system joints on the UHV side of the diffusion pump are of the Conflat variety, sealed with a copper gasket. The diffusion pump is fixed on the floating optical table via rubber mounts and the connection to the backing pump is made by a coiled rubber tube in order to minimise the transfer of pump vibrations to the laser cavities. Pressure measurements can be made at four points in the system. Two points on the backing line are monitored with Pirani pressure gauges (range 1 atmosphere - 10^{-3} torr). These gauges are used in roughing down the system pressure and as monitors of the health of the vital rotary backing pump. Two ion gauge heads (Edwards IG5G plus control unit Edwards Ion 7) are connected, one to the diffusion pump head and the other to the vacuum cell itself. These gauges measure pressure in the range 10^{-4} to 10^{-10} torr. Both gauges are connected to the system via valves to protect them from exposure to high ($>10^{-6}$ torr) rubidium pressures, as it was found that such exposure made them highly unreliable. However, they could be 'repaired' after such exposure by thorough baking out.

To prepare the vacuum cell for UHV operation, it was 'baked out' at 200°C for two weeks. The 'bake out' procedure consists of raising the temperature of the entire cell to around 200°C whilst pumping continuously with the diffusion pump, so as to remove a large part of the absorbed hydrogen and hence reduce the subsequent outgassing. An even temperature was achieved by wrapping the cell with electric heating tapes and insulating the whole with large glassfibre blankets. After baking out, the background pressure was measured to be 7 x 10^{-9} torr without liquid nitrogen and 4 x 10^{-9} torr when the nitrogen trap was filled. The pressure continued to drop slowly with subsequent pumping and after a further three months was 2 x 10^{-9} torr without liquid nitrogen.

Rubidium is stored in a reservoir attached via a valve to the vacuum cell. It can be distilled into the cell by opening the valve and heating the rubidium to ~45 °C. The cell is deemed to be 'charged' with rubidium as soon as the resonance fluorescence of a laser beam directed through the cell is bright. The reservoir valve is then shut and the system pumped on with the result that the rubidium pressure drops slowly. One such 'charge' of rubidium atoms allows trapping for about 8 hours before refilling is necessary. On the first occasion that rubidium was loaded into the cell, measurements of the absorption of a resonant laser beam in the cell showed that the number of atoms in the cell had a half-life of about ten minutes. However, after several cycles of charging the cell and pumping away the rubidium, the half-life settled to a value around seventy-five minutes. I do not know the explanation for this difference, but suspect that an important factor is whether the rubidium forms a monolayer with a large surface area or a compact multilayer when it condenses in the cell.

6.3.4 The 'metal' vacuum cell

A second vacuum cell, the 'metal' cell has also been constructed, but as yet has not been used. The prime considerations leading to this design, shown schematically in figure 6-20, were to produce a cell which enables: trapping and cooling with both 6-beam orthogonal and tetrahedral laser beam arrangements, the attachment and removal of very flat windows, a large range of probing angles and the attainment of an ultra-high vacuum. A secondary consideration was to keep the anti-Helmholtz coils as small as possible.

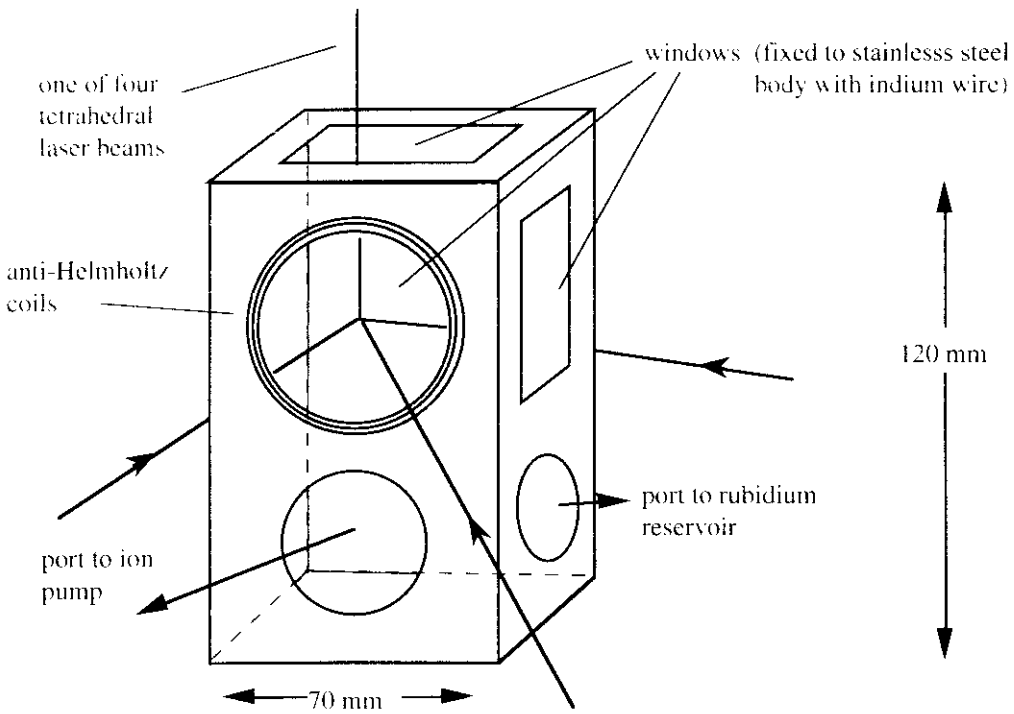

Figure 6-20 The shape of the metal cell

The metal cell was machined from a single piece of type-304 (non-magnetic) stainless steel. It is therefore compact in order to minimise the internal surface area of stainless steel, this

being the main source of outgassing. Outgassing rates for stainless steel depend on its bakeout condition, and are in the range ~10^{-8} to ~10^{-11} torr $ls^{-1}cm^{-2}$[265]. The internal steel surface area, including the short pump connecting tube, is 330 cm^2, which gives a total throughput of 3.3 x 10^{-8} torr ls^{-1}, assuming a reasonable outgassing rate of 10^{-10} torr $ls^{-1}cm^{-2}$. A large CF70 port connects the cell to an ion pump (PerkinElmer 20 litre sec^{-1} model 2032000) via a 15 cm stainless steel tube of diameter $1\,1/2$ inches. Dividing the throughput by the pump speed of 20 ls^{-1} gives an expected final pressure of ~2 x 10^{-9} torr, which is acceptable. As this estimate is based on a low outgassing rate, the cell will need to be thoroughly baked out. Two other ports allow connections to a vacuum roughing line and to a rubidium reservoir, both via bakeable all-metal UHV valves.

The cell windows are removeable, hence they can be matched to current experimental requirements, for instance anti-reflection coated for a specific wavelength, or polished to a high degree of flatness. Currently we have a set made of uncoated Spectrosil B, flat to $\lambda/5$ and scratch/dig 40/20, which meet my earlier criterion for low wavefront distortion and are thus suitable for experimental studies of large scale optical lattices (e.g.molasses clouds of 5 mm diameter). We also have one circular window made of sapphire, which is intended for studies on the $6P_{3/2} \rightarrow 6S_{1/2}$ Rb transition at a wavelength of 2.7 μm, for which sapphire has a good transmission of 82%. Sapphire also has good transmission properties throughout the visible and near infra-red spectrum. The windows are sealed to the polished (0.5 μm finish) stainless steel by a ring of indium wire, though nickel wire will be used whilst baking out the cell, as it has a higher melting point. My proposed procedure involves a swift changeover to indium wire after the bakeout, thus temporarily exposing the inside of the cell to the atmosphere, followed by rapid pumping down again. Provided this is done quickly, the outgassed material should not have time to rediffuse into the metal. The windows are shaped and positioned so as to allow the use of either six orthogonal or four tetrahedral cooling beams. They are also positioned so that the beams exit as well as enter through windows after passing through the trap, thus avoiding large amounts of unwanted stray light which would otherwise be reflected from the inner cell walls. Probing angles of up to 49° relative to the trapping beams are possible.

The anti-Helmholtz coils are positioned inside the vacuum chamber. They are wound with oxygen-free copper wire insulated by a Kapton (polyimide) coating and connected via beryllium/copper connectors to a UHV feedthrough in the vacuum cell wall. The proposed ion pump produces a very high local magnetic field of 600 Gauss at a distance of 1 cm, which falls off rapidly to a value less than that of the Earth (0.4 G) at a distance of 25 cm. It is desirable to position the pump close (~15 cm) to the cell in order to maximise the available pumping speed, hence it will be necessary to enclose the pump within a mu-metal cylinder.

This will shield the MOT zone from both the magnetic field and field gradient produced by the ion pump.

6.4 Diagnostic instruments

This short section describes the more important of the laboratory instruments used in our experimental work.

6.4.1 The CCD camera (charge-coupled device camera)

The cloud of trapped atoms may be viewed on a monochrome television monitor via an infra-red sensitive CCD camera (Cohu 4710), which has a peak sensitivity at 900 nm. The sensitive area is a rectangle 6.4 x 4.8 mm with 699 x 576 pixels. The fluorescence from the cloud is collected via a system of mirrors and a lens of numerical aperture 0.27 and focal length 145 mm (see figure 6-21). The system magnification is variable between x 0.5 and x 4. The solid angle of light collected varies with the magnification but is typically only 1/1000 of the total fluorescence emitted by the cloud. By imaging sharply defined test objects, I measured the depth of field of the imaging system to be better than ± 1 mm and the lateral resolution in the focal plane to be better than 50 μm at x1 magnification. These system details were measured by imaging test objects. A variable neutral density filter is included in the beam path, in order to avoid saturating the CCD chip when recording images.

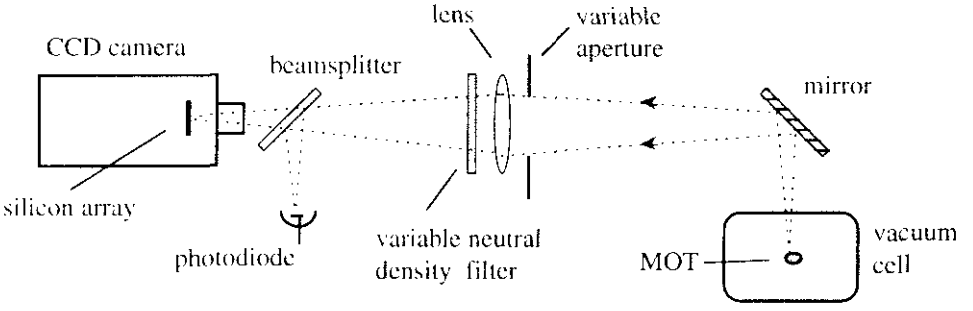

Figure 6-21 The trap imaging system

The video output from the CCD camera is also sent to a Macintosh LC computer where a frame-grabber software package called 'Mr Shot' from manufacturer 'Display Research Laboratories' allows the image to be digitised in a standard format (TIFF) and displayed on the computer screen. We also load the digitised pictures into another software (freeware) package 'NIH Image 1.49', which allows relative intensities at different points of the image to be determined. The CCD camera electronics are configured so as to give a digital output which is directly proportional to the input light intensity.

6.4.2 Light intensity measurement

Laser beam intensities are measured with a variety of silicon photodiodes. Thorlabs model FDS 010 and RS model BPX65 both have fast rise times of 0.9 ns and 3 ns respectively, and are suitable for examining the pulse shape of the N_2 laser used in this work(chapter 7). Thorlabs model FDS 100 is a general purpose high sensitivity, low-noise photodiode and is

used in the saturated absorption locking system. RS model 308-067 is also a useful general purpose photodiode as it contains an integral amplifier which results in a sensitivity of 4.5V μW^{-1}. A fraction of the fluorescence directed into the CCD is split off and an image of the cloud is focused on the active surface area of a photodiode (see figure 6-21). The photodiode signal can be used to calculate the total number of atoms in the cloud. Initially we used RS photodiode type RS308-067 for this purpose, however its active surface area is small (2.2 x 2.2 mm), and good alignment of the optics was critical. With a larger photodiode, RS 846-806, with area 6 x 6 mm, alignment is less critical and there is no danger that small movements in the position of the atom cloud will shift the cloud image too near the edge of the active area.

The absolute power of various laser beams is measured with a photodiode in a spherical integrator (Graseby model 2575) with a measurement range of 10^{-12} to 10^{-3} Watts and a sensitivity of $0.84 V m W^{-1}$ at 780 nm.

6.4.3 Miscellaneous diagnostic tools

The Burleigh WA-2000S wavemeter is a particularly useful instrument, giving quick readouts of the wavelength of sufficiently powerful laser beam (> ~0.1 mW) to within ±0.2Å. It can be used to monitor either the feedback conditions in the external cavity laser or the injection-locking conditions in the injected laser via a diagnostic output, which appears as a trace on an oscilloscope. This trace has a clear symmetry for a laser beam in a stable, narrow linewidth, monochromatic condition, but becomes disordered for other conditions, e.g.when sidebands are present, or mode-hopping is occurring. Occasional use is made of a Burleigh RC-46 spectrum analyser, with free spectral range 2 GHz and finesse 200, to determine laser linewidths, giving a resolution of 10 MHz. A handheld, battery-operated infra-red viewer (Electrophysics Electroviewer 7215) is a vitally useful tool in laser alignment procedures.

6.4.4 Computer control and data acquisition

We are able to control aspects of the experiment and acquire data with software (National Instruments 'NI-DAQ' version 4.6) run on two Macintosh LCII computers in the laboratory. The computers are fitted with digital to analogue circuit boards (National Instruments Lab-LC). A total of 16 analogue inputs and 4 outputs (–5 to +10V) are available. 24 lines of digital input/output and 6 counter/timer channels are also available. Possible functions include TTL switching, waveform and trigger generation, and data acquisition at rates up to 62,500 samples per second. At present we use the computer to switch the anti-Helmholtz coils and the acousto-optic modulator which controls the trapping frequency, and to record voltage data from any photodiode in our set-up.

6.5 Preliminary experiments

After a thorough bake-out, the glass cell was first used for magneto-optical trapping in August 1994. Since then various preliminary experiments have been performed as part of the process of testing and becoming familiar with the newly constructed system. These include experiments on the distribution of the atoms in the trap, and experiments aimed at maximising the number of trapped atoms. These experiments do not break any new ground, but they do constitute a prudent initial series of tests of our MOT apparatus, as our results may be compared with both theory and with the published results of other laser cooling groups.

6.5.1 Experiments on the distribution of trapped atoms

Studies of the distribution of atoms which we have made include the duplication of the collective effects reported in [175]. Figure 6-22 includes CCD images of our MOT with atoms in a gaussian 'ideal gas' mode (6-22a), in an 'orbital' mode (6-22b) and in an interesting 'helical' mode (6-22c), which, as far as I know, has not been previously reported. The final image (6-22d) shows evidence of large scale channeling of atoms[179] in a transient molasses obtained immediately after switching off the quadrupole magnetic field. The orbital mode picture was obtained by introducing large misalignments of ~20 mrad into two pairs of counterpropagating beams. The helical mode picture was produced by inserting a beamsplitter into the path of the trapping laser before it had been divided into three, and then adjusting its orientation until the helix was obtained. Presumably, the helix is caused by a combination of an orbital motion with a pushing force in the third dimension. The ideal gas mode picture was obtained by reducing the number of atoms in the trap. This can be done either by increasing the detuning or by decreasing the diameter of the trapping beams.

The spatial distribution of atoms in the cloud may be studied using the digitised CCD camera images, after loading them into the image analysis program 'NIH Image'. For the ideal gas mode, this enables measurement of the r.m.s radii of the cloud and confirmation of the expected gaussian distribution, as the intensity of the image is proportional to the (marginal) number density. As an example, I include results obtained for the ideal gas cloud imaged in figure 6-22a. The CCD camera views the cloud along a line perpendicular to the central axis through the two anti-Helmholtz coils (z axis) and figure 6-22a shows the expected ellipsoidal shape owing to the larger spring constant in the z direction. Figure 6-23 shows the fluorescence intensity profile plotted along a line passing through the cloud centre and parallel to the long axis. The intensity profile is well-matched by a gaussian curve, drawn by a computer curve-fitting program. After taking into account the CCD imaging system magnification of x1.5 to obtain the absolute horizontal scale, the r.m.s radii of the long and short cloud profiles were found to be 0.26 and 0.13 mm (±10%). The ratio of 2 to

1 is in accordance with MOT theory, whereby the spring constant along the x and y axes is half that along the z axis, i.e. proportional to the corresponding magnetic field gradients.

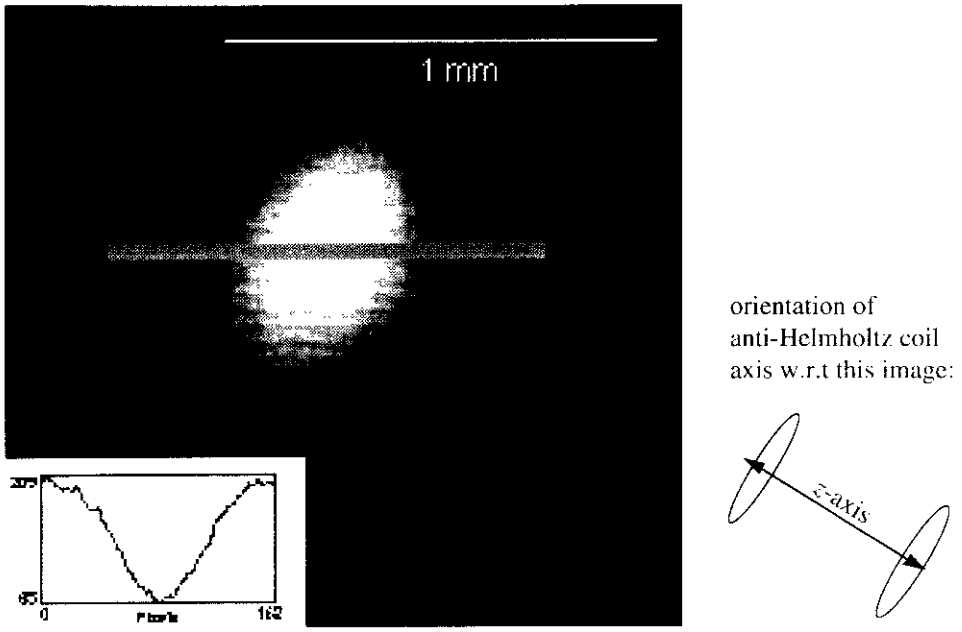

Figure 6-22a CCD camera image of the trapped cloud in the ideal gas mode with (inset) the (inverted) intensity profile averaged along the shaded bar.

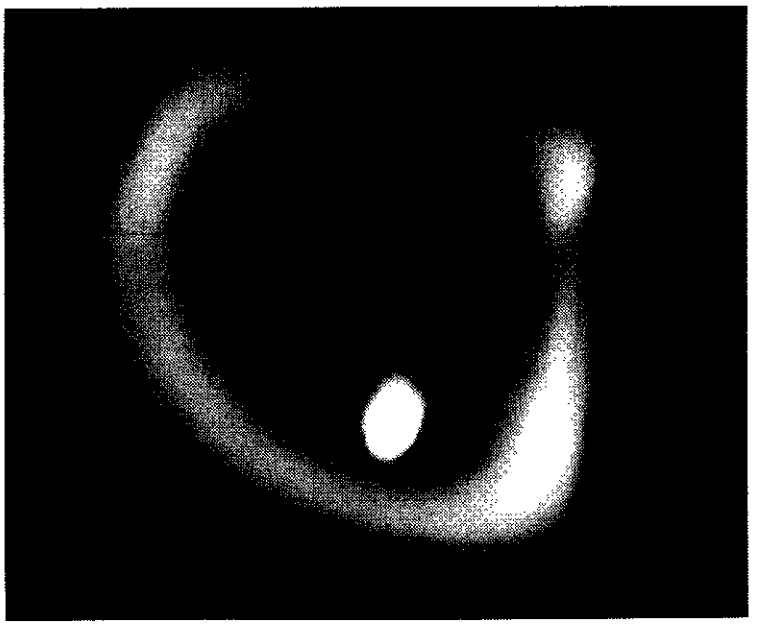

Figure 6-22b CCD camera image of the trapped cloud in the orbital mode

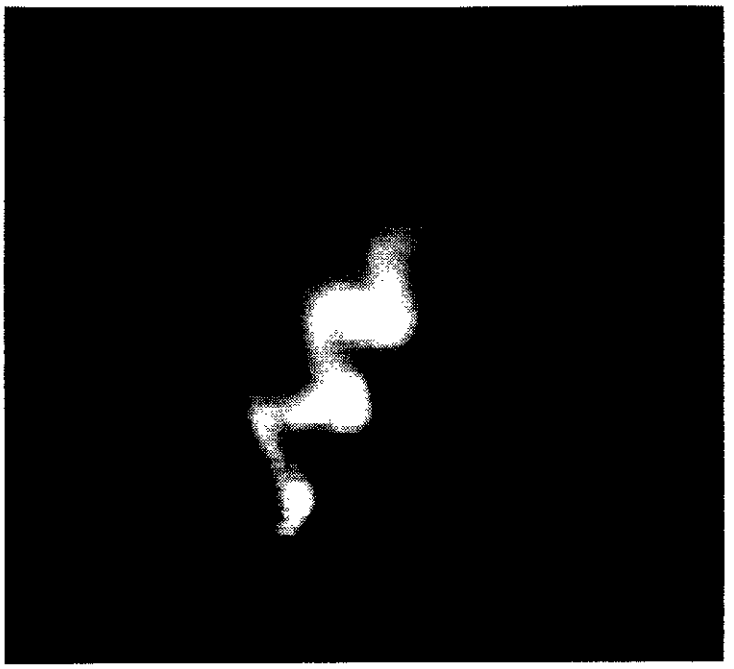

Figure 6-22c CCD camera image of the trapped cloud in the 'helical' mode

Figure 6-22d CCD camera image of transient molasses , showing large scale channelling of atoms

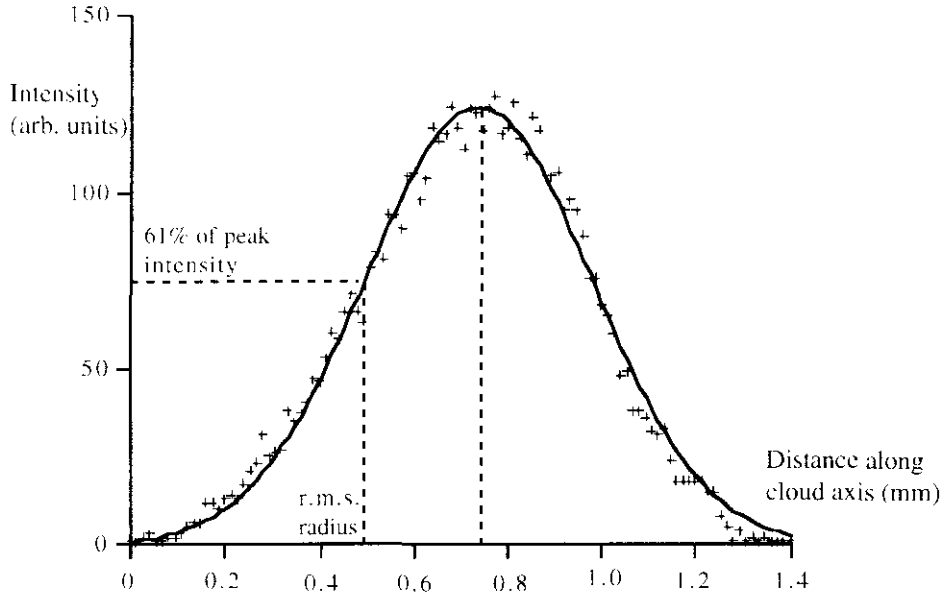

Figure 6-23 The intensity profile of MOT cloud fluorescence in the ideal gas mode (measured over the x-axis (long axis) of the cloud shown in figure 6-22a). The crosses are the measured data, the solid line is a fitted gaussian curve

6.5.2 Experiments on the number of atoms in the MOT

We have been particularly interested in the total number of atoms in our MOT, because preliminary calculations suggest that our proposed coherent transient experiments (chapter 7) will require $\geq 10^7$ trapped atoms. We determine the number of atoms in the MOT from a measurement of the intensity of the cloud fluorescence. The method is as follows. A beamsplitter in the imaging optics line diverts a part of the cloud fluorescence into a calibrated photodiode (see figure 6-21). The transmission factor for 780 nm light from the trap region through the various optics to the photodiode was measured to be 0.38 ± 5%, the remainder being diverted to the CCD camera or lost in reflections. The solid angle of fluorescence collected, which is determined by the distance of the variable aperture (figure 6-21) from the trap, is $6.77 \times 10^{-3} \pm 5$ % steradians. Thus the total cloud fluorescence may be calculated. (It is equal to 4880 times the power detected by the photodiode). Note that for each reading, it is necessary to subtract the small background fluorescence signal (~10%) due to the trapping beams alone, which is measured by turning off the magnetic field and thus losing the trapped atoms. In the final step, the number of trapped atoms is equal to the total fluorescence divided by the power scattered by one atom. The average power scattered by just one atom is calculated from the measured detuning and intensity of the trapping beams, as follows.

The fluorescence signal from the trapped atoms is almost entirely due to the $5S_{1/2}(F = 3)$ to $5P_{3/2}(F = 4)$ hyperfine component of the Rb D_2 line. This is because the laser

linewidth is less than the natural linewidth Γ of the transition, and any line-broadening (e.g. Zeeman or power broadening) present in the trap is of order Γ. Hence laser excitation of the nearby hyperfine transitions is negligibly small. The line strength of the $5S_{1/2}$ to $5P_{3/2}$ fine structure transition is obtained from tabulated results[269] and the electric dipole matrix element of the $F = 3$ to $F = 4$ hyperfine component[3] is then obtained via standard spectroscopic formulae[206,284]. The $F = 3$ to $F = 4$ hyperfine transition is a manifold of Zeeman transitions whose relative contributions to the fluorescence signal depend on the relative populations of the Zeeman sublevels and the local light field polarisation (via the Clebsch-Gordan coefficients). Although our MOT has uncontrolled time phases, the consequent fluctuations in the polarisation gradients are slow on the timescale for optical pumping, and so the average trapped atom is likely to be to some extent optically pumped. This matter has been studied in detail by Townsend et al[198], who point out that the effective (average) Clebsch-Gordan coefficient for the trap can lie between the limits of ~ 0.4, for a trap full of unpolarised atoms, to 1 for a trap full of polarised atoms cycling on the most stretched Zeeman transition. They measured the average Clebsch-Gordan coefficient for several caesium traps and found it to be 0.7 ± 0.2, i.e. that the average atom is partially polarised. I have assumed that the same value of 0.7 (and error of ±30%) applies to our rubidium trap when calculating the average power radiated by one atom.

This above method of determining the number of atoms is subject to several sources of error.

i) The photodiode is calibrated to ± 3%, and with the two 5% errors given for the optics transmission and solid angle above, this yields a combined error in the measurement of the total cloud fluorescence of ± 8%.

ii) The measured intensity of each trapping beam is subject to an error of ± 3%, primarily due to errors in measuring the beam waist. The absolute calibration of the detuning is subject to a large systematic error of $\pm\Gamma/4$, i.e.~10% to 20%, but relative measurements of detuning are precise to < 1%. Fortunately, the effect of the latter large systematic error on the calculation of the average scattering rate is small owing to the way the detuning appears in the calculation, and total errors in the average scattering rate are ± 3%.

iii) A third source of error is due to assumptions made in calculating the average scattering rate of one atom. The assumption that the trapped atoms scatter photons at an average rate given by 6 times the scattering rate of a single trapping beam will not be exactly correct, as it neglects the spatial variation of power-broadening due to gaussian beam profiles and to wavelength scale variations. The assumption that the atoms are partially polarised with an

---

[3] *The electric dipole matrix element is the same for each hyperfine transition, as opposed to the differing hyperfine line strengths given in appendix 8.*

average Clebsch-Gordan coefficient of 0.7 has its own error of ±30%, but this is diminished to <10% by the calculation when the atoms are strongly saturated, as in our case. After a careful analysis of these possible errors, I arrive at a conservative estimate of ±20%. Combining the various errors listed above yields a total error of ± 25%.

With the optical arrangement used when we first began trapping in the glass cell, we measured ~5 x 10^6 (±25%) trapped atoms for a detuning of ~ -1.5Γ, a power in each beam of 0.96 mW and a beam $1/e^2$ diameter of 5.5 mm. As one of our objectives was to trap more than 10^7 atoms, we decided to increase the diameter of the trapping beams which necessitated an increase in total trapping laser power in order to maintain the beam intensity. The necessary power was found by experimenting with different arrangements for the optical elements, particularly the AOM's, so as to minimise losses, and by increasing the injected laser drive current. The final arrangement is shown schematically in figure 6-1. We then expanded the $1/e^2$ beam diameter in stages from 5.5 mm to 9.2 mm and observed an increase in the maximum number of trapped atoms at each stage. We stopped at a diameter of 9.2 mm because this is the largest beam transmissible by our beamsplitters, waveplates and windows and also because it gives us a profile-averaged intensity slightly greater than the saturation intensity. The $1/e^2$ beam diameter is measured by scanning a 0.2 mm pinhole across the beam profile and recording the transmission as a function of the pinhole position.

Currently we have 10.6 mW available for trapping, to be divided between the three 1-D standing waves. Using the large diameter trapping beams, we have been able to trap as many as 5 x 10^7 atoms. The shape of the MOT cloud tends to be unstable for this number of atoms: it becomes very sensitive to laser frequency jitter, probably because of the intensity imbalance between counter-propagating beams. The number of atoms in the trap is also strongly dependent on the frequency of the repumping laser and the alignment of all the beams. All the measurements presented here were taken with the repumping laser tuned so as to give the maximum number of trapped atoms, but the alignment was not optimised to give a maximum number.

We have measured the variation of the number of trapped atoms with detuning and magnetic field gradient: the results are shown in figures 6-24a and 6-24b. Figure 6-24a shows that, with an intensity in each trapping beam close to the saturation intensity and for a fixed magnetic field gradient, magneto-optical trapping is possible for a range of detunings of width ~ 1.5Γ. The detuning which gives the maximum number of trapped atoms increases with the magnetic field gradient. Figure 6-24b shows that, for a fixed detuning and intensity, there is a value of the magnetic field gradient which maximises the number of atoms, and that larger gradients than this actually diminish the number of trapped atoms.

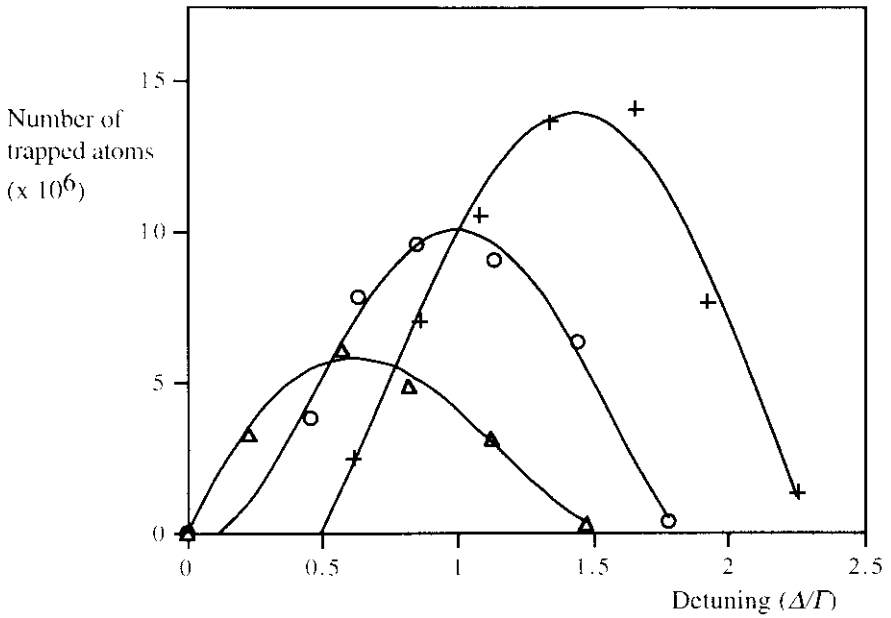

Figure 6-24a Graph of number of trapped atoms v. detuning for the MOT. The different symbols correspond to different values of the magnetic field gradient: triangles → 7 G cm^{-1}, circles → 12.25 G cm^{-1}, crosses → 17.5 G cm^{-1}. The Rabi frequency (1 beam) → 1.1Γ.

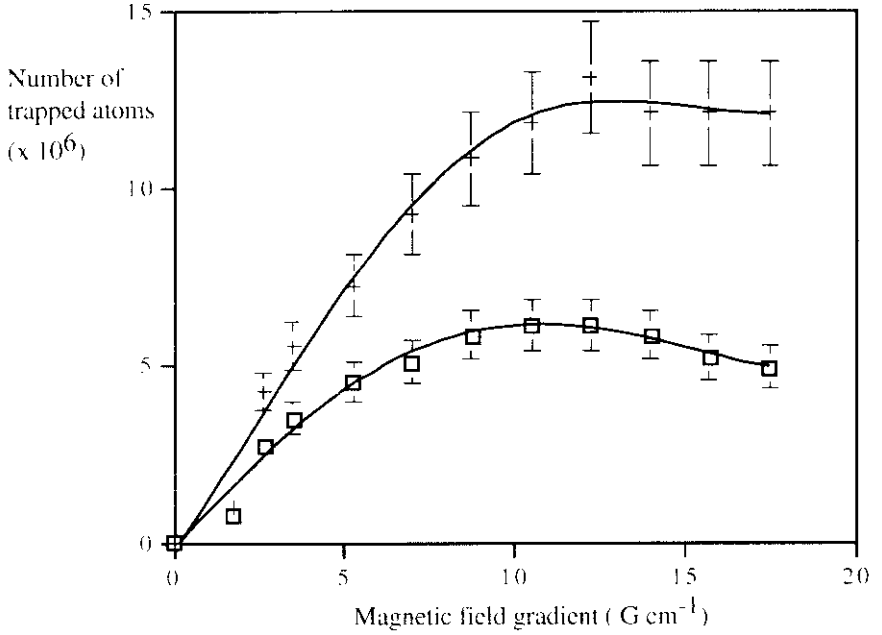

Figure 6-24b Plot of measured number of trapped atoms v. magnetic field gradient for the MOT. The crosses indicate a detuning of Δ = –1.2Γ, for the squares Δ = –0.85Γ. The Rabi frequency (one beam) → 1.1Γ

The results plotted in figures 6-24a and 6-24b are consistent with the theory of the MOT capture velocity described in sections 3.2 and 3.3.2, and in good agreement with results published in [57], which is a theoretical and experimental study of factors influencing the number of trapped atoms in an MOT. Increasing the detuning initially has the effect of

increasing the effective capture velocity and hence the number of atoms trapped (equation 3-12). However, as the detuning increases beyond the value corresponding to the maximum possible capture velocity (determined by the diameter of the cooling beams and the optimal deceleration) the number of trapped atoms diminishes. This behaviour is seen in figure 6-24a. Higher magnetic field gradients lead to a greater Zeeman shift for atoms in the outer capture regions of the trap. This can lead to a greater capture velocity, and hence to a greater number of trapped atoms, as discussed for a 1-D model of the trap in section 3.3.2. A 3-D analysis[57] of the MOT capture process with multilevel atoms is more complex, but can accurately predict the number of trapped atoms for all conditions. The results shown in figure 6-24b are in good agreement with those obtained in [57].

6.5.3 Conclusion of chapter 6

We have obtained results similar to those already observed by other groups, as a way of testing the design and construction of our apparatus and characterising our trap. In the light of the experience gained, possible improvements to our magneto-optical trap include the following:

Adaptation of the servo-lock electronics to include a small AC dither on the external cavity laser drive current. This should allow more precise location of the atomic resonance which is important, as detunings are measured relative to this reference. At present, our detuning measurements are only absolutely accurate to $\pm\Gamma/4 \approx 1.4$ MHz, though our relative detunings are known very precisely (< 10 kHz) as they are generated by an AOM.

Adaptation of the beam-routing so as to have six beams of equal intensity directed into the trap rather than three with subsequent retroreflection. This is because there is presently a large intensity imbalance of 78% between counterpropagating beams owing to reflective losses at our uncoated cell windows, which may be reducing the number of trapped atoms.

Normalisation of the saturated absorption signal used to lock the external cavity laser by referring it to the instantaneous intensity of the laser. This should eliminate the residual drift in the frequency of the laser, which is due to small fluctuations in the laser intensity affecting the frequency servolock stability. It may also be beneficial to stabilise the temperature of the saturated absorption cells against room temperature drifts.

At present, we are constructing and testing apparatus to make time-of flight temperature measurements, and expect[4] to have our first temperature measurements within weeks. As part of a programme to completely characterise our trap, other preliminary experiments currently in progress include a study of trap loading rates versus background pressure and a study of the number density of trapped atoms with intensity, detuning and magnetic field gradient.

---

[4] *The main delay is in fact due to waiting for parts to arrive!*

Chapter 7 Coherent optical transients and cold atoms

This chapter discusses the current and future work programme of our research group. Much of what is known about cold samples has come from experiments in which the sample is probed by continuous wave laser beams tuned around the cooling transition frequency. We intend to probe cold samples using pulsed laser beams tuned to resonance with transitions accessible from either the ground state or the excited state of the cooling transition (figure 7-1). The transient response of the system is expected to yield information on localisation, long-range order, light shifts and spectroscopic structure.

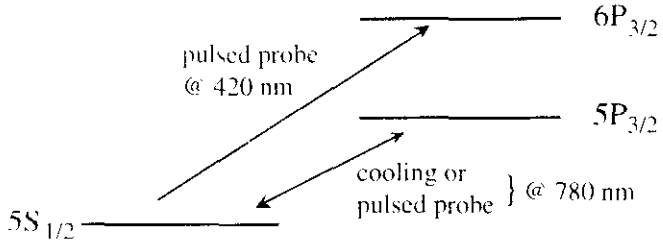

Figure 7-1 Rubidium pulsed probe transition

The use of resonant pulse sequences to probe spectroscopic samples has a long history. Various coherent optical transients have been used in Doppler-free studies of hot (room temperature) vapours to give information on level structures and collision processes. Some of these transient phenomena are discussed briefly in section 7.1. This is followed in section 7.2 by a description of a nitrogen-pumped dye laser that we have built to provide pulse sequences to probe laser-cooled rubidium. A proposal for a particular transient experiment for measuring velocity distribution (temperature measurements) in cold samples is described in section 7.3. Finally, in section 7.4, I discuss some of the factors that are likely to influence the time spectrum (pulse shape) of optical transients in cold samples.

7.1 Coherent optical transients and time domain spectroscopy

Time domain spectroscopy is a method of studying the interaction of light and matter using short laser pulses and is complementary to frequency domain, or continuous wave spectroscopy. Reviews are given by Berman et al[270], Shoemaker[7271], Mossberg et al[272] and Allen and Eberly[135]. The term 'coherent optical transient' refers to the coherent forward-scattered response of the probed sample to the pulse. In the domain of frequency spectroscopy, interest is often focused on the broadening of transition lines due to effects such as the natural lifetime, thermal motion or interatomic collisions. In time domain spectroscopy these effects result in different decay rates of optical transients following pulsed excitation. Coherent transients have been particularly useful as Doppler-free techniques for studying collisional decay processes in Doppler-broadened gases. There are the three main coherent optical transient effects, which are optical analogues of transient phenomena seen in pulsed nuclear magnetic resonance experiments on spin systems: 'optical nutation', 'free induction decay' and the 'photon echo'.

Optical nutation This is an alternating absorption and stimulated emission of radiation due to the Rabi oscillations which occurs transiently when an atom is first irradiated by continuous wave resonant light. For an isolated single atom, the oscillations are damped on a timescale of Γ, the natural lifetime of the transition. Nutation may be observed in an atomic sample at the beginning of irradiation and before the steady state population inversion is achieved, but the nutation damping rate is then also dependent on all the homogeneous line broadening mechanisms[271].

Free induction decay This is the rapid decay of the intensity of light emitted by a gas of atoms following pulsed excitation and is due to inhomogeneous broadening of the atomic transition. For instance immediately after the pulsed excitation of a room temperature gas, the radiation emitted in the forward direction by all the atoms is coherent and therefore has an intensity proportional to n^2, where n is the number density of the atoms. However the thermal motion of the atoms gives rise to Doppler shifts, and the spread of radiated frequencies causes a rapid dephasing of the radiation, which destroys the initial pulse-induced coherence. The time scale for free induction decay is approximately Δ_0^{-1} where Δ_0 is the frequency range excited by the laser pulse. If the whole Doppler profile of a room temperature gas is excited, the free induction decay time constant is of order 1 ns.

The photon (or optical) echo A photon echo is a delayed coherent emission of light from an inhomogeneously-broadened ensemble of atoms following a sequence of excitation pulses, due to a rephasing of the individual atomic dipoles. Photon echoes were first observed in solids (ruby) in 1964[274] and in gases in 1968[275]. The photon echo is the optical equivalent of the magnetic spin echo encountered in nuclear magnetic resonance experiments[276]. The simplest example is that of a two-pulse photon echo, which is

produced in an inhomogeneously-broadened sample of two-level atoms as follows. An atomic ensemble, initially in the ground state, is subjected to a short pulse of resonant light with pulse area[1] $\pi/2$, which puts all the atoms into a 50/50 superposition of the ground and excited states. This is depicted using Bloch vector diagrams in figures 7-2a and 7-2b. The Bloch vectors of the individual atoms then precess (in the rotating frame) at different rates owing to their different detunings, leading to a rapid dephasing of the macroscopic electric dipole moment (figure 7-2c). This is observed as a free induction decay. After a time τ, a second pulse with pulse area π is applied, which results in a 180° rotation of the Bloch vectors about the I axis (figure 7-2d). The individual Bloch vectors continue to precess, but now the dephasing process has been reversed, so that after a further time τ the Bloch vectors of all the atoms are 'rephased' on the II axis (figure 7-2e). At this point there is a macroscopic electric dipole moment, giving rise to coherent emission in the forward direction which is observed as a 'photon echo', provided that $2\tau \leq 1/\Gamma$, i.e. the atoms have not had time to decay spontaneously. However, the individual dipole moments continue to precess, so the echo is only a transient effect. Other diagrammatic treatments of photon echoes (in addition to the above Bloch vector picture) may be found in [272,277,278].

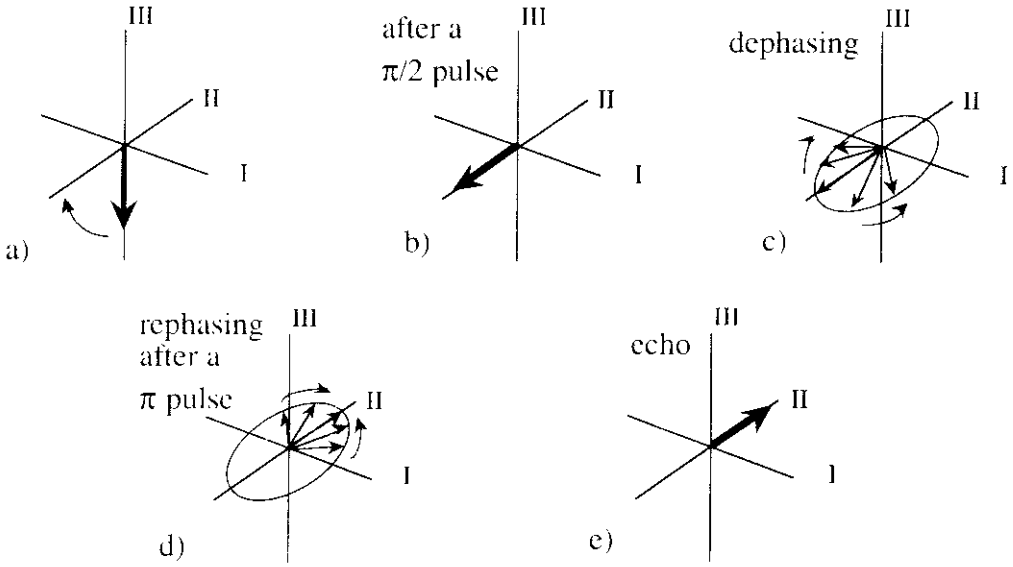

Figure 7-2 The formation of a two-pulse photon echo

7.2 A nitrogen-pumped dye laser for coherent transient studies of cold rubidium

The studies of coherent transients in cold rubidium atoms will be carried out using pulses from dye lasers on either the 5S to 6P lines at 420.2 and 421.5 nm or on the 5S to 5P lines at 780.0 and 794.8 nm, and this section describes some preliminary work involving the

[1] *Pulse area is defined by* $\int_0^{t_p} \Omega_0(t)\partial t$, *where* t_p *is the duration of a pulse which starts at* $t = 0$ *and* $\Omega_0(t)$ *is the Rabi frequency, which varies in time as the electric field amplitude in the pulse varies.*

production and testing of a dye laser operating at 420 nm. We were able to adapt a dye laser originally constructed to study the caesium line[279] at 457 nm.

7.4.1 The dye laser

The dye laser is pumped by a nitrogen laser (model LN 300 from Edinburgh Instruments) which produces pulses of duration 5 ns at 337 nm with a maximum repetition rate of 40 Hz. The bandwidth is about 150 GHz and the energy per pulse around 250 μJ, which is sufficient, when focused, to provide the high intensity ($>10^4$ W cm^{-2}) needed to pump a dye laser[280]. To operate the dye laser at 420 nm we use the dye 'Stillbene 420' from Exciton Ltd, which can lase in the range 400 to 450 nm. It is dissolved in methanol at a concentration of 2.0 x 10^{-3} molar (1.1 gm per litre) and contained in a cuvette with a magnetic stirrer. In order to obtain sufficient tuning precision and a sufficiently narrow linewidth, a 'grazing-incidence grating' arrangement[281,282] is employed, as shown in figure 7-3. The laser cavity is formed between two mirrors, of which one has a high reflectivity (>99%) and acts as a tuning mirror, whilst the other has a partial reflectivity around 85% and acts as the output mirror. The pump laser output is focused at a region just inside the dye cuvette by an elliptical lens which produces a cylindrical shaped region of high intensity pump light. Light in one or several of the dye laser cavity modes is amplified in the pumped dye region, and gains of up to 150 dB are possible after several passes[283]. The amplified light is incident at a large angle (88° to 90°) upon the diffraction grating and the first order of diffracted light is retro-reflected at the tuning mirror. The output wavelength of the dye laser is controlled by varying the angle of the tuning mirror relative to the blazed diffraction grating with 1200 lines mm^{-1}, thus retro-reflecting only a narrow band of wavelengths centred on the desired wavelength. The tuning mirror is a high quality etalon plate, flat to better than $\lambda/50$. The high angle of incidence results in a high intra-cavity dispersion, $\partial\theta/\partial\lambda \propto 1/\cos\theta$, where θ is the angle of incidence[280].

An additional laser amplification arrangement is available as shown, but preliminary measurements of power output suggest that it will not be required for our first experiments.

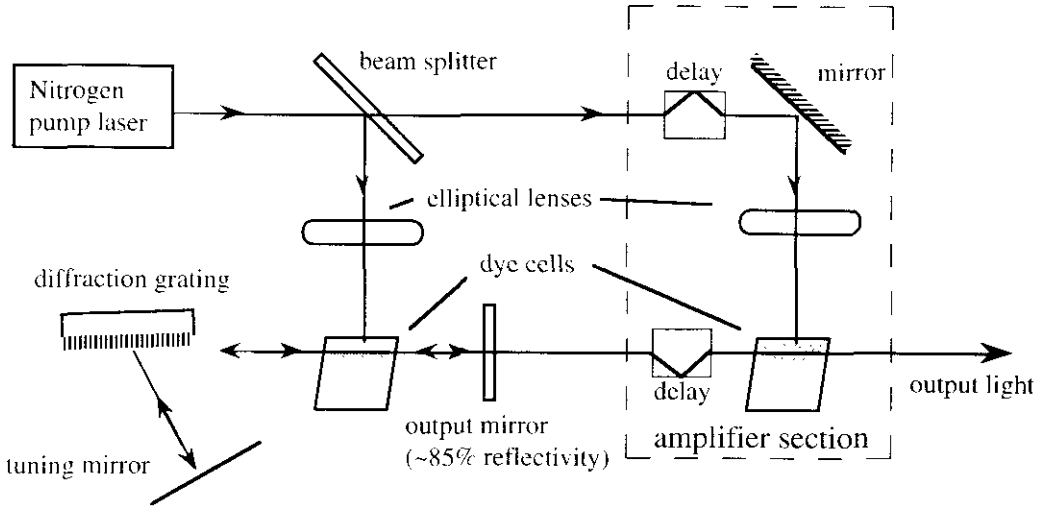

Figure 7-3 The dye laser and amplifier

Dye laser tuning

Coarse tuning of the dye laser is obtained by means of a fine-pitched screw (80 turns per inch) on the edge of the mirror mount and tunes at a rate 8.9 GHz per 1° of screw rotation. Fine tuning is obtained by a piezo-electric translator which pushes the edge of the mirror against the resistance of a flexed sheet of metal incorporated in the mirror mount. This allows tuning and scanning with a rate of 0.5 GHz per Volt over a 30 V range. Tuning is monitored in the first place by a monochromator which I calibrated using a rubidium spectral line lamp. The resolution of the monochromator is ± 0.1 nm, or ± 170 GHz. Tuning to within the rubidium transition is done by looking for fluorescence as the pulses pass through a rubidium vapour cell. To achieve this, it was necessary to heat the cell to > 200°C, whilst working in a completely dark laboratory. The acuity of the eye is considerably reduced at 420 nm, as it is close to the edge of the visible spectrum. Using a rubidium cell mounted so it may be heated with a hot-air gun and observed with a minimum of scattered light, tuning the laser close to the resonance is now relatively straightforward. The dye laser is first tuned close to the transition with the fine-pitched screw and may then be scanned by the piezo-electric control through the Doppler-broadened group of hyperfine lines which comprise the 5S to 6P transition. The Doppler width of each hyperfine component is 1.4 GHz FWHM at this temperature, and the total width of the group of lines about 4 GHz.

Dye laser mode structure and linewidth

The mode structure of the dye laser is monitored using a Fabry-Perot etalon with a free spectral range of 5 GHz, which produces a pattern of interference rings which are imaged by a Panasonic video camera. The etalon allows the output linewidth to be measured (as a fraction of the free spectral range) and adjusted by varying the angle of incidence of intra-cavity light at the diffraction grating. The high intra-cavity dispersion of the grazing-incidence design allows narrow output linewidths to be obtained, and I have measured linewidths in the range from a few GHz down to 250 MHz. When operating with lower

angles of incidence, i.e. with broader linewidths, several longitudinal modes of the laser cavity (mode spacing ~1.2 GHz) may be simultaneously active. With higher angles of incidence (narrower linewidths) we can achieve stable lasing where most of the output energy is in one cavity mode for > 80% of the pulse shots. When the angle of incidence is ~ 90° and intra-cavity dispersion at its highest, I found that the laser intensity fluctuates dramatically when the tuning is scanned. There are several possible explanations, one is that the narrow band of output wavelengths selected by the grating can fall between the mirror cavity modes, resulting in poor lasing action. Alternatively, at such a high angle of incidence, the effective reflectivity of the grating may be highly sensitive to small adjustments of the tuning angle; the blaze angle and the small area of grating which is normal to the beam may be relevant factors.

Our first proposed experiments (see section 7.3) require: the ability to tune the dye laser with an absolute resolution of ~200 MHz, a linewidth of ≤ 500 MHz and a frequency drift of ≤ 200 MHz for periods of several minutes. Tests conducted by observing how long the frequency remains within the 4 GHz Doppler width of the 420 nm transition show that the drift is less than 200 MHz per minute. Thus the frequency stability and linewidth are easily obtained with the current arrangement, however the absolute resolution, i.e. relative to the atomic transition, presents the following (temporary) difficulty.

The absolute calibration of the frequency relies at present on the identification of two distinct Doppler broadened peaks in the absorption profile, due to excitation of ^{85}Rb from the $F = 2$ and $F = 3$ hyperfine ground states respectively, separated by 3.04 GHz. Although we observe these peaks as the dye laser tuning mirror is scanned, to use them as a frequency reference, we must be sure that the scanning is continuous, i.e. that the laser does not mode-hop during the scanning process. From observations of the changes in the Fabry-Perot ring pattern when scanning, I estimate the tuning range achievable without cavity mode-hopping to be ~1GHz for high intra-cavity dispersion. With lower dispersion, a group of several adjacent modes are simultaneously active in different proportions from shot to shot. The frequencies of the laser modes are determined by the cavity length and the dominant mode(s) by the tuning mirror angle. At present the cavity length and tuning angle are coupled, as the pivoting action of the mirror affects the cavity length. This complicates systematic study of the scanning and mode-hopping. Several solutions are possible. Firstly, a second piezo may be added to the tuning mirror so that it pivots about its centre, i.e. with a piezo at each edge. Laser tuning may then be made either by rotating the tuning mirror with equal and opposite piezo movements or by altering the cavity length with equal and parallel piezo movements. A second solution is to rebuild the grating and mirror mounts with a geometry which results in the peak gain frequency of the grating scanning at the same rate as the frequency of the selected cavity mode. A third solution is to enclose the laser cavity in a pressure-controlled

box, in order to control the effective cavity length via the refractive index of the air. A fourth solution is to introduce a flat glass plate into the cavity, such that its rotation may produce small changes in the effective cavity length. Whichever solution is eventually adopted, the ensuing independent control of the two tuning factors should facilitate tuning of the laser to an absolute standard. This work will begin after submission of this thesis.

The output of the dye laser has been monitored with a fast rise-time photodiode (1 ns) fed into an oscilloscope and is seen to be roughly triangular shaped (rounded top!) with a FWHM of 5 ns.

Dye laser pulse energy

The output of our dye laser, when tuned to 420.2 nm, is measured with a silicon based pulse energy meter (Laser Precision model RJP 765) to be between 200 and 500 nJ per pulse depending on the linewidth in use. Narrower linewidths correspond to the lower pulse energies. The shot to shot pulse energies have a standard deviation of 7% when measured over 100 shots. I have calculated the energy P_π required for a pulse of area π on the Rb transition at 420 nm from first principles and with the aid of standard spectroscopic formulae[284]. I find that

$$P_\pi = \frac{\pi^3 h \varepsilon_0 m_e c^2 r^2}{3 f g e^2 \tau \lambda} \qquad (7\text{-}1)$$

where r is the radius of the laser beam (assumed circular with constant intensity profile), f is the oscillator strength (for absorption) of the transition, g is the (fine structure) Zeeman degeneracy of the ground state, τ is the pulse length and λ the wavelength of the transition. Using a reasonable experimental value of 2 mm for the diameter of the dye laser beam gives $P_\pi \approx 10$ nJ for $5S_{1/2}(F=3,m_F=3)$ to $6P_{3/2}(F=4,m_F=4)$ and σ^+ light. Comparing this with the typical output pulse energies of a few hundred nJ confirms that there is plenty of power in hand for diagnostics etc.

7.3 Proposed experiments on laser-cooled rubidium using coherent optical transients

7.3.1 Bragg diffraction from localised atoms

The direction and strength of transient response signals may provide information about the spatial distribution of cold atoms. The possibility of Bragg diffraction of light from the 'crystal' of atoms localised in optical potential wells was discussed in section 4.6.2. Short laser pulses with pulse area ~ π may be a useful tool to probe this spatial structure as each probe pulse involves only one photon recoil per atom, and the heating effect is thus minimal. Probe transitions other than the cooling laser transition may be used, allowing diffraction and detection at a variety of angles with respect to the cooling and probe beams. Thus, with a suitable choice of geometry and polarisation scheme for the cooling beams, it may be possible to unambiguously attribute Bragg reflection to atomic localisation[172,207].

7.3.2 Temperature measurement of laser-cooled atoms using coherent transients

Our first major experiment involving both coherent transients and cold atoms will be to measure the velocity distribution and temperature of laser-cooled atoms, as we proposed in [186]. The experiment has two steps. In the first step, two non-collinear laser 'pump' pulses are employed to imprint a spatial grating on the population of a chosen hyperfine ground state of rubidium atoms in either an MOT or molasses. Immediately after the two pulses, this grating will begin to disperse as a result of the atoms' thermal motion and collisional effects. In the second step, after a variable delay of order 1 to 10 μs, a laser 'probe' pulse is Bragg-reflected from this grating and the reflection detected. The intensity of the reflected signal will decrease as the variable delay is increased, because of the progressive dispersal of the population grating. The sequence of three pulses can be repeated many times at a rate of order 20 Hz to build up a curve showing the decay of the reflection intensity against the time delay of the probe pulse. This curve can be analysed to obtain the velocity distribution of the cold atoms. The above steps are now described in more detail.

Pulse sequence to write a ground state population grating

Figure 7-4 shows one of several possible pulse sequences to be employed in the proposed experiment. The three pulses may be derived from the same dye laser pulse by the use of beam splitters and optical delay lines, or by the use of two complete dye laser set-ups. The first two pulses, each of duration 5 ns, occur at times t_1 and t_2 and have wavevectors $\mathbf{k}_1$ and $\mathbf{k}_2$ at a relative angle α. They are applied immediately after the cooling/trapping beams are turned off, with $t_1 - t_2$ of the order of zero to 10 ns. The pulses, ideally both $\pi/2$ pulses, excite the ^{85}Rb transitions $5S_{1/2}(F=3)$ to $6P_{3/2}(F=2,3,4)$ at a wavelength $\lambda = 420.2$ nm. The pulse linewidths are of order 200 MHz, which is sufficiently broad to excite all three hyperfine levels (spacings ~30 MHz) of the excited state, whilst narrow enough to leave atoms in the $F=2$ hyperfine ground level (3 GHz away) unexcited.

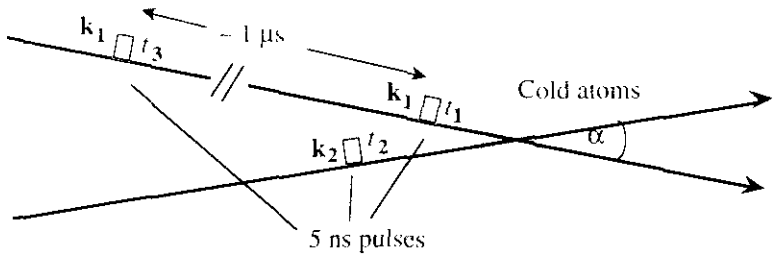

Figure 7-4 The pulse sequence to write and probe a population grating

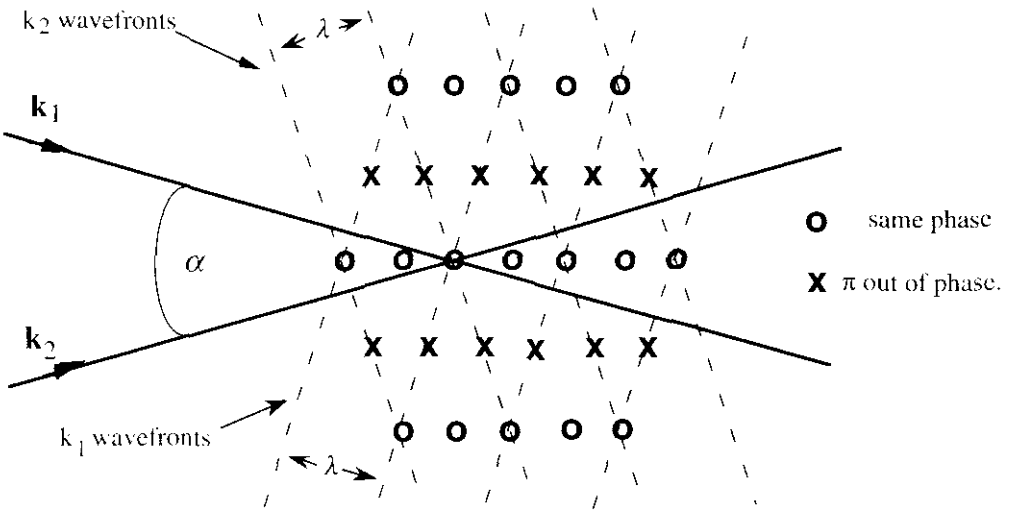

Figure 7-5 The interference of the first two pulses

Figure 7-5 shows the relative phases of the two pulses at selected points in space. At points labelled with a circle (O), the pulses arrive with the same phase, at points labelled with a cross (X), they arrive in antiphase. The relative phase $\Delta\phi$ at a point $\mathbf{r}$ is given by

$$\Delta\phi = (\mathbf{k}_2 - \mathbf{k}_1)\cdot\mathbf{r} + \omega(t_2 - t_1)$$

The important point is that the pulses have the same phase on parallel planes, forming a grating with a spacing $\frac{\lambda}{2\sin(\alpha/2)}$. For an angle $\alpha = 10^\circ$, this gives a grating spacing of 2.4 μm.

For atoms positioned along the lines (O) where the pulses are in phase, the effect of two almost consecutive π/2 pulses is the same as that of a single π pulse, and the atoms are raised to the excited state. Along the alternate lines (X) where the pulses are in antiphase, the effect of the first π/2 pulse, which is to put the atom into a superposition of the ground and excited state, is cancelled by the second π/2 pulse, which takes the atom back to the ground state (F=3). The excited atoms along the lines (O) then decay spontaneously into either of the F=3 or F=2 hyperfine ground states with a lifetime of 110 ns, and in a number ratio dependent on the line strengths and branching ratios.

Consider the effect of such a pulse sequence on the number of cold atoms in each of the two hyperfine ground states along lines (X) and (O), using approximate numbers to establish the principle. The relative populations before the two pulses depend on the intensity of the repumping beam; typically one might have steady state populations of (say) 95% and 5% in the F=3 and F=2 ground states respectively. Assume further for simplicity that in spontaneous decay approximately half the atoms decay to each of F =3 and F = 2. The result after the spontaneous decay is essentially complete (~200ns) is then as follows. Along lines (X) the populations of F =3 and F = 2 are in the ratio 95 : 5 (as before), but along the lines (O) the the ratio is ~ 50 : 50. Thus population gratings are created for both the hyperfine

ground states. In particular, comparing the populations of the F=2 state along the lines (O) and (X), we see that the ratio is approximately 10 to 1. This constitutes a 'ground state population grating' with high contrast. A more detailed version of the above argument must take account of the line strengths and branching ratios for each of the possible decay routes to the ground state, but results of the same order can be expected.

Transient reflection of a third pulse

A third pulse of 5 ns duration, ideally of pulse area $\pi/2$, and resonant with any transition starting from $5S_{1/2}$ will scatter coherently (be reflected) from the ground state population grating provided phase matching is respected (see figure 7-6). In our experiment, it will be convenient to use the $5S_{1/2}(F=2)$ to $6P_{3/2}(F=1,2,3)$ transitions accessible with our dye laser arrangement. Figure 7-7 illustrates the dispersal of the grating at a rate determined by the velocity distribution of the atoms. The energy of any reflected pulses will depend on the degree of contrast of the grating, and will diminish as the grating disperses. An estimate of the grating dispersal time T_g is given by the typical time taken for an atom travelling normal to the grating planes to travel quarter of a grating spacing

$$T_g \approx \frac{\lambda}{8v_0 \sin(\alpha/2)} \qquad (7\text{-}2)$$

where v_0 is the most probable velocity of the velocity distribution. T_g is of order 3 μs when the angle α betwen the first two pulse **k**-vectors is 10°. Note that in the ~200 ns required for the excited state population to decay to $1/e^2$ of its initial value, an atom with a velocity of 20 cm s^{-1} corresponding to the Doppler cooling limit will have travelled only ~40 nm, which is only 1/60 of the grating spacing.

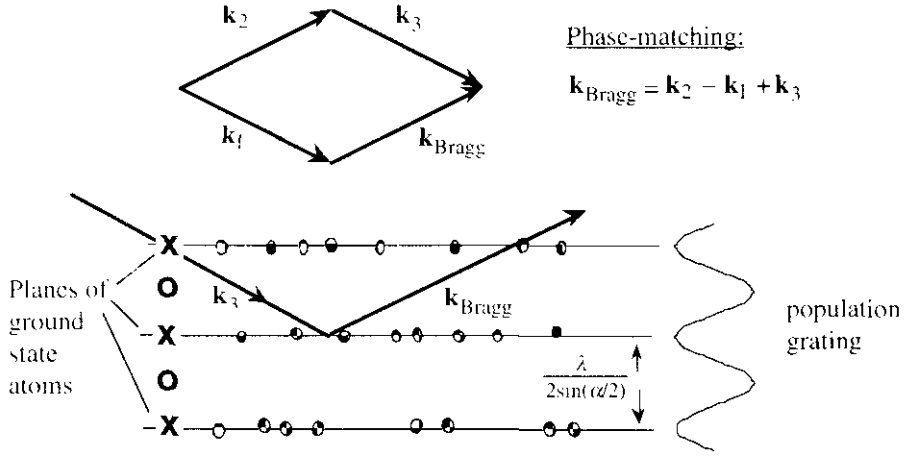

Figure 7-6 Bragg reflection of probe pulse and the phase-matching condition

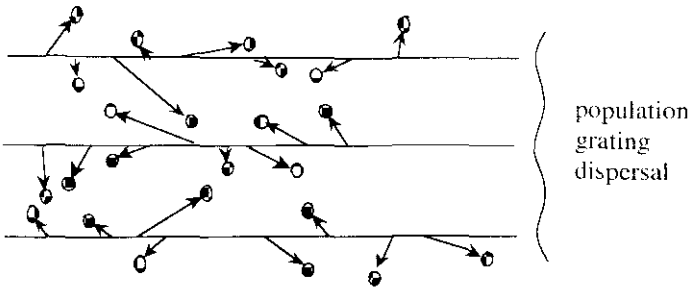

Figure 7-7 Probing the population grating and grating dispersal

We have calculated the reflected pulse energy P as a function of the time delay $t_3 - t_1$, where t_3 is the time at which the third 'probe' pulse occurs, and find that

$$P \propto \left[\int_{-\infty}^{\infty} \rho(v_n) \exp[-2iv_n k(t_3 - t_1)\sin(\alpha/2)] \partial v_n \right]^2 \qquad (7\text{-}3)$$

where $\rho(v_n)$ is the distribution of the velocity component v_n normal to the grating planes and k is the wavenumber of the probe pulse. Equation 7-3 shows that the reflected pulse energy as a function of $t_3 - t_1$ is the square of the Fourier transform of the velocity distribution normal to the grating. The velocity component v_n and the distribution constant $\sin(\alpha/2)$ can be chosen and adjusted by the experimenter through the **k**-vectors of the first two pulses. If $\rho(v_n)$ is Maxwell-Boltzmann, then carrying out the integral yields the gaussian

$$P \propto \exp\left(-2v_0^2 k^2 (t_3 - t_1)^2 \sin^2(\alpha/2)\right) \qquad (7\text{-}4)$$

where v_0 is the most probable atomic speed. Figure 7-8 is a plot of equation 7-4.

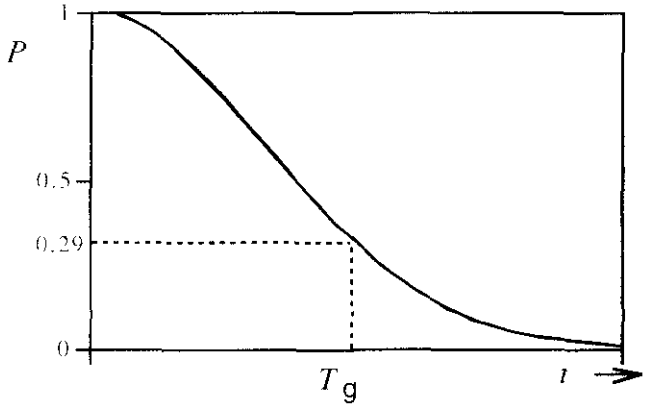

Figure 7-8 Predicted decay of reflected pulse energy for atoms with Maxwell-Boltzmann speed distribution

The strength of the reflected signal may be estimated as follows. The optical thickness of a sample of cold rubidium atoms in an MOT, for the pulsed transition at 420 nm, is < 1, i.e. it is an optically thin sample. Hence one may assume that there are no cooperative (superradiant) effects (section 7.4) involved on this transition, and the Bragg reflection is essentially a free induction decay in a specular direction. The intensity of a free induction decay from an optically thin cylindrical sample of length L and consisting of a gas of two

level atoms is given by, for example, equation 3-127 of [271]. Applying this equation to a laser-cooled homogeneously broadened sample, we obtain

$$I(t) = \frac{\mu^2 \omega_0^2 L^2 n_e^2}{8\varepsilon_0 c} \exp(-\Gamma t) \tag{7-5}$$

where μ is the electric dipole moment matrix element of the transition, ω_0 the angular frequency of the radiation and n_e is the number density of atoms in the excited state immediately after the probe pulse. For a laser pulse of pulse area $\pi/2$, we have $n_e = n/2$, where n is the number density of atoms in the F=2 ground state just before the probe pulse. Integrating equation 7-5 over t and and expressing μ in terms of Γ we obtain the total number of photons n_{coh} in the free induction decay signal,

$$n_{coh} \approx \left(\frac{3}{128\pi^2}\right)\left(\frac{N^2\lambda^2}{r^2}\right) \tag{7-6}$$

In obtaining equation 7-6, L has been replaced[2] by $4r/3$ to give an estimate appropriate to a sample in a spherical volume of radius r and N is the total number of ground state atoms in the sample prior to the probe pulse. With typical experimental parameters $\lambda = 420$ nm, $N = 2.5 \times 10^7$ and $r = 0.5$ mm, this gives $n_{coh} = 10^6$ equivalent to a pulse energy of 0.5 pJ, emitted over ~110 ns. Such a signal is easily detectable with either a photomultiplier tube or feasibly a fast photodiode and box-car integrator. The pulse-excited sample also emits incoherently n_{inc} photons where $n_{inc} \approx N/2 \approx 10^7$. This radiation is over all directions (dipole pattern) and occurs on a timescale of $1/\Gamma$. Although most of the energy absorbed from the laser probe pulse is emitted incoherently in this way, only a fraction of order $\lambda^2/r^2 \approx 10^{-6}$ is directed into the diffraction cone of the Bragg reflected pulse. Hence this noise source should not be a problem.

Experimental method

The experimental method will consist of varying the delay $t_3 - t_1$ of the probe pulse and recording the corresponding reflected pulse energy in order to plot curves similar to figure 7-4, but corresponding to the actual velocity distribution, which may be other than Maxwell-Boltzmann. One sequence of three pulses has a negligible heating effect on the cold sample and requires less than 10 µs, during which time the average atom has moved about 2 µm. Thus the atoms may be swiftly re-trapped and re-cooled in around a further 10 µs and the next sequence of three pulses applied. This allows the sequence to be repeated many times at each data point and the signal accumulated with a boxcar integrator. Discrimination against stray probe light may be achieved by a combination of spatial filtering and polarisation of

[2] *Equation 7-5 was for a cylindrical sample of length L and radius r, the factor of 4/3 preserves the volume and hence the total number of atoms.*

pulses. We hope by this method to obtain curves with good signal to noise ratio, allowing the velocity distribution $\rho(v_n)$ to be determined by the Fourier transform of equation 7-1.

This technique offers an alternative to the usual 'time of flight' method of temperature measurement, and it will be interesting to compare the results of the two methods. Being a Fourier transform, the largest signal is from the slowest atoms and the weakest contribution from the fast atoms, therefore systematic errors are different and complementary to those of time-of flight. This technique can be used to examine the distributions of velocity components in specific directions within the cold sample.

7.4 Factors influencing transient pulse shapes in cold samples

In order to interpret transient signals it is necessary to understand the factors that influence the time spectrum. In hot gases the dominant factor is the Doppler broadening which satisfies $\Delta_D >> \Gamma$ and leads to the rapid dephasing in free induction decay and the formation of distinct narrow echo pulses when sequences of excitation pulses are applied. In laser-cooled samples the Doppler broadening is essentially absent and the transient signals are expected to be determined by the natural decay time of the excited level and quantum beats due to hyperfine structure. In addition there may be various inhomogeneous broadening mechanisms and cooperative (superradiant) effects, which are now discussed. Possible inhomogeneous broadening mechanisms in an MOT or molasses include:

i) Zeeman broadening due to trap fields. This is of order $\Delta_{mag} \sim g_J \mu_B B / \hbar$ and is significant only in regions of the trap where $B \geq 2$ gauss, giving $\Delta_{mag} \geq \Gamma$.

ii) AC Stark shifts (light shifts) produced by the cooling and trapping beams. These vary from zero at the nodes of the light field to values of order 10Γ at antinodes depending on trapping beam intensity and detuning and the relative time phases of the beams.

iii) Broadening due to cold collisions. The frequency shift due to $1/r^3$ dipole–dipole interactions[90] between ground and excited state Rb atoms is of the order of Γ, when $r = \lambda/5$. For typical trap number densities of ~5 x 10^{10} cm^{-3}, the average atomic spacing is ~4λ.

The Zeeman and AC Stark broadening mechanisms are expected to produce a dephasing of the transient response of the sample leading to free induction decay and, if large enough, echo effects.

Additionally, we need to consider the possibility of cooperative radiation effects or superradiance[285,286]. Superradiant emission from N atoms has an intensity proportional to N^2, is highly directional for certain geometries of the atomic sample and is characterised by a time delay and duration both less than Γ^{-1}. A condition for superradiant emission is that the optical thickness is greater than one, $\alpha L >> 1$, where α is the absorption coefficient and L a dimension of the sample; this condition ensures that coherent cooperative decay processes dominate over incoherent decay. An interesting possibility is that coherent transients on the 6P to $5S_{1/2}$ ($\alpha L << 1$) transition may be dramatically affected and possibly

quenched by superradiant emission at 2.7 μm on the 6P to $6S_{1/2}$ branching transition (see figure 7-9) which has an optical thickness αL ~ 10 for a typical MOT sample.

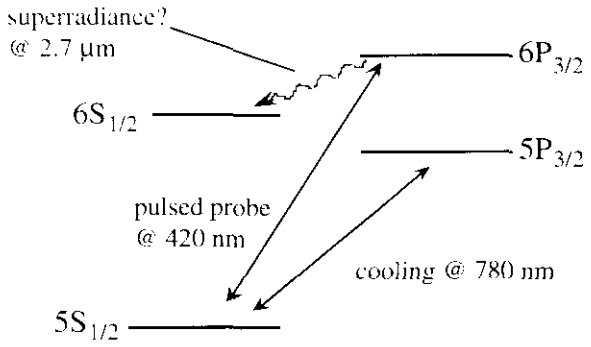

Figure 7-9 A transition scheme for possible superradiant emission

Superradiance has been observed for hot atoms on the infrared transitions of several molecules and the alkali metals, e.g. sodium[287] and caesium[288]. To ensure that we may observe superradiant emission (if it occurs) at 2.7 μm from cold Rb atoms, we have incorporated a sapphire window, transparent at 2.7 μm, in one of our vacuum cells and are currently designing a detection system for weak, short infrared pulses based on an InAs photodiode.

In the light of the above discussion, I conclude that our proposed work programme should open up a fertile new field of time domain spectroscopy of laser-cooled atoms.

TAMÁM SHUD

Appendices

A1 The Rabi frequency, the density matrix and the Bloch vector.

This appendix serves to establish some of the notation used in chapter 2.

The Rabi frequency

The optical Rabi frequency has its origins as follows (in the Schrödinger representation). Consider the two state atom depicted below

An arbitrary monochromatic laser field

$$\Longrightarrow \quad \mathbf{E} = \frac{1}{2}\boldsymbol{\varepsilon}(\mathbf{r})E_0(\mathbf{r})e^{-i\omega_L t} + \text{c.c.}$$

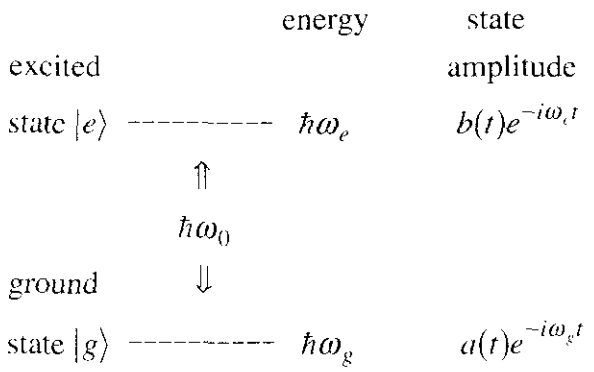

The system can be described at time t by an atom with state vector

$$|t\rangle = a(t)e^{-i\omega_g t}|g\rangle + b(t)e^{-i\omega_e t}|e\rangle \tag{A1-1}$$

The Schrödinger equation for the interaction is

$$\left(H_{\text{Atom}} - \mathbf{E}\cdot\mathbf{d}\right)|t\rangle = i\hbar\frac{d}{dt}|t\rangle \tag{A1-2}$$

where $\mathbf{d}$ is the atomic dipole operator.

Substituting equation A1-1 into equation A1-2, using the orthonormality of $|g\rangle$ and $|e\rangle$, the odd parity of $\mathbf{d}$ and the fact that $H_{\text{Atom}}|g\rangle = \hbar\omega_g|g\rangle$ etc leads to two coupled equations

$$\begin{aligned}\dot{a} &= ibe^{-i\omega_0 t}\frac{\langle g|\mathbf{d}\cdot\mathbf{E}|e\rangle}{\hbar}\\ \dot{b} &= iae^{i\omega_0 t}\frac{\langle e|\mathbf{d}\cdot\mathbf{E}|g\rangle}{\hbar}\end{aligned} \tag{A1-3}$$

Introducing the time dependence of $\mathbf{E}$ into equations A1-3 and making the 'rotating wave approximation' which neglects the fast-oscillating terms in $\omega_L + \omega_0$ we obtain

$$\dot{a} = \frac{i\Omega_0 e^{-i\theta}}{2}be^{i\Delta t} \tag{A1-4a}$$

$$\dot{b} = \frac{i\Omega_0 e^{i\theta}}{2}ae^{-i\Delta t} \tag{A1-4b}$$

where $\Delta = \omega_L - \omega_0$ is the 'detuning', and $\Omega_0 e^{i\theta} = \dfrac{E_0\langle e|\mathbf{d}\cdot\boldsymbol{\varepsilon}|g\rangle}{\hbar}$ is the 'complex Rabi frequency' expressed in exponential form (Ω_0, θ are both real).

The coupled equations A1-4 are easily solved, and assuming initial conditions $a(0)=1,\ b(0)=0$, which correspond to the atom starting in its ground state, the solution is:

$$\begin{aligned} a &= e^{\frac{i\Delta t}{2}}\left(\cos\frac{\Omega t}{2}-\frac{i\Delta}{\Omega}\sin\frac{\Omega t}{2}\right) \\ b &= e^{\frac{-i\Delta t}{2}}\frac{i\Omega_0 e^{i\theta}}{\Omega}\sin\frac{\Omega t}{2} \end{aligned} \qquad \text{(A1-5)}$$

where $\Omega=\sqrt{{\Omega_0}^2+\Delta^2}$ is called the 'generalised Rabi frequency'. The probability of the atom being in the excited state is therefore

$$|b|^2=\frac{{\Omega_0}^2}{\Omega^2}\sin^2\frac{\Omega t}{2}=\frac{{\Omega_0}^2}{2\Omega^2}(1-\cos\Omega t) \qquad \text{(A1-6)}$$

which shows that $|b|^2$ oscillates between values 0 and $\frac{{\Omega_0}^2}{\Omega^2}$ at a rate Ω, the generalised Rabi frequency. When the laser is resonant with the atomic transition, $\Omega=\Omega_0$, and the excited state probability oscillates between 0 and 1 at a rate Ω_0, the on-resonance Rabi frequency. Note that the rate of Rabi oscillations is determined by the modulus only of the 'complex Rabi frequency' and is not affected by the phase θ. This phase is nevertheless important in derivations of light forces.

The Density matrix

The density matrix ρ is an operator defined by $\overline{|t\rangle\langle t|}$, where the bar denotes the average over an ensemble of indistinguishable particles. Hence, in matrix form, for the two state atom of chapter 2 it is

$$\rho=\begin{bmatrix} a^*a & b^*ae^{i\omega_0 t} \\ a^*be^{-i\omega_0 t} & b^*b \end{bmatrix}$$

It has several useful properties:

i) If A is an operator corresponding to an observable, then the expectation value $\langle A\rangle = \text{Trace}(\rho A)$.

ii) If $|\chi\rangle$ is a possible state of the system $|t\rangle$, then the probability of finding the state in $|\chi\rangle$ is $\langle\chi|\rho|\chi\rangle$.

iii) Because it is an ensemble average, it is possible to incorporate phenomenological decay terms into its equation of motion.

iv) Schrödinger's equation can be written in terms of the density matrix and the system Hamiltonian as follows:

$$\frac{d\rho}{dt}=-\frac{i}{\hbar}[H,\rho] \qquad \text{(A1-7)}$$

where the square brackets indicate the commutator.

The Bloch vector

The Bloch vector is a mathematical tool originally devised in connection with nuclear magnetic resonance experiments which has also proved very useful in studying optical excitation of two-level atoms. The density matrix equation of motion (A1-7) for a two state atom yields four coupled equations, one for each of the elements of ρ. These four equations are partially decoupled by rewriting them in terms of three new variables u, v and w, which are specific linear combinations of the density matrix elements and defined by

$$\begin{aligned} u &= \rho_{eg} e^{i\omega_L t} e^{-i\theta} + \text{c.c.} \quad &= e^{-i\theta} e^{i\Delta t} a^* b + \text{c.c.} \\ v &= i\rho_{eg} e^{i\omega_L t} e^{-i\theta} + \text{c.c.} \quad &= ie^{-i\theta} e^{i\Delta t} a^* b + \text{c.c} \\ w &= \rho_{ee} - \rho_{gg} \quad &= |b|^2 - |a|^2 \end{aligned} \tag{A1-8}$$

The three new variables are the three components of the so-called Bloch vector. The resulting 'optical Bloch equations' (without decay terms) are

$$\begin{aligned} \dot{u} &= \Delta v \\ \dot{v} &= -\Delta u + \Omega_0 w \\ \dot{w} &= -\Omega_0 v \end{aligned} \tag{A1-9}$$

If the variables u, v and w are regarded as the components of a vector $\mathbf{B} = [u, v, w]$, equation A1-9 takes the form

$$\frac{d\mathbf{B}}{dt} = \mathbf{W} \times \mathbf{B} \tag{A1-10}$$

where $\mathbf{W}$ is the vector $\mathbf{W} = [-\Omega_0, 0, -\Delta]$. Equation A1-10 describes the precession of $\mathbf{B}$ around $\mathbf{W}$ in the mathematical space of these two vectors and therefore allows a corresponding pictorial visualisation. Such a model often aids understanding of complicated atom-laser interactions, e.g. figure 7-2 on page 169.

A2 Ehrenfest's theorem

Ehrenfest's theorem consists of two equations which apply to any quantum mechanical particle of mass m. The equations, which follow from Schrödinger's equation and the definition of an expectation value, are quantum-mechanically exact. They are

$$\frac{d\langle\hat{\mathbf{r}}\rangle}{dt} = \frac{\langle\hat{\mathbf{p}}\rangle}{m}$$
$$\frac{d\langle\hat{\mathbf{p}}\rangle}{dt} = -\langle\nabla\hat{V}\rangle \qquad \text{(A2-1)}$$

where $\hat{\mathbf{r}}$ and $\hat{\mathbf{p}}$ are the position and momentum operators for the particle and $\hat{V}$ is the potential energy operator, which may be time dependent. The triangular brackets denote expectation values.

They are often referred to as the quantum mechanical equivalent of Newton's laws, in that the classical position and momentum of Newtonian dynamics have been replaced by their corresponding quantum-mechanical expectation values. Furthermore, the quantum mechanical force operator is defined as the rate of change of the expectation value of momentum.

Ehrenfest's theorem and light forces

In the specific case considered in chapter 2, where a quantum mechanical two state atom interacts with a classical light field, the potential energy operator is given by $-\mathbf{E}\cdot\mathbf{d}$, where $\mathbf{E}$ is the electric field and $\mathbf{d}$ is the atomic dipole operator. Hence the mean force $\mathbf{F}$ is

$$\begin{aligned}
\mathbf{F} &= \langle\nabla(\mathbf{E}\cdot\mathbf{d})\rangle \\
&= \langle\nabla(d_x E_x + d_y E_y + d_z E_z)\rangle \\
&= \langle\nabla(d_x E_x)\rangle + \langle\nabla(d_y E_y)\rangle + \langle\nabla(d_z E_z)\rangle \\
&= \langle d_x\nabla E_x\rangle + \langle d_y\nabla E_y\rangle + \langle d_z\nabla E_z\rangle \\
&\quad (\mathbf{d} \text{ is not a function of the atomic centre of mass position}) \\
&= \nabla E_x\langle d_x\rangle + \nabla E_y\langle d_y\rangle + \nabla E_z\langle d_z\rangle \\
&\quad (\text{for a small classical atom, } \mathbf{E} \text{ varies little over the atomic wavepacket})
\end{aligned}$$

Thus, considering just one component of $\mathbf{F}$

$$\begin{aligned}
F_i &= \frac{dE_x}{dx_i}\langle d_x\rangle + \frac{dE_y}{dx_i}\langle d_y\rangle + \frac{dE_z}{dx_i}\langle d_z\rangle \\
&= \frac{d\mathbf{E}}{dx_i}\cdot\langle\mathbf{d}\rangle \qquad \text{which is the 'light force equation' 2-13}
\end{aligned}$$

A3 The Ehrenfest theorem expression for the light force in terms of the Bloch vector components, equation 2-14a

Starting from the light force equation 2-13

$$F_i = \langle \mathbf{d} \rangle \cdot \frac{d\mathbf{E}}{dx_i}$$

and using

$$\langle \mathbf{d} \rangle = \text{Trace}(\rho \mathbf{d}) \text{ or}$$

$$\langle \mathbf{d} \rangle = \langle t|\mathbf{d}|t \rangle = a^* b e^{-i\omega_0 t} \langle g|\mathbf{d}|e \rangle + \text{c.c.}$$

$$\mathbf{E} = \frac{1}{2}\mathbf{E}' e^{-i\omega_L t} + \text{c.c}$$

gives

$$F_i = \left(a^* b e^{-i\omega_0 t} \langle g|\mathbf{d}|e \rangle + \text{c.c.}\right)\left(\frac{1}{2} e^{-i\omega_L t} \frac{d\mathbf{E}'}{dx_i} + \text{c.c.}\right)$$

Neglecting the two fast oscillating terms gives the time dependent force in the R.W.A

$$F_i = \frac{1}{2} a^* b e^{i\Delta t} \langle g|\mathbf{d}|e \rangle \cdot \frac{d\mathbf{E}'}{dx_i} + \text{c.c.}$$

$$= \frac{1}{2} a^* b e^{i\Delta t} \frac{d}{dx_i} \langle g|\mathbf{E}' \cdot \mathbf{d}|e \rangle + \text{c.c.}$$

$$= \frac{1}{2} a^* b e^{i\Delta t} \frac{d}{dx_i} \left(\hbar \Omega_0^{c*}\right) + \text{c.c.}$$

$$= \frac{\hbar}{2} a^* b e^{i\Delta t} \frac{d}{dx_i} \left(\Omega_0 e^{-i\theta}\right) + \text{c.c.}$$

$$= \frac{\hbar}{2} a^* b e^{i\Delta t} e^{-i\theta} \left(\frac{d\Omega_0}{dx_i} - i\Omega_0 \frac{d\theta}{dx_i}\right) + \text{c.c.}$$

$$= \frac{\hbar}{2} \frac{d\Omega_0}{dx_i} \left(a^* b e^{i\Delta t} e^{-i\theta} + \text{c.c.}\right) - \frac{\hbar}{2} \Omega_0 \frac{d\theta}{dx_i} \left(i a^* b e^{i\Delta t} e^{-i\theta} + \text{c.c.}\right)$$

$$= \frac{\hbar}{2} \frac{d\Omega_0}{dx_i} u - \frac{\hbar}{2} \Omega_0 \frac{d\theta}{dx_i} v$$

and hence in three dimensions

$$\mathbf{F} = \frac{\hbar}{2}\left(u \nabla \Omega_0 - \Omega_0 v \nabla \theta\right) \qquad \text{which is equation 2-14a}$$

A4 The Ehrenfest theorem expression for the light force in terms of the atomic polarisability, equation 2-16

We start from the light force equation 2-13

$$F_i = \langle \mathbf{d} \rangle \cdot \frac{d\mathbf{E}}{dx_i} \tag{A4-1}$$

and write the light field in the form

$$\mathbf{E} = \sum_q \mathbf{e}_q E_q e^{i\omega_q t} + \text{c.c.} = \sum_q \mathbf{e}_q I_q^{\frac{1}{2}} e^{i\psi_q} e^{i\omega_q t} + \text{c.c.} \tag{A4-2}$$

where the $\mathbf{e}_q$ are the three Cartesian unit vectors and the E_q are complex. In this derivation, an isotropic atom is assumed, which means that the atomic polarisability is a complex scalar $\alpha = \alpha_{\text{Re}} + i\alpha_{\text{Im}}$. This treatment can be extended to the anisotropic case, in which case a tensor polarisability is required, but this is not done here. Thus

$$\langle \mathbf{d} \rangle = \alpha \mathbf{E} + \text{c.c.} \tag{A4-3}$$

Putting equations A4-2 and A4-3 into A4-1, we obtain

$$F_i = \left(\sum_q \alpha \mathbf{e}_q E_q e^{i\omega_q t} + \text{c.c.} \right) \left(\sum_{q'} \mathbf{e}_{q'} \frac{dE_{q'}}{dx_i} e^{i\omega_{q'} t} + \text{c.c.} \right)$$

Expanding the brackets and making the rotating wave approximation yields

$$F_i = \sum_q \alpha E_q \frac{dE_q^*}{dx_i} + \text{c.c.}$$

But $E_q = I_q^{\frac{1}{2}} e^{i\psi_q}$, hence

$$F_i = \sum_q (\alpha_{\text{Re}} + i\alpha_{\text{Im}}) \left(I_q^{\frac{1}{2}} \frac{dI_q^{\frac{1}{2}}}{dx_i} - iI_q \frac{d\psi_q}{dx_i} \right) + \text{c.c.}$$

$$= \sum_q \left(\alpha_{\text{Re}} \frac{dI_q}{dx_i} + 2\alpha_{\text{Im}} I_q \frac{d\psi_q}{dx_i} \right)$$

Finally, in three dimensions

$$\mathbf{F} = \sum_q \alpha_{\text{Re}} \nabla I_q + 2\alpha_{\text{Im}} \sum_q I_q \nabla \psi_q$$

or

$$\mathbf{F} = \alpha_{\text{Re}} \nabla I + 2\alpha_{\text{Im}} \sum_q I_q \nabla \psi_q \quad \text{which is equation 2-16}$$

where $I = \sum_q I_q$

A5 Scalar polarisability for a two-level atom

Let the general monochromatic light field be $\mathbf{E} = \frac{1}{2}\boldsymbol{\varepsilon}(\mathbf{r})E_0(\mathbf{r})e^{-i\omega_L t} + \text{c.c.}$ and the expectation value of the dipole moment be $\langle \mathbf{d} \rangle$. Then the complex polarisability α is defined by the equation $\langle \mathbf{d} \rangle = \alpha \mathbf{E} + \text{c.c.}$

$$\text{i.e.} \qquad \langle \mathbf{d} \rangle = \alpha \boldsymbol{\varepsilon} \frac{E_0}{2} e^{-i\omega_L t} + \text{c.c.} \tag{A5-1}$$

To calculate α, we proceed as follows. First, note that $\langle \mathbf{d} \rangle = \langle t|\mathbf{d}|t \rangle$ and as

$$|t\rangle = a(t)e^{-i\omega_g t}|g\rangle + b(t)e^{-i\omega_e t}|e\rangle$$

equation A5-1 becomes

$$a^* b e^{-i\omega_0 t}\langle g|\mathbf{d}|e\rangle + ab^* e^{i\omega_0 t}\langle e|\mathbf{d}|g\rangle = \alpha\boldsymbol{\varepsilon}\frac{E_0}{2}e^{-i\omega_L t} + \alpha^*\boldsymbol{\varepsilon}^*\frac{E_0}{2}e^{i\omega_L t}$$

Multiplying by $e^{i\omega_L t}$ and neglecting the fast-oscillating terms (RWA) gives

$$a^* b e^{i\Delta t}\langle g|\mathbf{d}|e\rangle = \alpha\boldsymbol{\varepsilon}\frac{E_0}{2}$$

Scalar multiplication by $\boldsymbol{\varepsilon}^* E_0$ and use of the definition $\Omega_0^c = \frac{E_0\langle e|\boldsymbol{\varepsilon}\cdot\mathbf{d}|g\rangle}{\hbar}$ gives

$$a^* b e^{i\Delta t}\hbar\Omega_0^c = \alpha\frac{E_0^2}{2}$$

$$\alpha = \frac{2a^* b e^{i\Delta t}\hbar\Omega_0 e^{-i\theta}}{E_0^2}$$

This may be re-expressed in terms of the Bloch vector components u and v:

$$\alpha = (u - iv)\frac{\hbar\Omega_0}{E_0^2}$$

The above result is still time dependent via u and v. If the steady state value is required, we substitute the steady state values of u and v:

$$\alpha = \frac{2\hbar\Omega_0^2}{E_0^2}\frac{-2\Delta + i\Gamma}{\Gamma^2 + 2\Omega_0^2 + 4\Delta^2} = \frac{\hbar\Omega_0^2}{2I}\frac{-2\Delta + i\Gamma}{\Gamma^2 + 2\Omega_0^2 + 4\Delta^2}$$

where $I = \frac{1}{2}\overline{\mathbf{E}\cdot\mathbf{E}} = \frac{1}{4}E_0^2$. This is equation 2-17 of chapter 2.

A6 The spin density of an electromagnetic field: Outline proof of equation 5-28, $\mathbf{L}_I = \varepsilon_0 \mathbf{E} \times \mathbf{A}$

The momentum density $\mathbf{g}$ of an electromagnetic field is well known to be given by $\mathbf{g} = \frac{\mathbf{S}}{c^2} = \frac{1}{c^2}\mathbf{E} \times \mathbf{H}$. Using $\mathbf{H} = \frac{1}{\mu_0}(\nabla \times \mathbf{A})$ gives $\mathbf{g} = \varepsilon_0(\mathbf{E} \times (\nabla \times \mathbf{A}))$. One can split $\mathbf{g}$ into two parts $\mathbf{g} = \mathbf{g}_1 + \mathbf{g}_2$, or in tensor notation $g_i = g_{1i} + g_{2i}$. After multiplying out $\mathbf{E} \times (\nabla \times \mathbf{A})$, the splitting can be done such that $g_{1i} = \varepsilon_0 \sum_j E_j \frac{\partial A_j}{\partial x_i}$ and $g_{2i} = -\varepsilon_0 \sum_j E_j \frac{\partial A_i}{\partial x_j}$.

Here i and j scan x, y and z.

It can then be shown, using integration by parts and $\nabla \cdot \mathbf{A} = 0$ that the volume integral of $\mathbf{g}_2$ is zero for either of two types of boundary condition. The first possible boundary condition, corresponding to a localised field, requires that the field strength goes to zero at a rate faster than $1/|\mathbf{r}|$ as $|\mathbf{r}|$ goes to infinity. The second possible boundary condition is that the field is periodic in a (usually) cubic volume of any size. The volume integral of the term $\mathbf{g}_1$ is not necessarily equal to zero and corresponds to the 'centre of mass' momentum of the field. The term $\mathbf{g}_2$ corresponds to momentum circulating within the field with a net volume integral of zero. The analogy with the two types of (linear) momentum possessed by a moving spinning ball is useful within its limitations.

The density of angular momentum with respect to an arbitrary origin is given by

$$\mathbf{L} = \mathbf{r} \times \mathbf{g} = \mathbf{r} \times \mathbf{g}_1 + \mathbf{r} \times \mathbf{g}_2$$

The part $\mathbf{L}_0 = \mathbf{r} \times \mathbf{g}_1$ corresponds to the density of orbital angular momentum and its volume integral can be made zero by a suitable choice of origin. The interesting part is $\mathbf{L}_I = \mathbf{r} \times \mathbf{g}_2$ which corresponds to the density of intrinsic angular momentum or spin. To show this, one makes the substitution $g_{2i} = -\varepsilon_0 \sum_j E_j \frac{\partial A_i}{\partial x_j}$ into $\mathbf{L}_I = \mathbf{r} \times \mathbf{g}_2$, and then calculates the volume integral of $\mathbf{L}_I$ using integration by parts and $\nabla \cdot \mathbf{E} = 0$. With the 'localised field' boundary condition[1], requiring that the field strength goes to zero at infinity at a rate faster than $1/|\mathbf{r}|$, one finds that

$$\iiint_{\text{space}} \mathbf{L}_I \, \partial^3 r = \iiint_{\text{space}} \varepsilon_0 \mathbf{E} \times \mathbf{A} \, \partial^3 r \qquad \text{(A6-1)}$$

The quantity on the righthand side is independent of $\mathbf{r}$, i.e. independent of the choice of coordinate system origin, thus reflecting the fact that it is the intrinsic angular momentum of the field. One can then deduce that, as equation A6-1 is an integral over an arbitrary volume, that the density of intrinsic angular momentum $\mathbf{L}_I$ is given by

$$\mathbf{L}_I = \varepsilon_0 \mathbf{E} \times \mathbf{A} \qquad \text{(5-28)}$$

---

[1] *It is interesting to note that the alternative 'periodic boundary condition' is no longer sufficient, although it can be used with the additional assumption of transversality, i.e. $\delta A_i / \delta x_i = 0$*

Appendix A7 Computer programme in C: Calculation of polarisation gradients in 6-beam standing waves(chapter 5)

The programme is written in three files: 6-header.c, 6-beams.c and 6-cases.c, which are reproduced below. The programme was compiled and run using "Think C" on a Macintosh LCII computer, and on a "Digital" DEC 3000 Workstation for long runs.

File 1) 6-header.c

```
/* This file contains the libraries and definitions common to all
   functions and some function prototypes.                    */

#include <stdio.h>
#include <time.h>
#include <stdlib.h>
#include <math.h>

#define SAFEZERO 0.001                  /* prevents division by zero */
#define PHASESTEPS 12                   /* number of divisions of phases  0 to π */
#define RELPH 0.8660254
#define PI 3.14159265
#define K        6.28318530             /* = 2π  */

#define EM_MIN        1                       /* number of different light fields */
#define EM_MAX        4                       /* to be done set with MIN and MAX  */

#define TOPO 'r'                        /* 'p'  for ellipticity, 'r' for helicity */
#define TRAJSTEPS 12            /* number of steps on each trajectory */

double varf_pr(int s,double th,double ph,int f,char c);

double calcf_p(double pos[], double unitvec[],double th,double ph,int f);
double calcf_r(double pos[], double unitvec[],double th,double ph,int f);
```

File 2) 6-beams.c

```
#include "6-header.c"       /* set most programme parameters in 6-header.c */
main() {
char c,flyname[]="EM",no[2],type[2]; /* file-naming variables */
int s,f,theye,pheye;                    /* theye, pheye will count time-phase steps */
                                        /* s = number of steps per trajectory */
                                        /* f =  number of light field name */
unsigned long int count,t;              /* t = number of trajectories run */
double sum_pr=0,var_pr,th,ph;   /* var_pr  is result of one trajectory */
                                        /* sum_pr is running total of var_pr */
                                        /* th = theta, ph = phi in radians */
clock_t start, finish;                  /* to record run-time */
FILE *ofp;
printf("%s\n%s\n",
"Busy! Calculating functions of ellipticity 'p' or helicity 'r' of ",
"E.M. fields (previously loaded) over a grid of relative time phases.");
printf("\nHow many atom trajectories?    ");
scanf("%lu",&t);
printf("\n");
s=TRAJSTEPS;
c=TOPO;
if(c!='p'&&c!='r'){
printf("\nBad value for TOPO\n");
exit(0);
}
for(f=EM_MIN;f<=EM_MAX;++f){            /* calculates for each field in turn */
sprintf(no,"%c",f+48);
```

```
sprintf(type,"%c",c);
strcpy(flyname+2,type);                    /* labels filename with p or r */
strcpy(flyname+3,"_new");                  /* new files tagged 'new' for safety */
strcpy(flyname+7,no);                      /* creates next filename in sequence */
ofp= fopen(flyname,"w");                   /* opens current file for writing */
start=clock();                                  /* starts run-time clock */
srand(time(NULL));                              /* seeds random number gen. from time */

for(thcyc=0;thcyc<=PHASESTEPS;++thcyc){         /* cycles theta values */
th = thcyc*PI/PHASESTEPS;
for(phcyc=0;phcyc<=PHASESTEPS;++phcyc){         /* cycles phi values */
ph = phcyc*PI/PHASESTEPS;

sum_pr=0;
for(count=1;count<=t;++count){             /* cycles trajectories */
var_pr = varf_pr(s,th,ph,f,c);             /* calculates Ξ(p)^2 or Ξ(r)^2 for 1 traj. */
sum_pr += sqrt(var_pr);          /*  running total of Ξ(p) or Ξ(r) over trajectories */
}                                               /* end of trajectory loop */
fprintf(ofp,"%d %d %lf\n",thcyc,phcyc,sum_pr/(double)t);
                                                /* puts result of one phase pair to file */
}
 fprintf(stderr,"%d  ",thcyc);             /*  screen marker of run progress */

fprintf(ofp,"\n");
}
fclose(ofp);                               /* closes active file */
finish=clock();                       /* stops run-time clock */
printf("\n%s%d%s%lu seconds\n",
"Field EM",f," done! in ",(finish-start)/CLOCKS_PER_SEC);
}       /* end of field-number loop */
}       /*End of main */

/* FUNCTION: varf_pr() calculates either Ξ(p)^2 or Ξ(r)^2
                                  along one trajectory */

double varf_pr(int s,double th,double ph,int f,char c) {
double  st[3],dir[3],magdir,unitvec[3],pos[3],calc_pr,
                pstep=0,ppstep=0,var_pr,rrstep=0;
int count,i;

for(i=0;i<3;++i){                               /* i scans x,y and z components */
st[i]=rand()/(double)RAND_MAX;                  /* random start point */
dir[i]=(rand()-RAND_MAX/2)/(double)RAND_MAX;
                                                /* random direction for trajectory */
}
magdir=sqrt(dir[0]*dir[0]+dir[1]*dir[1]+dir[2]*dir[2]);
                                                /* magnitude of direction vector */
for(i=0;i<3;++i)
unitvec[i]=dir[i]/magdir+SAFEZERO;         /* makes unit vector for direction */
for(count=0;count<s;++count) {             /* cycles through s steps on trajectory */
for(i=0;i<3;++i)
pos[i]=st[i]+unitvec[i]*count/s;
                                                /* pos[i] is the coordinate of current step */
if(c=='p'){                                     /* either calculates Ξ(p)^2*/
calc_pr = calcf_p(pos,unitvec,th,ph,f);
                                                /* calc_pr is the local value of pN
                                                as returned by calcf_p() */
pstep += calc_pr;
                                           /* pstep = running total of pN along the trajectory */
ppstep += calc_pr*calc_pr;
                              /* ppstep = running total of pN squared along the trajectory */
```

```
}       /* end of 'if p' loop */
if(c=='r'){                                     /* or calculates Ξ(r)^2*/
calc_pr = calcf_r(pos,unitvec,th,ph,f);
rrstep += calc_pr*calc_pr;
                        /* rrstep = running total of r_N squared along the trajectory */
}                       /* end of 'if r' loop */
} /* end of s steps loop */
if(c=='p')
var_pr = 2*(ppstep/s - pstep*pstep/(s*s));
                                /* Here var_pr = 2 x variance of p_N along the trajectory */
if(c=='r')
var_pr = rrstep/s;
                        /* Here var_pr = r_N squared and summed along the trajectory */
return var_pr;
}       /* end of function varf_pr */
```

File 3) 6-cases.c

```
/* This file contains the source trignometric functions for various
  light fields so that p and r may be calculated */

#include "6-header.c"

/* FUNCTION: calcf_p() calculates p_N at a point pos[]
  and with respect to unit vector unitvec[] for a field number f and
   with phases th and ph. */

double calcf_p(double pos[],double unitvec[],double th,double ph,int f) {

double spin[3],scalar=0,magE=0;
int i;
switch (f) {

case 1: /* Field EM1 spin density components and magnitude */
        spin[0] = -8*cos(K*pos[0])*cos(K*pos[1])*sin(th-ph) ;
        spin[1] = -8*cos(K*pos[1])*cos(K*pos[2])*sin(ph) ;
        spin[2] = -8*cos(K*pos[2])*cos(K*pos[0])*sin(-th) ;

        magE = 2*(cos(K*pos[0])*cos(K*pos[0])+cos(K*pos[1])*cos(K*pos[1])+
                        cos(K*pos[2])*cos(K*pos[2]));
        /* magE is independent of phases for this field */
break;

case 2:
        /* Field EM2 spin density components and magnitude  */
        spin[0] = -4*(cos(K*pos[0])*cos(K*pos[1])*sin(th-ph)-
                        cos(K*pos[1])*sin(K*pos[2])*sin(ph)-
                        sin(K*pos[2])*sin(K*pos[0])*sin(-th));
        spin[1] = -4*(cos(K*pos[1])*cos(K*pos[2])*sin(ph)+
                        cos(K*pos[2])*sin(K*pos[0])*sin(-th)+
                        sin(K*pos[0])*sin(K*pos[1])*sin(th-ph));
        spin[2] = -4*(cos(K*pos[2])*cos(K*pos[0])*sin(-th)+
                        cos(K*pos[0])*sin(K*pos[1])*sin(th-ph)-
                        sin(K*pos[1])*sin(K*pos[2])*sin(ph));

        magE = 2*(1.5-cos(K*pos[2])*sin(K*pos[1])*cos(ph)+
                        cos(K*pos[0])*sin(K*pos[2])*cos(th)-
                        cos(K*pos[1])*sin(K*pos[0])*cos(th-ph));
break;

case 3:
        /* Field EM3 spin density components and magnitude  */
        spin[0] = -2*(sin(2*K*pos[0])+sin(K*pos[0]-K*pos[1]+th-ph)-
```

```
                    sin(K*pos[2]-K*pos[0]+th)-sin(K*pos[1]+K*pos[2]+ph));
        spin[1] = -2*(sin(2*K*pos[1])+sin(K*pos[1]-K*pos[2]+ph)-
                    sin(K*pos[0]-K*pos[1]+ph-th)-sin(K*pos[2]+K*pos[0]-th));
        spin[2] = -2*(sin(2*K*pos[2])+sin(K*pos[2]-K*pos[0]-th)-
                    sin(K*pos[1]-K*pos[2]-ph)-sin(K*pos[0]+K*pos[1]+th-ph));

        magE = 3+cos(K*pos[1]+K*pos[2]-ph)+cos(K*pos[2]+K*pos[0]+th)+
                    cos(K*pos[0]+K*pos[1]-th+ph);
break;

case 4:
        /* Field EM4 spin density components and magnitude  */
        spin[0] = -4*(cos(K*pos[0])*cos(K*pos[0])+
                    cos(K*pos[0])*cos(K*pos[1])*sin(th-ph)-
                    cos(K*pos[1])*cos(K*pos[2])*cos(ph)+
                    cos(K*pos[2])*cos(K*pos[0])*sin(-th));
        spin[1] = -4*(cos(K*pos[1])*cos(K*pos[1])+
                    cos(K*pos[1])*cos(K*pos[2])*sin(ph)-
                    cos(K*pos[2])*cos(K*pos[0])*cos(-th)+
                    cos(K*pos[0])*cos(K*pos[1])*sin(th-ph));
        spin[2] = -4*(cos(K*pos[2])*cos(K*pos[2])+
                    cos(K*pos[2])*cos(K*pos[0])*sin(-th)-
                    cos(K*pos[0])*cos(K*pos[1])*cos(th-ph)+
                    cos(K*pos[1])*cos(K*pos[2])*sin(ph));

magE = 2*(cos(K*pos[0])*cos(K*pos[0])+cos(K*pos[1])*cos(K*pos[1])+
            cos(K*pos[2])*cos(K*pos[2])+cos(K*pos[1])*cos(K*pos[2])*sin(ph)+
            cos(K*pos[2])*cos(K*pos[0])*sin(-th)+
            cos(K*pos[0])*cos(K*pos[1])*sin(th-ph));
break;

case 5:
        /* Field EM5 is a 1-D sisyphus standing wave */
        /* Use PHASESTEPS = 1 */
        spin[0] = 0;
        spin[1] = 0;
        spin[2] = -2*sin(2*K*pos[2]);
        magE = 1;
break;

default:
return 0;
}                       /* end of switch */

for(i=0;i<3;++i)
scalar += spin[i]*unitvec[i];
        /* scalar is the projection of the spin density onto unitvec */
return scalar/(2*magE+SAFEZERO);        /* returns p_N.
                                    Note the 2 is necessary for correct normalisation */
} /* End of function calcf_p() */

/* FUNCTION: calcf_r() calculates r_N at a point pos[] and with respect to unit vector unitvec[] for a field
number f and with phases th and ph.*/

double calcf_r(double pos[],double unitvec[],double th,double ph,int f) {

double flux[3][3],scalar=0,magE=0,ps=0;
int i,j;                /* i and j scan the tensor components xx, xy etc */

switch (f) {
```

```
case 1:
        /* Field EM1 spin flux components and magnitude  */
        flux[0][0] = -4*cos(K*pos[1])*sin(K*pos[0])*cos(th-ph) ;
        flux[0][1] = 0 ;
        flux[0][2] = 4*cos(K*pos[2])*sin(K*pos[0])*cos(ps-th) ;
        flux[1][0] = 4*cos(K*pos[0])*sin(K*pos[1])*cos(th-ph) ;
        flux[1][1] = -4*cos(K*pos[2])*sin(K*pos[1])*cos(ph-ps) ;
        flux[1][2] = 0 ;
        flux[2][0] = 0 ;
        flux[2][1] = 4*cos(K*pos[1])*sin(K*pos[2])*cos(ph-ps) ;
        flux[2][2] = -4*cos(K*pos[0])*sin(K*pos[2])*cos(ps-th) ;

        magE = 2*(cos(K*pos[0])*cos(K*pos[0])+cos(K*pos[1])*cos(K*pos[1])+
                        cos(K*pos[2])*cos(K*pos[2]));
        /* magE is independent of phases for this field */
break;

case 2:
        /* Field EM2 spin flux components and magnitude  */
        flux[0][0] = 2*(1+sin(K*pos[2])*cos(K*pos[0])*cos(ps-th)-
                        cos(K*pos[1])*sin(K*pos[0])*cos(th-ph)) ;
        flux[0][1] = 2*(-cos(K*pos[2])*cos(K*pos[0])*cos(th-ps)+
                        cos(K*pos[0])*sin(K*pos[1])*cos(ph-th)) ;
        flux[0][2] = -2*(-sin(K*pos[0])*cos(K*pos[2])*cos(th-ps)+
                        sin(K*pos[0])*sin(K*pos[1])*cos(ph-th)) ;
        flux[1][0] = 2*(sin(K*pos[1])*cos(K*pos[0])*cos(ph-th)+
                        sin(K*pos[1])*sin(K*pos[2])*cos(ps-ph)) ;
        flux[1][1] = 2*(1-sin(K*pos[1])*cos(K*pos[2])*cos(ph-ps)-
                        cos(K*pos[1])*sin(K*pos[0])*cos(th-ph)) ;
        flux[1][2] = -2*(cos(K*pos[0])*cos(K*pos[1])*cos(th-ph)+
                        cos(K*pos[1])*sin(K*pos[2])*cos(ps-ph)) ;
        flux[2][0] = 2*(cos(K*pos[1])*cos(K*pos[2])*cos(ph-ps)-
                        cos(K*pos[2])*sin(K*pos[0])*cos(ps-th)) ;
        flux[2][1] = 2*(sin(K*pos[2])*cos(K*pos[1])*cos(ph-ps)-
                        sin(K*pos[2])*sin(K*pos[0])*cos(ps-th)) ;
        flux[2][2] = -2*(1-sin(K*pos[1])*cos(K*pos[2])*cos(ph-ps)+
                        cos(K*pos[0])*sin(K*pos[2])*cos(ps-th)) ;

        magE = 2*(1.5-cos(K*pos[2])*sin(K*pos[1])*cos(ph)+
                        cos(K*pos[0])*sin(K*pos[2])*cos(th)-
                        cos(K*pos[1])*sin(K*pos[0])*cos(th-ph));
break;

case 3:
        /* Field EM3 spin flux components and magnitude  */
flux[0][0] = -(sin(K*pos[0]-K*pos[1]+th-ph)+sin(K*pos[2]-K*pos[0]+th-ps));
flux[0][1] = -(sin(K*pos[2]+K*pos[0]+ps-th)+sin(K*pos[0]-K*pos[1]-th+ph));
flux[0][2] = -(sin(K*pos[2]-K*pos[0]+ps-th)-sin(K*pos[1]+K*pos[0]+th-ph));
flux[1][0] = -(sin(K*pos[0]-K*pos[1]+th-ph)-sin(K*pos[2]+K*pos[1]+ph-ps));
flux[1][1] = -(sin(K*pos[1]-K*pos[2]+ph-ps)+sin(K*pos[0]-K*pos[1]+ph-th));
flux[1][2] = -(sin(K*pos[0]+K*pos[1]+th-ph)+sin(K*pos[1]-K*pos[2]-ph+ps));
flux[2][0] = -(sin(K*pos[1]+K*pos[2]+ph-ps)+sin(K*pos[2]-K*pos[0]-ps+th));
flux[2][1] = -(sin(K*pos[1]-K*pos[2]+ph-ps)-sin(K*pos[0]+K*pos[2]+ps-th));
flux[2][2] = -(sin(K*pos[2]-K*pos[0]+ps-th)+sin(K*pos[1]-K*pos[2]+ps-ph));

        magE = 3+cos(K*pos[1]+K*pos[2]-ph)+cos(K*pos[2]+K*pos[0]+th)+
                        cos(K*pos[0]+K*pos[1]-th+ph);
break;

case 4:
        /* Field EM4 spin flux components and magnitude  */
```

```
        flux[0][0] = 2*(sin(K*pos[0])*cos(K*pos[2])*cos(ps-th)-
                                sin(K*pos[0])*cos(K*pos[1])*cos(th-ph)) ;
        flux[0][1] = 2*sin(K*pos[0])*(cos(K*pos[2])*sin(ps-th)-
                                cos(K*pos[1])*cos(th-ph)) ;
        flux[0][2] = 2*sin(K*pos[0])*(cos(K*pos[1])*sin(th-ph)-
                                cos(K*pos[2])*cos(ps-th)) ;
        flux[1][0] = 2*sin(K*pos[1])*(cos(K*pos[2])*sin(ph-ps)-
                                cos(K*pos[0])*cos(th-ph)) ;
        flux[1][1] = 2*(sin(K*pos[1])*cos(K*pos[0])*cos(th-ph)-
                                sin(K*pos[1])*cos(K*pos[2])*cos(ph-ps)) ;
        flux[1][2] = 2*sin(K*pos[1])*(cos(K*pos[0])*sin(th-ph)-
                                cos(K*pos[2])*cos(ph-ps)) ;
        flux[2][0] = 2*sin(K*pos[2])*(cos(K*pos[1])*sin(ph-ps)-
                                cos(K*pos[0])*cos(ps-th)) ;
        flux[2][1] = 2*sin(K*pos[2])*(cos(K*pos[0])*sin(ps-th)-
                                cos(K*pos[1])*cos(ph-ps)) ;
        flux[2][2] = 2*(sin(K*pos[2])*cos(K*pos[1])*cos(ph-ps)-
                                sin(K*pos[2])*cos(K*pos[0])*cos(ps-th)) ;

magE = 2*(cos(K*pos[0])*cos(K*pos[0])+cos(K*pos[1])*cos(K*pos[1])+
                cos(K*pos[2])*cos(K*pos[2])+cos(K*pos[1])*cos(K*pos[2])*sin(ph)+
                cos(K*pos[2])*cos(K*pos[0])*sin(-th)+
                cos(K*pos[0])*cos(K*pos[1])*sin(th-ph));
break;

case 6:
        /* Field EM6 is a 1-D corkscrew standing wave */
        /* Use PHASESTEPS = 1 */
        flux[0][0] = 0 ;
        flux[0][1] = 0 ;
        flux[0][2] = 0 ;
        flux[1][0] = 0 ;
        flux[1][1] = 0 ;
        flux[1][2] = 0 ;
        flux[2][0] = 0 ;
        flux[2][1] = 0 ;
        flux[2][2] = 2 ;
        magE = 1;
break;

default:
return 0;
}                       /* end of switch */

for(i=0;i<3;++i)
for(j=0;j<3;++j)
scalar += flux[i][j]*unitvec[i]*unitvec[j];
 /* scalar is the projection of the spin flux tensor onto unitvec tensor */

return scalar/(2*magE+SAFEZERO);
                        /* returns r_N.
                        Note that the 2 is necessary for correct normalisation */
} /* End of function calcf_r() */
```

Appendix A8 Spectroscopic data for rubidium

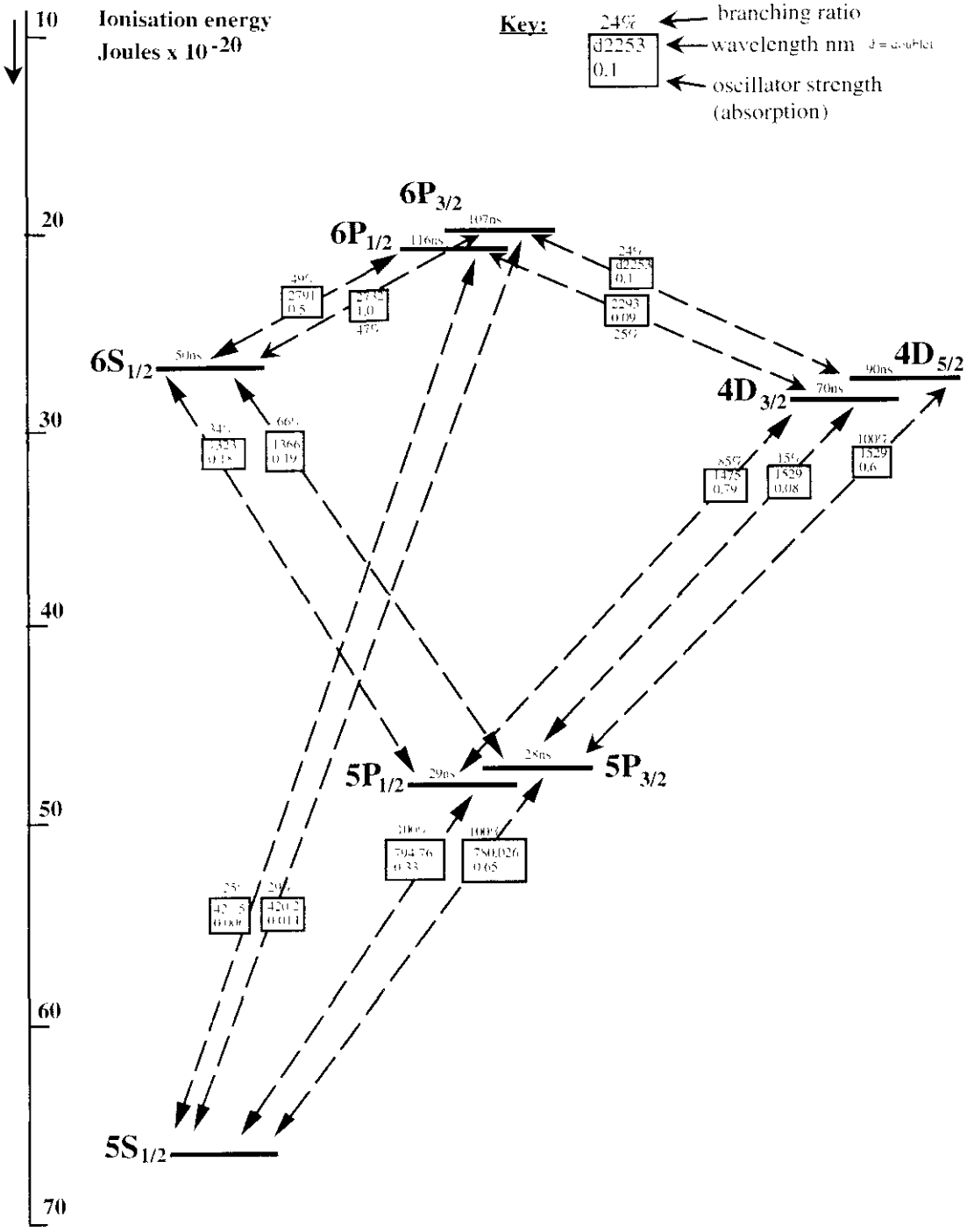

Figure A8-1 The gross structure of rubidium energy levels

Rubidium Atomic number Z = 37, Relative atomic mass = 85.47

^{85}Rb: Isotopic spin *I* 5/2; Relative abundance 72%

^{87}Rb: " *I* = 3/2: " 28%

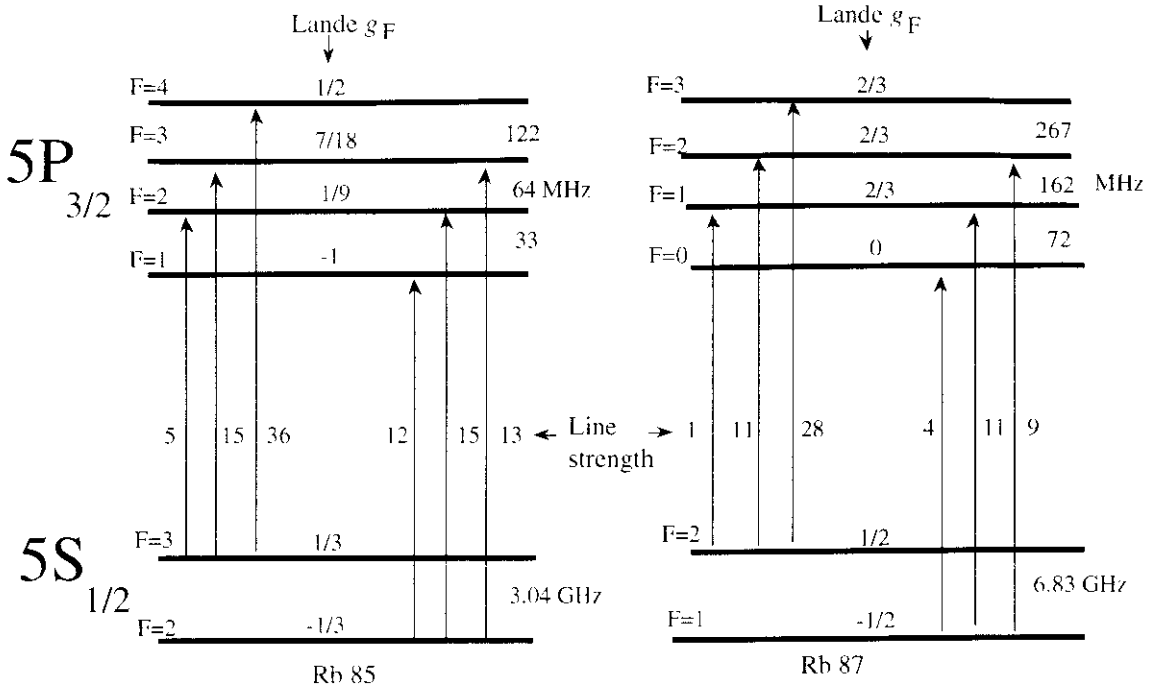

Figure A8-2 The hyperfine structure of the D_2 line of natural rubidium, showing energy spacings, Landé g factors and line strengths

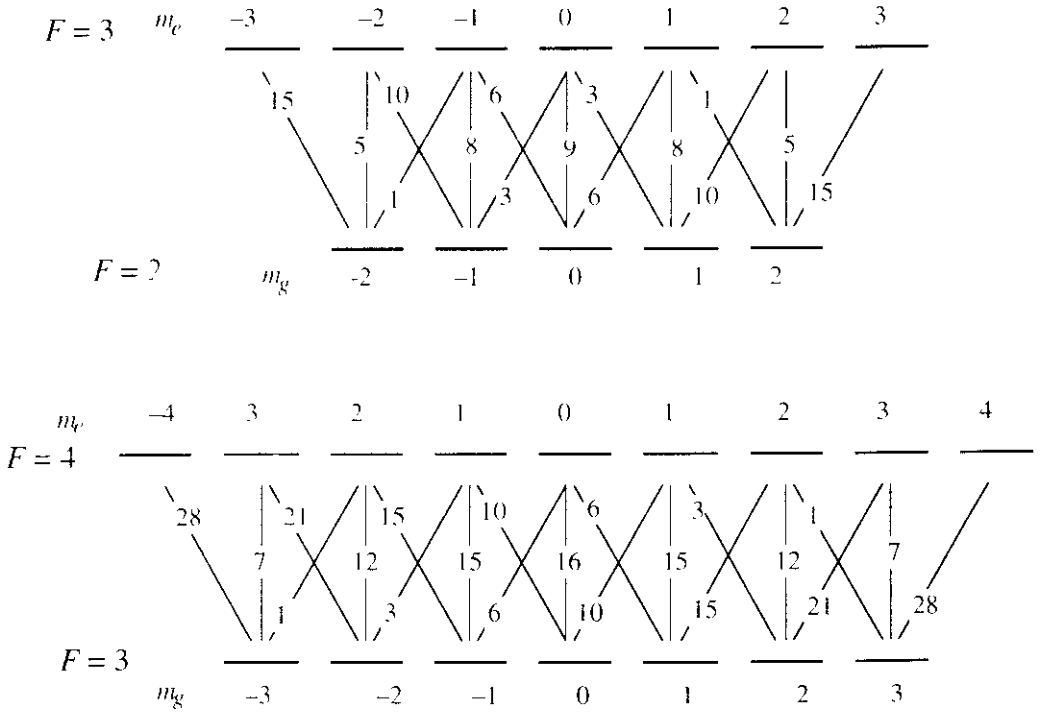

Figure A8-3 Clebsch-Gordan coefficients for F = 2 to F' = 3 and F = 3 to F' = 4 hyperfine transitions

Table A8-1 Useful formulae and data for rubidium

a) for D_2 line ($5S_{1/2}$ –$5P_{3/2}$) @ 780.027 nm

Line strength $S = \Sigma\mu^2$ $\quad S = \dfrac{3g_2\varepsilon_0\hbar\lambda^3\Gamma}{8\pi^2}$ = 2.44 x 10^{-57} C^2m^2, where g_2 is the Zeeman degeneracy of the excited state (=4).

Saturation intensity $\quad I_s = \dfrac{2\pi^2\hbar c\Gamma}{3\lambda^3}$ = 1.59 mW cm^{-2} (At resonance)

Spontaneous decay rate $\quad \Gamma$ = 2π x 5.76 MHz (D_2 line); natural lifetime = 28 ns

= 2π x 5.49 MHz (D_1 line); " " = 29 ns

Doppler width $\quad \Delta_D = \dfrac{2}{\lambda}\left[\dfrac{2k_BT\log_e 2}{m_{Rb}}\right]^{\frac{1}{2}}$ = 516 MHz at 300 K.

b) for ($5S_{1/2}$ –$6P_{3/2}$) @ 420.18 nm

Line strength $S = \Sigma\mu^2$ $\quad S = \dfrac{3g_2\varepsilon_0\hbar\lambda^3\Gamma}{8\pi^2}$ = 2.82 x 10^{-59} C^2m^2, where g_2 is the Zeeman degeneracy of the excited state (=4).

Spontaneous decay rate $\quad \Gamma$ = 2.67 MHz (two-level only); natural lifetime = 107 ns

Note that the natural lifetime includes decays to <u>all</u> levels

General formulae and quantities

Absorption coefficient $\quad \alpha(\omega) = \dfrac{ne^2f}{4\varepsilon_0 m_e c}S(\omega)\partial\omega$ where $\int_{-\infty}^{\infty} S(\omega)\partial\omega = 1$, n is the number density and f the oscillator strength.

Oscillator strength $\quad f_{1\to 2} = \dfrac{1}{g_1}\dfrac{4\pi m_e c\mu^2}{3e^2\hbar\lambda}$, g_1 is the Zeeman degeneracy of state 1.

$g_1 f_{1\to 2} = -g_2 f_{2\to 1}$

Doppler cooling limit T_D (780 nm) = 136 μK

" " speed = 16.3 cm s^{-1}

Photon recoil limit T_R (780 nm) = 0.184 μK

" " speed = 6.0 mm s^{-1}

Bibliography

Chapter1

1 S.Chu, L.Hollberg, J.E.Bjorkholm, A.Cable and A.Ashkin, *Three-dimensional viscous confinement and cooling of atoms by resonance radiation pressure*, Phys.Rev.Lett. **55**, 48 (1985).

2 S.Chu, J.E.Bjorkholm, A.Ashkin and A.Cable, *Experimental observation of optically trapped atoms*, Phys.Rev.Lett. **57**, 314 (1986).

3 A.P.Kazantsev, G.A.Ryabenko, G.I.Surdutovich and V.P.Yakovlev, *Scattering of atoms by light*, Physics Reports **129**, 75 (1985).

4 W.D.Phillips, P.L.Gould and P.D.Lett, *Cooling, stopping and trapping atoms*, Science **239**, 877 (1988).

5 D.J.Wineland and W.M.Itano, *Laser cooling*, Physics Today June 1987, p34.

6 J.Kepler, "De Cometis", (1619).

7 L.Motz and A.Duveen, "Essentials of Astronomy", (Columbia University Press 1971)

8 J.C.Maxwell, "A treatise on electricity and magnetism, article 792 (1897)", (Dover Publications, 1954).

9 V.G.Minogin and V.S.Letokhov, "Laser light pressure on atoms", (Gordon and Breach 1987).

10 P.Lebedev, Annalen der Physik. **6**, 433 (1901).

11 E.F.Nichols and G.F.Hull, Phys.Rev. **17**, 26 (1903).

12 P.Lebedev, Annalen der Physik **32**,411 (1910).

13 A.Einstein, Physik.Zeitschrift **18**, 121 (1917).

14 O.R.Frisch, Physik.Zeitschrift **86**, 42 (1933).

15 R.A.Beth, *Mechanical detection and measurement of the angular momentum of light*, Phys.Rev. **50**, 115 (1936).

16 A.Ashkin, Sci.Amer. **226**, 63 (1972).

17 J.-L.Picqué and J.-L.Vialle, *Atomic-beam deflection and broadening by recoils due to photon absorption or emission*, Opt.Comm. **5**, 402 (1972).

18 R.Schieder, H.Walther and L.Wöste, *Atomic beam deflection by the light of a tunable dye laser*, Opt.Comm. **5**, 337 (1972).

19 P.Jacquinot, S.Liberman, J.-L.Picqué and J.Pinard, *High resolution spectroscopic application of atomic beam deflection by resonant light*, Opt.Comm. **8**, 163 (1973).

20 D.J.Wineland and H.Dehmelt, Bull.Amer.Phys.Soc. **20**, 637 (1975).

21 T.W.Hänsch and A.L.Schawlow, *Cooling of gases by laser radiation*, Opt.Comm. **13**, 68 (1974).

22 W.Neuhauser, M.Hohenstatt, P.Toshek and H.Dehmelt, Phys.Rev.Lett. **41**, 233 (1978).
D.J.Wineland, R.E.Drullinger and F.L.Walls, Phys.Rev.Lett. **40**, 1639 (1978).

23 J.V.Prodan,W.D.Phillips and H.Metcalf, *Laser production of a very slow monoenergetic atomic beam,* Phys.Rev.Lett. **49**, 1149 (1982).
J.V.Prodan, A.Migdall,W.D.Phillips, I.So, H.Metcalf and J.Dalibard, *Stopping atoms with laser light,* Phys.Rev.Lett. **54**. 992 (1985).

24 V.I.Balykin, V.S.Letokhov, V.G.Minogin, Y.V.Roshdestvensky and A.I.Sidorov, *Radiative collimation of atomic beams,* J.Opt.Soc.Am. **B2**, 1776 (1985).

25 P.Moskowitz, P.L.Gould, S.Atlas and D.E.Pritchard, *Diffraction of an atomic beam by standing-wave radiation*, Phys.Rev.Lett. **51**, 370 (1983).

26 P.L.Gould, G.A.Ruff and D.E.Pritchard, *Diffraction of atoms by light: The near-resonant Kapitza-Dirac effect,* Phys.Rev.Lett. **56**. 827 (1986).

27 P.Martin, B.Oldaker, A.Miklich and D.E Pritchard, *Bragg scattering of atoms from a standing light wave,* Phys.Rev.Lett. **60**. 515 (1988).

28 E.L.Raab, M.Prentiss, A.Cable, S.Chu and D.E.Pritchard, *Trapping of neutral sodium atoms with radiation pressure*, Phys.Rev.Lett. **59**, 2631 (1987).

29 C.Monroe, W.Swann, H.Robinson and C.Wieman, *Very cold atoms trapped in a vapour cell*, Phys.Rev.Lett. **65**, 1571 (1990).

30 A.L.Migdall, J.V.Prodan, W.D.Phillips, T.H.Bergeman and H.J.Metcalf, *First observation of magnetically trapped neutral atoms,* Phys.Rev.Lett. **54**, 2596 (1985).

31 A.H.Compton, Phys.Rev. **22**, 409 (1923).

32 J.J.Tollett, C.C.Bradley, C.A.Sackett and R.G.Hulet, *Permanent magnet trap for cold atoms,* Phys.Rev.A **51**, R22 (1995).

33 W.Petrich, M.H.Anderson, J.R.Ensher and E.A.Cornell, *Stable,tightly confining magnetic trap for evaporative cooling of neutral atoms,* Phys.Rev.Lett. **74**, 3352 (1995).

34 M.H.Anderson, J.R.Ensher, M.R.Matthews, C.E.Wieman and E.A.Cornell, *Observation of Bose-Einstein condensation in a dilute atomic vapour,* Science **269**, 198 (1995).

35 P.Gill, H.A.Klein, A.P.Levick, M.Roberts, W.R.C.Rowley, P.Taylor, Phys.Rev.A **52**, R909 (1995).
E.Peik, G.Hollemann and H.Walther, *Laser cooling and quantum jumps of a single indium ion,* Phys.Rev.A **49**, 402 (1994).

36 P.D.Lett, R.N.Watts, C.I.Westbrook, W.D.Phillips, P.L.Gould and H.J.Metcalf, *Observation of atoms laser cooled below the Doppler limit*, Phys.Rev.Lett. **61**, 169 (1988).

37 Y.Shevy, D.Weiss, S.Chu, in "Spin polarised quantum systems" edited by S.Stringari, p287 (World Scientific 1989).

38 J.Dalibard, C.Salomon, A.Aspect, E.Arimondo, R.Kaiser, N.Vansteenkiste and C.Cohen-Tannoudji, in "Atomic physics 11" edited by S.Haroche, J.C.Gay and G.Grynberg, p199, (World Scientific 1989).

39 J.Dalibard and C.Cohen-Tannoudji, *Laser cooling below the Doppler limit by polarisation gradients: simple theoretical models*, J.Opt.Soc.Am.B **6**, 2023 (1989).

40 P.J.Ungar, D.S.Weiss, E.Riis and S.Chu, *Optical molasses and multilevel atoms: theory*, J.Opt.Soc.Am.B **6**, 2058 (1989).

41 C.Cohen-Tannoudji, *Les Houches, Session LIII 1990, Fundamental systems in quantum optics*, (Elsevier Science 1992).

42 A.Aspect, E.Arimondo, R.Kaiser, N.Vansteenkiste and C.Cohen-Tannoudji, *Laser cooling below the one-photon recoil energy by velocity-selective coherent population trapping*, Phys.Rev.Lett. **61**, 826 (1988).

43 N.Davidson, H-J.Lee, M.Kasevich and S.Chu, *Raman cooling of atoms in two and three dimensions*, Phys.Rev.Lett. **72**, 3158 (1994).

44 J.Reichel, O.Morice, G.M.Tino and C.Salomon, *Subrecoil Raman cooling of caesium atoms*, Europhys.Lett. **28**, 477 (1994).

45 E.Riis, D.S.Weiss, K.A.Moler and S.Chu, *Atom funnel for the production of a slow, high-density atomic beam*, Phys.Rev.Lett. **64**, 1658 (1990).

46 M.Kasevich, E.Riis, S.Chu and R.G.DeVoe, *rf spectoscopy in an atomic fountain*, Phys.Rev.Lett. **63**, 612 (1989).

47 C.S.Adams, H.J.Lee, N.Davison, M.Kasevich and S.Chu, *Evaporative cooling in a crossed dipole trap*, Phys.Rev.Lett. **74**, 3577 (1995).

48 K.B.Davis, M.Mewes, M Joffe, M.R.Andrews and W. Ketterle, *Evaporative cooling of sodium atoms*, Phys.Rev.Lett. **74**, 5202 (1995).

49 G.Grynberg and J.-Y.Courtois, *Proposal for a magneto-optical lattice for trapping atoms in nearly-dark states*, Europhys.Lett. **27**, 41 (1994).

50 A.Hemmerich, M.Weidmüller, T.Esslinger, C.Zimmerman and T.W.Hänsch, *Trapping atoms in a dark lattice*, Phys.Rev.Lett. **75**, 37 (1995).

51 L.Goldner, C.Gerz, R.Spreeuw,S.Rolston,C.Westbrook and W.Phillips, *Momentum transfer in laser-cooled cesium by adiabatic passage in a light field*, Phys.Rev.Lett **72**, 997 (1994).

52 C.J.Foot, *Laser cooling and trapping of atoms,* Contemporary Physics **32**, 369 (1991).

53 S.Chu, *Laser manipulation of atoms and particles,* Science **253**, 861 (1991).

54 S.Chu and C.Wieman (Eds), Special issue of J.Opt.Soc.Am.B, Vol **6**, devoted to laser cooling and trapping (1989).

55 H.Wallis, *Quantum theory of atomic motion in laser light,* Physics Reports **255**, 203 (1995).

56 H.Wallis, J.Werner and W.Ertmer, *Magneto-optical trapping of atoms,* Comments At.Mol.Phys. **28**, 275 (Gordon and Breach 1993)

57 K.Lindquist, M.Stephens and C.Wieman, *Experimental and theoretical study of the vapor-cell Zeeman optical trap*, Phys.Rev.A **46**, 4082 (1992).

58 J.Lawall, F.Bardou, B.Saubamea, K.Shimizu, M.Leduc, A.Aspect and C.Cohen-Tannoudji, *Two-dimensional subrecoil laser cooling*, Phys.Rev.Lett. **73**, 1915 (1994).

59 M.Kasevich and S.Chu, *Laser cooling below a photon recoil with 3-level atoms*, Phys.Rev.Lett. **69**, 1741 (1992).

60 C.Monroe, H.Robinson and C.Wieman, *Observation of the cesium clock transition using laser-cooled atoms in a vapor cell,* Opt.Lett **16**, 50 (1991).

61 A.Clairon, C.Salomon, S.Guellati and W.D.Phillips, *Ramsey resonance in a Zacharias fountain,* Europhys.Lett. **16**, 165 (1991).

62 N.F.Ramsey, *A molecular beam resonance method with separated oscillating fields,* Phys.Rev. **78**, 695 (1950).
N.F.Ramsey, *Experiments with separated oscillatory fields and hydrogen masers,* Reviews of Modern Physics, **62**, 541 (1990).

63 F.Nez, F.Biraben et al, *Determination of the Rydberg constant by direct measurement,* IEEE Trans. Instrumentation and Measurement, **44**, 568 (1995).

64 A.Ashkin, *Atomic-beam deflection by resonance-radiation pressure,* Phys.Rev.Lett. **25**, 1321 (1970).

65 A.F.Bernhardt, D.E.Duerre, J.R.Simpson and L.L.Wood, App.Phys.Lett **25**, 617 (1974).

66 Z-T.Lu et al, *Laser trapping of short-lived radioactive isotopes,* Phys.Rev.Lett. **72**, 3791 (1994).

67 G.Gwinner et al, *Magneto-optic trapping of radioactive ^{79}Rb,* Phys.Rev.Lett. **72**, 3795 (1994).

68 R.S.Schappe et al, *Electron collision cross-sections measured with the use os a magneto-optical trap,* Europhys.Lett. **29**, 439 (1995).

69 H.J.Miesner et al. *Indirect transverse laser cooling of a 7.3 MeV $^9Be^+$ ion beam in a storage ring,* Proc E.Q.E.C 1994 Amsterdam, session QThA4 p 182 (1994).

70 A.Ashkin and J.M.Dziedzic, Science **235**, 1517 (1987).

71 R.Pool and D.Pritchard, *Optics' new focus: beams of atoms,* Science **255**, 1513 (1992).

72 M.Brune and S.Haroche, Proceedings of 'Quantum dynamics of simple systems', 44th Scottish Universities summer school, Stirling August 1994.
M.Brune et al Phys.Rev.A **50**, R895 (1994).
M.Brune et al Phys.Rev.Lett. **72**, 3339 (1994) and Phys.Rev.Lett. **71**, 2360 (1993).

73 D.Cho, K.Sangster and E.A.Hinds, *An experiment to measure the Schiff interaction in TlF,* Phys.Rev.A **44**, 2783 (1991).
B.E.Sauer, J.Wang and E.A.Hinds, Phys.Rev.Lett. **74**, 1554 (1995).

74 M.C.Noecker, B.P.Masterson and C.E.Wieman, *Precision measurement of parity nonconservation in atomic cesium: a low-energy test of the electroweak theory,* Phys.Rev.Lett. **61**, 310 (1988).

75 D.S.Weiss, E.Riis, M.Kasevich, K.Moler and S.Chu, in "Light induced kinetic effects p35" L.Moi, E.Arimondo, Eds. (ETS Editions Pisa 1991).

76 B.Lounis, P.Verkerk, J-Y.Courtois, C.Salomon and G.Grynberg, *Quantised atomic motion in 1D Cesium molasses with magnetic field,* Europhys.Lett. **21**, 13 (1993).

77 A.Hemmerich, M.Weidmüller, T.Esslinger and T.W.Hänsch, *Collective atomic dynamics in a magneto-optical trap,* Europhys.Lett. **21**, 445 (1993).

78 A.Hemmerich and T.W.Hänsch, *Two-dimensional atomic crystal bound by light,* Phys.Rev.Lett. **70**, 410 (1993).

79 A.Hemmerich, C.Zimmerman and T.W.Hänsch, *Sub-kHz Rayleigh resonance in a cubic atomic crystal,* Europhys.Lett. **22**, 89 (1993).

80 A.Hemmerich and T.W.Hänsch, *Line strengths in vibrational spectra of a two-dimensional optical crystal,* Phys.Rev.A **48**, R1753 (1993).

81 A.Hemmerich, C.Zimmerman and T.W.Hänsch, *Multiphoton transitions in a spin-polarised 3D optical lattice,* Phys.Rev.Lett. **72**, 625 (1994).

82 A.Hemmerich, M.Weidmüller and T.W.Hänsch, *Four-wave mixing in a 3D optical lattice,* Europhys.Lett. **27**, 427 (1994).

83 P.Verkerk, D.R.Meacher, A.B.Coates, J-Y.Courtois, S.Guibal, B.Lounis, C.Salomon and G.Grynberg, *Designing optical lattices: an investigation with cesium atoms,* Europhys.Lett. **26**, 171 (1994).

84 D.R.Meacher, S.Guibal, C.Mennerat, J-Y.Courtois, K.I.Petsas and G.Grynberg, *Paramagnetism in a cesium optical lattice,* Phys.Rev.Lett. **74**, 1958 (1995).

85 J.-Y.Courtois, G.Grynberg, B.Lounis and P.Verkerk, *Recoil-induced resonances in cesium: An anology to the free-electron laser,* Phys.Rev.Lett. **72**, 3017 (1994).

86 K.I.Petsas, A.B.Coates and G.Grynberg, *Crystallography of optical lattices,* Phys.Rev.A **50**, 5173 (1994).

87 D.Sesko, T.Walker, C.Monroe, A.Gallagher and C.Wieman, *Collisional losses from a light-force atom trap*, Phys.Rev.Lett. **63**, 961 (1989).

88 M.Prentiss, A.Cable, J.E.Bjorkholm, S.Chu, E.L.Raab and D.Pritchard, *Atomic-density-dependent losses in an optical trap*, Opt.Lett. **13**, 452 (1988).

89 A.Cable, M.Prentiss and N.P.Bigelow, *Observations of sodium atoms in a magnetic molasses trap loaded by a continuous uncooled source*, Opt.Lett. **15**, 507 (1990).

90 D.Hoffman, P.Feng and T.Walker, *Measurements of Rb trap-loss collision spectra*, J.Opt.Soc.Am.B **11**, 712 (1994).

91 C.D.Wallace, T.P.Dineen, K-Y.N.Tan, TT.Grove and P.L.Gould, *Isotopic difference in trap loss collisions of laser cooled rubidium atoms,* Phys.Rev.Lett. **69**, 897 (1992).

92 A.Gallagher and D.E.Pritchard *Exoergic collisions of cold Na*-Na*, Phys.Rev.Lett. **63**, 957 (1989).

93 D.Hoffman, P.Feng, R.S.Williamson and T.Walker, *Excited-state collisions of trapped ^{85}Rb atoms*, Phys.Rev.Lett. **69**, 753 (1992).

94 S.Bali, D.Hoffman and T.Walker, *Novel intensity dependence of ultracold collisions involving repulsive states*, Europhys.Lett. **27**, 273 (1994).

95 C.D.Wallace, V.Sanchez-Villicana, T.P.Dineen and P.L.Gould, *Suppression of trap loss collisions at low temperature*, Phys.Rev.Lett. **74**, 1087 (1995).

96 P.S.Julienne, R.Heather and J.Vigue, *Theory of atomic collisions at ultracold temperatures,* Atomic Physics **12**, 116 (edited by J.Zorn and R.Lewis, AIP, New York 1991).

97 A.M.Smith and K.Burnett, *Effect of diffusion on laser cooling of atoms with long-range collisions,* J.Opt.Soc.Am.B **9**, 1240 (1992).

98 J.Gardner, R.Cline, J.Miller D.Heinzen, H.Boesten and B.Verhaar, *Collisions of doubly spin-polarised ultracold ^{85}Rb atoms,* Phys.Rev.Lett. **74**, 3764 (1995).

99 V.Sanchez-Villicana, S.Genemer, K.Tan, A.Kumarakrishnan, T.Dineen, W.Supitz and P.Gould, *Suppression of ultracold ground-state hyperfine-changing collisions with laser light,* Phys.Rev.Lett. **74**, 4619 (1995).

100 L.Marcassa, S.Muniz, E.deQueiroz, S.Zilio, V.Bagnato, J.Weiner, P.Julienne and K.-A.Suominen,*Optical suppression of photoassociative ionisation in a magnet-optical trap,* Phys.Rev.Lett. **73**, 1911 (1994).

101 R.Cline, J.Miller and D.Heinzen, *Study of Rb_2 long-range states by high-resolution photoassociation spectroscopy*, Phys.Rev.Lett. **73**, 632 (1994).
M.Holland, K.-A.Suominen and K.Burnett, *Quantal treatment of cold collisions in a laser field*, Phys.Rev.Lett. **72**, 2367 (1994).

102 C.Monroe, E.Cornell, C.Sackett,C.Myatt and C.Wieman, *Measurement of Cs-Cs elastic scattering at $T = 30\ \mu K$*, Phys.Rev.Lett. **70**, 414 (1993).

103 F.Riehle, Th.Kisters, A.Witte and J.Helmcke, *Optical Ramsey spectroscopy in a rotating frame: Sagnac effect in a matter-wave interferometer*, Phys.Rev.Lett. **67**, 177 (1991).

104 M.Weitz, B.Young and S.Chu, *Atom manipulation based on delayed laser pulses in three- and four-level systems: Light shifts and transfer efficiencies*, Phys.Rev.A **50**, 2438 (1994).

105 D.W.Keith, C.R.Ekstrom, Q.A.Turchette and D.E.Pritchard, *An interferometer for atoms*, Phys.Rev.Lett. **66**, 2693 (1991).

106 J.Schmiedmayer, M.S Chapman, C.R.Ekstrom, T.D.Hammond, S.Wehinger and D.E.Pritchard, *Index of refraction of various gases for sodium matter waves*, Phys.Rev.Lett. **74**, 1043 (1995).

107 M.Kasevich and S.Chu, *Laser cooling below a photon recoil with three-level atoms*, Phys.Rev.Lett. **69**, 1741 (1992).

108 K.E.Gibble, S.Kasapi and S.Chu, *Improved magneto-optic trapping in a vapor cell*, Opt.Lett. **17**, 526 (1992)

109 J.Tabosa, S.S.Vianna and C.A.Benevides, *Loading mechanism in a two-beam magneto-optical trap*, Opt.Comm. **116**, 77 (1995).

110 C.Wieman, G.Flowers and S.Gilbert, *Inexpensive laser cooling and trapping experiment for undergraduate laboratories*, Am.J.Phys. **63**, 317 (1995).

111 J.Dalibard, Y.Castin and K.Molmer, *Wave-function approach to dissipative processes in quantum optics*, Phys.Rev.Lett. **68**, 580 (1992).

112 K.Molmer, Y.Castin and J.Dalibard, *Monte Carlo wave-function method in quantum optics*, J.Opt.Soc.Am.B **10**, 524 (1993).

113 H.J.Carmichael and L.Tian, *Quantum measurement theory of photoelectric detection*, in "Opt.Soc.Am. Annual Meeting Technical Digest 1990, vol 15 of series".

114 P.Marte, R.Dum, R.Taïeb, P.D.Lett and P.Zoller, *Quantum wave function simulation of the resonance fluorescence spectrum from one-dimensional optical molasses*, Phys.Rev.Lett. **71**, 1335 (1993).

115 Y.Castin and K.Molmer, *Monte Carlo wave -function analysis of 3-D optical molasses*, Phys.Rev.Lett. **74**, 3772 (1995).

116 G.Nienhuis, J.de Kloe and P.van der Straten, *Quantum-trajectory pictures of laser cooling,* J.Opt.Soc.Am.B **12**, 520 (1995).

117 R.Taïeb, R.Dum, J.Cirac, P.Marte and P.Zoller, *Cooling and localisation of atoms in laser-induced potential wells,* Phys.Rev.A **49**, 4876 (1994).

118 M.Kasevich, E.Riis and S.Chu, *Normal-incidence reflection of slow atoms from an optical evanescent wave,* Optics Lett. **15**, 607 (1990).

119 C.G.Aminoff, A.M.Steane, P.Bouyer, P.Desboilles, J.Dalibard and C.Cohen-Tannoudji, *Cesium atoms bouncing in a stable gravitational cavity,* Phys.Rev.Lett. **71**, 3083 (1993).

120 V.Balykin, V.Letokhov, Y.B.Ovchinnikov and A.Sidorov, *Quantum-state-selective mirror reflection of atoms by laser light,* Phys.Rev.Lett. **60**, 2137 (1988).

121 T.M.Roach, H.Abele, M.G.Boshier, H.L.Grossman, K.P.Zetie and E.A.Hinds, *Realisation of a magnetic mirror for cold atoms,* Phys.Rev.Lett., **75**, 629 (1995).

122 CC.Bradley, C.A.Sackett, J.J.Tollett and R.G.Hulet, *Evidence of Bose-Einstein condensation in an atomic gas with attractive interactions,* Phys.Rev.Lett. **75**, 1687 (1995).

123 V.Bagnato, D.E.Pritchard and D.Kleppner, *Bose-Einstein condensation in an external potential,* Phys.Rev.A, **35**, 4354 (1987).

124 V.S.Letokhov and V.G.Minogin, *Laser radiation pressure on free atoms,* Physics Reports **73**, 1 (1981).

125 S.Stenholm, *The semiclassical theory of laser cooling,* Reviews of Modern Physics **58**, 699 (1986).

126 R.J. Cook, *Atomic motion in resonant radiation: An application of Ehrenfest's theorem,* Phys.Rev.A **20**, 224 (1979).

127 J.P.Gordon and A.Ashkin, *Motion of atoms in a radiation trap,* Phys.Rev.A **21**, 1606 (1980).

128 S. Stenholm, "Foundations of Laser Spectroscopy", (Wiley-Interscience 1984).

129 H.Haken, "Light, volume 1", (North-Holland 1981).

130 P.L.Knight, *The Rabi frequency in optical spectra,* Physics Reports **66**, 21 (1980).

131 S.Feneuille, *Interaction of laser radiation with free atoms,* in "Lasers in applied and fundamental research", edited by S.Stenholm, (Hilger 1985)

132 A.Hemmerich and T.W.Hänsch, *Radiation pressure vortices in two crossed standing waves,* Phys.Rev.Lett. **68**, 1492 (1992).

133 A.V.Durrant, K.E.Hill, S.Hopkins and E.Usadi, *A field-momentum approach to the semiclassical theory of light forces,* J.Mod.Opt. **42**, 131 (1995)

134 R.L.Shoemaker, *Coherent transient infrared spectroscopy,* in "Laser and Coherence Spectroscopy", edited by J.I.Steinfeld (Plenum Press 1978)

135 L.Allen and J.H.Eberly, "Optical resonance and two-level atoms", (Dover 1987)

136 R.P Feynman, F.L.Vernon and R.W.Hellwarth, *Geometrical representation of the Schrödinger equation for solving maser problems,* J. of App. Phys. (1957).

137 C.Cohen-Tannoudji, *Les Houches, Session XXVII 1975, Frontiers in laser spectroscopy,* 1 (North-Holland 1977).

138 A.Ashkin, *Trapping of atoms by resonance radiation pressure,* Phys.Rev.Lett **40**, 729 (1978).

139 S.Stenholm, *Laser cooling and trapping,* Eur. J.Phys. **9**, 242 (1988).

140 G.Nienhuis, P.van der Straten and S-Q.Shang, *Operator description of laser cooling below the Doppler limit,* Phys.Rev.A **44**, 462 (1991).

141 N.Davison, H.Lee, C.S.Adams, M.Kasevich and S.Chu, *Long atomic coherence times in an optical dipole trap,* Phys.Rev.Lett. **74**, 1311 (1995).

J.Chen, J.Story, J.J.Tollett and R.G.Hulet, *Adiabatic cooling of atoms by an intense standing wave,* Phys.Rev.Lett. **69**, 1344 (1992).

R.J.Spreeuw, C.Gerz, L.Goldner, W.D.Phillips, S.L.Rolston and C.Westbrook, *Demonstration of neutral atom trapping with microwaves,* Phys.Rev.Lett. **72**, 3162 (1994).

142 J.D.Miller, R.A.Cline and D.J.Heinzen, *Far-off-resonance optical trapping of atoms,* Phys.Rev.A **47**, R4567 (1993).

143 D.F.Lawden, "Tensor calculus and relativity", (Chapman & Hall Science 1975).

144 C.Baxter, M.Babiker and R.Loudon, *Canonical approach to photon pressure,* Phys.Rev.A **47**, 1278 (1993).

145 V.S.Letokhov, V.G.Minogin and B.D.Pavlik, *Cooling and capture of atoms and molecules by a resonant light field,* Sov. Phys. JETP **45**, 698 (1977).

146 V.G.Minogin and O.T.Serimaa, *Resonant light pressure forces in a strong standing laser wave,* Opt. Comm. **30b**, 373 (1979).

147 S.Stenholm and W.E.Lamb Jr, *Semiclassical theory of a high-intensity laser,* Phys.Rev. **181**, 618 (1969).

E.Kyrölä and S Stenholm, *Velocity tuned resonances as multi-doppleron processes,* Opt.Comm **22**, 123 (1977).

148 J.J.Tollett, J.Chen, J.G.Story, N.Ritchie, C.C.Bradley and R.G.Hulet, *Observation of velocity-tuned multiphoton "Doppleron" resonances in laser-cooled atoms,* Phys.Rev.Lett. **65**, 559 (1990).

149 N.P.Bigelow and M.G.Prentiss, *Direct observation of the influence of Doppler-induced resonances on atomic velocities,* Phys.Rev.Lett. **65**, 555 (1990).

150 J Dalibard and C.Cohen-Tannoudji, *Dressed-atom approach to atomic motion in laser light: the dipole force revisited,* J.Opt.Soc.Am.B **2**, 1707 (1985).

151 A.Einstein, *On the theory of Brownian motion,* Ann.Physik **19**, 371 (1906).

152 H.Risken, "The Fokker-Planck equation", (Springer-Verlag 1989).

153 R.P.Feynmann, "The Feynmann lectures on physics, Vol I", (Addison-Wesley 1963)

154 W.M.Itano and D.J.Wineland, *Laser cooling of ions stored in harmonic and Penning traps,* Phys.Rev.A **25**, 35 (1982).

155 R.J.Cook, *Quantum-mechanical fluctuations of the resonance radiation force,* Phys.Rev.Lett **44**, 976 (1980).

156 R.J.Cook, *Directions in the theory of resonance-radiation pressure,* Comments Atom.Mol.Phys. **10**, 267 (Gordon and Breach 1981).

157 R.J.Cook, *Theory of resonance-radiation pressure,* Phys.Rev.A **22**, 1078 (1980).

158 J.Dalibard and C.Cohen-Tannoudji, *Atomic motion in laser light: connection between semiclassical and quantum descriptions,* J.Phys.B:At.Mol.Phys **18**, 1661 (1985).

159 E.Wigner, Phys.Rev. **40**, 749 (1932).

160 J.Javanainen, *Realistic laser cooling theory for multi-state atoms,* Opt Comm **86**, 475 (1991).

161 P.D.Lett, W.D.Phillips, S.L.Rolston, C.E.Tanner, R.N.Watts and C.I.Westbrook, *Optical molasses,* J.Opt.Soc.Am.B **6**, 2084 (1989).

162 A.M.Steane, M.Chowdhury and C.J.Foot, *Radiation force in the magneto-optical trap,* J.Opt.Soc.Am.B **9**, 2142 (1992).

163 S.Chu, M.Prentiss, A.Cable and J.Bjorkholm, *Laser cooling and trapping of atoms,* Proc.Int.Conf.Laser Spectroscopy VIII, p58 (Springer-Verlag 1987).

164 A.Ashkin and J.P.Gordon, *Stability of radiation-pressure particle traps: an optical Earnshaw theorem,* Opt.Lett. **8**, 511 (1983).

165 D.E.Pritchard, E.L.Raab, V.Bagnato, C.E.Wieman and R.N.Watts, *Light traps using spontaneous forces,* Phys.Rev.Lett. **57**, 310 (1986).

166 D.Haubrich, A.Höpe and D.Meschede, *A simple model for optical capture of atoms in strong magnetic quadrupole fields,* Opt.Comm. **102**, 225 (1993).

167 W.Petrich, M.H.Anderson, J.R.Ensher and E.A Cornell, *Behaviour of atoms in a compressed magneto-optical trap,* J.Opt.Soc.Am.B, **11**, 1332 (1994).

168 M.Gajda and J.Mostowski, *Three-dimensional theory of the magneto-optical trap: Doppler cooling in the low intensity limit,* Phys.Rev.A, **49**, 4864 (1994).

169 A.Steane, D.Phil thesis , *Laser cooling of atoms,* Oxford University (1991).

170 W.Ertmer, R.Blatt, J.L.Hall and M.Zhu, *Laser manipulation of atomic beam velocities: demonstration of stopped atoms and velocity reversal,* Phys.Rev.Lett. **54**, 996 (1985).

171 W.D. Phillips and H.J.Metcalf, *Laser deceleration of an atomic beam*, Phys.Rev.Lett. **48**, 596 (1982).

172 G.Birkl, MGatzke, I.H.Deutsch, S.L.Rolston and W.D.Phillips, *Bragg scattering from atoms in optical lattices*, Phys.Rev.Lett. **75**, 2823 (1995).

173 M.Weidmüller, A.Hemmerich, A.Görlitz, T.Esslinger and T.W.Hänsch, *Bragg diffraction in an atomic lattice bound by light*, Phys.Rev.Lett. **75**, 4583 (1995).

174 A.G.Sinclair, E.Riis and M.J.Snadden, *Improved trapping in a vapor-cell magneto-optical trap with multiple laser frequencies*, J.Opt.Soc.Am.B **11**, 2333 (1994).

175 C.Wieman, T.Walker, D.Sesko and C.Monroe, *Curious behaviour of optically trapped neutral atoms*, Proc.Int.Conf.Atomic Physics **12**, 58 (ed. J.Zorn and R.Lewis, AIP Press 1991).

176 T.Walker, D.Sesko and C.Wieman, *Collective behaviour of optically trapped neutral atoms*, Phys.Rev.Lett. **64**, 408 (1990).

177 J.Dalibard, *Laser cooling of an optically thick gas: the simplest radiation pressure trap?*, Opt.Comm. **68**, 203 (1988).

178 D.W.Sesko, T.G.Walker and C.E.Wieman, *Behaviour of neutral atoms in a spontaneous force trap*, J.Opt.Soc.Am.B **8**, 946 (1991).

179 N.P.Bigelow and M.G.Prentiss, *Observation of channeling of atoms in the three-dimensional interference pattern of optical standing waves*, Phys.Rev.Lett, **65**, 29 (1990).

180 B.R.Mollow, *Power spectrum of light scattered by two-level systems*, Phys.Review **188**, 1969 (1969).

181 V.S.Bagnato, L.G.Marcassa, M.Oria, G.I.Surdutovich, R.Vitlina and S.C.Zilio, *Spatial distribution of atoms in a magneto-optical trap*, Phys.Rev.A **48**, 3771 (1993).

182 I.Guedes, M.T.de Araujo, D. Milori, G.I.Surdutovich, V.S.Bagnato and S.C.Zilio, *Forces acting on magneto-optically trapped atoms*, J.Opt.Soc.Am.B **11**, 1935 (1994).

183 P.Kohns, P.Buch, W.Supitz, C.Csambal and W.Ertmer, *On-line measurement of sub-Doppler temperatures in a Rb Magneto-optical trap by trap centre oscillations*, Europhys.Lett. **22**, 517 (1993).

184 D.R.Meacher, D.Boiron, H.Metcalf, C.Salomon and G.Grynberg, *Method for velocimetry of cold atoms*, Phys.Rev.A **50,** R1992 (1994).

185 M.Kasevich, D.S.Weiss, E.Riis, K.Moler, S.Kasapi and S.Chu, *Atomic velocity selection using stimulated Raman transitions*, Phys.Rev.Lett. **66**, 2297 (1991).

186 A.V.Durrant, E.Usadi, K.E.Hill and S.Hopkins, *Proposed temperature measurements of laser-cooled samples by coherent optical transients*, in "IEEE

Technical Digest 1994 European Quantum Electronics Conference, Amsterdam, session QTuG5".

187 A.M.Steane and C.J.Foot, *Laser cooling below the Doppler limit in a magneto-optical trap*, Europhys.Lett. **14**, 231 (1991).

188 C.D.Wallace, T.P.Dinceen, K.Y.N.Tan, A.Kumarakrishnan, P.L.Gould and J.Javanainen, *Measurements of temperature and spring constant in a magneto-optical trap*, J.Opt.Soc.Am.B **11**, 703 (1994).

189 J.Lawall, F.Bardou, B.Sauamea, K.Shimizu, M.Leduc, A.Aspect and C.Cohen-Tannoudji, *Two-dimensional subrecoil laser cooling*, Phys.Rev.Lett. **73**, 1915 (1994).

190 C.J.Cooper, G.Hildenbrand, J.Rink, C.Townsend, K.Zetie and C.J.Foot, *The temperature of atoms in a magneto-optical trap*, Europhys.Lett., **28**, 397 (1994).

191 C.Salomon, J.Dalibard, W.D.Phillips, A.Clairon and S.Guellati, *Laser cooling of caesium atoms below 3 μK*, Europhys.Lett. **12**, 683 (1990).

192 Y.Castin and J.Dalibard, *Quantization of atomic motion in optical molasses*, Europhys.Lett. **14**, 761 (1991).

193 K.Berg-Sorensen, Y.Castin, K.Molmer and J.Dalibard, *Cooling and tunnelling of atoms in a 2D laser field*, Europhys.Lett. **22**, 663 (1993).

194 B.Sheehy, S.Q.Shang, P.van der Straten, S.Hatamian and H.Metcalf, *Magnetic-field-induced laser cooling below the Doppler limit*, Phys.Rev.Lett. **64**, 858 (1990).

195 S.Q.Shang, B.Sheehy, P.van der Straten and H.Metcalf, *Velocity-selective magnetic-resonance laser cooling*, Phys.Rev.Lett. **65**, 317 (1990).

196 S.Q.Shang, B.Sheehy, H.Metcalf, P.van der Straten and G.Nienhuis, *Velocity-selective resonances and sub-Doppler laser cooling*, Phys.Rev.Lett. **67**, 1094 (1991).

197 A.M.Steane, G.Hillenbrand and C.J.Foot, *Polarisation gradient cooling in a one-dimensional $\sigma^+\sigma^-$ configuration for any atomic transition*, J.Phys.B: At.Mol.Opt Phys. **25**, 4721 (1992).

198 C.G.Townsend, N.H.Edwards, C.J.Cooper, K.P.Zetie and C.J.Foot, *Phase-space density in the magneto-optical trap*, Phys.Rev.A **52**, 1423 (1995).

199 K.Molmer, *Friction and diffusion coefficients for cooling of atoms in laser fields with multidimensional periodicity*, Phys.Rev.A **44**, 5820 (1991).

200 M.Walhout, J.Dalibard, S.L.Rolston and W.D.Phillips, *σ^+-σ^- Optical molasses in a longitudinal magnetic field*, J.Opt.Soc.Am.B, **9**, 1997 (1992).

201 C.Salomon, J.Dalibard, A.Aspect, H.Metcalf and C.Cohen-Tannoudji, *Channelling atoms in a laser standing wave*, Phys.Rev.Lett. **59**, 1659 (1987).

202 C.I.Westbrook, R.N.Watts, C.E.Tanner, S.L.Rolston, W.D.Phillips and P.D.Lett. *Localisation of atoms in a three-dimensional standing wave*, Phys.Rev.Lett. **65**, 33 (1990).

203 P.Verkerk, B.Lounis, C.Salomon, C.Cohen-Tannoudji, J-Y.Courtois and G.Grynberg, *Dynamics and spatial order of cold caesium atoms in a periodic optical potential*, Phys.Rev.Lett. **68**, 3861 (1992).

204 P.S.Jessen, C.Gerz, P.D.Lett, W.D.Phillips, S.L.Rolston, R.J.C.Spreeuw and C.I.Westbrook, *Observation of quantised motion of Rb atoms in an optical field*, Phys.Rev.Lett. **69**, 49 (1992).

205 G.Grynberg, B.Lounis, P.Verkerk, J-Y.Courtois and C.Salomon, *Quantised motion of cold caesium atoms in two- and three-dimensional optical potentials*, Phys.Rev.Lett. **70**, 2249 (1993).

206 P.W.Milonni and J.H.Eberly, in "Lasers", chapters 17 and 18, (John Wiley 1988).

207 I.H.Deutsch, R.J.C.Spreeuw, S.L.Rolston and W.D.Phillips, *Photonic bandgaps in optical lattices*, Phys.Rev.A **52**, 1394 (1995).

208 C.Gerz, T.Hodapp, P.Jessen, K.M.Jones, W.D.Phillips, C.Westbrook and K.Molmer, *The temperature of optical molasses for two different atomic angular momenta*, Europhys.Lett. **21**, 661 (1993).

209 J.Guo, P.R.Berman, B.Dubetsky and G.Grynberg, *Recoil-induced resonances in nonlinear spectroscopy*, Phys.Rev.A **46**, 1426 (1992).

210 J.Guo, *Four-wave mixing in one-dimensional optical molasses*, Phys.Rev.A **51**, 2338 (1995).

211 D.Grison, B.Lounis, C.Salomon, J-Y.Courtois and G.Grynberg, *Raman spectroscopy of cesium atoms in a laser trap*, Europhys.Lett. **15**, 149 (1991).

212 J.Tabosa, G.Chen, Z.Hu, R.B.Lee and H.J.Kimble, *Nonlinear spectroscopy of cold atoms in a spontaneous-force optical trap*, Phys.Rev.Lett. **66**, 3245 (1991).

213 L.Hilico, C.Fabre and E.Giacobino, *Operation of a 'cold-atom laser' in a magneto-optical trap*, Europhys.Lett. **18**, 685 (1992).

214 B.Lounis, J-Y.Courtois, P.Verkerk, C.Salomon and G.Grynberg, *Measurement of the friction coefficient in 1D corkscrew optical molasses by stimulated Rayleigh spectroscopy*, Phys.Rev.Lett. **69**, 3029 (1992).

215 R.H.Dicke, *The effect of collisions upon the Doppler width of spectral lines*, Phys.Rev. **89**, 472 (1953).

216 D.Wineland and W.Itano, *Laser cooling of atoms*, Phys.Rev.A **20**, 1521 (1979). C.Cohen-Tannoudji, Personal communication (re Mossbauer effect).

217 R.Dum, P.Marte, T.Pellizzari and P.Zoller, *Laser cooling to a single quantum state in a trap*, Phys.Rev.Lett. **73**, 2829 (1994).

218 A.V.Bezverbnyî and V.S.Smirnov, *Probe-field spectroscopy in atomic media optically oriented in the ground state*, JETP **78**, 33 (1994).

219 As surmised from the number of speakers at EQEC 1994, Amsterdam who mentioned Bragg diffraction from localised atoms.

220 A.Aspect, J.Dalibard, A.Heidmann, C.Salomon and C.Cohen-Tannoudji, *Cooling atoms with stimulated emission*, Phys.Rev.Lett. **57**, 1688 (1986).

221 M.Weidmüller, T.Esslinger, M.A.Ol'shanii, A.Hemmerich and T.W.Hänsch, *A novel scheme for efficient cooling below the photon recoil limit*, Europhys.Lett. **27**, 109 (1994).

222 G.Grynberg and J-Y.Courtois, *Proposal for a magneto-optical lattice for trapping atoms in nearly-dark states*, Europhys.Lett. **27**, 41 (1994).

223 A.Aspect, E.Arimondo, R.Kaiser, N.Vansteenkiste and C.Cohen-Tannoudji, *Laser cooling below the one photon recoil energy by velocity-selective coherent population trapping: theoretical analysis*, J.Opt.Soc.Am.B **6**, 2112 (1989).

224 M.A.Ol'shanii and V.G.Minogin, *Three-dimensional velocity-selective coherent population trapping of a (3+3)-level atom*, Opt.Comm. **89**, 393 (1992).

225 F.Papoff, F.Mauri and E.Arimondo, *Transient velocity-selective coherent population trapping in one dimension*, J.Opt.Soc.Am.B **9**, 324 (1992).

226 P.Bouyer, P.Lemonde, M.Ben-Dahan, A.Michaud, C.Salomon and J.Dalibard, *An atom trap relying on optical pumping*, Europhys.Lett. **27**, 569 (1994).

227 J.Söding, R.Grimm, J.Kowalski, Y.B.Ovchinnikov and A.I.Sidorov, *Observation of the magneto-optical radiation force by laser spectroscopy*, Europhys.Lett. **20**, 101 (1992).

228 R.Grimm, J.Söding, Y.B.Ovchinnikov and A.I.Sidorov, *Sub-Doppler manifestation of the magneto-optical radiation force*, Opt.Comm. **98**, 54 (1993).

229 O.Emile, F.Bardou, C.Salomon, P.Laurent, A.Nadir and A.Clairon, *Observation of a new magneto-optical trap*, Europhys.Lett. **20**, 687 (1992).

230 T.Walker, P.Feng, D.Hoffman and R.S.Williamson, *Spin-polarized spontaneous-force atom trap*, Phys.Rev.Lett. **69**, 2168 (1992).

231 T.Walker, P.Feng, D.Hoffman and R.S.Williamson, *A vortex-force atom trap*, Phys.Lett.A, **163**, 309 (1992).

232 R.Gupta, C.Xie, S.Padua, H.Batelaan and H.Metcalf, *Bichromatic laser cooling in a three-level system*, Phys.Rev.Lett. **71**, 3087 (1993).

233 W.Ketterle, K.B.Davis, M.Joffe, A.Martin and D.E.Pritchard, *High densities of cold atoms in a dark spontaneous force optical trap*, Phys.Rev.Lett. **70**, 2253 (1993).

234 A.Höpe, D.Haubrich, H.Schadwinkel, F.Strauch and D.Meschede, *Optical trapping in a caesium cell with linearly polarised light and at zero magnetic field*, Europhys.Lett. **28**, 7 (1994).

235 H.Hess et al, *Magnetic trapping of spin-polarised atomic hydrogen*, Phys.Rev.Lett. **59**, 672 (1987).

236 K.Huang, "Statistical Mechanics", (Wiley, New York 1963).

237 M.Born and E.Wolf, "Principles of Optics", (Pergamon, New York 1970).

238 A.Hemmerich and T.Hänsch, *Radiation pressure vortices in two crossed standing waves*, Phys.Rev.Lett. **68**, 1492 (1992).

239 A.Hemmerich, D.Schropp.Jr and T.Hänsch, *Light forces in two crossed standing waves with controlled time-phase difference*, Phys.Rev.A **44**,1910 (1991).

240 F.Shimizu, K.Shimizu and H.Takuma, *Four-beam laser trap of neutral atoms*, Opt.Lett. **16**, 339 (1991).

241 B.A.Robson, "The theory of polarisation phenomena", (Clarendon Press 1974).

242 E.Hecht and A.Zajac, "Optics", (Addison-Wesley 1974).

243 J.D.Jackson, "Classical electrodynamics", (J.Wiley & sons 1962).

244 J.Aharoni, "The special theory of relativity", (Clarendon press 1965).

245 J.Hilgevoord and E.A.deKerf, *The covariant definition of spin in relativistic quantum field theory*, Physica **31**, 1002 (1965).

246 F.Belinfante, Physica **6**, 887 (1939).
L.Rosenfeld, Mém.Acad.Roy.Belg. **18**, 6 (1940).

247 K.B.McAdam, A.Steinbach and C.Wieman, *A narrow-band tunable diode laser system with grating feedback, and a saturated absorption spectrometer for Cs and Rb*, Am.J.Phys. **60**, 1098 (1992).

248 R.N.Watts and C.E.Wieman, *Manipulating atomic velocities using diode lasers*, Opt.Lett. **11**, 291 (1986).

249 D.Sesko, C.G.Fan and C.E.Wieman, *Production of a cold atomic vapor using diode-laser cooling*, J.Opt.Soc.Am. **5**, 1225 (1988).
C.Wieman and L.Hollberg, *Using diode lasers for atomic physics*, Rev.Sci.Instrum. **62**, 1 (1991).

250 R.Watts and C.Wieman, *Stopping atoms with diode lasers*, Proc.Int.Conf.Laser Spectroscopy VII, Maui, Hawaii, p20, (ed. T.W.Hänsch and Y.R.Shen, Springer-Verlag Berlin 1985).

251 M. Ohtsu, "Highly Coherent Semiconductor Lasers", (Artech House 1992).

252 J.C.Camparo, *The diode laser in atomic physics*, Contemp.Phys. **26**, 443 (1985).

253 E.Usadi, *Diode laser system for atomic physics*, Open University Physics Department internal report PD 9406, (1994).

254 C.C.Bradley, J.Chen and Randall G. Hulet, *Instrumentation for the stable operation of laser diodes*, Rev.Sci.Instrum. **61**, 2097 (1990).

255 A.Corney, "Atomic and Laser Spectroscopy", chapter 13, (Clarendon Press 1977).

256 S.Nakayama, *Theoretical analysis of Rb and Cs D_2 lines in Doppler-free spectroscopic tecniques with optical pumping*, Japanese J.Phys. **24**, 1 (1985).

257 M.Têtu, B.Villeneuve, N.Cyr, P.Tremblay, S.Thériault and M.Breton, *Multiwavelength sources using laser diodes frequency-locked to atomic resonances*, Journal of Lightwave.Technology **7**, 1540 (1989).
G.P.Barwood, P.Gill and W.R.C.Rowley, *Frequency measurements on optically narrowed Rb-stabilised laser diodes at 780 nm and 795 nm*, App.Phys.B **53**, 142 (1991).

258 B.Dahmani, L.Hollberg and R.Drullinger, *Frequency stabilisation of semiconductor lasers by resonant optical feedback*, Opt.Lett. **12**, 876 (1987).

259 G.P.Barwood, P.Gill and W.R.C.Rowley, *An optically narrowed diode laser for Rb saturation spectroscopy*, Journal of Modern Optics, **37**, 749 (1990).

260 R.Wyatt and W.J.Devlin, *10 kHz linewidth 1.5 μm InGaAsP external cavity laser with 55 nm tuning range*, Electron.Lett. **19**, 110 (1983).

261 K.C.Harvey and C.J.Myatt, *Extenal-cavity diode laser using a grazing incidence diffraction grating*, Opt.Lett. **16**, 910 (1991).

262 K.Matsuda, H.Minemoto, O.Kamada and S.Ishizuka, *Bi-substituted rare-earth iron garnet composite film with temperature independent Faraday rotation for optical isolators*, IEEE Transactions on Magnetics **23**, 3479 (1987).

263 P.Spano, S.Piazolla and M.Tamburrini, *Frequency and intensity noise in injection-locked semiconductor lasers: theory and experiments*, IEEE Journal of Quantum.Electronics, **QE22**, 427 (1986).
G.R.Hadley, *Injection locking of diode lasers*, IEEE Journal of Quantum.Electronics, **QE22**, 419 (1986).

264 Sharp (laser diode manufacturers) "Laser diode user's manual".

265 H.A.Steinherz, "Handbook of high-vacuum engineering", (Reinhold 1963).
J.H.Moore, C.C.Davis, M.A.Coplan, "Building scientific apparatus", (Addison-Wesley 1989 edition).

266 R.Honig and D.Kramer, *Vapour pressure data for the solid and liquid elements*, RCA Review **29**, 285 (RCA Laboratories, Princeton, N.J. 1968).

267 M.Stephens and C.Wieman, *High collection efficiency in a laser trap*, Phys.Rev.Lett. **72**, 3787 (1994).

268 Melles-Griot Inc. (optics manufacturers), "Optics guide 5", (1993).

269 S.Nakayama, *Spectroscopic data of Rydberg states in alkali atoms*, Faculty of Science and Technology, Sophia University Tokyo (1981).

270 P.R.Berman, J.M.Levy and R.G.Brewer, Phys.Rev.A **11**, 1668 (1975).

271 R.L.Shoemaker, *Coherent transient infrared spectroscopy* in "Laser and coherence spectroscopy", p197, ed. J.I.Steinfield (New York Plenum 1978).

272 T.W.Mossberg and S.R.Hartmann, Phys.Rev.A **23**, 1271 (1981).

273 A.Rümmager and A.Spielbinder, *Public keys in quantum cryptography*, J.Arc.Res.Auth. **1**, 111, (Questor 1999).

274 N.A.Kurnit, I.D.Abella and S.R.Hartmann, *Observation of a photon echo*, Phys.Rev.Lett. **13**, 567 (1964).

275 C.K.N.Patel and R.E.Slusher, *Photon echoes in gases*, Phys.Rev.Lett. **20**, 1027 (1968).

276 E.L.Hahn, Phys.Rev. **80**, 580 (1950).

277 R.Beach, S.R.Hartmann and R.Friedberg, *Billiard-ball echo model*, Phys.Rev.A **25**, 2658 (1982).

278 A.V.Durrant, J.Manners and P.M.Clark, *Understanding optical echoes using Schrödinger's equation*, Eur.J.Phys. **10**, 291 (1989).

279 A.V.Durrant and J.Manners, *Collision cross-sections for the noble-gas broadening of the Cs 6S-7P doublet using photon echoes*, J.Phys.B: At.Mol.Phys. **17**, L701 (1984).

280 J.Manners, D.Phil thesis, Oxford University (1981)

281 I.Shoshan, N.N.Danon and U.P.Oppenheim, *Narrowband operation of a pulsed dye laser without intracavity beam expansion*, J.App.Phys. **48**, 4495 (1977).

282 J.Lawler, W.Fitzsimmons and L.Anderson, *Narrow bandwidth dye laser suitable for pumping by a short pulse duration N_2 laser*, Applied Optics **15**, 1083 (1976).

283 T.W.Hänsch, *Repetitively pulsed tunable dye laser for high resolution spectroscopy*, Applied Optics **11**, 895 (1972).

284 A.P Thorne, "Spectrophysics" (Chapman and Hall 1988), and reference[206].

285 R.H.Dicke, *Coherence in spontaneous radiation processes*, Phys.Rev. **93**, 99 (1954).

286 J.C.Macgillivray and M.S.Feld, *Superradiance in atoms and molecules*, Contemp.Phys. **22**, 299 (1981).

287 M.Gross, C.Fabre, P.Pillet and S.Haroche, *Observation of near-infrared superradiance on cascading transitions in atomic sodium*, Phys.Rev.Lett. **36**, 1035 (1976).

288 H.M.Gibbs, Q.H.Vrehen and H.M Hikspoors, Phys.Rev.Lett. **39**, 547 (1977).